UNIVERSITÉ DE LORRAINE | BIBLIOTHÈQUES UNIVERSITAIRES

AVERTISSEMENT
DROIT D'AUTEUR

Ce document est le fruit d'un long travail approuvé par le jury de soutenance et mis à disposition de l'ensemble de la communauté universitaire élargie.

Il est soumis à la propriété intellectuelle de l'auteur. Ceci implique une obligation de citation et de référencement lors de l'utilisation de ce document. Toute contrefaçon, plagiat ou reproduction illicite encourt une poursuite pénale.

Contact bibliothèque : ddoc-theses-contact@univ-lorraine.fr
(Cette adresse ne permet pas de contacter les auteurs)

Code de la Propriété Intellectuelle. articles L 122. 4
Code de la Propriété Intellectuelle. articles L 335.2- L 335.10

UNIVERSITÉ DE LORRAINE
34 COURS LÉOPOLD — CS 25233
54052 NANCY CEDEX
TÉL : 03 54 50 54 00
CONTACT@UNIV-LORRAINE.FR
WWW.UNIV-LORRAINE.FR

Thèse

Présentée et soutenue publiquement pour l'obtention du titre de

DOCTEUR DE l'UNIVERSITE DE LORRAINE

Mention : Génie des Procédés, des Produits et des Molécules

Par Omar ALJASEM ALHMIEDY

Sous la direction de :

Dr. Bouchra BELAISSAOUI

Pr. Sabine RODE

Hollow fiber membrane contactors for intensification of stripping operations, generic approach and application to water treatment

Présentée en vue d'une soutenance le 15 Décembre 2025

Membres du jury :

Directeur(s) de thèse :	**Dr. Bouchra BELAISSAOUI**	**Maîtresse de conférences HDR à l'Université de Lorraine, ENSIC, ENSAIA, LRGP, Nancy.**
	Pr. Sabine RODE	**Professeure à l'Université de Lorraine, ENSIC, LRGP, Nancy.**
Président de jury :	**Pr. Barbara ERNST**	**Professeure à l'Université de Strasbourg, CNRS, IPHC, RePSeM, ECPM, Strasbourg.**
Rapporteurs :	**Pr. Jean-Christophe REMIGY**	**Professeur à l'Université Paul Sabatier, Toulouse 3, Toulouse.**
	Dr. Marwen MOUSSA	**Maître de conférences HDR à l'Université Paris-Saclay, INRAE, AgroParisTech, UMR SayFood, Palaiseau.**
Examinateurs :	**Pr. Barbara ERNST**	**Professeure à l'Université de Strasbourg, CNRS, IPHC, RePSeM, ECPM, Strasbourg.**
	Dr. Rainier HREIZ	**Maître de conférences à l'Université de Lorraine, ENSIC, LRGP, Nancy.**

Contents

LIST OF FIGURES **6**

LIST OF TABLES **9**

NOMENCLATURE **12**

ABSTRACT **15**

RESUME **16**

GENERAL INTRODUCTION **18**

CHAPTER 1. STRIPPING OPERATION CONVENTIONAL AND ALTERNATIVE TECHNOLOGY 21

1.1 INTRODUCTION 22
1.2 OVERVIEW OF STRIPPING OPERATIONS 23
1.3 CONVENTIONAL STRIPPING TECHNOLOGIES : APPLICATIONS AND EXAMPLES 25
1.3.1 Stripping Technologies 25
1.3.2 Stripping applications and examples 25
1.4 OVERCOMING CONVENTIONAL STRIPPING CHALLENGES WITH MEMBRANE CONTACTORS 40
1.5 CONCLUSION 41
1.6 REFERENCES 42

CHAPTER 2. MEMBRANE CONTACTOR FOR STRIPPING OPERATION 45

2.1 INTRODUCTION 46
2.2 FUNDAMENTALS OF HFMC DESIGN 48
2.2.1 Core Principles: Design, Fluidics, and Trade-offs 48
2.2.2 Module geometries 54
2.2.3 Membrane materials and properties 55
2.3 APPLICATIONS AND EXAMPLES 57
2.3.1 Removal of dissolved oxygen (DO) from water 57
2.3.2 Recovery of dissolved methane from anaerobic effluents 67
2.3.3 Removal of Volatile organic compound (VOC) from water 79
2.4 CONCLUSION 80
2.5 REFERENCES 81

CHAPTER 3. MODELING MASS TRANSFER EFFICIENCY IN LUMEN-SIDE HFMC FOR LIQUID DEGASSING 86

3.1 INTRODUCTION 87
3.2 MODELING OF STRIPPING OPERATION IN HFMCS 88
3.2.1 Species transfer in a HFMC: resistances in series model 89
3.2.2 HFMC model assumptions used for both vacuum and sweep gas stripping 93
3.2.3 HFMC model for vacuum stripping 94

3.2.4 HFMC models for stripping with a sweep gas or in combo mode 96
3.2.5 Appropriate operating condition of HFMC stripping 99
3.2.6 Liquid pressure drop and optimal fiber length 100
3.3 Model validation by comparison with published data 101
3.3.1 Geometric characteristics of the commercial HFMC modules 101
3.3.2 Physical systems and operating modes and ranges 102
3.3.3 Physicochemical and thermodynamic data 103
3.3.4 Supplier data for vacuum stripping of oxygen in Liqui-Cel modules 103
3.3.5 Methane stripping from water in combo mode using the MM 1x5.5 Liqui-Cel module 105
3.3.6 Supplier data for vacuum stripping of oxygen in SEPAREL modules 108
3.4 Main findings and outlook 112
3.5 References 114

CHAPTER 4. MODELING MASS TRANSFER EFFICIENCY IN SHELL-SIDE HFMC FOR LIQUID DEGASSING 116

4.1 Introduction 117
4.2 Mass transfer model of degassing in a cross-flow liquid-in-shell configuration 119
4.2.1 Short literature review of reactor models 119
4.2.2 The challenge of estimating the external mass-transfer coefficient 120
4.2.3 Modelling of the external mass transfer coefficient in axial flow 121
4.2.4 Modelling of the external mass transfer coefficient in cross-flow 125
4.2.5 Estimation of the external mass transfer coefficient in cross-flow through commercial HFMCs 126
4.2.6 Resistances in series model to estimate the overall mass transfer coefficient in a HFMCs 127
4.2.7 HFMC model for degassing in vacuum mode and in excess sweep gas mode 132
4.2.8 Appropriate operating condition of HFMC vacuum and excess sweep gas stripping and comparison with liquid in lumen configuration 134
4.2.9 Friction-induced liquid pressure drop and relation with the fiber bundle dimensions 136
4.3 Model validation through comparison with published data 138
4.3.1 Geometric characteristics of the HFMC modules 138
4.3.2 Oxygen stripping in combo-mode with excess sweep gas in Liqui-Cel™ EXF modules 141
4.3.3 Oxygen stripping of salt solutions in vacuum mode in a Liqui-Cel™ EXF 2.5x8 module 146
4.3.4 Methane stripping of anaerobic effluents in sweep-gas mode in a Liqui-Cel™ EXF 2.5x8 module 149
4.3.5 Vacuum stripping of oxygen in SEPAREL® EF modules 149
4.3.6 Comparison between mass transfer in Liqui-Cel™ EXF and SEPAREL® EF modules 151
4.3.7 Supplier data for liquid pressure drop in Liqui-Cel™ EXF and SEPAREL® EF modules 152
4.4 Main findings 152
4.5 References 154

CHAPTER 5. RESIDENCE TIME DISTRIBUTION ANALYSIS IN COMMERCIAL HFMC 156

5.1 Introduction and Theoretical Background 157
5.2 Experimental Design and System Characterization 163

5.3 CONDUCTIVITY SENSOR CALIBRATION AND RESPONSE TIME CHARACTERIZATION 164
5.3.1 Conductivity Sensor Calibration 164
5.3.2 Characterization of Sensor Dynamic Response 165
5.4 DATA PROCESSING 167
5.5 MODELING APPROACH (APPLICATION OF DTS PRO SOFTWARE) 169
5.5.1 Shell side configuration 170
5.5.2 Lumen side configuration 172
5.6 RESULTS AND DISCUSSION 174
5.6.1 Shell side configuration 174
5.6.2 Lumen side configuration 183
5.6.3 Residence time distribution analysis in the shell side 185
5.7 CONCLUSIONS AND PERSPECTIVES 186
5.8 REFERENCES 187

GENERAL CONCLUSIONS AND PERSPECTIVES 189

RESUME EN FRANÇAIS 191

APPENDIX 2-A (DISSOLVED OXYGEN PERMEABILITY) 196

APPENDIX 5-A DECONVOLUTION WITH CRITICALLY DAMPED SECOND-ORDER MODEL .. 207

APPENDIX 5-B COMPARISON OF RAW AND PROCESSED CONDUCTIVITY SIGNALS AT THE INLET AND THE OUTLET TRANSMITTERS 210

List of Figures

Figure 1.1 Overview on **kL**. **aLG** values for gas-liquid contactors according to. 25
Figure 1.2 Sectors contributing to global anthropogenic methane emissions, Karakurt *et al*.. 30
Figure 1.3 A packed column air stripper. 35
Figure 1.4 Tray-type air stripper. 38
Figure 2.1. Essential elements of typical HFMC modules. 49
Figure 2.2. Schematic illustration of a hollow fiber membrane contactor module in (a) parallel flow with co-current configuration in sweep gas mode (b) parallel flow with counter-current configuration in sweep gas mode (c) cross-flow configuration in sweep gas mode (module with baffle) (d) cross-flow configuration in vacuum mode (module without baffle). 51
Figure 2.3 . Schematic cross-sectional view of a cross-flow HFMC module, illustrating Radial liquid flow. 52
Figure 2.4. Schematic diagram of membrane structural construction. 55
Figure 2.5. Structure of a multi-layered hollow fiber membrane. 56
Figure 2.6. Oxygen mass transfer coefficient of membrane contactor at different pressures and fluxes. 59
Figure 2.7. The effect of permeate side pressure to the DO removal efficiency of the vacuum degassing process. 61
Figure 2.8 . Representative DO removal performance with respect to membrane area in lab-scale HFMC deoxygenation process (operating condition: feedwater temperature of 25ºC and flow rate of 30 ml min-1). 62
Figure 2.9 .Effect of operation mode on degassing performance of membrane contactor packed woven fabric (shell: water, Module outer diameter 0.2 m, fiber effective length 0.5 m, membrane surface area 52 m2 ,vacuum 6000 Pa) 64
Figure 2.10 .Typical configuration of a membrane contactor degassing industrial systems in combo mode operation. 65
Figure 2.11. Pressure drop in the shell side of the simulated HFMCs for the energetic balance calculation. The curve for the baffled HFMC and for the other non-baffled HFMC were taken from their respective providers 68
Figure 3.1 HFMC module and mass transfer gradients for liquid in lumen flow for sweep gas stripping 89
Figure 3.2: Mass transfer efficiency as a function of the specific liquid flowrate, supplier data [1] compared to vacuum model; vacuum set to 6.67 kPa; 20°C. 104
Figure 3.3: Sherwood number as a function of the specific liquid flow rate, Vacuum model using supplier data [1] ; vacuum set to 6.67 kPa; 20°C; comparison with Graetz correlation 105
Figure 3.4: Parity plot comparing experimental and calculated mole fractions of methane in the outlet gas phase considering the Vacuum model (see Table 3.7). Measurements taken from literature [17]; vacuum levels between 51.3 and 91.3 kPa; 25 °C ; a) $\boldsymbol{Csw\ L\ in} = 0$; b) $\boldsymbol{Csw\ L\ in}$ in equilibrium with P_{sw} = 1 atm. 106
Figure 3.5: Sherwood number as a function of the specific liquid flow rate, sweep gas model using literature data [17]; vacuum levels between 51.3 and 91.3 kPa; 25 °C; comparison with Graetz correlation 107

Figure 3.6: Sherwood number as a function of the specific liquid flow rate, Vacuum model using literature data [17]; vacuum levels between 51.3 and 91.3 kPa; 25 °C; comparison with Graetz correlation 108
Figure 3.7: Parity plot comparing experimental oxygen outlet pressures [1] to that estimated using a mass balance; vacuum levels of 5.3, 8, 13.3, 18.6, and 24 kPa; 25°C. 109
Figure 3.8 : Mass transfer efficiency as a function of the specific liquid flowrate, supplier data compared to the Vacuum model; vacuum levels of 5.3, 13.3, 18.6, and 24 kPa; 25°C; diameter distribution with a standard deviation of 15 µm. 110
Figure 3.9: Sherwood number as a function of the specific liquid flow rate, Vacuum model using supplier data [2]; vacuum levels of 5.3, 13.3, 18.6, and 24 kPa; 25°C; comparison with Graetz correlation for a uniform diameter and a Gaussian diameter distribution 111
Figure 4.1: Schematic view of a Liqu-cel™ EXF module operated in combo mode 118
Figure 4.2: Schematic view of a SEPAREL® EF module operated in vacuum mode 118
Figure 4.3 : Limiting Sherwood number for external parallel flow in regular fiber arrays as a function of array compacity [12] 123
Figure 4.4: Correlation of the mean Sherwood number as a function of the Graetz number. Correlation established in this work for cross flow in commercial HFMCs and correlations of Mitayake for external axial flow in regular fiber arrays for different array geometries and compacities [12] 124
Figure 4.5: Flow directions and concentration gradients for liquid-in shell cross-flow in combo mode 128
Figure 4.6: Cross-section of the fiber-bundle of a Liqui-Cel™ EXF 2.5x8 module obtained by MRI measurements. 139
Figure 4.7: (a) Mass transfer efficiency (b) liquid Sherwood number from measurements made in Liqui-Cel™ EXF modules as a function of the specific liquid flow rate. Measurements made in vacuum mode (6.67 kPa) and excess sweep gas combo mode. Model calculations from Table 4.8 and mass transfer correlation from Table 4.3. Geometries of the modules given in Table 4.12. 143
Figure 4.8: (a) Mass transfer efficiency (b) liquid Sherwood number from measurements made in Liqui-Cel™ EXF modules as function of the specific liquid flow rate, data from [16] compared to excess sweep gas model using the Sherwood - Graetz correlation. The geometries of the modules are given in Table 4.12. For the 10x28 module, the geometry given in [7] is taken into account instead of that given in [16]. Mass transfer correlation from Table 4.3. 144
Figure 4.9: Sherwood numbers from measurements made in Liqui-Cel™ EXF modules as a function of the superficial liquid cross-flow Reynolds number (a) data from supplier [19] and (b) data from [16]. 145
Figure 4.10: Sherwood numbers from measurement made in a Liqui-Cel™ EXF 2.5x8 module as a function of the Graetz number. Data from [20]; vacuum stripping at 7.0 kPa; physicochemical parameters given in [20], geometrical parameters given in Table 4.12. Mass transfer correlations from Table 4.3 (solid line) and Table 4.15 (dotted line). 148
Figure 4.11: (a) Mass transfer efficiency (b) liquid Sherwood number from measurements made in SEPAREL® EF modules; supplier data [18] compared to vacuum model; vacuum set to 2.7, 6.7 and 13.3 kPa; 25°C. Geometric parameters of Table 4.13. 151
Figure 5.1 Schematic of experimental set up used for determining RTD in Liqui-cel EXF 2.5x8 164
Figure 5.2 Electrical conductivity as a function of NaCl concentration in aqueous solution 165

List of Figures

Figure 5.3 Step response of conductivity sensor. 167
Figure 5.4 Residuals of model fits. 167
Figure 5.5 Schematic of data processing steps to achieve the dimensionless concentration profile. 168
Figure 5.6. Treated conductivity signals (with second order deconvolution correction) at Q_L = 100 L/h showing mean residence time τ = 8.89 s. 169
Figure 5.7 Illustrated CSTR in series model (CSTRs) 171
Figure 5.8 Schematic of plug flow reactor closed to the diffusion (PFR-D) 171
Figure 5.9 . Perfect mixing cells in series exchanging with a dead volume 172
Figure 5.10. Two CSTRs in parallel configuration 172
Figure 5.11 Lumen side configuration with the distribution chambers modeled as two continuously stirred tank reactors (CSTRs) and the fiber bundle as plug flow reactor 173
Figure 5.12 Comparison of Experimental Dimensionless Concentration Curve and CSTRs Model Prediction at 100 L/h (Shell-Side). 175
Figure 5.13 Fitted Péclet Number (Pe) as a Function of Shell-Side Flow Rate (Q_L) for the PFR-D Model 176
Figure 5.14 Comparison of experimental dimensionless concentration curve and PFR-D model prediction at 100 L/h (shell-side). 177
Figure 5.15 Comparison of experimental dimensionless concentration curve and CSTRs exchanging with dead zone model prediction at 145 L/h (shell-side). 179
Figure 5.16 Regressed Parameters for the CSTRs with Dead Zone Model as a Function of Shell-Side Flow Rate (Q_L): a) Dead Zone Ratio K and Exchange Proportion β. b) Number of CSTRs J 180
Figure 5.17 Comparison of experimental dimensionless concentration profile and two CSTRs in Parallel model prediction at Q_L 235 L/h 182
Figure 5.18 Fitted Parameters (Volumes V1 and V2, Number of CSTRs J1 and J2) for the Two CSTRs in Parallel Model Across Shell-Side Flow Rates. 183
Figure 5.19 Comparison between the dimensionless concentration curve and the proposed model at flowrate 70 L/h (lumen side). 184
Figure 5.20 Fitted Péclet Number as a Function of Lumen-Side Flow Rate (Q_L) 185
Figure 5.21 Simulated RTD *E(t)* Curves for Shell-Side at 145 L/h Using Average Fitted Parameters. 186
Figure 5.22 Simulated Dimensionless RTD *E(θ)* Curves for Shell-Side at 145 L/h Using Average Fitted Parameters. 186

List of Tables

Table 1.1: Process characteristics of conventional gas-liquid direct-contact technologies [28] 24
Table 1.2. Methods used for degassing DO from purified water at laboratory-scale [34]. 27
Table 1.3. DO removal by nitrogen purging method [16,35]. 28
Table 1.4. Various designs of anaerobic wastewater treatment reactors in the literature [39]. 31
Table 1.5. Desorption-based technology to remove/recover the dissolved methane from anaerobic effluents [41]. 31
Table 1.6. General information and key parameters of the case studies [12]. 36
Table 1.7. Comparison of Ammonia Removal Technologies 39
Table 1.8. The different approaches used for the recovery of dissolved methane from wastewater [54]. 41
Table 3.1 Characteristic diameters, mass transfer coefficient and resistances in the four domains 90
Table 3.2: Local molar flux and associated transfer coefficients and resistances 91
Table 3.3: Mass transfer resistance ratios in HFMCs for typical geometrical and physical parameters 93
Table 3.4: HFMC mass transfer model for vacuum stripping 94
Table 3.5: Gas flow rate and composition in the vacuum stripping of multi-component mixtures 96
Table 3.6: HFMC mass transfer model for stripping with a sweep gas assuming ideal counter-current plug flow 97
Table 3.7: Gas flow rate and composition in sweep gas and combo mode stripping 98
Table 3.8: Appropriate operating conditions of HFMC stripping operations 99
Table 3.9: Liquid side frictional pressure drop 101
Table 3.10: Geometrical characteristics of the commercial HFMC modules and analysis of their pressure drop 102
Table 3.11: Physical systems and operating modes and ranges 102
Table 4.1: Geometries, definitions and correlations of external mass transfer in axial flow through regular arrays of cylinders [12] 122
Table 4.2: Axial Graetz number as a function of axial liquid velocity and as a function of the ratio between liquid flow rate and external fiber area 124
Table 4.3: Correlation of the external mass transfer coefficient in cross-flow 127
Table 4.4: Notations and definitions relative to the resistance in series model 129
Table 4.5: Overall mass transfer coefficient and additivity of the partial resistances 129
Table 4.6: Mass transfer coefficient estimates in the different domains in HFMCs 130
Table 4.7: Ratios of the mass transfer resistances in HFMCs for typical parameter values 131
Table 4.8: Mass transfer model for vacuum stripping and stripping with excess sweep gas in HFMCs 133
Table 4.9: Gas flow rate and composition in the vacuum stripping of multi-component mixtures 134
Table 4.10: Appropriate operating conditions of HFMC stripping operations in liquid in shell cross-flow and comparison with liquid in lumen flow 135
Table 4.11: Liquid frictional pressure drop and optimal fiber bundle dimensions 136
Table 4.12: Geometrical characteristics of the Liqui-Cel™ EXF modules considered in the following 140

Table 4.13: Geometrical characteristics of the SEPAREL® EF modules considered in the following 141
Table 4.14: Relation between dimensionless numbers in mass transfer correlations..... 146
Table 4.15: Mass transfer correlation proposed by Kattan *et al*. [20] 147
Table 5.1. Calibration of conductivity sensors with standards solutions at 21°C 165
Table 5.2. Parameters required for each reactor model. 173
Table 5.3 Derived parameters for CSTRs reactor model 175
Table 5.4 Derived parameters for PFR-D reactor model 178
Table 5.5 Derived Parameters for the CSTRs exchanging with dead volume model 178
Table 5.6 Average fitted parameters for the two CSTRs in parallel model 181

Acknowledgement

As I reach the end of this long and rewarding PhD journey, I want to pause and thank the extraordinary people who made it not only possible, but meaningful.

My deepest gratitude goes to Sabine Rode, whose brilliant scientific guidance and unwavering personal encouragement were my anchor throughout this voyage. I also sincerely thank Bouchra Belaissaoui for her dedicated supervision and for sharing her invaluable expertise so generously.

A special and warm thank you to Professor Rainier. His thoughtful advice guided me through difficult moments, and his infectious joy truly made him the heart and soul of our laboratory.

I am deeply grateful to Madi Moussa and Hervé Simonaire for their patient technical support with my experimental setup. They made things work when I needed it most, and I could not have done it without them.

I extend heartfelt thanks to the IMOSYCCA project, which generously funded my travels and let me present my work at every conference I attended.

Above all, my family carried me through this.

I thank my dear mother, whose morning calls filled each day with energy and love. I dedicate this work to the memory of my beloved father, taken from us in the Syrian civil war. He lives in my heart, and his strength pushes me forward every day.

To my beloved wife, Samah, I owe everything. Thank you, from the bottom of my heart, for your endless patience and for raising our two wonderful heroes, Mohammed and Yousef, almost single-handedly while I was immersed in this work. Thank you also to my four amazing sisters for your constant love and support.

Finally, my profound thanks to the friends and colleagues who became my family here. Omar Abdulmajid welcomed me with open arms from my very first day. From the deepest part of my heart, I thank Zahia, the quiet hero who always helped without asking for recognition. Omran, Yakoub, and Zakarya stood by me as true brothers. Laëtitia, Margarita, Mathilde, and Audrey brought daily laughter and light. My newer friends Agil, Jawad, Batoul, and Rim felt like old friends almost instantly.

And to everyone in the LRGP, I cannot name you all, but you know who you are. Each of you holds a special place in my heart.

Nomenclature

N.B.: Symbols which are used in a single table are not defined in this section.

Latin symbols

$a_{M\,ext}$	Specific shell-side membrane area ($m^2.m^{-3}$)
$A_{M\,ext}$	Total shell-side membrane area (m^2)
$A_{M\,int}$	Total lumen-side membrane area (m^2)
$C_{i\,j}$	Molar concentration of species *i* in phase *j* ($mol.m^{-3}$)
$C^*_{i\,G}$	Gas molar concentration of species *i* in equilibrium with $C_{i\,L}$ ($mol_i m_G^{-3}$)
$C(t)$	Outlet tracer concentration (g/L)
$C^*(t)$	Dimensionless concentration (-)
CV	Coefficient of variation (-)
$d_{M\,ext}$	Fiber external diameter (m)
$d_{M\,int}$	Fiber internal diameter (m)
d_h	Hydraulic diameter (m]
$D_{fb\,ext}$, $D_{fb\,int}$	External and internal diameters of the fiber bundle (m)
D_{ij}	Diffusion coefficient of species *i* in phase *j* ($m^2.\ s^{-1}$)
$E(t)$	RTD function (1/s)
$E(\theta)$	Dimensionless RTD (-)
f	Compacity of the fiber bundle; i.e. fiber volume fraction (-)
Gz_{ij}	Graetz number for species *i* in phase *j* (-)
$h_{B\,cross}$	Burke constant of the Ergun equation in cross flow (-)
$h_{K\,cross}$	Kozeny constant of the Ergun equation in cross flow (-)
J	Number of mixing cells (-)
K	Volume ratio V2/V1 in dead zone model (-)
k_{ij}	Volumetric mass transfer coefficient of species *i* (in phase j $m.s^{-1}$)
$K_{i\,OL}$	Overall volumetric liquid side mass transfer coefficient of *i* ($m^3.m^{-2}.\ s^{-1}$)
m_i	Volumetric partition coefficient of species *i* ($m_G^3.m_L^{-3}$)
N_b	Number of baffles of the HFMC module
N_i	Molar flux of species *i* ($mol.m^{-2}$)
$NTU_{i\,OL}$	Liquid side number of transfer units of species *i* (-)
P	Pressure (Pa or kPa)
Pe	Péclet number (-)
$\mathcal{P}_i$	Permeability of species *i* in the dense skin (mol m^{-1} s^{-1} Pa^{-1} or barrer)
Q_j	Volumetric flow rate of phase *j* ($m^3.s^{-1}$)
R	Ideal gas constant (J/mol/K)
R_i	Mass transfer resistance of species *i* ($s.\ m^{-1}$)
RR_i	Recovery rate of the transferred species *i* (-)
$S(t)$	Sensor response (µS/cm)
Sh_{ij}	Logarithmic mean Sherwood number of species *i* in phase *j* (-)
SSE	Sum of squared errors (-)
T	Temperature (K)
u_L	Superficial velocity of the liquid phase in the flow direction ($m\ s^{-1}$)
V_{fb}	Volume of the fiber bundle (m^3)
x_i	Mole fraction of component *i* in the gas phase (-)
Z_{fb}	Effective fiber length (m)

Greek and mixed symbols

δ	Membrane thickness (m)
$\Delta P_{f\,L}$	Frictional pressure of the liquid phase (Pa)
ε_M	Membrane porosity (-)
η_{ij}	Mass transfer efficiency of species *i* in phase *j*
$\eta_{i\,L}$	Mass transfer efficiency of species *i* in the liquid phase
λ_i	Partition ratio of species *i* (-)
θ	Dimensionless time (-)
μ	Mean value (-)
μ_L	Dynamic viscosity of the liquid phase (Pa s)
σ	Standard deviation (-)
σ^2	Variance (s^2)
σ_θ^2	Dimensionless variance (-)
ρ_L	Density of the liquid phase (kg m^{-3})
τ_M	Membrane tortuosity (-)
Ω	Area perpendicular to the liquid flow direction

Subscripts and superscripts

am	Arithmetic mean
axial	Relative to the axial direction of the fiber bundle
cross	Relative to the radial direction of the fiber bundle
ext	Relative to the external dimensions of the hollow fibers or the fiber bundle
fb	Relative to the fiber bundle
G	Gas phase
hm	Harmonic mean
i	Relative to the transferred species (O_2, N_2, $CH_{4...}$)
in	Relative to the inlet of the HFMC module
int	Relative to the internal dimensions of the hollow fibers or the fiber bundle
j	Relative to the phase (*G, L*)
L	Liquid phase
lm	Logarithmic mean
ls	Lumen-side
M d	Relative to the dense membrane
M p	Relative to the porous membrane
out	Relative to the outlet of the HFMC module
pore	Relative to the membrane pores
sat	Saturation vapor
solvent	Solvent
ss	Shell-side
sw	Sweep gas
vac	Vacuum side

Acronyms

HFMC	Hollow-fiber membrane contactors
CSTR	Continuous Stirred-Tank Reactor
DTS Pro	Software for RTD analysis
NTP	Normal temperature and pressure (293.15 K, 101.325 kPa)
PDMS	Polydimethylsiloxane

PMP	Poly(4-methyl-1-pentene)
PP	Polypropylene
PVDF	Polyvinyl fluoride
RMT	Relative membrane thickness
RTD	Residence Time Distribution
UL PROPULS	Company developing DTS Pro
VOCs	Volatile organic compounds
X-50, X-40	Commercial Polypropylene fibers used by 3M and in the Liqui-cel™ EXF devices

Abstract

The removal of dissolved gases such as oxygen (O_2), methane (CH_4), and volatile organic compounds (VOCs) from liquids is critical in water treatment and industrial processes, including pharmaceuticals, food and beverage, and chemical manufacturing. These contaminants can degrade product quality, cause oxidative damage, and pose safety risks. Conventional stripping technologies, such as packed columns and bubble reactors, rely on dispersive gas-liquid contact but suffer from operational limitations including foaming, entrainment, flooding at high liquid velocities, and partial wetting for packed columns at low velocities, leading to inefficiencies, high maintenance costs, and scalability challenges.

This thesis explores the use of hollow fiber membrane contactors (HFMCs) as an advanced, non-dispersive alternative for stripping operations. HFMCs align with the principles of process intensification to enable compact design and enhanced mass transfer efficiency. HFMCs utilize commercial modules (e.g., Liqui-Cel™ and SEPAREL®) that have a high surface area to volume ratio. This enables stable performance across a wide range of flow rates without issues of phase interdependence. A review of stripping processes outlines the advantages and disadvantages of conventional technologies, emphasizing the potential of HFMCs to address these issues through indirect contact and geometric optimization.

Degassing of liquids using HFMCs operating in lumen-side and shell-side HFMC configurations is modelled. For lumen-side liquid flow (suited to low-flow, lab-scale applications like Liqui-Cel™ MM series), the model directly correlates mass transfer efficiency with the liquid flow rate per internal membrane area and predicts frictional pressure drops via Hagen-Poiseuille's law, facilitating practical sizing of commercial modules. Validation against experimental data shows high accuracy in predicting O_2/CH_4 removal efficiencies. The framework extends to shell-side liquid cross-flow, prevalent in high-capacity modules like Liqui-Cel™ EXF and SEPAREL® EF, through a novel Sherwood–Graetz correlation. This correlation effectively predicts mass transfer coefficients and shows strong agreement with experimental data from commercial modules of varying sizes. In this configuration, the mass transfer efficiency for a given process depends solely on the specific liquid flow rate, independent of the module's size or geometry. This is because the number of transfer units (NTU) is a function of the Graetz number alone. Moreover, the frictional liquid pressure drop can be estimated successfully by using an Ergun type equation.

For validating the plug flow behavior that is assumed in the presented model, hydrodynamic characterization of a commercial HFMC performed on both the shell and lumen sides through Residence Time Distribution (RTD) experimental analysis, employing pulse tracer techniques (e.g., NaCl). The

RTD analysis results confirms that the hollow fiber membrane contactor exhibits strong, dominant plug-flow behavior on both the shell and lumen sides.

This integrated modelling and experimental approach establishes a versatile, predictive framework for optimizing HFMC performance across diverse scales and configurations. Overall, this thesis delivers practical design guidelines for commercial hollow fiber membrane contactors (HFMCs), enabling optimal operating conditions and module performance. Future work could extend these models to incorporate wetting dynamics and multi-component simulations.

Résumé

L'élimination des gaz dissous tels que l'oxygène (O_2), le méthane (CH_4) et les composés organiques volatils (COV) des liquides est cruciale dans le traitement de l'eau et les procédés industriels, notamment dans les secteurs pharmaceutique, agroalimentaire et de l'industrie chimique. Ces contaminants peuvent dégrader la qualité des produits, causer des dommages oxydatifs et présenter des risques pour la sécurité. Les technologies conventionnelles de dégazage, telles que les colonnes garnies et les réacteurs à bulles, reposant sur un contact dispersif gaz-liquide, présentent des limitations opérationnelles, comme le moussage, l'entraînement et l'engorgement, l'inond à grande vitesse et le non-chargement à petite vitesse. Ces limitations entraînent des inefficacités, des coûts d'entretien élevés et des difficultés de mise à l'échelle.

Cette thèse explore l'utilisation des contacteurs à membrane à fibres creuses (HFMC) comme alternative avancée et non-dispersive pour les opérations de dégazage. Les HFMC s'alignent sur les principes d'intensification des procédés pour permettre des conceptions compactes et une efficacité de transfert de matière accrue. Les HFMC exploitent des modules commerciaux (par exemple, Liqui-Cel™ et SEPAREL®) dotés d'un rapport surface d'échange sur volume élevé, ce qui assure une performance stable dans une large gamme de débits sans problèmes d'interdépendance des phases. Un examen des procédés de dégazage met en évidence les avantages et inconvénients des technologies conventionnelles, soulignant le potentiel des HFMC pour remédier à ces problèmes par un contact indirect des phases et une optimisation géométrique.

Le dégazage des liquides à l'aide de HFMC fonctionnant en configurations lumen-side et shell-side est modélisé. Pour l'écoulement en lumen-side (adapté aux applications à faible débit, à l'échelle laboratoire comme la série Liqui-Cel™ MM), le modèle corrèle directement l'efficacité de transfert de masse avec le débit liquide par unité de surface membranaire interne et prédit les pertes de charges via la loi de Hagen-Poiseuille, facilitant le dimensionnement pratique des modules commerciaux. La validation par rapport à des données expérimentales démontre une haute précision dans la prédiction des efficacités d'élimination de l'O_2 et du CH_4. Ce cadre s'étend à l'écoulement transversal en shell-side,

prévalent dans les modules à haute capacité comme Liqui-Cel™ EXF et SEPAREL® EF, par une corrélation novatrice de Sherwood–Graetz. Cette corrélation prédit efficacement les coefficients de transfert de matière et présente un fort accord avec les données expérimentales issues de modules commerciaux de tailles variées. Dans cette configuration, l'efficacité de transfert de matière pour un procédé donné dépend uniquement du débit liquide spécifique, indépendamment de la taille ou de la géométrie du module. Cela s'explique par le fait que le nombre d'unités de transfert (NTU) est une fonction uniquement du nombre de Graetz. De plus, les pertes de charges cotés liquide peuvent être estimée avec succès en utilisant une équation de type Ergun.

Pour valider le comportement d'écoulement piston supposé dans notre modèle, une caractérisation hydrodynamique d'un HFMC commercial a été réalisée sur les côtés shell et lumen par une analyse expérimentale de la distribution des temps de séjour (RTD), en employant des techniques de traçage par impulsions (par exemple, NaCl). Les résultats de l'analyse RTD confirment que le contacteur à membrane à fibres creuses présente un comportement d'écoulement piston fort et dominant sur les deux côtés shell et lumen.

Cette approche intégrée de modélisation et d'expérimentation établit un cadre prédictif polyvalent pour optimiser les performances des HFMC à travers diverses échelles et configurations. Dans l'ensemble, cette thèse fournit des directives de conception pratiques pour les contacteurs membranaires à fibres creuses commerciaux (HFMC), permettant des conditions d'opération optimales et des performances de module améliorées. Des travaux futurs pourraient étendre ces modèles afin d'intégrer la dynamique de mouillage et les simulations multi constituants.

General introduction

In many industrial processes, liquid streams contain dissolved gases at low concentrations. These gases must be removed to ensure product quality, process efficiency, and to minimize operational costs. To achieve this, the liquid stream brought into close contact with a sweeping agent and a concentration gradient is created between the two phases. The stripping agent may be a vacuum, a sweep gas or a combination of the two. It dilutes the solute in the gas phase, creating a driving force for mass transfer from liquid to gas. The sweep gas is generally an inert gas, such as nitrogen or air, which does not react with the solute and does not introduce additional contaminants into the system.

Stripping is very important in purifying liquid streams across sectors such as water treatment, pharmaceuticals, food and beverage, and chemical manufacturing. It removes volatile contaminants, including oxygen (O_2), methane (CH_4), and volatile organic compounds (VOCs). These impurities degrade product quality, trigger corrosion, and increase operational risks. For example, dissolved oxygen in water accelerates corrosion in boilers and pipelines. VOCs contribute to air pollution and can violate environmental regulations. Effective degassing can enhance process reliability, extend equipment life, and maintain compliance with safety and environmental standards.

A wide range of techniques have been developed to effectively remove these dissolved gases, particularly, from water, employing various mechanisms based on chemical, physical, and biological separation processes. The selection of a particular approach depends on several factors, including the specific application, the concentration of dissolved gases in the water, and the desired level of removal. Physical methods play a significant role in gas removal and include packed columns, bubble columns, spray aeration, tray aerators, and diffused aeration. These technologies facilitate direct contact between the liquid stream and the gas stream, enabling effective gas transfer. Direct contact technologies, including counter-current gravity-fed packed columns, bubble columns and tray columns, dominate the chemical industry. However, these systems suffer from inherent limitations: at low gas velocities relative to liquid flow, they experience flooding and entrainment, leading to operational inefficiencies, increased maintenance costs, and scalability issues. Bubble columns, suitable for low gas flows, exhibit significant axial dispersions in both phases, severely reducing performance. Overall, these contactors provide specific interfacial areas below 500 m^2/m^3 and low liquid-side mass transfer coefficients, resulting in modest mass fluxes per unit volume and requiring large equipment volumes.

Process intensification, a paradigm shift originating in the 1970s, seeks to revolutionize chemical engineering by reducing plant size, energy consumption, and costs while preserving productivity. Innovations such as static mixers and membrane contactors exemplify this approach, enabling compact and efficient processes. Hollow fiber membrane contactors (HFMCs) emerge as a promising alternative technology, operating in non-dispersive mode to eliminate flooding and entrainment risks. By

leveraging submillimeter fiber diameters, HFMCs achieve high specific interfacial areas up to 25000 m^2/m^3 and elevated liquid-side mass transfer coefficients, potentially yielding substantial volumetric reductions compared to conventional systems. Moreover, they support counter-current operation with minimal axial dispersion, accommodating low gas-to-liquid ratios unsuitable for packed or tray columns.

One of the key advantages of HFMCs is their compact design, which allows for space-efficient installation and integration into existing systems. This compactness renders them an optimal choice for retrofitting or upgrading existing infrastructure without necessitating significant modifications. Their compatibility with various process conditions and adaptability to different scenarios render them versatile and practical for a wide range of applications.

Key challenges include minimizing transmembrane resistance, achieved via porous membranes or thin permeable dense skins to prevent wetting, while ensuring material compatibility and optimizing geometric configurations like fiber and module dimensions to avoid pressure drops and maldistribution. Commercial examples, such as 3M's Liqui-Cel™ and DIC Corporation's SEPAREL®, demonstrate viability in applications like ink degassing and post-combustion CO_2 capture, with pilot tests logging thousands of operational hours.

This thesis aims to fill these gaps by developing a generic approach for optimal design of hollow fiber membrane contactors in stripping operations. Indeed, each stripping operation is characterized by specific physicochemical and thermodynamic properties of both, the gas and the liquid phase. This leads to distinctive optimum operating characteristics, which, in turn, determine the choice of membrane material and structure as well as the optimal geometry of the contactor.

This thesis is structured into five chapters. Together, they provide a comprehensive overview of HFMCs for stripping. The first chapter provides a foundational overview of stripping processes in water treatment, emphasizing the removal of dissolved gases and VOCs to maintain product quality and safety. It delineates the advantages and disadvantages of conventional gas-liquid contactors, such as packed columns, tray columns, and bubble columns, which grapple with foaming, entrainment, flooding, and axial dispersions, issues exacerbated at low gas-to-liquid ratios typical in degassing. These limitations result in low specific areas and mass transfer coefficients, inflating equipment volumes. In contrast, indirect-contact membrane technologies are introduced as alternatives, offering higher interfacial areas and coefficients while mitigating phase interdependence. The discussion aligns with process intensification principles, underscoring HFMCs' role in addressing conventional shortcomings. The chapter concludes by positioning HFMCs as a novel solution for stripping, setting the stage for subsequent modeling and analysis.

The second chapter explore the fundamentals of HFMC design and operation, detailing the core principles governing their functionality. This chapter highlights the advantages of using HFMCs over

conventional gas-liquid contact technologies, particularly their ability to operate effectively under varying flow conditions. Key design elements, including membrane materials and module geometries, are examined to demonstrate how they contribute to improved mass transfer and operational efficiency.

The third chapter moves to numbers. It presents a detailed modeling approach for lumen-side HFMCs, linking mass transfer efficiency to liquid flow rates across the internal membrane area. By applying Hagen–Poiseuille's law to predict frictional pressure drops, this chapter provides essential insights into the practical sizing of commercial modules, such as the Liqui-Cel series. The model's validation against experimental data on oxygen and methane stripping illustrates its applicability across various industrial scenarios, paving the way for optimizing system performance.

In Chapter 4, the modeling framework is extended to encompass shell-side cross-flow configurations. It explores mass transfer mechanisms, primarily governed by liquid-side diffusion, and develops a Sherwood-Graetz correlation for shell-side cross-flow to predict transfer coefficients. The model incorporates resistances in series for overall mass transfer, assuming ideal plug flow and uniform gas composition in vacuum or excess sweep gas modes. It relates mass transfer efficiency to operational parameters like liquid flow rate and external membrane area, enabling simplified HFMC sizing. Pressure drop is analyzed using an Ergun-type equation, linked to fiber bundle dimensions for process optimization. Validation draws on commercial modules like Liqui-Cel™ EXF and SEPAREL® EF, highlighting advantages over lumen-side flow.

The fifth chapter investigates experimentally residence time distribution (RTD) in a commercial hollow fiber membrane contactor (Liqui-Cel 2.5x8) to confirm the plug flow behavior in such models. It reviews theoretical foundations of RTD, tracer methods (pulse injection with NaCl), and detection techniques, alongside prior studies on flow maldistribution in HFMCs. Experiments employ conductivity sensors for real-time monitoring across shell-side and lumen-side liquid flows. Simulation uses DTS Pro software to fit experimental curves to reactor analogies like CSTRs in series, Plug flow with boundary limits, CSTRs with dead zones, and two parallel CSTRs. The RTD analysis results confirms that the hollow fiber membrane contactor exhibits strong, dominant plug-flow behavior on both the shell and lumen sides.

Chapter 1. Stripping operation conventional and alternative technology

1.1 Introduction

The removal of contaminants and impurities constitutes a foundational aspect of proper water treatment and a necessity for a multitude of industrial processes. In sectors such as pharmaceuticals, food and beverage, and chemical manufacturing, the quality of water exerts a direct influence on operational efficiency, product integrity, and equipment longevity. The implementation of proper treatment of water enhances the performance of industrial machinery and contributes to overall sustainability and cost-effectiveness by reducing maintenance needs and downtime. One of the important aspects of water treatment is the removal of dissolved gases (degassing), including oxygen (O_2), methane (CH_4), and volatile organic compounds (VOCs) [1]. These gases can have a considerable impact on industrial processes and equipment. For instance, dissolved oxygen can lead to oxidative reactions that degrade sensitive materials, affect product quality, and foster the growth of undesirable microorganisms. Similarly, the presence of methane and VOCs can result in hazardous conditions, product contamination, and regulatory compliance issues [2]. Consequently, the process of degassing has become essential for maintaining product quality, ensuring safety, and enhancing the efficiency of industrial operations.

Although columns and other conventional gas-liquid contactors have long been the main technologies used in the chemical industry, one of the main problems is the interdependence of the two phases, which can lead to difficulties such as foaming, entrainment and liquid overloading. These issues often lead to operational inefficiencies, increased maintenance costs, and limitations in scalability [3]. Indirect contact via membranes is an alternative technology which eliminates these difficulties while offering potential opportunities for process intensification. Indeed, they present higher specific contact areas and mass-transfer coefficients. One of the challenges in the development of membrane contactors is their geometrical optimization, including fiber and module dimensions. In particular, prohibitive pressure drop as well as fluids maldistribution must be avoided for the two phases involved [4].

The development of membrane contactors aligns with the broader concept of process intensification, which emerged in the 1970s to revolutionize chemical engineering by reducing plant size, energy use, and costs while maintaining productivity [5]. As Ramshaw [6] noted, process intensification drives innovations like static mixers and membrane contactors, enabling more compact and efficient industrial processes.

The purpose of this chapter is to provide an overview of the state of the art in stripping operations, addressing the conventional technologies employed and their respective limitations. The chapter begins with a comprehensive description of stripping processes, noting the advantages and disadvantages of conventional technologies. Hollow fiber membrane contactors (HFMCs) are then presented as an advanced and novel technology for stripping operations, highlighting their potential to address the shortcomings of conventional systems. The chapter concludes with the importance of HFMCs in

stripping operations and their potential for future applications in water treatment. The next chapter discusses the principles and applications of membrane contactors for stripping operations.

1.2 Overview of Stripping Operations

A stripping operation is a process designed to remove solutes with very low concentrations of dissolved gases or volatile substances from a liquid medium. To achieve this, the liquid and gas phases are brought into close contact, and a concentration gradient is created between the two phases using a stripping agent. The stripping agent may be a vacuum, a sweep gas or a combination of the two. It dilutes the solute in the gas phase, creating a driving force for mass transfer from liquid to gas. The sweeping gas is generally an inert gas, such as nitrogen or air, which does not react with the solute and does not introduce additional contaminants into the system.

The efficiency of the stripping operation is highly dependent on the mass transfer mechanisms, mainly represented by diffusion, as indicated by the Fick's law [7]. Diffusion drives dissolved gases or volatiles from the liquid to the gas phase due to the concentration gradient between the two phases. The choice of sweeping agent further enhances the efficiency of the process [8]. For instance, the use of vacuum as a stripping agent reduces the partial pressure of the gas phase, creating a strong driving force for mass transfer and enabling efficient degassing. Moreover, combining vacuum with an inert gas, such as nitrogen, can remarkably increase efficiency. The inert gas dilutes the solutes transferred to the gas phase, maintaining a low partial pressure and ensuring a continuous concentration gradient [9].

The efficiency of the stripping process is also proportional to the distribution of the solute between the liquid and gas phases, which is described by Henry's Law. Henry's Law states that the concentration of a gas in a liquid is proportional to its partial pressure in the gas phase at equilibrium. This relationship can also be expressed as the ratio of the molar concentration of the solute in the liquid phase to its molar concentration in the gas phase [10].

To maximize stripping efficiency, the system must operate under conditions where the concentration of the solute in the liquid phase is well above its equilibrium concentration. This creates a strong driving force for mass transfer, ensuring that the solute moves efficiently from the liquid to the gas phase [10].

Stripping operation has been applied in various industrial processes such as drinking water [11,12], wastewater [13,14] as well as industrial water treatment [15]. Typical stripping applications are water deoxygenation [16,17], de-methanization [18] and volatile organic compounds (VOCs) removal [19]. Moreover, stripping also permits ammonia removal [20] from wastewater as well as sour water treatment in crude-oil refineries [21]. Finally, stripping is used in the framework of de-solvation [22] and de-odorization in oil processing [23].

In general, industrial-scale stripping is carried out using the technologies listed in Table 1-1. However, over the past decade, the use of membrane contactors for stripping has been considered for the removal of dissolved oxygen from water [24], the recovery of VOCs from wastewater, and for ammonia stripping from industrial water [25–27]. These investigations clearly demonstrate that HFMC has the potential to outperform traditional separation columns in many respects.

Table 1.1: Process characteristics of conventional gas-liquid direct-contact technologies [28]

Characteristics	**Packed bed**	**Tray columns**	**Bubble column**
Residence time distribution of the liquid phase for the overall device	Plug flow	Plug flow	Perfectly mixed flow
Residence time distribution of the gas phase for the overall device	Plug flow	Plug flow	Perfectly mixed or dispersed plug flow
Mode of operation in stripping	Counter-current	Counter-current	Co-current
Continuous phase	Gas	Gas between the trays	Liquid
Solid volumetric holdup (-)	$0.05 < \varepsilon_S < 0.3$	$0.01 < \varepsilon_S < 0.03$	0
Liquid volumetric holdup (-)	$0.05 < \varepsilon_L < 0.2$	$0.05 < \varepsilon_L < 0.2$	$0.75 < \varepsilon_L < 0.85$
Gas volumetric holdup (-)	$0.5 < \varepsilon_G < 0.9$	$0.77 < \varepsilon_G < 0.95$	$0.15 < \varepsilon_G < 0.25$
Specific gas-liquid interfacial area ($m^2.m^{-3}$)	$100 < a_{LG} < 500$	$100 < a_{LG} < 500$	$50 < a_{LG} < 100$
Specific pressure drops	About 150 to 400 Pa per theoretical plate	About 103 Pa per theoretical plate	About 8 $x10^3$ Pa per meter
Illustration	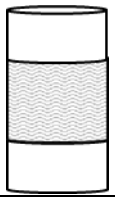	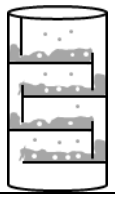	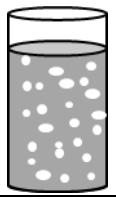

1.3 Conventional Stripping Technologies: applications and examples

1.3.1 Stripping Technologies

Stripping technologies are devices that facilitate gas-liquid contact and provide sufficient surface area for contact between species in various applications. [29]. The performance of a gas-liquid contactor can be evaluated in terms of volumetric mass transfer coefficients (k_L and k_G) in relation to the effective specific interfacial area (a_{LG}) [30]. It has been established that a higher $k_L.a_{LG}$ value correlates with reduced equipment size for gas-liquid contactors. Countercurrent packed columns are widely regarded as the best standard design for degassing applications according to its facility of scaling up and handling a wide range of liquid flow rate [31]. Figure 1-1. illustrates that the spread of $k_L.a_{LG}$ includes several orders of magnitude.

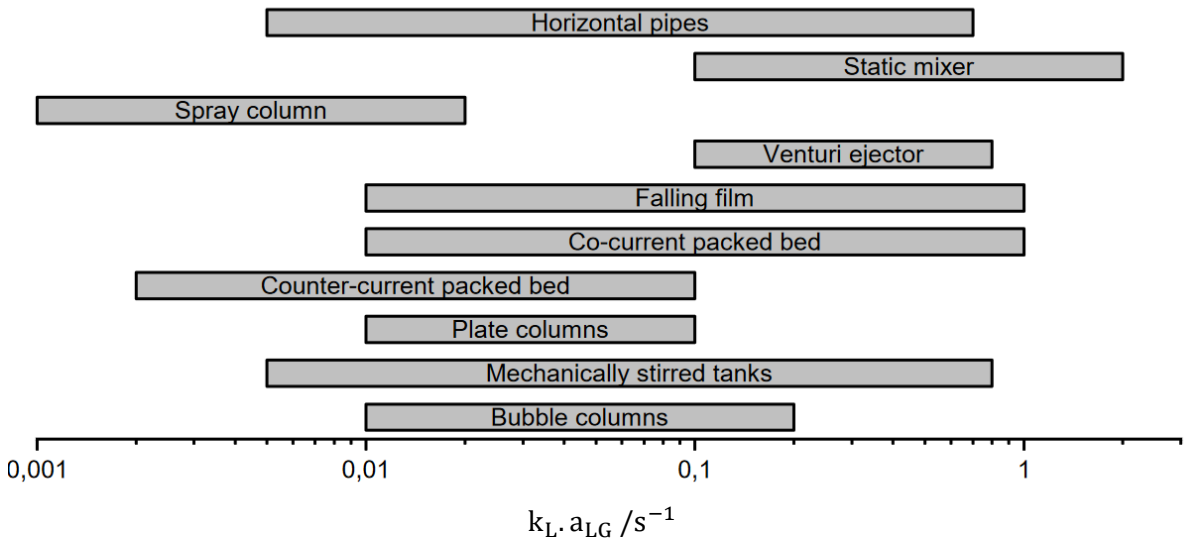

Figure 1.1 Overview on $k_L.a_{LG}$ values for gas-liquid contactors according to [31].

Packed columns, tray columns and bubble columns are traditionally used for degassing applications. These technologies facilitate direct contact between gas and liquid phases. The main challenge in designing and operating these systems is to increase the mass transfer rate and to obtain the largest possible specific interfacial area. In the case of packed columns, this requires careful selection of packing material and geometry, as well as inlet fluid distribution [3].

1.3.2 Stripping applications and examples

A. Removal of dissolved oxygen (DO) from water

Dissolved Oxygen (DO) in liquids is typically present due to the solubility of oxygen in water. The removal of DO from water is an important area of research with many practical applications.

One such application is in the food industry, where DO can cause oxidation and spoilage of products [32]. By removing DO from water, the shelf life of food products can be extended and their quality can be improved. In addition to the food industry, the removal of DO is also important in other industries such as semiconductor manufacturing and ultra-pure water systems [33].

In produced water (i.e., water associated with oil), DO can degrade polymeric additives such as polyacrylamide, which is commonly injected during enhanced oil recovery (EOR) to increase water viscosity and improve oil displacement. This process of degradation leads to the formation of by-products and the stimulation of microbial growth [16]. In these applications, even small amounts of DO can have a negative impact on the quality of the final product.

For laboratory-scale applications (not more than 1 L of purified water), four common methods are available for removing dissolved oxygen from water [34]; purging with nitrogen, boiling at atmospheric pressure, boiling under reduced pressure, and reduced pressure sonication. The four available techniques are listed in Table 1-2.

The optimization of nitrogen purging for oxygen degassing process involves key parameters such as packing material, gas flow rate, bubble size, and flow orientation. Al Dawery *et al*. investigated these factors across two studies [16,35]. Their initial work [16] established that a combination of spherical glass balls, counter-current flow, ultra-fine bubbles, and a nitrogen flow rate of 3-5 L/min could reduce dissolved oxygen from 6 ppm to <1 ppm in three minutes. Notably, flow rates beyond 6 L/min induced foam formation without improving efficiency.

Their follow-up study [35] achieved complete deoxygenation (0 ppm DO) of produced water within two minutes. This enhanced performance was accomplished by implementing an inline DO measurement system to avoid sample reabsorption, determining an optimal volumetric liquid-to-gas ratio of 1:3, and establishing the superiority of the once-through mode, where water passes through the column a single time in counter-current flow with the nitrogen gas, over recirculation. A comparative summary of these results is provided in Table 1-3.

In a paper by Zhao *et al*.[36], the authors presented a rotor-stator reactor (RSR) as a technology for DO removal from water. The study combined nitrogen stripping and vacuum degassing to enhance the deoxygenation process. The RSR, which creates a high-gravity environment, improved mass transfer and deoxygenation efficiency. Under the best conditions (600 rpm for rotational speed, 0.4 m^3/h for liquid flow, 3 m^3/h for gas flow, and 0.06 MPa for vacuum degree), the deoxygenation removal rate and mass transfer coefficient ($k_L.a_{LG}$) reached 97.34% and 0.0882 s^{-1}, respectively.

Table 1.2. Methods used for degassing DO from purified water at laboratory-scale [34].

Description	**Remarks**
Purging 1 L of purified water with nitrogen at a flow rate of 25 mL/s for 20-40 minutes.	✓ Efficient and practical for most experimental setups. ✓ Reducing the dissolved oxygen concentration to 0.2-0.4 ppm.
Boiling under reduced pressure	✓ Less effective than purging with nitrogen ✓ Reducing oxygen levels to 0.3 ppm. ✓ Requires special equipment, such as a vacuum pump, and takes longer.
Boiling at atmospheric pressure.	✓ Less effective than boiling under reduced pressure. ✓ Reducing the oxygen concentration to 1.2 ppm, which is higher than the equilibrium oxygen concentration at 100°C (6.17 ppm). ✓ The turbulent surface during boiling allows atmospheric oxygen to redissolve in the water
Reduced pressure sonication	✓ The least effective method. ✓ This method is more useful for heating water than for oxygen removal. ✓ Sonication alone is inefficient, and significant deoxygenation does not occur until the water temperature reaches 45°C.

Table 1.3. DO removal by nitrogen purging method [16,35].

Criteria	**Classical process** [16]	**Optimized process** [35]
Column Height	1.2 m	1.3 m
Column Diameter	10 cm	10 cm
Packing Material	✓ Unpacked: No packing ✓ Packed: Polyethylene rushing rings and spherical glass balls	✓ Packed: Spherical glass balls (120 cm packing layer)
Water Used	✓ Tap Water (TW) ✓ Produced Water (PW) ✓ Produced Water with Polyacrylamide (PWP)	✓ Tap Water (TW) ✓ Produced Water (PW) ✓ Produced Water with Polyacrylamide (PWP)
DO Measurement Method	✓ Offline DO measurement (samples collected and measured on the bench)	✓ Inline DO measurement (real-time measurement within the column)
Residual DO Levels	✓ Residual DO levels of 0.5 ppm remained after purging.	✓ Complete deoxygenation (0 ppm) achieved within 2 minutes using inline measurement.
Purging Schemes	✓ Semi-batch ✓ Counter-current	✓ Semi-batch ✓ Counter-current ✓ Once-through mode
Nitrogen Flow Rate	✓ Tested range: 2–6 L/min	✓ Tested range: 2–6 L/min (extended to 8 L/min in some cases)
Liquid Flow Rate	✓ Not explicitly varied	✓ Varied between 1–3 L/min

Foam Formation	✓ Foam formation is observed at high nitrogen flow rates, especially for high polymer concentrations.	✓ Foam formation controlled by reducing liquid flow rates for high-viscosity samples.
Polymer Degradation	✓ Polymer degradation due to dissolved oxygen was a concern.	✓ Viscosity reduction observed after multiple nitrogen purging runs, indicating partial polymer degradation.
Time to Achieve 0 ppm DO	✓ Residual DO levels of 0.5 ppm remained even after 300 minutes of purging.	✓ Complete deoxygenation (0 ppm) achieved within 2 minutes using inline measurement.
Industrial Applicability	✓ Limited by residual DO levels and foam formation.	✓ Highly suitable for industrial applications due to faster deoxygenation and controlled foam formation.
Temperature Consideration	✓ Temperature effects were not considered.	✓ Temperature effects were not considered, but future studies are planned to investigate this factor.
Key Advancements	✓ Demonstrated effectiveness of nitrogen purging for DO removal. ✓ Identified limitations of offline DO measurement.	✓ Introduced inline DO measurement for accurate results. ✓ Achieved complete deoxygenation within 2 minutes. ✓ Introduced once-through mode for industrial scalability. ✓ The optimum volumetric liquid-to-gas ratio is 1:3

B. Recovery of dissolved methane from anaerobic effluents

Methane, a potent greenhouse gas (GHG), is released from various natural and anthropogenic sources. Over a 100-year timescale, methane possesses a global warming potential of 28 to 34 times greater than carbon dioxide, the most prevalent greenhouse gas [37].

The global sources of methane are the result of both natural and anthropogenic activities. The latter accounts for 60% of methane sources, which are further classified into the agriculture, energy,

waste, and industrial sectors. Figure 1-2 shows the contribution of each sector to the total emissions. The waste sector is responsible for a significant portion of methane emissions from solid waste and wastewater treatment [38].

Methane is emitted incidentally and deliberately during the handling and treatment of municipal and industrial wastewater. The organic material present in wastewater undergoes decomposition under anaerobic conditions, resulting in the production of methane. In contrast, most developed countries employ centralized aerobic wastewater treatment systems, which significantly reduce methane emissions. However, in developing countries with limited or no wastewater collection and treatment infrastructure, anaerobic systems are more prevalent [38]

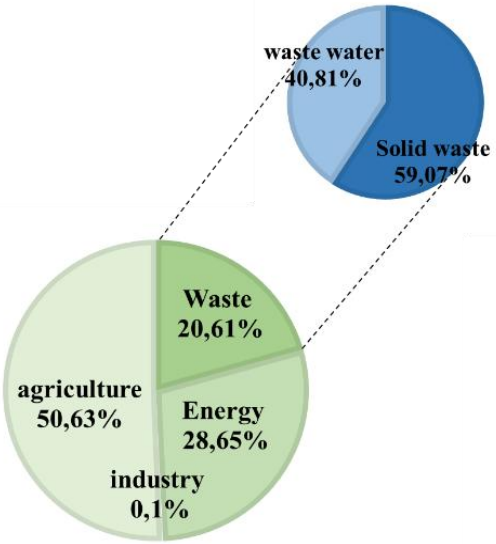

Figure 1.2 Sectors contributing to global anthropogenic methane emissions, Karakurt *et al*. [38].

There are many different designs of anaerobic wastewater treatment reactors (UASB, EGSB, SAF-MBR, AnMBR…) currently in use [39]. A brief description of some of these reactors is provided in Table 1-4. It is worth to notice that not all methane produced by these systems is completely recovered [40]. In practice, for the desorption of dissolved CH_4 from anaerobic effluents, two options have been tested, depending on the operating conditions for the desorption units:

- Transference of CH_4 to a diluted waste gas which must be treated (oxidized) downflow.
- Transference of CH_4 to a rich gas which can be energetically used, alone or mixed with biogas.

In both cases, the waste/recovered gas should be treated or upgraded downstream. Table 1-5 summarizes the various technologies available for the desorption of dissolved methane from anaerobic effluents. Each technology is evaluated based on its key parameters, performance, and associated challenges, providing a comprehensive overview of the options for mitigating CH_4 emissions [41].

Table 1.4. Various designs of anaerobic wastewater treatment reactors in the literature [39].

Reactor	Description
UASB (Up flow Anaerobic Sludge Blanket)	A high-rate anaerobic digestion system where wastewater flows upward through a dense blanket of anaerobic sludge. Microorganisms in the sludge break down organic matter, producing biogas (mainly methane and carbon dioxide) and treating the effluent.
EGSB (Expanded Granular Sludge Bed)	An advanced version of UASB, EGSB reactors operate at higher upward flow velocities, causing the sludge bed to expand. This allows for better contact between wastewater and biomass, improving treatment efficiency, especially for high-strength wastewaters.
SAF-MBR (Submerged Aerobic Fixed-film Membrane Bioreactor)	A hybrid system combining fixed-film aerobic treatment with membrane filtration. Microorganisms grow on a fixed media for organic matter degradation, while membrane filters treat the effluent, ensuring high-quality output.
AnMBR (Anaerobic Membrane Bioreactor)	A system that integrates anaerobic digestion with membrane filtration. Anaerobic microorganisms degrade organic matter, producing biogas, while a membrane separates solids from the treated effluent, resulting in high-quality output and reduced sludge production.

Table 1.5. Desorption-based technology to remove/recover the dissolved methane from anaerobic effluents [41].

Technique	Description	Key Parameters	Performance	Challenges/ Limitations
Diffused Aeration	Aeration of UASB effluent in a tank using compressed air at the bottom to strip D-CH_4.	- HRT[1]: 15–60 min - G/L ratio[2]: 5–37	- No specific data for D-CH_4 removal from UASB effluents. - 99% CH_4 removal in landfill leachate.	- High G/L ratios dilute CH_4, making recovery unfeasible.

[1] HRT: Hydraulic retention time.

[2] G/L ratio: Gas-to-liquid volumetric flow ratio.

		- DO: 1–6 mg/L		- High energy consumption.
Simplified Desorption Chamber	A closed tower where UASB effluent falls freely, and air is introduced at the bottom to strip D-CH_4.	- Water fall: 1.0–1.5 m - G/L ratio: 2–10 - HLR[3]: 0.10–0.30 $m^3/m^2/min$	- 61–73% D- CH_4 removal. - CH_4 content in waste gas <1% at high G/L ratios.	- High G/L ratios reduce CH_4 concentration in waste gas, making energy recovery unfeasible.
Packed Desorption Chamber	A desorption chamber with packing material to increase air/water contact surface area, enhancing D-CH_4 removal.	- Packed height: 1.0 m - G/L ratio: 0.03–4 - HLR: 0.10–1.70 $m^3/m^2/min$	- 40–99% D-CH_4 removal. - CH_4 content in waste gas: up to 22% at low G/L ratios.	- Clogging risk due to suspended solids in UASB effluent. - Performance depends on pH and HLR.
Closed Downflow Hanging Sponge (DHS) Reactor	A two-stage system where D-CH_4 is desorbed and biologically oxidized in a sponge-packed reactor.	- G/L ratio: 0.048–0.071 (1st stage), 0.48 (2nd stage) - HRT: 2 h per stage	- 70% D-CH_4 removal in 1st stage. - 99% D-CH_4 removal in both stages. - CH_4 content: 30–40%.	- Requires two stages for effective removal. - Limited oxygen availability in the first stage.
Vacuum-Assisted Chamber	A system where vacuum is applied to a thin layer of UASB effluent to strip D-CH_4.	- Vacuum pressure: Not specified	- 75% D-CH_4 removal. - CH_4 content in waste gas: Not reported.	- Limited data available on CH_4 content in waste gas. - Requires further validation at larger scales.

[3] HLR: Hydraulic loading rate.

C. Removal of Volatile organic compound (VOC) from water

VOCs are a group of chemicals that can easily evaporate into air at room temperature, including solvents, fuels, and other chemicals commonly used in industrial processes. VOCs can be harmful to human health and the environment, and their presence in wastewater can also cause odor, taste and color issues. The effectiveness of the stripping process is determined by various parameters, including the type and concentration of VOCs present in the water or wastewater, temperature and system pressure [42].

Traditionally, the removal of VOCs from water has been accomplished using air stripping technologies, which take advantage of contaminants' volatility to transfer them from the liquid phase to the gas phase. The most common systems include packed column air strippers, tray-type (sieve plate) air strippers, and diffused aeration systems. These systems can remove over 90% of common VOCs like benzene, toluene and chloroform when properly configured [13].

The packed column air stripper operates through a carefully designed process. It is the adopted technology for the removal of VOCs such as benzene, toluene and chloroform from industrial wastewater and contaminated groundwater [13]. It consists, as shown in Figure 1-3, of a column (diameter of 0.3-3 m, length of 3-10 m) filled with packing materials (e.g., Raschig rings), and a spray nozzle for water distribution at the top of the column. The column also has an air distribution system at the bottom. The water trickles down through the spaces between the packing materials to the bottom of the column while the air moves up in a countercurrent operation. Optimal performance is achieved at liquid flow rates of 0.8-1.8 (m^3/min) per square meter of column cross-sectional area and air-to-water (A/W) flow ratios of 10:1 to 30:1. The system achieves removal of most VOCs with pressure drops maintained at 200-400 Pa per meter of packing height to prevent clogging, while this depends on many factors such as the characteristics of the volatile (partial pressure, Henry's constant, gas transfer resistance, etc.), water and ambient air temperature, gas and liquid phase turbulence, A/W ratio, column height, and exposure time [13].

Although it has some advantages, such as a low price, scalability, and sensitivity to hybrid systems (e.g., preceded by adsorption or plasma treatment), it still lacks limitations in fouling potential, the need for off-gas treatment, and poor efficiency when used for low volatility or highly soluble compounds [13].

Packed column air stripper is also used in order to remove trihalomethanes (THMs[4]) from drinking water [12]. Canosa and Martí have shown three case studies of air stripping columns; small-scale conducted in Córdoba, Spain, intermediate scale in San Diego, Venezuela, and large-scale in Barcelona, Spain. These studies demonstrate the applicability of packed column air stripper across different treatment capacities. Table 1-6 below summarizes comparative key parameters. The three case studies showed increasing size of the column due to greater airflow and greater removal of THMs. In the third case study, the direct application of the water flow yielded a height value of 17.43 m and a diameter of 10.95 m, both of which are not mechanically feasible according to well-known rules of thumb (Internal diameter: (0.5–3 m)). The design solution for the third case study consisted in dividing the treatment capacity flow into different parallel columns maintaining the height and a diameter equal to or less than 3 m. Splitting the total flow of 14 stripping columns in parallel several times was required.

[4] Trihalomethanes (THMs) in drinking water are disinfection byproducts formed by the action of chlorine derivatives on precursors (organic matter, bromide) present in the final steps of drinking water treatment plants.

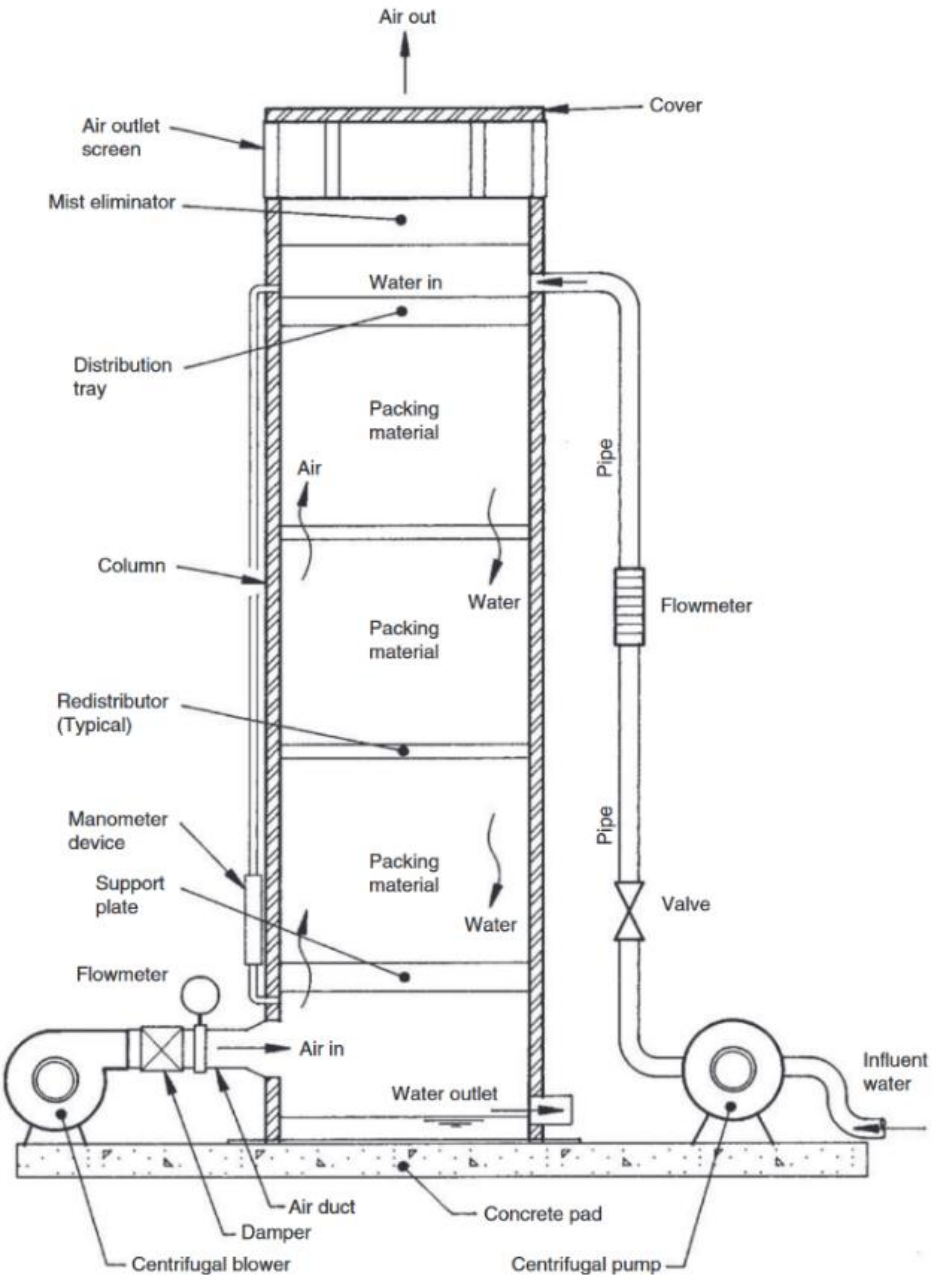

Figure 1.3 A packed column air stripper [13].

Table 1.6. General information and key parameters of the case studies [12].

	Case study 1	**Case study 2**	**Case study 3**
Location	Córdoba (ES)	San Diego (VE)	Sant Joan Despí (ES)
Water flow rate ($L.min^{-1}$)	1260	15,000	23500
THMs Input concentration ($\mu g.L^{-1}$)	22	82	96.5
THMs Removal rate (%)	54.6	74.4	77.6
Number of columns, n	1	1	14
G/L volumetric ratio (-)	5.9	6.2	14.7
Packing materials	Hiflow ring Plastic-3.1/2"	Hiflow ring Plastic-3.1/2"	Envipac ring Plastic-3.1/8"
a (m^{-1})	103	103	95
H_{column} (m)	5.55	13.95	17.43

The effects of various parameters such as column pressure, temperature, gas-liquid flow rate, and inlet VOC concentration on the efficiency of packed column strippers have been investigated in numerous research papers. For example, Ghoreyshi and Sadeghifar [11] presented a mathematical mass transfer model to investigate the ability of packed towers to reduce the concentration of pollutants to acceptable levels. It was found that these parameters can affect the removal of different VOCs differently, and the required tower height is significantly dependent on VOC solubility.

Their results also indicate that the gas-phase resistance contributes only 2.8% of the total resistance for carbon tetrachloride, while it contributes 22.8% for dichlorobenzene. Inclusion of the gas phase resistance in the series resistance model does not change the removal efficiency value for carbon tetrachloride but does decrease the removal efficiency for dichlorobenzene.

The removal efficiency of trichloroethane at G/L = 25 (volume/volume) is only 4% higher than at G/L = 5. For dichlorobenzene, the air-to-water ratio makes a significant difference, increasing the removal efficiency from 35% at G/L = 5 to 85% at G/L = 25 [11].

Using a high vacuum (P = 0.1 atm) and preheating the water to 30 °C was found to be very effective for the removal of more volatile compounds, while the effect is insignificant for more soluble compounds. It is possible to reduce the concentration of more volatile organics such as carbon tetrachloride to acceptable levels using a packed tower of economic height. However, it is not possible

to extrapolate these results to highly soluble compounds because the operation and tower size become uneconomical. Therefore, it is recommended that other separation processes such as air stripping-carbon adsorption hybrid processes or membrane separation processes (pervaporation) have to be considered for the desorption of less volatile organic compounds from water [11] .

Other studies have also attempted to enhance column characterization to improve its efficiency as well as the process intensification. Hassan-Beck [43] proposed the rotating packed beds (RPBs) for the removal of ethylene dichloride (EDC) from water. However, there are some challenges associated with this method like high-speed operation of RPB needs effective sealing systems, such as face seals or labyrinth seals, similar to pumps and compressors. In addition, the number of theoretical stages achievable is limited to about 20–25 per rotor, and thus multiple rotors in series or parallel must be used to achieve complex separations. RPBs also incur relatively high pressure drops compared to conventional packed beds, largely due to high friction losses from high centrifugal forces, which result in an energy penalty, especially at high liquid velocities.

Burger *et al.* [44] conducted an economic cost study to design a cost-effective stripping column for reducing trichloroethylene (TCE), tetrachloroethylene (PCE), and chloroform concentrations in effluent to below 5 ppm. The design was based on a feed water flow rate of 1000 m^3/day. Their analysis determined that a column with a diameter of 0.5564 m and a height of 8.272 m, packed with 1/2-inch Berl saddles and operated with an air-to-water ratio of approximately 8.8:1 (an air flow rate of ~8833 m^3/day), was required to achieve the target efficiency. The total capital cost, including the column and a necessary heat exchanger, was estimated at $129,344.83.

Another example of traditional technology used in VOC removal from water is the tray-type (Shallow Tray) air stripper, noted in Figure 1-4, as studied by LaBranche and Collins [45]. This system demonstrated effective removal of trichloroethylene (TCE), tetrachloroethylene (PCE), and total petroleum hydrocarbons (TPH) from contaminated groundwater. Operating with ambient air as the stripping agent, the technology achieved exceptional VOC removal efficiencies (>99.99%) across liquid flow rates of 18.9–75.7 L/min, utilizing high air-to-water ratios (100–900). While VOC removal was consistent under varying conditions, TPH removal showed strong temperature dependence, improving by 2.61% per °C increase, with optimal performance observed between 16–28°C. The compact design (2.12 m height, modular trays with polypropylene packing) minimized fouling risks due to its self-cleaning bubble action. However, a key limitation of this air-based approach is the requirement for additional off-gas treatment (catalytic oxidation and NaOH scrubbing) to prevent atmospheric pollution. Energy demand for air blowers and oxidation represented the primary operating costs. Although highly effective for volatile compounds, the system's reduced efficiency for less volatile TPH requiring temperatures ≥ 27°C for complete removal underscores why industries often consider steam stripping

or hybrid systems for complex contamination scenarios, particularly in petroleum remediation applications.

A comparative analysis demonstrated the superior operability and economic viability of steam stripping over air stripping [46]. Despite higher initial steam costs, steam stripping simplifies the process by condensing pollutants into a reusable distillate, thereby avoiding the need for complex off-gas treatment. In a case study on pharmaceutical wastewater, steam stripping reduced total annual costs by 17% and achieved adsorbable organically bound halogens (AOX) concentrations below 0.5 ppm. The study positions steam stripping as a greener alternative, particularly when solvent recovery is feasible, aligning with sustainable industrial practices.

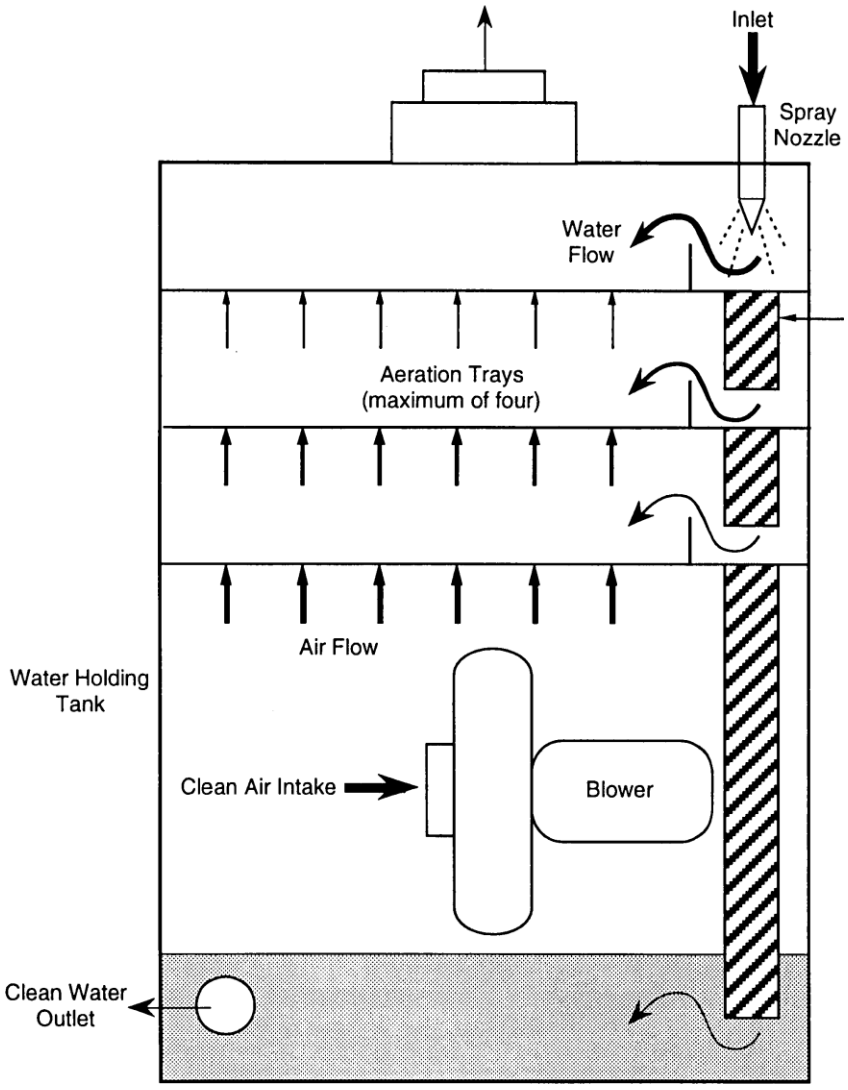

Figure 1.4 Tray-type air stripper [45].

D. Other applications of conventional water degassing technologies

Conventional degassing technologies have been implemented in various sectors to address complex environmental, safety, and product quality issues. For example, ammonia stripping, once reserved for industrial wastewater treatment, is now essential in fertilizer production and municipal wastewater treatment [47].

The considerations for technological selection are based upon characteristics of wastewater as well as other classical concerns i.e., operational cost, maintenance, and feasibility. Air stripping can be an attractive option of technology that offers ammonia/ammonium removal and recovery [48].

Water spray reactors have been successfully practiced treating varying wastewater from municipal to industrial, as well as landfill leachates and anaerobic digestate. Maghfiroh *et al*. [49] evaluated a water spray reactor for ammonia removal via air stripping, identifying optimal conditions for high efficiency (99% removal after 7 hours) with a mass transfer coefficient ($k_L.a_{LG}$) of 0.0114 min^{-1}. Key parameters included a water flow rate of 10 L/min, air flow rate of 120 L/min, and pH 11. The reactor demonstrated lower air consumption (2016 L air/L liquid) compared to other systems like jet loop reactors (2266 L/L) and water-sparged aero-cyclones (2394 L/L). Table 1-7 shows the technologies used for ammonia removal from water.

Table 1.7. Comparison of Ammonia Removal Technologies [49].

	pH	**Air Consumption (L air/L liquid)**	**Removal Efficiency (%)**	**Volumetric mass Transfer Coefficient (min^{-1})**
Water Spray Reactor	11	2016	99.0	0.0114
Packed Tower	8.5	1572	57.1	0.00323
Jet Loop Reactor	11	2266	81.5	0.00165
Water-Sparged Aero-cyclone	11	2394	98.0	0.00200

Similarly, sour water stripping in petroleum refineries uses tray or packed columns to remove hydrogen sulfide (H_2S), preventing equipment corrosion and toxic emissions [21]. There are several

techniques for sour water treatments; stripping with steam or flue gas, air oxidation to convert sulfides to thiosulfates, or vaporization and incineration. The most used one for sour water is steam stripping [15,50,51].

1.4 Overcoming Conventional Stripping Challenges with Membrane Contactors

Having already covered conventional stripping technologies and their limitations in previous sections, this section emphasizes the novel features of HFMCs, their advantages and their potential to overcome traditional challenges.

Hollow Fiber Membrane Contactors (HFMCs) overcome the long-standing challenges of conventional packed column mass transfer devices. Unlike other systems that suffer from flow-dependent limitations - overloading at high flow rates, unloading at low flow rates - HFMCs work equally well under all conditions due to their innovative non-dispersive contact mechanism. This advanced solution not only prevents emulsion formation, but also eliminates the need for density differences between liquids, providing unparalleled freedom in system design and orientation [3].

The benefits extend to operational scalability. While conventional systems require complex redesigns for scale-up, HFMCs achieve capacity expansion through simple modular addition. This linear scalability, combined with consistent performance, makes them particularly valuable for applications requiring precise solvent/feed ratios or future expansion [52] .

While HFMCs introduce new concerns such as membrane resistance and potential shell-side bypass, ongoing design improvements continue to minimize these concerns. The additional membrane resistance is typically modest in practice, and modern module design effectively minimizes flow bypass. Although factors such as fouling, membrane lifetime and solvent compatibility must be considered, these are usually outweighed by the operational advantages of HFMCs - and this is why they are beginning to find numerous applications from wastewater treatment to chemical processing.

As the technology overcomes existing limitations with improved materials and module designs, membrane contactors could be the mass transfer technology of the future, offering reliability, flexibility and scalability that traditional systems simply cannot match. Hollow fibers membranes are preferred due to distinct advantages over flat or tubular membranes, such as a large effective surface-to-volume ratio, conceptual simplicity, easy incorporation into flow streams and broad availability [53].

For instance, in methane degassing from wastewater [54], for recovering dissolved methane from anaerobic membrane bioreactor (AnMBR) effluents, membrane contactors can achieve dissolved methane recovery rates of up to 100%, demonstrating their effectiveness and efficiency in resource recovery. Among three primary technologies for dissolved methane recovery: aeration, gas stripping,

and membrane-based systems, HFMCs outshine them all. As can be noted from Table 1-8 which summarizes the different approaches used for the recovery of dissolved methane from wastewater.

Table 1.8. The different approaches used for the recovery of dissolved methane from wastewater [54].

	Aeration	**Stripping gas**	**Membrane**
Example	Bubble column	Packed column	HFMC
Mass transfer area	Relatively low (50 - 100 m^2/m^3)	Relatively high (250 m^2/m^3)	High (25000 m^2/m^3)
Operation	Difficult	Easy	Easy
Scale up	Difficult	Easy	Easy
Removal rate of CH_4	Up to 73%	Up to 70%	Up to 96 %
Problems	Difficult to operate and scale-up	Flooding and foaming	Require maintenance due to membrane fouling

The following chapter will delve into the fundamental principles governing membrane contactor operation, exploring their mechanistic advantages and diverse applications in stripping processes across water treatment and resource recovery.

1.5 Conclusion

One of the major operations in industrial processes is stripping. The need for effective stripping technologies cannot be overstated, particularly in the pharmaceutical, food and beverage, and chemical process industries, where water purity has a direct impact on plant efficiency and product integrity.

Although widely used, conventional stripping technologies have several limitations in terms of operation and mass transfer. These limitations require other options that can provide improved performance and scalability. HFMCs offer an excellent alternative by overcoming the shortcomings of traditional systems through improved mass transfer characteristics and versatile operation.

As industrial processes are optimized, the future of striping processes lies in the wider application of membrane-based technologies. HFMCs can not only increase efficiency but also offer opportunities for resource recovery and sustainability. Research and development in this area will also drive these technologies towards wider applications in water treatment and environmental management.

The literature survey presented here emphasize the need for appropriate technology selection, depending on the needs of individual industries, to achieve optimum performance.

1.6 References

[1] K. Ramaswamy, MWH's Water Treatment, Third Edition, n.d. https://www.academia.edu/34924046/MWHs_Water_Treatment (accessed March 12, 2025).

[2] G. Tchobanoglous, L.M. Franklin, E. Burton, H. Stensel, Wastewater Engineering Treatment and Reuse (Fourth Edition), in: 2011. https://www.semanticscholar.org/paper/Wastewater-Engineering-Treatment-and-Reuse-(-Fourth-Tchobanoglous-Franklin/f65f8e459abc86496e7658ee7e7203855c159ea3 (accessed February 28, 2025).

[3] A. Gabelman, S.-T. Hwang, Hollow fiber membrane contactors, J. Membr. Sci. 159 (1999) 61–106. https://doi.org/10.1016/S0376-7388(99)00040-X.

[4] Y. Zhang, R. Wang, Gas–liquid membrane contactors for acid gas removal: recent advances and future challenges, Curr. Opin. Chem. Eng. 2 (2013) 255–262. https://doi.org/10.1016/j.coche.2013.03.008.

[5] Z.Y. Kong, E. Sánchez-Ramírez, A. Yang, W. Shen, J.G. Segovia-Hernández, J. Sunarso, Process intensification from conventional to advanced distillations: Past, present, and future, Chem. Eng. Res. Des. 188 (2022) 378–392. https://doi.org/10.1016/j.cherd.2022.09.056.

[6] F.J. Keil, Process intensification, Rev. Chem. Eng. 34 (2018) 135–200. https://doi.org/10.1515/revce-2017-0085.

[7] M. Rezakazemi, M. Younas, eds., Membrane Contactor Technology, in: Membr. Contactor Technol., 1st ed., Wiley, 2022. https://doi.org/10.1002/9783527831036.fmatter.

[8] A.B. de Haan, H.B. Eral, B. Schuur, Chapter 3. Absorption and Stripping, in: Ind. Sep. Process., De Gruyter, 2020: pp. 57–80. https://www.degruyterbrill.com/document/doi/10.1515/9783110654806-003/pdf?licenseType=restricted&srsltid=AfmBOoqzrthnGiSSWXJgNa_ST29BzhArHQoPHstZMnGMNz3imZb0nRqE (accessed April 15, 2025).

[9] R. Jiménez-Robles, C. Gabaldón, V. Martínez-Soria, M. Izquierdo, Simultaneous application of vacuum and sweep gas in a polypropylene membrane contactor for the recovery of dissolved methane from water, J. Membr. Sci. 617 (2021) 118560. https://doi.org/10.1016/j.memsci.2020.118560.

[10] R.H. Perry, D.W. Green, eds., Section 14 - gas absorption and gas-liquid system design, in: Perrys Chem. Eng. Handb., 7. ed, 1997: pp. 1340–1431.

[11] A.A. Ghoreyshi, H. Sadeghifar, F. Entezarion, Efficiency assessment of air stripping packed towers for removal of VOCs (volatile organic compounds) from industrial and drinking waters, Energy 73 (2014) 838–843. https://doi.org/10.1016/j.energy.2014.06.090.

[12] J. Canosa, V. Martí, Design of Stripping Columns Applied to Drinking Water to Minimize Carcinogenic Risk from Trihalomethanes (THMs), Toxics 6 (2018) 18. https://doi.org/10.3390/toxics6010018.

[13] M.E. Abdullahi, M.A. Abu Hassan, Z.Z. Noor, R.K.R. Ibrahim, Application of a packed column air stripper in the removal of volatile organic compounds from wastewater, Rev. Chem. Eng. 30 (2014). https://doi.org/10.1515/revce-2014-0003.

[14] W.M.K.R.T.W. Bandara, H. Satoh, M. Sasakawa, Y. Nakahara, M. Takahashi, S. Okabe, Removal of residual dissolved methane gas in an upflow anaerobic sludge blanket reactor treating low-strength wastewater at low temperature with degassing membrane, Water Res. 45 (2011) 3533–3540. https://doi.org/10.1016/j.watres.2011.04.030.

[15] H. Gai, S. Chen, K. Lin, X. Zhang, C. Wang, M. Xiao, T. Huang, H. Song, Conceptual design of energy-saving stripping process for industrial sour water, Chin. J. Chem. Eng. 28 (2020) 1277–1284. https://doi.org/10.1016/j.cjche.2019.12.020.

[16] S. Al Dawery, W. AbdulMajeed, S. Al Shukaili, C. Thotireddy, I. Al Amri, Produced Water Deoxygenation: Investigation of Nitrogen Purging scheme– Parametric Study – Part1, Eng. Technol. J. 40 (2022) 1090–1104. https://doi.org/10.30684/etj.2022.133677.1200.

[17] J. Lee, S.-M. Baek, C. Boo, A. Son, H. Jung, S.S. Park, S.W. Hong, Water deoxygenation using a hollow fiber membrane contactor to prevent pipe corrosion for sustainable management of district heating systems: A pilot-scale study, J. Clean. Prod. 277 (2020) 124049. https://doi.org/10.1016/j.jclepro.2020.124049.

[18] E. Centeno Mora, C. de L. Chernicharo, Use of membrane contactors for removing and recovering dissolved methane from anaerobic reactors effluents: state-of-the-art, challenges, and perspectives, Rev. Environ. Sci. Biotechnol. 19 (2020) 673–697. https://doi.org/10.1007/s11157-020-09546-w.
[19] R.-S. Juang, S.-H. Lin, M.-C. Yang, Mass transfer analysis on air stripping of VOCs from water in microporous hollow fibers, J. Membr. Sci. 255 (2005) 79–87. https://doi.org/10.1016/j.memsci.2005.01.022.
[20] S.N. Ashrafizadeh, Z. Khorasani, Ammonia removal from aqueous solutions using hollow-fiber membrane contactors, Chem. Eng. J. 162 (2010) 242–249. https://doi.org/10.1016/j.cej.2010.05.036.
[21] A.E. Frederick, C.T. Leach, C.U. Nayandi, Alternative Technology for Sour Water Stripping, (n.d.).
[22] J. Wang, X. Li, G. Ma, H. Sui, L. He, R. Liu, Removal of residual solvent from solvent-extracted unconventional oil ores gangue by gas bubbling, Sep. Purif. Technol. 254 (2021) 117551. https://doi.org/10.1016/j.seppur.2020.117551.
[23] A.J. Dijkstra, Edible Oil Processing from a Patent Perspective, Springer US, Boston, MA, 2013. https://doi.org/10.1007/978-1-4614-3351-4.
[24] D. Bhaumik, S. Majumdar, Q. Fan, K.K. Sirkar, Hollow fiber membrane degassing in ultrapure water and microbiocontamination, J. Membr. Sci. 235 (2004) 31–41. https://doi.org/10.1016/j.memsci.2003.12.022.
[25] A. Mandowara, P.K. Bhattacharya, Membrane contactor as degasser operated under vacuum for ammonia removal from water: A numerical simulation of mass transfer under laminar flow conditions, Comput. Chem. Eng. 33 (2009) 1123–1131. https://doi.org/10.1016/j.compchemeng.2008.12.005.
[26] M. Darestani, V. Haigh, S.J. Couperthwaite, G.J. Millar, L.D. Nghiem, Hollow fibre membrane contactors for ammonia recovery: Current status and future developments, J. Environ. Chem. Eng. 5 (2017) 1349–1359. https://doi.org/10.1016/j.jece.2017.02.016.
[27] N. van Linden, Y. Wang, E. Sudhölter, H. Spanjers, J.B. van Lier, Selectivity of vacuum ammonia stripping using porous gas-permeable and dense pervaporation membranes under various hydraulic conditions and feed water compositions, J. Membr. Sci. 642 (2022) 120005. https://doi.org/10.1016/j.memsci.2021.120005.
[28] S. Rode, Opérations polyphasiques en génie des procédés: hydrodynamique, transferts, réactions, séparations mécaniques, Ellipses, Paris, 2019.
[29] D. Roizard, Gas–Liquid Membrane Contactor, in: Encycl. Membr., Springer, Berlin, Heidelberg, 2015: pp. 1–4. https://doi.org/10.1007/978-3-642-40872-4_265-1.
[30] K.M. Groß, Deaeration in Rotating Packed Beds, (2021). http://hdl.handle.net/2003/40163 (accessed September 26, 2025).
[31] Trambouze, P.; Euzen, J.-P. Chemical reactors. From design to operation / Pierre Trambouze, Jean-Paul Euzen ; translated by Robert Bononno, [Rev. ed.]; Institut français du pétrole publications; Editions TECHNIP: Paris, 2004.
[32] L. Jacxsens, F. Devlieghere, C. Van der Steen, J. Debevere, Effect of high oxygen modified atmosphere packaging on microbial growth and sensorial qualities of fresh-cut produce, Int. J. Food Microbiol. 71 (2001) 197–210. https://doi.org/10.1016/S0168-1605(01)00616-X.
[33] T. Suwa, A. Teramoto, Y. Shirai, T. Matsuo, N. Mizutani, S. Sugawa, Study on Influence of O2 Concentration in Wafer Cleaning Ambient for Smoothness of Silicon (110) Surface Appearing at Sidewall of Three-Dimensional Transistors, ECS Trans. 97 (2020) 23. https://doi.org/10.1149/09703.0023ecst.
[34] I.B. Butler, M.A.A. Schoonen, D.T. Rickard, Removal of dissolved oxygen from water: A comparison of four common techniques, Talanta 41 (1994) 211–215. https://doi.org/10.1016/0039-9140(94)80110-X.
[35] S.K. Al Dawery, W.S. AbdulMajeed, S. Al Shukaili, C. Thotireddy, I. Al Amri, Produced Water Deoxygenation via Nitrogen Purging Scheme– Parametric Study – Part 2, Eng. Technol. J. 40 (2022) 1260–1274. https://doi.org/10.30684/etj.2022.134758.1248.
[36] Z. Zhao, Z. Liu, Y. Xiang, M. Arowo, L. Shao, Removal of Dissolved Oxygen from Water by Nitrogen Stripping Coupled with Vacuum Degassing in a Rotor–Stator Reactor, Processes 9 (2021) 1354. https://doi.org/10.3390/pr9081354.

[37] Policymaker Framework | Global Methane Initiative, (n.d.). https://globalmethane.org/pmf/ (accessed March 18, 2025).
[38] I. Karakurt, G. Aydin, K. Aydiner, Sources and mitigation of methane emissions by sectors: A critical review, Renew. Energy 39 (2012) 40–48. https://doi.org/10.1016/j.renene.2011.09.006.
[39] E. Centeno Mora, C.L. Souza, T. Bressani-Ribeiro, C. a. L. Chernicharo, Dissolved methane, (2024). https://doi.org/10.2166/9781789063479_0207.
[40] P. Velasco, V. Jegatheesan, M. Othman, Recovery of Dissolved Methane From Anaerobic Membrane Bioreactor Using Degassing Membrane Contactors, Front. Environ. Sci. 6 (2018). https://www.frontiersin.org/articles/10.3389/fenvs.2018.00151 (accessed March 21, 2023).
[41] E. Centeno-Mora, P.R. Fonseca, W.L. Andreão, E.M.F. Brandt, C.L. De Souza, C. De Lemos Chernicharo, Mitigation of diffuse CH4 and H2S emissions from the liquid phase of UASB-based sewage treatment plants: challenges, techniques, and perspectives, Environ. Sci. Pollut. Res. 27 (2020) 35979–35992. https://doi.org/10.1007/s11356-020-08644-0.
[42] E. David, V.-C. Niculescu, Volatile Organic Compounds (VOCs) as Environmental Pollutants: Occurrence and Mitigation Using Nanomaterials, Int. J. Environ. Res. Public. Health 18 (2021) 13147. https://doi.org/10.3390/ijerph182413147.
[43] H.M. Hassan-Beck, Process Intensification: Mass Transfer and Pressure Drop for Countercurrent Rotating Packed Beds., (n.d.).
[44] B. Burger, R. Huff, C. Nowak, C. Mahon, R. Benoit, Design of a Cost-Effective Gas Stripping Column, (2015).
[45] D.F. Labranche, M.R. Collins, Stripping Volatile Organic Compounds and Petroleum Hydrocarbons from Water by Tray Aeration.:, Defense Technical Information Center, Fort Belvoir, VA, 1997. https://doi.org/10.21236/ADA323603.
[46] A.J. Toth, P. Mizsey, Comparison of air and steam stripping: removal of organic halogen compounds from process wastewaters, Int. J. Environ. Sci. Technol. 12 (2015) 1321–1330. https://doi.org/10.1007/s13762-014-0511-5.
[47] M. Sheikh, H.R. Harami, M. Rezakazemi, J.L. Cortina, T.M. Aminabhavi, C. Valderrama, Towards a sustainable transformation of municipal wastewater treatment plants into biofactories using advanced NH3-N recovery technologies: A review, Sci. Total Environ. 904 (2023) 166077. https://doi.org/10.1016/j.scitotenv.2023.166077.
[48] J.C. Campos, Moura ,Denise, Costa ,Ana Paula, Yokoyama ,Lidia, Araujo ,Fabiana Valeria da Fonseca, Cammarota ,Magali Christe, L. and Cardillo, Evaluation of pH, alkalinity and temperature during air stripping process for ammonia removal from landfill leachate, J. Environ. Sci. Health Part A 48 (2013) 1105–1113. https://doi.org/10.1080/10934529.2013.774658.
[49] M. Maghfiroh, N. Park, H. Chang, J. Jung, K. Ahn, H. Lim, W. Kim, Water spray reactor for ammonia removal via air stripping: An evaluation on mass transfer and process efficiency, J. Environ. Chem. Eng. 10 (2022) 108498. https://doi.org/10.1016/j.jece.2022.108498.
[50] Y. Zhang, Z. Fan, G. Jing, M.M.A. Saif, Optimization of Sour Water Stripping Unit Using Artificial Neural Network–Particle Swarm Optimization Algorithm, Processes 10 (2022) 1431. https://doi.org/10.3390/pr10081431.
[51] N. Quirante, J.A. Caballero, Large scale optimization of a sour water stripping plant using surrogate models, Comput. Chem. Eng. 92 (2016) 143–162. https://doi.org/10.1016/j.compchemeng.2016.04.039.
[52] A. Sengupta, P.A. Peterson, B.D. Miller, J. Schneider, C.W. Fulk, Large-scale application of membrane contactors for gas transfer from or to ultrapure water, Sep. Purif. Technol. 14 (1998) 189–200. https://doi.org/10.1016/S1383-5866(98)00074-4.
[53] E. Drioli, L. Giorno, E. Fontananova, Comprehensive Membrane Science and Engineering, Elsevier, 2017.
[54] P. Velasco, V. Jegatheesan, K. Thangavadivel, M. Othman, Y. Zhang, A focused review on membrane contactors for the recovery of dissolved methane from anaerobic membrane bioreactor (AnMBR) effluents, Chemosphere 278 (2021) 130448. https://doi.org/10.1016/j.chemosphere.2021.130448.

Chapter 2. Membrane contactor for stripping operation

2.1 Introduction

Membrane science and technology had a long historical journey of development in laboratory research before realizing its first significant industrial application. After years of rapid development, membrane-based processes today enjoy numerous industrial applications and have brought great benefits to improve human life [1]. Among various membrane-based processes, hollow fiber membrane contactors (HFMCs) have gained significant attention due to their ability to enhance mass transfer efficiency while operating at low or atmospheric pressure, making them ideal for process intensification in stripping operations [2].

The development of hollow-fiber membrane technology has been greatly inspired by intensive research and development of reverse-osmosis membranes during the 1960s. Du Pont's pioneer aramid polymer device was commercialized in 1969, followed by a cellulose triacetate polymer developed by the Dow Chemical Co. and Toyobo Co. Ltd. (Japan). Hollow fiber membranes have since become prevalent in water treatment, desalination, cell culture, medicine, and tissue engineering. Most commercial hollow fiber membranes are packed into cartridges which can be used for a variety of liquid and gaseous separations [3].

Developments in module design and membrane manufacturing did not occur until the 1990s [2]. The performance testing of membrane contactors began in 1995 at Kværner Process Systems (KPS) for post-combustion carbon capture (PCC), which carried out new gas treatment contactors using membrane technology. Through their work on the project, KPS and their technology partners have established a basic understanding of a membrane gas/liquid contactor and the potential for process optimization when using membrane gas/liquid contactors. W.L. Gore & Associates GmbH (GORE) provides the membranes, SGL Carbon Group (SGL) provides the modules and Ottestad Breathing Systems (OBS) provides the membrane protection system. Between 1998 and 2001, large-scale pilot tests were carried out with eight membrane modules for a total of 7,000 hours. The longest continuous operation was approximately 5,000 hours with a single module [4,5].

Gas-liquid separation processes, including methane recovery from wastewater and the removal of volatile organic compounds (VOCs) and other dissolved gases from various water resources, traditionally rely on energy-intensive methods such as packed or bubble columns. [6]. However, HFMCs offer a compact, modular, and energy-efficient alternative, leveraging a high surface-area-to-volume ratio to maximize interfacial contact between liquid and gas phases [7] .

As concluded in Chapter 1, packed columns and bubble reactors suffer from flow-dependent limitations such as overloading at high velocities and unloading at low velocities [2]. Membrane contactors are not subject to such limitations as they operate in a non-dispersive contact mode, allowing them to maintain constant performance over a wide range of flow conditions. This, together with their

compactness and modularity for scalability, has led to their increasing use where tight control of dissolved gases is required, such as in semiconductor manufacturing [8], district heating systems operating [9], and many other industrial purposes [10].

The intrinsic advantage of HFMCs is that they can achieve very high surface area to volume ratios (approximately 25000 m^2/m^3) compared to conventional contactors (50-500m^2/m^3) [5]. Geometrical intensification means that this translates into a significantly higher mass transfer rate, with $k_L.a_{LG}$ values for oxygen transfer of 0.05 - 0.5 s^{-1} possible with properly designed systems, whereas it is between 0.005 and 0.12 s^{-1} for a bubble column and between 0.0004 and 0.07 s^{-1} for a packed column [12]. In addition, independent control of gas and liquid flow eliminates the dependance on phase density differences, resulting in freedom of system orientation and ease of process integration [13].

Commercial applications of HFMC technology have developed over several generations. Early applications in the 1990s were aimed at oxygen stripping for ultrapure water production [14], and the stripping of volatile organic compounds from industrial wastewater [15], while current applications already extend to the recovery of dissolved methane from anaerobic digesters [11,16–18].

This has been made possible by advances in membrane materials, and modern systems use specially tailored polymers such as polypropylene (PP), polyvinylidene fluoride (PVDF) and polytetrafluoroethylene (PTFE) to balance hydrophobicity, chemical stability and mechanical strength [19].

The operational flexibility of HFMCs is particularly exploited in water deaeration applications, where they are able to use different driving forces such as vacuum, sweep gas or hybrid combinations [20]. For example, the study of Martić *et al*. [21] was interested in the influence of the purity of nitrogen (as sweep gas) in the de-oxygenation of water, showing the effectiveness of HFMC in the operation (with removal efficiencies of approximately 99%), and estimating that the cost was significant lower (~50%) than conventional degassing processes. Similarly, Lee *et al.* [9] described the stripping of oxygen from 8 mg/L to <10 µg/L from district heating systems using compact HFMC units, demonstrating their potential for large-scale application.

This chapter presents HFMC technology for stripping applications in a logical sequence, beginning with basic design principles and progressing to specific applications in water degassing. Module geometry and membrane material are also described and detailed. This fundamentals-to-applications approach is adapted to several water degassing applications, demonstrating the versatility of membrane contactor technology in different industries.

2.2 Fundamentals of HFMC Design

2.2.1 Core Principles: Design, Fluidics, and Trade-offs

A membrane contactor is a device where separation of compounds is accomplished due to a specific driving force through the membrane from the one phase to the other on opposite sides. This module achieves gas/liquid or liquid/liquid mass transfer without dispersion of either phase into the other [22].

The module design of membrane contactors depends on factors such as application, manufacturer specifications, membrane material, and operating scale [2,20]. Despite the complexity of classification, most membrane modules can be categorized into two primary geometries: flat sheet and tubular. Further classification is based on membrane material, packing density, and module structure, with common configurations including spiral wound, hollow fiber, plate-and-frame, tubular, and capillary designs [23]. Planar geometries (e.g., plate-and-frame and spiral-wound modules) differ from cylindrical geometries (e.g., tubular and hollow fiber modules). Each module type performs different functions, and the selection criteria depend on the target performance of a given application. For practical industrial use, an ideal membrane contactor module should balance efficiency, economy, compactness, and ease of maintenance or replacement [24].

A wide variety of HFMC modules are commercially available with different morphologies, transport properties, and separation mechanisms. These properties are mainly influenced by the membrane material properties and the manufacturing techniques.

Therefore, the selection of the appropriate membrane material is critical as it has a direct impact on the following:

- Transmembrane flux (increasing process efficiency)
- Polarization phenomena (reducing concentration and temperature polarization)
- Fouling resistance (extending membrane life)[24].

Hollow fiber modules are widely used in large-scale membrane applications [2]. Their structure, as illustrated in Figure 2-1, is similar to a shell-and-tube heat exchanger but the metal tubes are replaced with hollow fiber semi-permeable membranes that allow simultaneous heat and mass transfer between the working fluids [25]. It consists of a fine package of membrane fibers bundled into a cylindrical casing or shell. The two ends of the fiber bundle are placed in the shell with a potting material which can be different from the material of the fibers. In the lumen side, the fluid enters a hub (entry distribution zone), which is distributed in each fiber, and then leaves the other side of the fibers through an exit collection zone. The shell also has two ports, one for the fluid inlet and the other for the exit of that fluid.

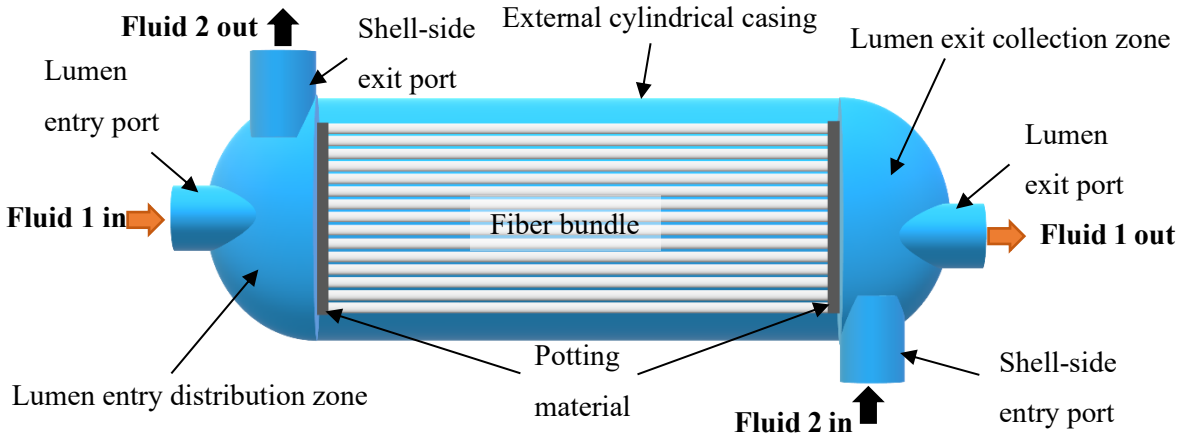

Figure 2.1. Essential elements of typical HFMC modules.

Within the membrane module, one phase (gas or liquid) is channeled into the hollow fibers on the lumen side and the other phase flows on the shell side in different configurations, including parallel flow (co-current and counter-current) and cross-flow [26]. A schematic of a commercially available contactor with different flow configurations is illustrated in Figure 2-2. A key drawback of parallel-flow designs is shell-side flow maldistribution, often caused by non-uniform fiber packing. To mitigate this, earlier designs directed liquid flow through the fiber lumens, but the resulting high pressure drop limited scalability [20].

(a) Parallel flow with co-current configuration: sweep gas

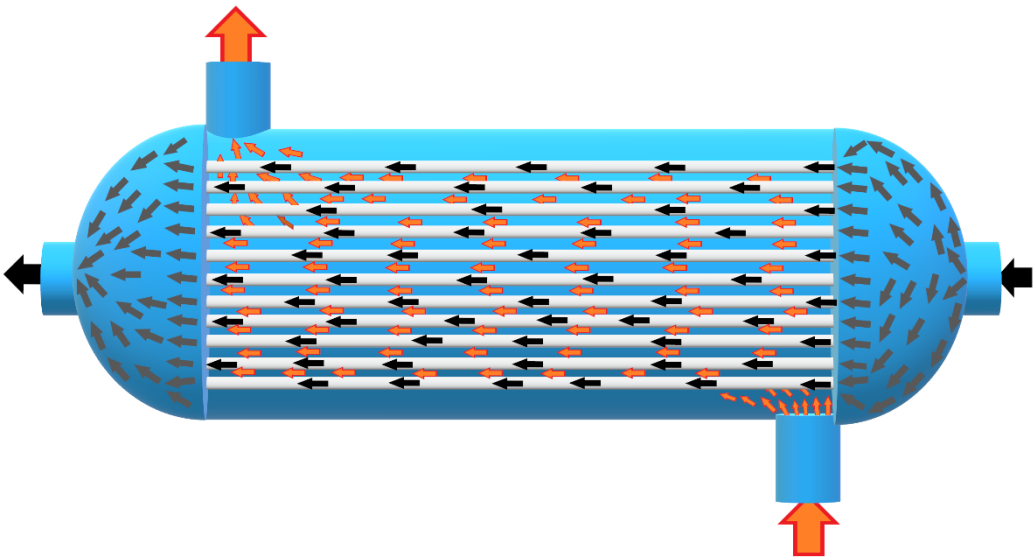

(b) Parallel flow with counter-current configuration: sweep gas

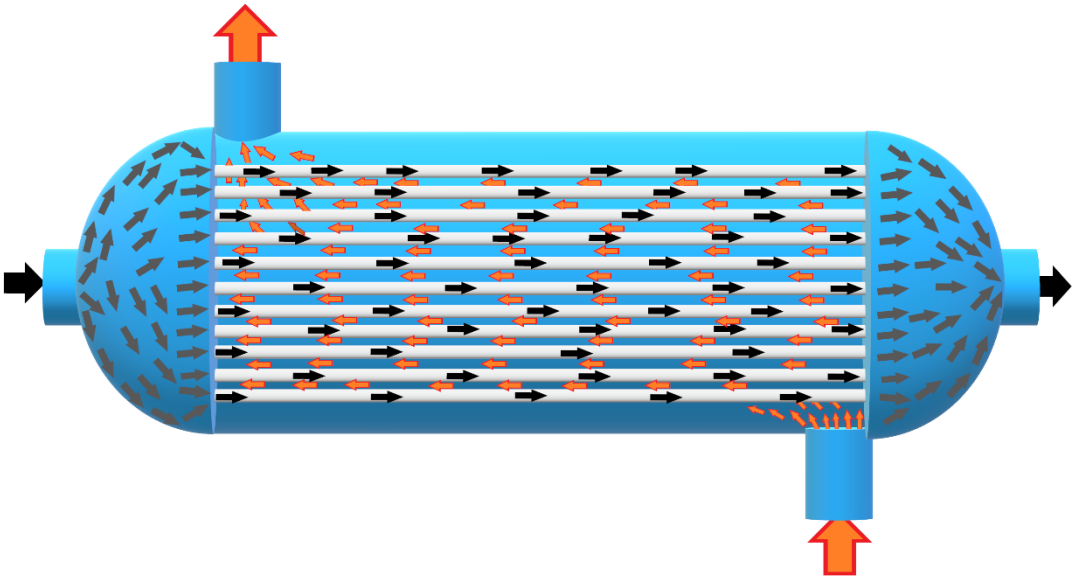

(c) Cross flow: sweep gas, with baffle in the liquid central distributor

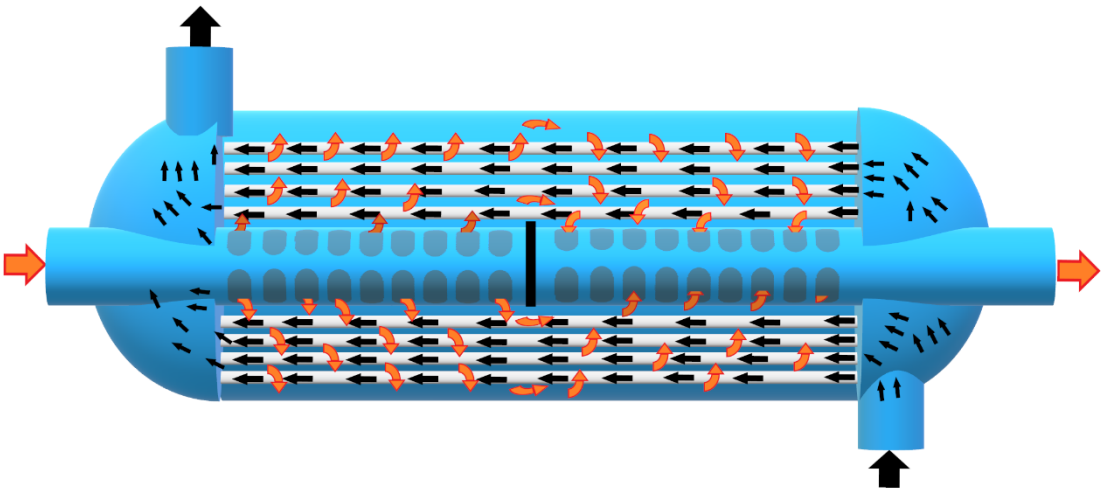

(d) Cross flow: vacuum, without baffle in the liquid central distributor)

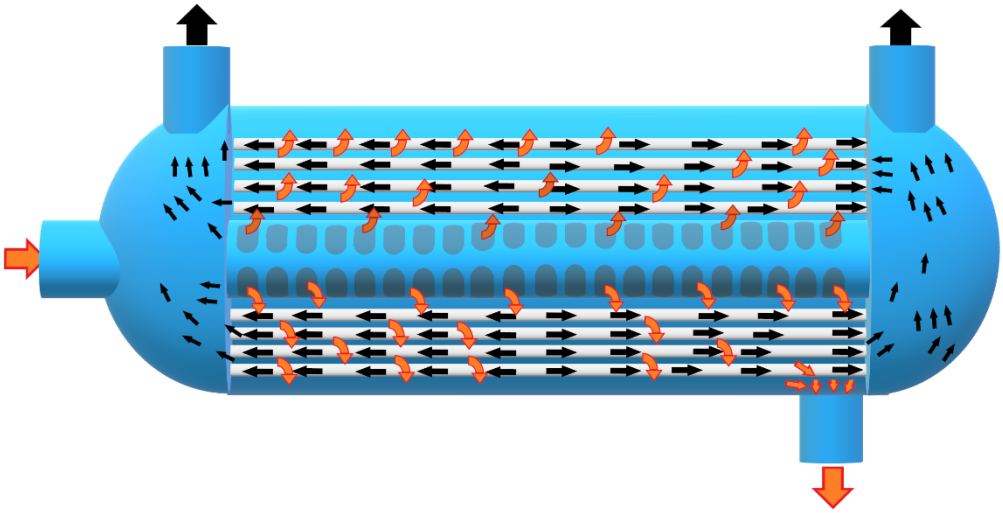

Figure 2.2. Schematic illustration of a hollow fiber membrane contactor module in (a) parallel flow with co-current configuration in sweep gas mode (b) parallel flow with counter-current configuration in sweep gas mode (c) cross-flow configuration in sweep gas mode (module with baffle) (d) cross-flow configuration in vacuum mode (module without baffle).

Directing the liquid flow on the shell side parallel to the fibers reduces the pressure drop, but introduced unpredictability in performance due to uneven shell-side hydrodynamics [20]. To address these challenges, transverse (radial cross-flow) configurations have been developed, incorporating a central perforated distribution tube to enhance shell-side flow uniformity (See figure 2-3). This design improves mass transfer efficiency by: (1) reducing concentration polarization, and (2) enhancing scalability, particularly in larger-diameter systems [27]. Transverse-flow modules have been intensively reported to offer higher mass transfer coefficient, minimal flow channeling, better hydraulic behavior and better scale-up characteristics [22,27,28]. This design may also employ one or more baffles on the shell side to optimize fluid flow dynamics. In this configuration, feed water enters the module through a central porous distributor. When a central baffle is implemented within this tube (Figure 1c), it forces the fluid to diverge radially outwards. The baffle, strategically placed in the center of the fiber bundle, ensures that the fluid flows perpendicular to the hollow fibers, which are axially aligned with the distribution tube. As the fluid flows outwards, it traverses the first half of the fiber bundle before reaching the outer periphery of the module. Here the flow passes through the annular gap between the fiber bundle and the module shell. The fluid then reverses direction and flows radially inwards over the second half of the fiber bundle. This counter-directional flow ensures efficient mass transfer while minimizing concentration polarization. Finally, the treated stream converges at the opposite end of the module. [20].

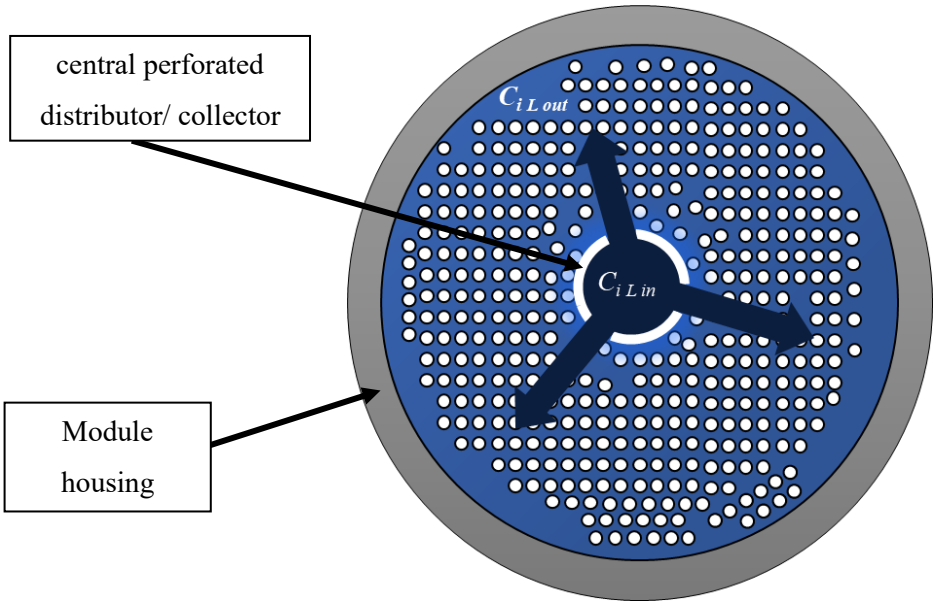

Figure 2.3 . Schematic cross-sectional view of a cross-flow HFMC module, illustrating Radial liquid flow.

While parallel-flow modules remain preferable when membrane or tube-side resistance dominates, cross-flow designs outperform them in shell-side-controlled systems by mitigating flow maldistribution. Baffled modules strike a balance, blending countercurrent and cross-flow elements to boost efficiency though at the expense of higher pressure drops and greater construction complexity [29].

The driving force for mass transfer in hollow-fiber membrane contactors (HFMCs) is generated by three primary methods: (1) applying vacuum, (2) supplying a sweep gas to remove target species, or (3) using a hybrid "combo" approach that combines a low sweep gas flow with vacuum to enhance the separation driving force while maintaining a vacuum on the gas side. For the vacuum method, optimal separation is achieved when vacuum is applied to both ends of the membrane (gas inlet and outlet) [20,25,26].

The choice of operating mode depends on the membrane material and the intended use of the recovered gases. Sweep gas operation is typically preferred for porous HFMCs, as it minimizes pore-wetting risks and improves the gas-side mass transfer coefficients. However, the recovered gas is diluted by the sweeping gas stream. In contrast, vacuum operation is more suitable for non-porous membranes and provides high purity gases, but requires more energy input to maintain the transmembrane pressure difference [30].

HFMCs offer high surface-area-to-volume ratios and modular scalability, but face challenges such as membrane wetting, fouling, and trade-offs between selectivity and permeability. A

comprehensive comparison of the advantages and disadvantages of HFMCs is summarized in Table 2-1 [31].

Table 2-1.Advantages and disadvantages of membrane contactors [31].

Advantages	**Disadvantages**
✓ In contrast to the absorption column, the membrane contactors provide a fixed contact area between the two phases. Thus, scaling up can be done according to the required contact area. ✓ Unlike traditional strippers, the interfacial area is independent of the flow rates of either of the fluids. ✓ Membrane contactors can be operated with a variety of fluid densities unlike the stripping column, which can only be brought into use if the contacting fluids have a considerable density difference. ✓ In membrane contactors, fluids do not disperse into each other, so there is no chance of emulsion formation. ✓ Thanks to the modularity of membrane contactor modules, scaling up of the process in membrane contactors is feasible by numbering up. On the other hand, in conventional processes, scaling up is not that easy. ✓ Membrane contactors provide 30 times more contact area as compared with the conventional columns, thus decreasing the height of the transfer unit (HTU). ✓ In comparison with the mechanical separation equipment, membrane contactors have no moving part. ✓ The opportunity for back mixing of the dispersed phase is reduced. ✓ The ease of coupling the unit operations in one step like absorption and stripping, extraction and regeneration, and reaction and separation.	✓ In membrane contactors, the membrane itself represents an additional resistance to mass transfer, ✓ Membranes suffer from fouling during their operation, and it is more obvious in the pressure-driven processes as compared with the concentration driven once. ✓ Membranes have a limited lifetime and often after a certain period of use they need to be replaced. ✓ Wettability of porous-based membrane contactor is another issue. It decreases the mass transfer to six times as compared with the non-wetted pores ✓ Normally membrane contactor modules are formed by combining a bundle of fibers in a single module using epoxy as an adhesive material. However, these potting materials are often susceptible to chemical and thermal attacks. ✓ For mass transfer to occur, membrane contactors are dependent upon the equilibrium stages, but sometimes, equilibrium stages are limited by pressure drop constraints along the length of the membrane contactor module, thus causing additional loss of separation efficiency. ✓ Unlike conventional columns, membrane contactors cannot handle solid particles in separation processes. ✓ Channeling and bypassing of fluids. ✓ Pretreatment before membrane contactor separation is needed.

2.2.2 Module geometries

The performance and efficiency of HFMC modules are significantly influenced by their geometric and structural characteristics [32]. Over recent decades, extensive efforts have been made to develop innovative membrane modules with optimized geometries and flow disruptors components to enhance species permeation while minimizing undesirable effects such as concentration polarization, fluid leakage, and membrane deterioration [27]. Two primary approaches have been employed to improve membrane performance:

Passive Enhancement: This involves modifying the membrane structure or module geometry to influence fluid dynamics. By incorporating spacers, secondary flow patterns, or flow instabilities, passive strategies improve mass transfer while reducing boundary layer effects.

Active Enhancement; This technique utilizes external energy (e.g., vibrations, pulsations, or electric fields) to induce high shear rates near the membrane surface, enhancing mixing and reducing boundary layer thickness [27].

In general, the HFMC consists of a bundle of cylindrical hollow fibers. The individual hollow fiber has an effective fiber length, l_{eff}, an external diameter, d_{ext}, and a relative membrane thickness, RMT. The arrangement of the fibers within the module defines the packing volume of the fibers within the module. The packing volume fraction, φ, is crucial for determining the overall efficiency and performance of the module. It directly impacts factors such as pressure drop, fluid flow distribution, and separation efficiency. Some geometrical characteristics of the HFMC are defined as shown in Table 2-2 [33].

Table 2-2. Some important geometrical parameters of the hollow fiber membrane contactor [33].

Parameter	**Mathematical expression**	**units**
Fiber thickness	$\delta = \frac{(dext-dint)}{2}$	m
Relative membrane thickness	$\frac{membrane\ thickness}{external\ fiber\ radius}$; $RMT = \frac{2\delta}{d_{ext}}$	$-$
Hydraulic diameter	$d_{h_ext} = d_{ext}\frac{1-\varphi}{\varphi}$, $d_{h_int} = d_{ext} - 2\delta$	m
Membrane surface area	$A_{int} = \pi \mathrm{d}_{int} l_{eff} N$, $A_{ext} = \pi \mathrm{d}_{ext} l_{eff} N$ $A_{ext} = A_{int}\ \frac{d_{ext}}{d_{int}}$	m^2
Packing volume fraction	$\varphi = N\left(\frac{d_{ext}}{\mathrm{D}}\right)^2$ for modules without central distributor $\varphi = N\ \frac{d_{ext}^2}{(D^2 - D_{cent\ dist}^2)}$ for modules with central distributor D Fiber bundle diameter, m	$-$
Number of fibers	$N = \frac{A_{ext}}{\pi d_{ext} l_{eff}}$	$-$

2.2.3 Membrane materials and properties

Membranes are thin films made from synthetic organic or inorganic (e.g., ceramic) materials, engineered with specialized structures to enable selective separation of components in fluid phases. Broadly, membranes are classified into two structural categories, as shown in Figure 2-4: isotropic (including microporous, mesoporous, nonporous (dense), and electrically charged membranes) and anisotropic (encompassing phase separation, composite, and nano-polymer membranes) [23] .

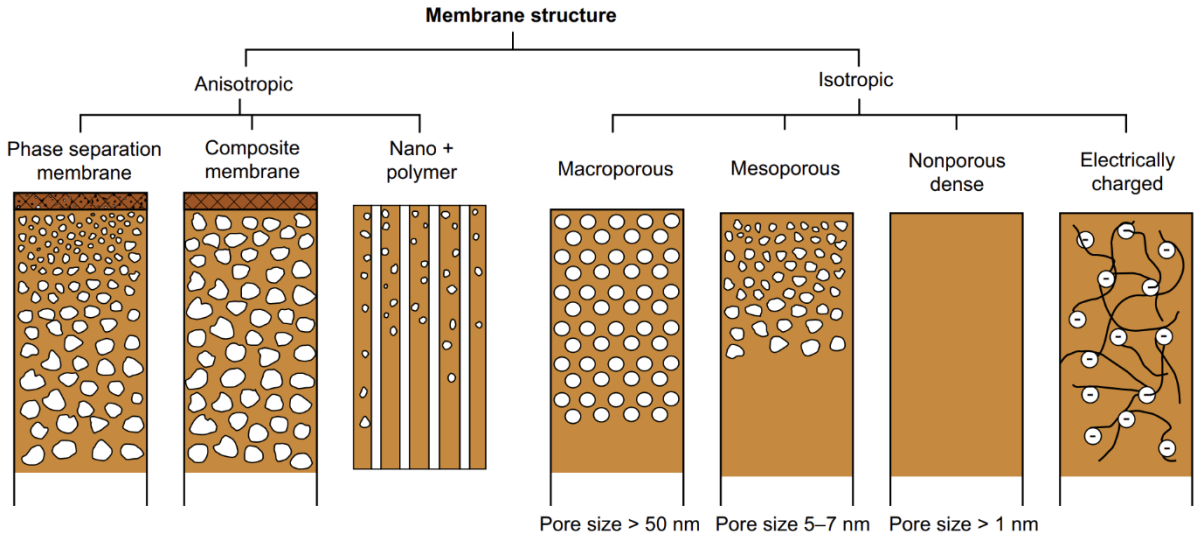

Figure 2.4. Schematic diagram of membrane structural construction [23].

Based on porosity, membranes are further divided into three types: porous [34,35], nanoporous [36], and dual-layered (combining porous and nanoporous layers) [9]. To enhance chemical resistance, particularly for handling aggressive chemical liquids, a three-layer membrane structure is often employed (as illustrated in Figure 2-5). This configuration provides superior strength and durability, mitigating the degrading effects of harsh chemicals [37].

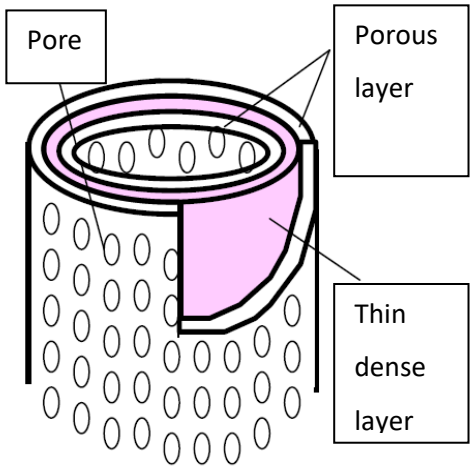

Figure 2.5. Structure of a multi-layered hollow fiber membrane [37].

Organic materials are promising candidates for the fabrication of hollow fiber membranes due to their cost effectiveness, ease of processing and scalability [38]. Over the past few decades, significant research efforts have focused on the development of polymeric hollow fiber membranes. Commonly used polymers include polypropylene (PP) [39], polyvinylidene fluoride (PVDF) [40], poly-di-methyl-siloxane [41] and so many other examples. The manufacturing process typically follows conventional methods, often including post-treatment steps such as silicone rubber coating to seal membrane defects and improve separation performance. However, significant challenges remain for polymer-based membranes, including achieving robustness under harsh operating conditions and producing an ultra-thin layer with maximum transport efficiency [38].

Selecting an appropriate material for fabricating dense membrane is crucial for achieving optimal performance. Key considerations include overcoming the permeability/selectivity trade-off, operating conditions, target removal efficiency, and compatibility with the process stream [42]. Additionally, mechanical strength, chemical resistance, and anti-fouling properties are vital for ensuring long-term operational stability [25]. For example, oxygen permeability through a polymer membrane is influenced by factors such as chemical composition, molecular weight, and crystallinity, which collectively determine the ease with which oxygen molecules traverse the membrane [43]. Detailed comparative data on oxygen permeability for different polymers are provided in Appendix 2-A (Tables A2-1 and A2-2).

For porous membranes, the choice of material is less critical than for dense membranes, as the polymer's intrinsic properties, particularly permeability, directly impact process productivity. Key properties, such as glass transition temperature and crystallinity, significantly influence membrane performance [43]. In water degassing applications, hydrophobic materials are preferred to prevent pore wetting by aqueous solutions, thereby maintaining permeability and ensuring effective separation [25].

Unlike conventional membrane technologies, where separation is driven primarily by transmembrane pressure, the driving force in membrane contactors is mainly the concentration gradient, so the membrane is mostly implemented as a barrier to isolate both phases, through which a mass-transfer is established from the phase to the other one [26].

2.3 Applications and examples

Stripping operation using HFMCs has been applied in various industrial processes such as water/wastewater treatment, and organic solvent treatment. For example, in the production of ultra-pure water, hollow fiber membrane contactors have been used for the removal of dissolved oxygen from water, for the recovery of volatile organic compounds from wastewater, and for ammonia stripping from industrial water [8].

For different gas-liquid contacting processes, HFMC has undergone substantial studies. In fact, it is obvious that HFMC has the potential to outperform traditional separation columns in many respects.

2.3.1 Removal of dissolved oxygen (DO) from water

Membrane degassing of liquids, particularly the removal of dissolved oxygen (DO) from water, is the second most important field of membrane contactor studies [25]. Removal of DO from water is a necessary process in many industries, including pharmaceutical, food, power, and semiconductors. For example, in the power industry removal of DO to levels of around 5 ppm is required to prevent corrosion in boilers and pipes [35]. In comparison, ultra-pure water, as used in the washing of silicon wafers in the semiconductor industry, is perhaps the most demanding in terms of DO level with some applications requiring extremely low DO levels of around 0.1 ppb [44]. Recently, HFMCs with different membrane materials were examined for stripping dissolved oxygen from water [45]. For example, some studies use hydrophobic micro-porous membranes [34], while others use porous membranes with ultra-thin non-porous coatings [36,37]. The studies also discuss factors that can affect the efficiency of the membranes, such as mass transfer coefficients, contact time, and temperature. Furthermore, some of the researchers present models in order to predict contactor performance [46].

Bhaumik *et al*. (2004) [8] investigated the use of HFMCs for ultrapure water (UPW) degassing in semiconductor manufacturing, where residual dissolved gases (CO_2, O_2) from advanced oxidation processes (AOPs) should be removed. The study employed a hydrophobic, porous polypropylene (PP) hollow fiber (Celgard X-30) in a lab-scale cross-flow module (Medtronic Minimax Plus™ blood oxygenator). The fibers were coated with PDD-TFE (a fluoropolymer) copolymer on the outer diameter to resist oxidative agents (e.g., O_3, H_2O_2) and biofouling. The system was operated with water on the shell side and vacuum (1-5 Torr) on the lumen side, achieving more than 90% removal of CO_2 and O_2 at water flow rates of 30-850 mL/min. They also found that the shell side liquid phase mass transfer coefficients of the dissolved gases in the cross-flow membrane modules ($k_L = AQ^b$) used varied with

b = 0.77 power of the volumetric liquid flow rate. This flow rate dependence is not far removed from the higher ranges of b values reported in the literature for a variety of cross-flow hollow fiber membrane modules.

Breniaux *et al*. (2019) [45] explored a lab-scale HFMC system for oxygen management in wine, comparing polypropylene (PP) and PP coated with Teflon AF2400 (PPT) membranes, with contact area of both membrane contactors (0.200 m^2 for PPT coated and 0.180 m^2 for PP), achieving 86–93% oxygen removal (final O_2 ~0.2 mg/L) in ultrapure water and red wines, at a liquid flow rate of 300 mL/min and gas flow of 120 mL/min CO_2 through the lumen, with the PPT coating reducing fouling in high-fouling-index wines; the study emphasized minimal organoleptic changes but noted losses of volatile esters.

Han *et al*. (2021) [46] investigated oxygen mass transfer in a polypropylene (PP) hollow fiber membrane contactor using pure water and pure oxygen. The study employed a module with 1560 randomly packed PP fibers (20 cm length, 0.5 mm outside diameter) in a bench-scale setup, with oxygen flowing through the lumen and water through the shell side at various liquid flowrates (100–320 L/h) and gas intake pressures (0.12–0.14 MPa). The results highlighted that, unlike classical theory, the intrinsic mass transfer coefficient ($K_x a$; total mass transfer coefficient of oxygen, in $mol \cdot m^{-3} \cdot s^{-1}$) did not increase monotonically with water flowrate (see figure 2-6); instead, it showed a peak and then declined before stabilizing at high velocities. This complex behavior was attributed to the interplay between the liquid film renewal time and the solubility equilibrium time at the gas–liquid interface. The study concluded that liquid-phase resistance dominated the process, and higher oxygen pressures enhanced mass transfer by modifying the interface properties. Specifically, by compressing the liquid film boundary, which reduces film thickness and accelerates renewal and diffusion rates (as per the proposed compressed liquid film model).

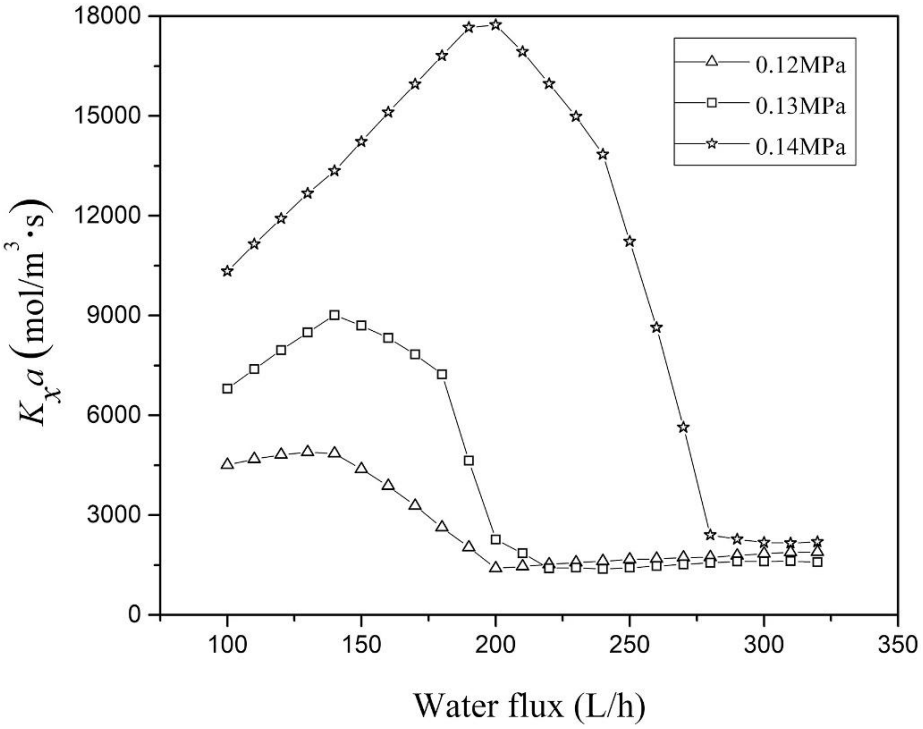

Figure 2.6. Oxygen mass transfer coefficient of membrane contactor at different pressures and fluxes [46].

Ito *et al*. (1998) [36] evaluated the removal of dissolved oxygen from ultrapure water using a non-porous silicone rubber hollow fiber membrane contactor. Their system consisted of 6000 silicone rubber fibers (320 μm outer diameter, 200 μm inner diameter, 14 cm effective length, 4950 cm^2 membrane area) arranged in a module where water was pumped through the lumen side, while the shell side was subjected to vacuum or swept with nitrogen as a striping gas. The study focused on bench-scale operation and evaluated vacuum degassing mode. They measured the gas permeabilities independently and developed a gas-phase driving force model that accounted for simultaneous transfer of oxygen, nitrogen, and water vapor. Operating conditions included varying the permeate side pressure (vacuum level) and water flow rate (in the laminar regime). The results showed (as illustrated in Figure 2-7) that lowering the shell-side pressure (stronger vacuum) significantly increased oxygen removal efficiency, reducing outlet DO from 6 mg/L to as low as 2 mg/L, and that lower water flow rates further enhanced deoxygenation. Model predictions matched experimental data well when liquid-phase mass transfer resistance was included, confirming that while membrane permeation could control the overall rate during deep vacuum operation, liquid-side resistance became more important at higher liquid flow rates. The authors concluded that non-porous silicone hollow fiber modules offer an effective, controllable method for deoxygenating water, with operational flexibility depending on the balance of membrane and liquid-side resistances, and their modeling approach can be extended to related gas transfer processes.

HFMCs have been explored as an innovative solution for deoxygenating salt solutions by Kattan *et al*. (2018) [47] demonstrating their feasibility for removing dissolved oxygen from concentrated sodium chloride (NaCl) solutions, a critical process to mitigate corrosion in industrial applications. The study focused on de-aerating salt solutions with NaCl concentrations ranging from 0.1 to 25.3 wt%, representative of brines used in chemical processing, rather than drinking water or wastewater. The experiments utilized a Liqui-Cel® 2.5 × 8 Extra-Flow module provided by 3M, featuring hydrophobic polypropylene (PP) hollow fibers with a total membrane area of approximately 1.4 m², configured in a cylindrical geometry. The system operated at a pilot scale, processing liquid flow rates of 0.1 to 0.7 m³/h, with the salt solution flowing on the shell side and a vacuum (50–80 mbar) applied to the lumen side as the sweeping agent, without any sweep gas. Operating conditions included temperatures of 20–40°C, with the highest oxygen removal efficiency (up to 98%) achieved at 40°C and 70 mbar, yielding outlet oxygen concentrations as low as 70 ppb. The study's primary motivation was to extend HFMC applications beyond ultrapure water to concentrated salt solutions, addressing a gap in the literature and enabling corrosion control in industries processing brines. Mass transfer correlations were developed, showing a higher-than-expected dependence of the Sherwood number on the Schmidt number (γ=0.44, where γ is the exponent in the correlation $Sh = \alpha\, Re^{\beta}\, Sc^{\gamma}$, quantifying the Schmidt number influence on mass transfer due to viscosity effects in high-salt solutions). Notably, no fouling or membrane weeping due to salt crystallization was observed, enhancing the technology's practical viability. The authors estimated that commercial-scale de-aeration of saturated NaCl solutions (100–900 m^3/h) to below 50 ppb oxygen would require 455–4105 m^2 of membrane area using Liqui-Cel® 14 × 40 modules, with two-stage operation of smaller Liqui-Cel® 10 × 28 modules reducing membrane surface area needs by 20% compared to single-stage operation of the same modules. These findings underscore HFMCs' potential for efficient, scalable deoxygenation of challenging salt solutions, with ongoing research needed to model water vapor effects and optimize mass transfer for broader industrial adoption. Due to the rich content of this paper, their results were used to validate the model developed in this thesis (see Chapter 4).

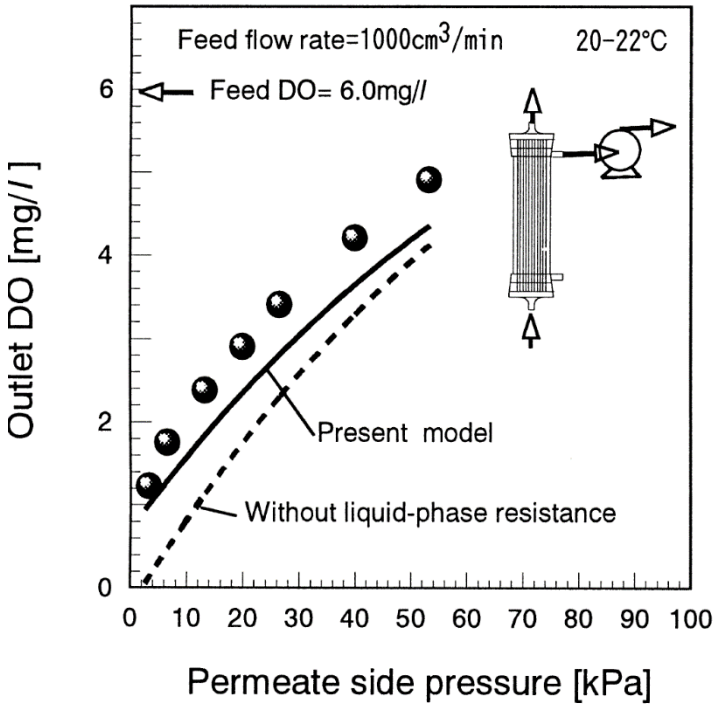

Figure 2.7. The effect of permeate side pressure to the DO removal efficiency of the vacuum degassing process [36].

Lee *et al*. (2020) [9] conducted a pilot-scale study on water deoxygenation in district heating systems (DHS) using a HFMC to mitigate steel pipe corrosion. The research used make-up water and district heating return water sourced from a real DHS, both of which contained organic matter and hardness ions. The contactor employed hydrophobic poly-4-methylpenten-1 (PMP) hollow fiber membranes (pilot scale: 40 m^2 area, treating 1 m^3/day) provided by SEPAREL, with water flowing on the shell side and a vacuum applied to the lumen side to strip dissolved oxygen. The system was tested under various conditions of membrane area, flow rate, and temperature, showing that effective deoxygenation (>99.9% DO removal, permeate DO <10 mg/L) was achieved when the applied vacuum was below the saturated vapor pressure of water at the working temperature. The study also found that organic fouling (mainly humic substances) was a major challenge, suggesting pre-filtration with ultrafiltration or nanofiltration for long-term stable operation. Corrosion tests with steel coupons demonstrated a dramatic decrease in corrosion rate and weight loss after deoxygenation, confirming the practical benefit of HFMCs for DHS management.

The authors also demonstrated the removal performance of the HFMC deoxygenation process across different membrane areas in lab-scale modules, as illustrated in Figure 2-8.

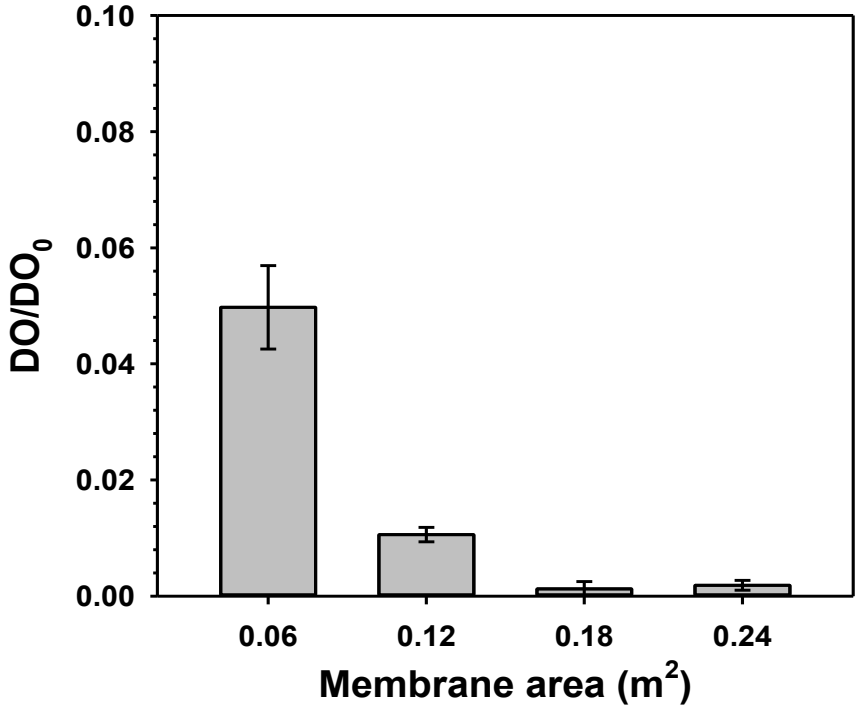

Figure 2.8 . Representative DO removal performance with respect to membrane area in lab-scale HFMC deoxygenation process (operating condition: feedwater temperature of 25ºC and flow rate of 30 ml min-1) [9].

In the study by Martić *et al*. (2014) [21], a pilot plant-scale HFMC system was developed and investigated for the removal of dissolved oxygen from water, using nitrogen as an inert sweeping gas. The primary motivation for this work was to address the need for efficient deoxygenation to protect industrial equipment like boilers and heat exchangers from corrosion and reduced efficiency. The feed water treated in this study was demineralized or pre-treated water. The membrane modules utilized were Liqui-Cel X-IN hollow fiber membranes provided from 3M. The experimental system operated on a pilot plant scale, featuring three membrane modules arranged in series to achieve lower oxygen concentrations at the outlet, with a maximum water flow capacity of 450 m^3/h and the capability to reduce oxygen concentration to as low as 7.5 ppb. In terms of process geometry, the water stream was introduced on the shell side of the membrane module, while high-purity nitrogen gas was applied under vacuum to the lumen side of the fibers, effectively sweeping out the dissolved oxygen. The typical operating conditions included a water flow rate of 20 m^3/h at an inlet temperature of 12°C, a nitrogen flow rate of 6 m^3/h per module, and a vacuum level of 150 mm Hg. The study specifically investigated the impact of nitrogen purity (ranging from 50% to 99.99%) on the efficiency of oxygen removal. Results indicated that higher nitrogen purity led to significantly lower residual oxygen concentrations and higher removal efficiencies, with the system achieving up to 98.7% oxygen removal at 99.99% nitrogen purity. The study also provided empirical equations correlating nitrogen purity with both outlet oxygen concentration and overall deoxygenation efficiency, which are necessary for the design and

optimization of such systems under similar conditions. For benchmarking, the authors compared the membrane-based process to conventional thermal degasification, highlighting that the membrane approach offers some advantages in terms of energy efficiency, cost, and ecological impact, producing no emissions and requiring less space. However, they also noted limitations such as the need for nitrogen supply and specialized operational knowledge.

Peng *et al*. (2008)[34] discussed the performance of polypropylene (PP) hollow fiber membrane contactors for the deoxygenation of water in a pilot-scale system, specifically targeting the stringent requirements for dissolved oxygen removal in ultrapure water production lines, such as those used in semiconductor, pharmaceutical, and power industries. The work was carried out using reverse osmosis (RO) permeate as the feed water. The membrane material employed was polypropylene, manufactured in both conventional hollow fiber bundles and an innovative woven fabric configuration, with the latter aligned as parallel weft fibers wrapped by yarn. System scaling ranged from small modules (0.08 m outer diameter, 0.3 m length, 3.7 m² surface area) up to larger modules (0.2 m OD, 1.0 m length, 81 m² surface area). The woven fabric geometry was specifically designed to induce transverse flow within the shell side, thereby enhancing mass transfer and mitigating common issues such as channeling and bypass seen in conventional parallel flow modules. The membrane characteristics included an inner/outer diameter of 400/300 μm, 50 μm wall thickness, 0.08 μm pore size, and 40% porosity. The degassing system operated at 25°C under vacuum conditions (typically 6000 Pa applied to the lumen side), with water consistently flowing through the shell side of the contactor, a configuration chosen to minimize pressure drop and risk of leakage, and to maximize module utilization and scalability. No sweeping gas was required; vacuum was used as the driving force for oxygen removal. The experimental results demonstrated that the woven fabric modules achieved superior degassing efficiencies (up to 97.5% O_2 removal at 1.44 m^3/h flow rate using a module with 36 m² membrane surface area in a transverse flow arrangement) and higher overall mass transfer coefficients than bundle-packed modules, primarily due to the effective transverse flow and full fiber utilization. Pressure drops across the modules were modest, well below the 9 bar breakthrough pressure of the PP fibers, ensuring safe operation. The study also examined the effect of module orientation (vertical or horizontal) on a module with a 0.2 m outer diameter, 0.7 m length, 0.5 m fiber effective length, and 52 m² membrane surface area. The results indicated that the vacuum application place had a negligible impact on performance, as shown in Figure 2-9. Long-term integration of the degassing system into a working RO production line showed stable oxygen removal and no detectable impact on water quality or membrane fouling, with regular total organic carbon (TOC) monitoring confirming the integrity of the process.

One of the most important contributions to the field of water deoxygenation using HFMCs is the work of Sengupta *et al*. (1998) [20], which serves as the basis for our research work. The authors conducted a comprehensive study on the large-scale application of HFMCs for gas transfer in ultrapure water, specifically targeting dissolved oxygen (O_2) removal. The work employed various transverse-

flow contactors provided by Liqui-cel 3M, which have a significant advancement over traditional parallel-flow contactors. In this design, the water flowed radially across the shell side of the fiber bundle, directed by baffles while the gas phase (N_2 and vacuum) passed through the lumen side. For more details about this work see Chapter 4.

Industrial systems design (as illustrated in Figure 2-10) often employed several contactor modules in parallel configuration for increasing the capacity or in series configuration for higher purity, with modularity allowing retrofits.

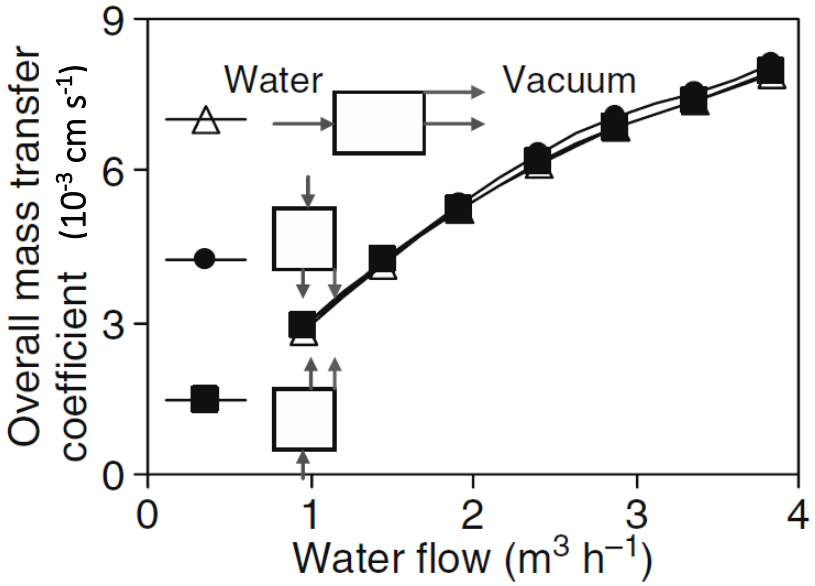

Figure 2.9 .Effect of operation mode on degassing performance of membrane contactor packed woven fabric (shell: water, Module outer diameter 0.2 m, fiber effective length 0.5 m, membrane surface area 52 m2 ,vacuum 6000 Pa) [34].

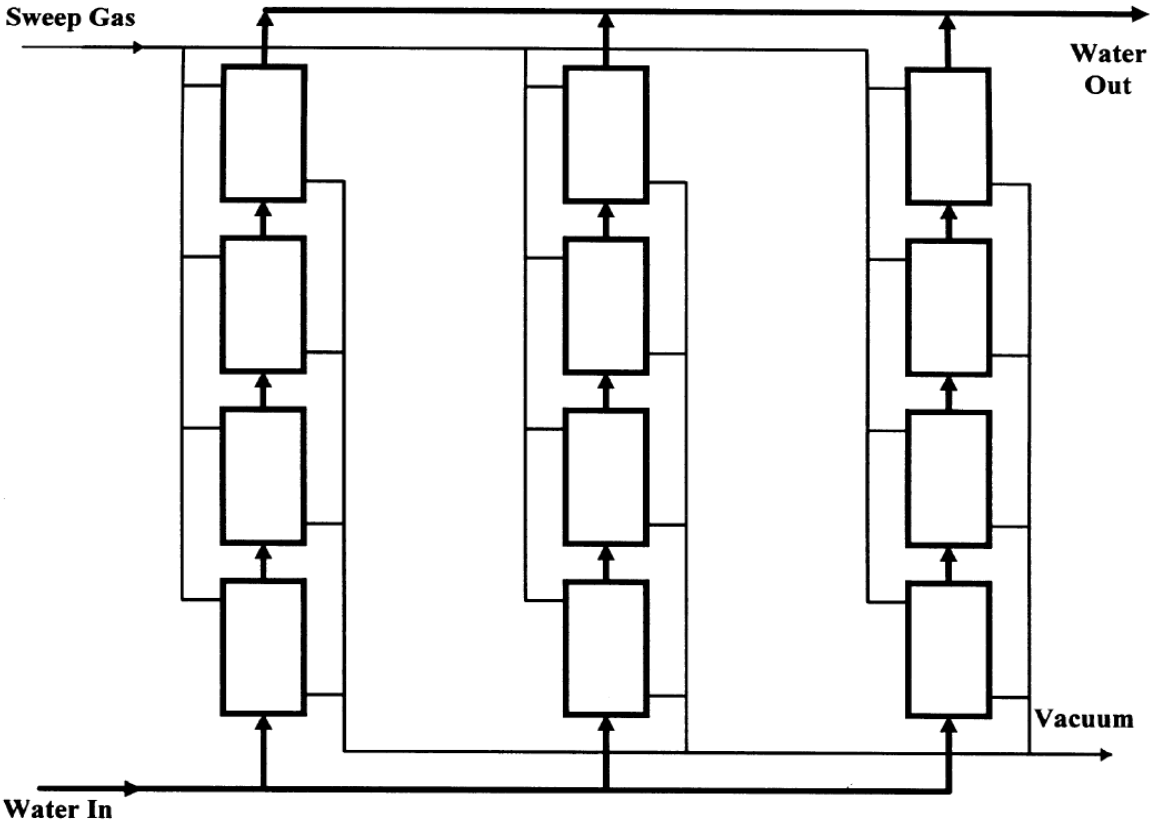

Figure 2.10 .Typical configuration of a membrane contactor degassing industrial systems in combo mode operation [20].

Shao *et al*. (2008) [35] developed a pilot-scale HFMC system for dissolved oxygen (O_2) removal from boiler feed water. The study utilized hydrophobic polypropylene hollow fibers (300 μm OD, 100 μm wall thickness) with a 42 m^2 surface area per module, configured with shell-side liquid flow (boiler feed water) and lumen-side vacuum application (a vacuum level of 0.095 MPa, reported as gauge pressure, corresponding to an absolute pressure of approximately 0.006 MPa in the lumen)). Experiments investigated the effects of flow rate (0.2–4.9 m^3/h), vacuum level (0.090 to 0.100 MPa), and temperature (10–25°C). The results showed that:

- O_2 removal efficiency peaked at 96% for low flow rates (0.2 m^3/h) but plateaued at ~80% for higher rates (4.9 m^3/h), balancing efficiency with throughput.
- Mass transfer coefficients followed a power-law relationship. It increases with the liquid flow rate, but not linearly. The exponent 0.71 shows a sub-linear dependence.
- Vacuum of 0.095 MPa achieved maximal efficiency (92%) without excessive energy use.

- Temperature had negligible impact on efficiency but lowered dissolved O_2 solubility at higher temperatures.

Another key point addressed was membrane fouling behavior in full-scale systems, comparing groundwater and surface water sources. Surface water caused severe fouling (efficiency drop to 60% within 6 months) due to organic matter (polysaccharides, carboxylates) and aluminum silicate deposits, identified via SEM, FTIR, and EDX (95.5% C, 4.21% O, 0.16% Al, 0.12% Si). Groundwater, with lower organics (TOC: 0.70 vs. 3.21 mg/L), showed slower fouling. The fouling resistance (26 s/cm) was quantified via Wilson plot analysis, revealing dominant organic-silicate synergy.

For cleaning, air backwashing (lumen-side air injection + shell-side water flow) restored efficiency to 80%, outperforming chemical methods (acid/alkali recirculation) by avoiding waste disposal issues.

Tan *et al*. (2005) [44] developed a mathematical model to analyze dissolved oxygen (DO) removal in HFMC modules, emphasizing the role of water vapor permeation in vacuum degassing. The study used silicone rubber hollow fibers (0.64 mm OD, 0.30 mm ID) with a non-porous structure, enabling high transmembrane pressure operation without bubble formation. Experiments and simulations compared lumen-feed (liquid inside fibers) and shell-feed (liquid outside fibers) configurations for ultrapure water applications (target: 0.1 ppb DO). Key findings include:

- Water vapor permeation enhanced DO removal by reducing oxygen partial pressure in the gas phase, increasing the driving force. This effect was more pronounced in lumen-feed (20–30% higher efficiency) due to lower gas-phase pressure drop.
- Mass transfer coefficients were correlated via Sherwood (Sh) and Reynolds (Re) numbers. For lumen-feed, Sh followed the Lévêque solution, while shell-feed required a custom fitting correlation.
- Optimal module length was ≤1.6 m longer modules diminished water vapor's beneficial effect due to pressure drop in the lumen (shell-feed) or saturation of vapor permeation (lumen-feed).
- Vacuum level critically impacted performance: DO removal reached 90% at 4 kPa (absolute pressure) but declined sharply above 20 kPa.
- Experimental validation confirmed model accuracy, with deviation, between predicted and measured DO concentrations, below 5%

These studies collectively highlight HFMCs' advantages over traditional methods, such as compact design, high surface area, and pollution-free operation, with applications spanning boiler feed water, district heating, and potentially ultra-pure water production for semiconductors. Operating conditions typically involve liquid flowing on the shell or lumen side, with vacuum or nitrogen sweep

enhancing mass transfer. However, challenges such as membrane wetting and fouling persist, particularly with wastewater or surface water. The primary motivation across these works is to mitigate the negative effect of O_2, improve energy efficiency, and meet stringent industrial water quality standards. Ongoing research focuses on optimizing membrane materials (e.g., PP, PVDF, PTFE) and hydrodynamic conditions to enhance long-term stability and scalability.

2.3.2 Recovery of dissolved methane from anaerobic effluents

Methane, as discussed in the first chapter, is a potent greenhouse gas produced in municipal and industrial wastewater through the anaerobic decomposition of organic matter. Hollow fiber membrane contactors have emerged as an efficient technology for recovering dissolved methane from anaerobic effluents, using membranes to separate methane from liquid streams. This approach delivers significant environmental benefits, including enhanced energy recovery, reduced greenhouse gas emissions, and improved sustainability of wastewater treatment.

Many studies have been conducted in this area. For example, Mora *et al* (2022)[28] developed and validated a mechanistic model for transverse-flow HFMCs, specifically targeting efficient methane recovery from real anaerobic effluents. Motivated by the substantial energy losses and emissions associated with methane escape from municipal wastewater treatment, their research was grounded in field data from a full-scale sewage treatment plant serving approximately one million people. They employed demonstration-scale HFMC modules LiquiCel EXF 2.5×8, circulating filtered anaerobic effluent through the shell side and introducing atmospheric air as a cost-effective sweeping agent into the lumen. Their experiments covered a broad range of operating conditions, with liquid flow rates from 103 to 1050 $mL.min^{-1}$and sweeping gas flows from 10 to 500 $mL.min^{-1}$, achieving gas-to-liquid (G/L) ratios suitable for recovering methane-rich gas for energy use.

The study also found that existing literature does not provide a reliable expression for the pressure drop in the shell side of transverse-flow HFMCs. Notably, the Ergun Equation significantly underestimates this pressure drop, as indicated by previous research. Consequently, the simulations utilized the HFMC provider's pressure-drop curve, calculated using liquid velocity.

The results, illustrated in Fig. 2-11, show that non-baffled HFMCs exhibited a pressure drop about half that of baffled units, as the liquid only flows once through the membrane zone. This curve aligns more closely with data from another provider's non-baffled HFMC than with the Ergun Equation, which was ultimately excluded from the analysis.

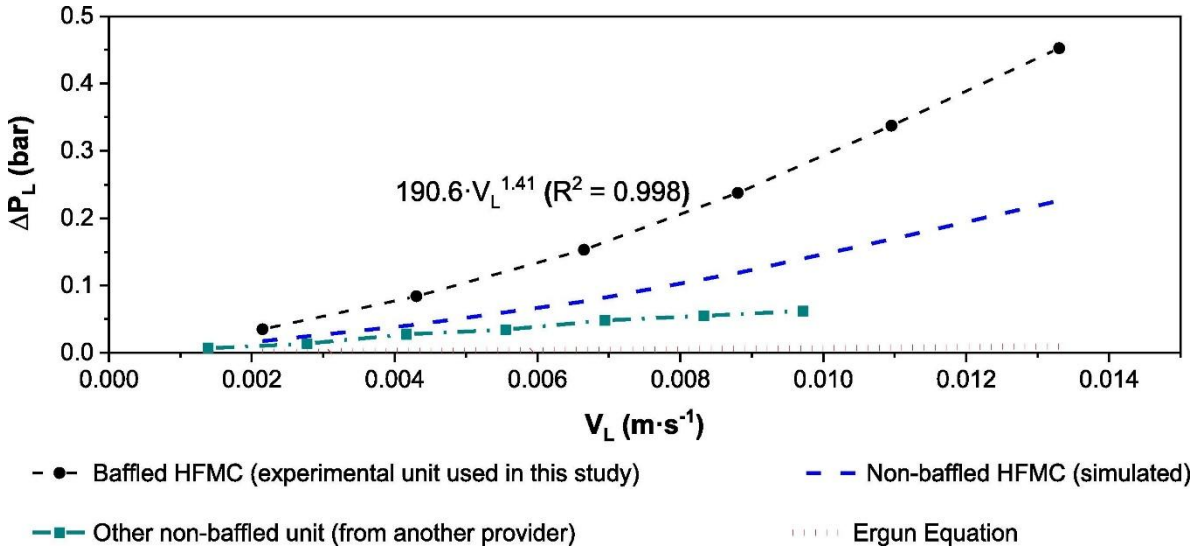

Figure 2.11. Pressure drop in the shell side of the simulated HFMCs for the energetic balance calculation. The curve for the baffled HFMC and for the other non-baffled HFMC were taken from their respective providers [28].

Uniquely, their study addressed the lack of robust models for transverse-flow HFMCs at low G/L ratios, where spatial heterogeneity in the driving force challenges conventional "black-box" models. Their two-dimensional finite-element model accurately resolved internal concentration gradients and outperformed empirical models, revealing new insights into the interplay between module geometry, hydrodynamics, and energy efficiency. The findings demonstrated that while baffled HFMCs achieve higher liquid velocities and mass transfer coefficients, non-baffled modules distribute the driving force more favorably at low G/L ratios, optimizing both energy use and methane recovery. Importantly, mass transfer resistance was found primarily in the liquid phase, with membrane resistance negligible for the polypropylene modules used. This insight is critical for HFMC scale-up and design.

Building on these methodological advances, Centeno Mora extended this research to the simultaneous removal of dissolved methane and sulfide (S^{-2}) [17], again utilizing demonstration-scale transverse-flow HFMCs. This work compared polypropylene (microporous) and polydimethylsiloxane (dense silicone) membranes under various operating conditions, including both air-sweep and vacuum modes. The HFMC contactors were configured in a transverse-flow geometry with shell-side liquid flow and lumen-side gas/vacuum, using modules optimized for high mass transfer. Using real UASB effluent, they demonstrated that both gases could be efficiently removed, up to 99% for methane and 100% for sulfide (S^{-2}), the latter via physical desorption and chemical oxidation by transferred oxygen, with higher efficiencies reported for the dense HFMC and air as sweeping gas; additionally, air sweeping led to nearly O_2-saturated effluents (higher in the microporous HFMC), while CO_2 transfer showed variable absorption/desorption patterns. System geometry and flow configuration, as elucidated in their earlier

modeling study, were decisive: transverse-flow modules with shell-side liquid flow facilitated high mass transfer rates and, with tailored G/L ratios, enabled not only energy-efficient methane capture but also generated oxygen-enriched effluent beneficial for downstream aerobic treatment. Across all conditions, mass transfer was primarily limited by the liquid phase.

Centeno Mora also contributed to two comprehensive review articles in 2020 and 2024. The first [48] systematically analyzed a wide range of studies focusing on both real municipal and synthetic wastewaters with high chemical oxygen demand (COD) to address the energetic and environmental drawbacks of methane dissolution in treated effluents, which leads to greenhouse gas emissions and energy loss in anaerobic systems. The review identified that the most studied membrane materials are microporous polypropylene (PP), dense polydimethylsiloxane (PDMS), and, occasionally, modified polyvinylidene fluoride (PVDF) or composite membranes. While most experiments are bench-scale, full-scale trials, such as the deployment of commercial PDMS modules with 2.1 m² membrane area, have been reported.

The second review [49] synthesized key findings on HFMCs for direct methane recovery from anaerobic effluents of systems like UASB reactors and AnMBRs, highlighting recovery efficiencies up to 99% for D-CH_4 in pilot-scale setups. Compared to alternatives like packed beds, HFMCs offer higher mass transfer rates due to large contact areas, though they require pre-treatment to prevent clogging and face challenges with membrane wetting. Studies showed that using vacuum (up to 900 mbar) or low Q_G/Q_L ratios (<0.10) with N_2 sweep gas yields methane-rich streams (85-95% v/v CH_4) suitable for energy use after upgrading, while air sweeping leads to oxidation of H_2S but dilutes CH_4 with N_2 (40-60% v/v). Long-term operations confirmed stability, with dense membranes reducing wetting risks over microporous ones (pore size ~0.5 μm).

Velasco has also conducted extensive research on CH_4 recovery from wastewater treatment systems. In 2018 [50], authors reviewed advancements in recovering dissolved methane from AnMBR effluents, focusing on mitigating greenhouse gas emissions and enhancing energy recovery from wastewater treatment systems. The work synthesized findings from multiple pilot- and lab-scale studies treating municipal and industrial wastewater, where dissolved methane in effluent poses environmental risks due to its high global warming potential. Researchers explored degassing membrane contactors, primarily using hollow fiber membranes made of materials like polypropylene (PP), polydimethylsiloxane (PDMS), polyethylene (PE), and polyvinylidene difluoride (PVDF). Porous or micro-porous membranes (e.g., PP) demonstrated higher recovery efficiencies (up to 99%) compared to non-porous variants but were prone to pore wetting. The systems operated under low liquid velocities (e.g., 0.0004 m/s) and high transmembrane pressures to maximize methane diffusion, with liquid typically flowing through the lumen side to improve mass transfer. Some studies incorporated carbon dioxide desorption as a sweeping agent to enhance methane recovery. The review highlighted challenges

such as balancing membrane durability with performance, particularly at higher liquid fluxes, and emphasized the need for energy analyses to validate scalability. In 2021 [11], the review expanded to address challenges like pore wetting and fouling, which have led to research into Janus/omniphobic membranes and solvent-based contactors to enhance durability. The additional energy required for methane recovery is minimal (~0.01 kWh/m³), with potential net energy gains of 0.05–0.17 kWh/m³ when combined with AnMBR biogas. Future directions include pilot-scale validation, optimizing membrane materials (e.g., PTMSP for higher methane permeability), and integrating with biogas upgrading technologies to enhance scalability and economic viability. In 2022, [51] developed a numerical model, building on Rongwong *et al*. [52], to optimize HFMC design for large-scale applications, focusing on methane removal efficiency, methane content in recovered gas (y_{CH4}), and net energy gain (Net E, defined as the energy from recovered methane minus the energy for pumping and vacuum, in $MJ.m^{-3}$). Experiments were conducted at bench scale using porous polypropylene (40% porosity, 0.02 µm pores) and dense polydimethylsiloxane (PDMS) HFMCs, with nitrogen as the sweep gas. Feed fluxes ranged from 27.02 to 108.07 $L.h^{-1}.m^{-2}$ for porous HFMCs and 44.58 to 222.89 $L.h^{-1}.m^{-2}$ for dense HFMCs, with a constant 120 $L.h^{-1}$ nitrogen flow. Results showed higher methane removal efficiency at lower feed fluxes (53.39 % at 27.02 $L.h^{-1}.m^{-2}$ for porous, 31.24 % at 44.58 $L.h^{-1}.m^{-2}$ for dense), while desorption flux increased with feed flux, reaching 7.04×10^{-6} $mol.m^{-2}.s^{-1}$ (porous) and 8.30×10^{-6} $mol.m^{-2}.s^{-1}$ (dense). The model, calibrated with literature and experimental data, showed relative errors below 10%, confirming its accuracy. It uses a 1D approach, focusing on liquid-phase mass transfer resistance, and incorporates a distribution factor (m) for dense HFMCs. Practically, achieving ≥88% of methane removal efficiency and ≥35% of desorption flux requires low feed fluxes or longer membranes, but a feed flux of 90–230 $L.h^{-1}.m^{-2}$ is needed for 7 years payback period. Scaling to 500 $m^3.d^{-1}$ requires 46 HFMC modules, producing power of 2 kW, while 10,000 modules could yield 430 kW.

In another work of the same year [53], Velasco, tested solids-laden wastewater coming from anaerobic reactors with two types of HFMCs: one with porous membranes and another with dense membranes, both crafted from polypropylene, a material chosen for its hydrophobic nature and ability to facilitate gas transfer while resisting liquid intrusion. The porous membranes had tiny pores to allow methane diffusion, while the dense membranes relied on their permeability to achieve the same goal. The scale of their experiment was a bench-scale setup, a controlled environment where they could meticulously monitor performance for over a month without cleaning the membranes. The wastewater flowed through the lumen side while a sweeping gas, nitrogen, coursed through the shell side, creating a concentration gradient to draw methane out. Nitrogen was chosen for its inertness, ensuring no unwanted reactions, and its cost-effectiveness, making it practical for large-scale applications. Operating conditions were practical, with feed flux rates varying to test performance limits: 27.02, 54.04, and 108.07 $L.h^{-1}.m^{-2}$ for porous HFMCs, 44.58, 74.30, and 222.89 $L.h^{-1}.m^{-2}$ for dense HFMCs. The system

ran at ambient conditions, likely around 25°C and atmospheric pressure, to mimic real-world, energy-efficient scenarios. The goal was to recover at least 88% of the dissolved methane, the threshold for a carbon-neutral system, and to produce a gas mixture with 29% methane content, suitable for energy generation. Their energy analysis revealed that both systems yielded a net energy of 0.25 MJ/m^3, equivalent to 0.03 kWh/d for porous HFMCs and 0.02 kWh/d for dense HFMCs, highlighting their potential as low-energy solutions. One striking observation was the impact of long-term operation: without cleaning, both systems saw a decline in performance, with porous HFMCs dropping by 24% and dense HFMCs by 38% in methane removal efficiency at a feed flux of 90 $L.h^{-1}.m^{-2}$ over a one-month test period. Yet, the dense HFMCs held an edge for longer operations, suggesting their suitability for practical industrial applications.

The research in this domain is very extensive, making it impractical to detail every study. Therefore, is provided a table summarizing the key points highlighted in several of these studies in Tables 2.3a–c.

Table 2-3a. A Review of HFMCs for CH_4 Removal in Water Systems.

Category	Mora *et al*.[48]	Mora *et al*.[28]	Mora *et al*. [17]	Cookney *et al.* [18,41]	Henares *et al* [54]
Study Type	Review paper	Experimental modeling and optimization	Experimental research	Experimental research	Experimental research
Type of Water Used	Anaerobic reactor effluents (UASB, EGSB, AnMBR), synthetic wastewater, sewage	Anaerobic effluents (wastewater)	Anaerobic effluents (wastewater)	Anaerobic effluents (domestic wastewater)	Anaerobic effluent from Expanded Granular Sludge Bed (EGSB) reactor
Sweeping Agent Used	-	Atmospheric air	Atmospheric air (sweeping gas) or vacuum	Nitrogen	Nitrogen gas or vacuum
Flow Rates and Vacuum Pressure	-	Q_L: 103 to 1050 mL/min Q_G: 10 to 500 mL/min	Q_L: 206 mL/min to 1050 mL/min Q_G: 20 to 500 mL/min Vacuum: 130, 270, 410, 570, 750, and 900 mbar.	Q_L: 40 mL/min to 780 mL/min Q_G: 0.6 to 15mL/min	Q_L: Varied; Q_L/A_m ranging from 22.6 to 377.4 L/h/m² Q_G: QN_2/A_m ranging from 0.14 to 4.44×10^3 L/h/m² Vacuum: 140 to 800 mbar
Operating Conditions	-	G/L ratios between 0.019 and 2.42; D-CH_4 concentration at inlet: 9.5 to 19.8 mg/L	D-CH_4 concentrations: 17.5 ± 2.4 mg/L; S^{-2} concentrations: 7.7 ± 1.8 mg/L; average temperature: 27.4 ± 1.9 °C; pH: 7.1 ± 0.1	Average effluent temperature: 16 °C; dissolved methane concentration: 25.4 mg/L; COD removal efficiency: 64%	-
Liquid Side Configuration	-	Shell side /the transverse-flow	Shell side (cross flow for the porous module and counter-current for the dense one)	Shell side / counter-current/parallel flow	Different modes of operation (lumen side and shell side) /parallel flow

Membrane contactor for stripping operation

Membrane Contactor Module Characteristics	-	LiquiCel EXF 2.5×8 module	LiquiCel EXF 2.5×8 module (porous) / PDMS module with 1 m^2 membrane surface area.	0.139 m^2 (PDMS; Sterilin Ltd UK) dense membrane 0.094 m^2 (PDMS; Sterilin Ltd UK) dense membrane 0.58 (PP, Membrana, Wuppertal, Germany)	PDMS (non-porous) and PP (microporous) membranes; effective areas: 0.0159 m^2 (PDMS), 0.18 m^2 (PP)
Key Findings	- D-CH_4 removal efficiencies: 26–98% (highest for pressurized modules)- Microporous membranes show lower mass transfer resistance but are prone to wetting - Fouling and clogging are major concerns for high-TSS effluents - Theoretical energy recovery potential: 0.01–0.14 kWh/m^3 - Recovered CH_4 concentration: Up to 63% (vacuum mode) or 30–40% (sweeping gas mode)	Better D-CH_4 desorption efficiencies at lower liquid flow rates and higher gas flow rates; non-baffled HFMCs showed better performance in energy optimization.	Removal efficiencies up to 99% for D-CH_4 and 100% for S^{-2}; higher efficiencies with dense HFMC; oxidation mechanism for S^{-2} removal noted.	Methane recovery efficiencies up to 72% at low liquid velocities; significant fugitive methane emissions without recovery; potential for net positive carbon footprint. Methane removal efficiencies up to 98.9%; supersaturation of anaerobic effluent increased mass transfer; low liquid velocities enhance recovery efficiency.	Methane removal efficiencies up to 98%; microporous membranes performed better at lower liquid flow rates; non-porous membranes showed better performance under vacuum.

Membrane contactor for stripping operation

Remarks	- Pre-treatment (e.g., 5–10 µm filtration) recommended for high-TSS effluents - Dense membranes preferred for vacuum operation to avoid wetting - Economic feasibility depends on scale and CH_4 recovery efficiency - Lack of full-scale studies and recovered gas composition data	Importance of driving force and mass-transfer coefficients; potential for net energy production from recovered gas; need for further studies on optimization.	The presence of dissolved oxygen (DO) increased during sweeping gas operation; significant mass transfer differences between membrane types were observed.	Need for optimization of gas-side hydrodynamics; potential impacts of biofouling on long-term performance; vacuum operation shows promise for higher gas purity.	Need for optimization to prevent membrane wetting; simultaneous removal of CO_2 less efficient than CH_4; operational conditions significantly affect performance.

Table 2-4b Review of HFMCs for CH4 Removal in Water Systems (continued).

Category	Henares *et al* [55]	Henares *et al* [56]	Rongwong *et al* [57]	. Sethunga *et al* [58]	Sethunga *et al* [59]
Study Type	Experimental research	Experimental research on methane recovery	Experimental research on methane recovery	Experimental	Experimental
Type of Water Used	Anaerobic effluent from Expanded Granular Sludge Bed (EGSB) reactor	Anaerobic effluent from an Expanded Granular Sludge Bed (EGSB) reactor	Anaerobic effluents (AnMBR and UASB)	Anaerobic effluents (AnMBR and UASB)	Anaerobic effluents (AnMBR and UASB)
Sweeping Agent Used	Vacuum or nitrogen gas (sweep gas)	Vacuum pressure and nitrogen gas	Nitrogen (N_2)	Nitrogen (N_2)	Nitrogen (N_2)
Flow Rates and Vacuum Pressure	Q_L :0.4 to 10.8 L/h Q_G: 2.7 to 27.0 L/h Vacuum: 140 to 800 mbar	Q_L :0.4 to 10.8 L/h Q_G: 2.7 to 27.0 L/h Vacuum: 140 to 800 mbar	Q_L: AnMBR: 1×10^{-7} m^3/s; UASB: 7.5×10^{-7} m^3/s Q_G: 10 mL/min (approx. 1.67×10^{-7} m^3/s)	Q_L: 0.06 m/s (varies by membrane) Q_G: 20 SCCM (0.03 m^3/day)	Q_L: 4.3 to 81 × 10-3 m3/day Q_G: 20 SCCM (0.03 m3/day)
Operating Conditions	-	-	Operated under atmospheric pressure	Room temperature; atmospheric pressure	-
Liquid Side Configuration	Lumen side	Lumen side	AnMBR: Liquid fed to lumen; UASB: Liquid fed to shell side	Lumen side	Lumen side
Membrane Contactor	PDMS hollow fiber membrane; effective area:	PP (1×5.5 MiniModule, Liqui-Cel, Membrana GmbH, Germany);	Polyvinylidene difluoride (PVDF) Module Length: 18.5 cm	Commercial and in-house membranes/ PDMS-coated PVDF hollow fiber membranes	PHM-PVDF membrane

Membrane contactor for stripping operation

Module Characteristics	0.0159 m²; 320 fibers; packing fraction: 0.113	effective area: 0.180 m²; 2300 fibers; packing fraction: 0.33	Module Diameter: 0.62 cm Number of Fibers: 6 or 10	Inner Diameter: 540 to 710 µm; Outer Diameter: 800 to 985 µm; Porosity: 74% to 85%	Inner Diameter: 189 to 636 µm; Outer Diameter: 300 to 912 µm; Porosity: 49% to 79%
Key Findings	Methane removal efficiencies up to 77%; influence of liquid oversaturation on mass transfer; fouling observed with shell side operation.	Removal efficiencies up to 98%; higher efficiency in lumen side operation; need for regular cleaning to maintain performance.	UASB effluent caused more severe fouling than AnMBR effluent; fouling dominated by protein-like substances.	PDMS-coated membranes showed higher CH_4 recovery; lumen modification preserves bulk porosity.	Capillary pressure, pore wetting, and membrane resistance affect CH_4 flux; optimized parameters enhance recovery.
Remarks	Energy production exceeded energy requirements; significant reduction in CO_2 emissions; need for regular cleaning to maintain efficiency.	Long-term operation showed less impact from fouling in lumen side; cleaning strategies optimized for membrane efficiency; confirmed presence of biofouling.	Membrane fouling impacts CH_4 desorption; effective fouling control requires managing extracellular polymeric substances (EPS) and soluble microbial products (SMP) levels in effluents.	The study conducted different types of commercial and in-house membranes. The commercial membrane (LM-05.0) performed best in long-term tests, with only a 20% flux decline in UASB effluent.	The PHM-PVDF membrane showed better performance due to its hydrophobicity and porosity.

Table 2-5c. Review of HFMCs for CH_4 Removal in Water Systems (continued).

Category	Bandara *et al* [16]	Cao *et al* [60]	Jiménez *et al* [61]	McLeod *et al* [62]	Song *et al* [30]
Study Type	Experimental	Experimental	Experimental	Experimental	Experimental & Modelling
Type of Water Used	Synthetic wastewater and anaerobic effluents (AnMBR, UASB)	Aqueous solutions with dissolved methane (D-CH_4)	Aqueous solutions with dissolved methane (D-CH_4)	Aqueous solutions with dissolved methane and Carbone dioxide (D-CH_4 / CO_2)	Pure water with (H_2, CH_4, mixtures)
Sweeping Agent Used	Vacuum	Vacuum	combo mode	N2	Vacuum
Flow Rates and Vacuum Pressure	Q_L :150 L/day in UASB Vacuum: 50 kPa and 80 kPa	Not specified	Q_L: 5.0 to 28.0 L/h Q_G: 0.5 to 1.5 L/h (N2) Vacuum: 0 to 480 mbar	Q_L: 0.25× 10-5 m^3/s Q_G: 1.7 × 10-4 to 1.7 × 10-6 m^3/s	QL: 50–800 mL/min (linear flow velocity: 2.3–36.7 cm/s) Vacuum: -60 to -80 kPa
Operating Conditions	Temperatures: 15 °C, 25 °C, and 35 °C; HRT: 3.3 to 10 hours	Temperatures: 15 °C, 25 °C, 35 °C; various permeate pressures	Room temperature (23 °C ± 3 °C)	-	Temperature: 20–40°C
Liquid Side Configuration	Liquid fed to the lumen side	Liquid fed to the lumen side	Liquid fed to the lumen side	Liquid fed to the lumen side	Liquid fed to the lumen side
Membrane Contactor Module Characteristics	Non-porous layer for degassing: Polyethylene Porous layer: Polyurethane Outer diameter of a hollow fiber 280 µm	Types: PDMS, PEBA (nonporous); PTFE (microporous); thickness 5 µm; porosity for PTFE: 85%	PP (1 × 5.5 Mini-Module, Liqui-Cel, Membrane GmbH, Germany).	PP (Liqui-Cel 1.7x5.5 Mini-Modules, Membrana GmbH, Germany)	Material: PDMS (dense); Module: PDMSXA1000; Area: 1000 cm^2; Fiber dimensions: 190 µm (inner diameter), 300 µm (outer diameter); Length: 8.41 cm

	Inner diameter of a hollow fiber 200 µm Thickness 40 µm Length 360 mm Number of hollow fibers: 5500 Total membrane area: 1.7 m^2 Membrane volume: 0.4 L				
Key Findings	D-CH4 concentration reduced from 63 mg COD/L to 15 mg COD/L; total CH_4 recovery efficiency increased significantly.	Microporous PTFE membrane outperforms nanoporous membranes; concentration polarization significantly affects performance.	>90% methane removal efficiency at optimal conditions; combination mode enhances performance over single modes.	Maximum removal efficiency of 97% at high sweep-gas flow rates; influence of liquid velocity on mass transfer noted	Model predicted gas recovery with 13% avg. error; H_2/CH_4 recovery ratio shifts with pressure and HRT; Max removal: ~80% CH_4 (literature comparison)
Remarks	Performance is stable over multiple temperatures and HRTs.	Membrane fouling and concentration polarization are critical factors in methane extraction efficiency.	Combination of vacuum and sweep gas improves methane recovery and energy efficiency.	Potential for carbon neutrality in energy generation; further optimization required for membrane design and operational parameters.	Model validated for steady state; Transient analysis potential noted; Water vapor permeation is accounted for.

2.3.3 Removal of Volatile organic compound (VOC) from water

VOCs, as mentioned in our first chapter, are a group of chemicals that can easily evaporate into air at room temperature, including solvents, fuels, and other chemicals commonly used in industrial processes. Several studies have examined the effects of process variables and the feasibility of using HFMCs to treat water containing VOCs. The study by Barati *et al* [63] simulated toluene removal from wastewater using a single porous hollow-fiber membrane contactor (inner diameter 0.6 mm, outer diameter 1 mm, length 240 mm, porosity 0.7, tortuosity 2.6), employing computational fluid dynamics (CFD) via COMSOL Multiphysics to model mass and momentum transfer across three compartments: tube side (VOC-contaminated water), porous membrane, and shell side (air as stripping gas). The model, validated with less than 5% deviation from literature data, showed an initial toluene concentration reduction due to a high concentration gradient, stabilizing after approximately 50 minutes, with enhanced removal at higher air flow rates, but noted challenges in scaling due to efficiency decline over time.

The study by Juang *et al.* [64] investigates membrane air stripping (MAS) of volatile organic compounds (VOCs) like o-xylene and chloroform from water using microporous polypropylene (PP) hollow-fiber membranes, with the VOC-laden water flowing through the fiber lumen and air as the stripping gas on the shell side. The experiments were conducted at liquid flow rates of 8–16 cm^3/min, gas flow rates of 60–180 cm^3/min, VOC concentrations of 100–1000 ppm, and temperatures of 24 – 35°C. The results showed that removal efficiency increases with higher VOC concentrations, flow rates, and temperatures, with toluene exhibiting higher efficiency than phenol due to its greater volatility (higher Henry's constant). The overall volumetric mass transfer coefficient (K_la) is up to 100 times higher than in packed towers, requiring a lower air-to-water ratio. The membrane mass transfer coefficient (k_m) accounts for pores partially filled with gas (gas-to-water filling ratio of 0.65–1.0). Calculated K_L values (e.g., 5.26×10^{-6} m/s for toluene) overestimate measured values (e.g., 1.72×10^{-6} m/s), and HTU is underestimated (0.19 m vs. 0.58 m), indicating model limitations due to simplified assumptions like uniform pores. Compared to Haghshenas *et al*. (2016) [65], which aimed to use a mathematical modeling of aroma compound recovery from natural sources using hollow fiber membrane contactors with small packing fraction, Juang's air stripping model is more suited for VOC removal, though both highlight the need for optimized flow and membrane properties for industrial scaling. The 2002 study by Mahmud *et al.* [66] examines mass transport in the membrane air-stripping process for removing VOCs, specifically toluene and chloroform, from aqueous feeds using microporous polypropylene (PP) hollow-fiber membranes. In the experimental setup, the aqueous feed flows on the shell side in cross-flow, while air passes through the fiber lumen. Key findings indicate that the initial chloroform concentration (21–851 ppm) does not affect the dimensionless Henry's Law Constant (HLC), but toluene's high adsorption to the PP membrane in the aqueous phase, potentially swelling the polymer matrix, reduces the HLC and mass transfer efficiency. The overall mass transfer coefficient

(K_L) for both compounds was lower than predicted. For toluene, at an air velocity of 0.13 m/s and solution velocity of 5.95×10^{-3} m/s, the rate constant k (min^{-1}) was lower than for chloroform, reflecting toluene's stronger interaction with the membrane. Compared to Juang *et al.* [64], who studied toluene and phenol with water flowing through the lumen, Mahmud's shell-side flow configuration highlights different mass transfer dynamics, with toluene's adsorption posing a unique challenge. Both studies note that MAS outperforms conventional packed towers, but Mahmud emphasizes toluene's membrane interactions as a limiting factor, necessitating further optimization of membrane properties and flow conditions for industrial applications. Tarafder *et al.* [67] explores vacuum-assisted removal of 12 volatile to semi-volatile organic contaminants (VOCs) from water using a Liqui-Cel polypropylene hollow fiber membrane with an extra-flow design (water on shell side, gas on lumen side) at low strip gas to water flow ratios (≤5:1). Removal efficiencies strongly depended on Henry's Law Constants (HLC, 0.017–1.195), with higher HLC compounds like 1,1-dichloroethylene (1,1-DCE) showing better removal than low HLC ones like naphthalene (~50% at 0.4 l/min water, 0.4 l/min gas, 0.051×10^5 Pa). Vacuum (down to 0.035×10^5 Pa) boosted efficiencies by increasing the gas-to-water flowrate ratio (a/w up to 28.6) or allowed reduced gas flow while maintaining efficiency, without membrane wetting. Semmens *et al.* [15] evaluates the use of microporous polypropylene hollow fiber membranes (120 fibers, 400 μm inner diameter, 18.8 cm length, 25 μm thickness, 0.02–0.04 μm pores, 40% porosity) for air-stripping volatile organic contaminants (VOCs) from water, focusing on chloroform, tetrachloroethylene, carbon tetrachloride, 1,1,2-trichloroethane, and trichloroethylene. Water flowed through the fiber lumen, while countercurrent air stripped VOCs on the shell side. VOC removal rates aligned with theoretical predictions based on empirical correlations. Mass transfer coefficients (K_L) increased with liquid flow rate but were less dependent on air flowrate, unlike packed towers, due to constant specific interfacial area ($a = 4/d$, where d is the fiber inner diameter). Despite varying Henry's constants (0.0321–0.985), K_L values remained within a factor of two, driven by similar diffusivities.

Compared to Tarafder *et al.* [67] and Wu *et al.* [68], Semmens' system offered higher K_la, no gas flow rate limits, and a compact design without tall structures or mist elimination, making it efficient for groundwater remediation, though less focused on vacuum-enhanced recovery.

2.4 Conclusion

Hollow fiber membrane contactors (HFMCs) represent a transformative technology for stripping operations, offering several advantages over traditional gas-liquid separation methods like packed or bubble columns. Their high surface-area-to-volume ratios (up to 25,000 m^2/m^3), compact modular design, and operational flexibility enable efficient mass transfer across diverse applications, including water deoxygenation, dissolved methane recovery from anaerobic effluents, and volatile organic compound (VOC) removal from contaminated water. These systems excel in maintaining consistent performance across a wide range of flow conditions, overcoming limitations such as unloading inherent

in conventional contactors. Many different membrane materials have been discussed in the literature, such as polypropylene (PP), polyvinylidene fluoride (PVDF), and polydimethylsiloxane (PDMS), with different levels of hydrophobicity, chemical stability, fouling resistance, performance and durability. Studies demonstrate remarkable removal efficiencies, up to 99% for oxygen and methane, and high VOC recovery while achieving energy efficiencies that support sustainable industrial processes. For instance, methane recovery from wastewater, not only mitigates greenhouse gas emissions ,but also enables energy recovery, with potential net energy gains of 0.05–0.17 kWh/m³. However, challenges such as membrane wetting, fouling (particularly with high-total suspended solid effluents in methane recovery from anaerobic), and scalability limitations persist, necessitating ongoing research into omniphobic membranes, optimized module geometries (e.g., transverse-flow designs), and effective cleaning strategies such as air backwashing. The integration of vacuum, sweep gas, or hybrid driving forces alongside tailored hydrodynamic conditions, continues to enhance HFMC versatility. As evidenced by large-scale pilot tests and mechanistic models, HFMCs are poised for broader industrial adoption, with future efforts focusing on full-scale validation, cost optimization, and material innovations to ensure long-term stability and economic viability across water treatment, energy recovery, and environmental protection applications.

2.5 References

[1] A.G. (Tony) Fane, R. Wang, Y. Jia, Membrane Technology: Past, Present and Future, in: Membr. Desalination Technol., Humana Press, Totowa, NJ, 2011: pp. 1–45. https://doi.org/10.1007/978-1-59745-278-6_1.

[2] A. Gabelman, S.-T. Hwang, Hollow fiber membrane contactors, J. Membr. Sci. 159 (1999) 61–106. https://doi.org/10.1016/S0376-7388(99)00040-X.

[3] I. Moch, Membranes, Hollow-Fiber, in: Kirk-Othmer (Ed.), Kirk-Othmer Encycl. Chem. Technol., 1st ed., Wiley, 2005. https://doi.org/10.1002/0471238961.0815121213150308.a01.pub2.

[4] S. Zhao, P.H.M. Feron, L. Deng, E. Favre, E. Chabanon, S. Yan, J. Hou, V. Chen, H. Qi, Status and progress of membrane contactors in post-combustion carbon capture: A state-of-the-art review of new developments, J. Membr. Sci. 511 (2016) 180–206. https://doi.org/10.1016/j.memsci.2016.03.051.

[5] K. Villeneuve, D. Albarracin Zaidiza, D. Roizard, S. Rode, Modeling and simulation of CO2 capture in aqueous ammonia with hollow fiber composite membrane contactors using a selective dense layer, Chem. Eng. Sci. 190 (2018) 345–360. https://doi.org/10.1016/j.ces.2018.06.016.

[6] R. Klaassen, P.H.M. Feron, A.E. Jansen, Membrane Contactors in Industrial Applications, Chem. Eng. Res. Des. 83 (2005) 234–246. https://doi.org/10.1205/cherd.04196.

[7] D. Albarracin-Zaidiza, B. Belaissaoui, S. Rode, Hybrid amine-based PCC processes, membrane contactors for PCC, in: Absorpt.-Based Post-Combust. Capture Carbon Dioxide, Elsevier, 2016: pp. 365–395. https://doi.org/10.1016/B978-0-08-100514-9.00015-9.

[8] D. Bhaumik, S. Majumdar, Q. Fan, K.K. Sirkar, Hollow fiber membrane degassing in ultrapure water and microbiocontamination, J. Membr. Sci. 235 (2004) 31–41. https://doi.org/10.1016/j.memsci.2003.12.022.

[9] J. Lee, S.-M. Baek, C. Boo, A. Son, H. Jung, S.S. Park, S.W. Hong, Water deoxygenation using a hollow fiber membrane contactor to prevent pipe corrosion for sustainable management of district heating systems: A pilot-scale study, J. Clean. Prod. 277 (2020) 124049. https://doi.org/10.1016/j.jclepro.2020.124049.

[10] T. Li, P. Yu, Y. Luo, Deoxygenation performance of polydimethylsiloxane mixed-matrix membranes for dissolved oxygen removal from water, J. Appl. Polym. Sci. 132 (2015). https://doi.org/10.1002/app.41350.
[11] P. Velasco, V. Jegatheesan, K. Thangavadivel, M. Othman, Y. Zhang, A focused review on membrane contactors for the recovery of dissolved methane from anaerobic membrane bioreactor (AnMBR) effluents, Chemosphere 278 (2021) 130448. https://doi.org/10.1016/j.chemosphere.2021.130448.
[12] A. Schmitt, J. Mendret, M. Roustan, S. Brosillon, Ozonation using hollow fiber contactor technology and its perspectives for micropollutants removal in water: A review, Sci. Total Environ. 729 (2020) 138664. https://doi.org/10.1016/j.scitotenv.2020.138664.
[13] V.Y. Dindore, D.W.F. Brilman, P.H.M. Feron, G.F. Versteeg, CO2 absorption at elevated pressures using a hollow fiber membrane contactor, J. Membr. Sci. 235 (2004) 99–109. https://doi.org/10.1016/j.memsci.2003.12.029.
[14] M.S.L. Tai, I. Chua, K. Li, W.J. Ng, W.K. Teo, Removal of dissolved oxygen in ultrapure water production using microporous membrane modules, J. Membr. Sci. 87 (1994) 99–105. https://doi.org/10.1016/0376-7388(93)E0086-S.
[15] M.J. Semmens, R. Qin, A. Zander, Using a Microporous Hollow-Fiber Membrane to Separate VOCs From Water, J. AWWA 81 (1989) 162–167. https://doi.org/10.1002/j.1551-8833.1989.tb03195.x.
[16] W.M.K.R.T.W. Bandara, H. Satoh, M. Sasakawa, Y. Nakahara, M. Takahashi, S. Okabe, Removal of residual dissolved methane gas in an upflow anaerobic sludge blanket reactor treating low-strength wastewater at low temperature with degassing membrane, Water Res. 45 (2011) 3533–3540. https://doi.org/10.1016/j.watres.2011.04.030.
[17] E. Centeno Mora, C.A. De Lemos Chernicharo, Simultaneous removal of dissolved sulphide and dissolved methane from anaerobic effluents with hollow fibre membrane contactors, Environ. Sci. Pollut. Res. 29 (2022) 90549–90566. https://doi.org/10.1007/s11356-022-22074-0.
[18] J. Cookney, A. Mcleod, V. Mathioudakis, P. Ncube, A. Soares, B. Jefferson, E.J. McAdam, Dissolved methane recovery from anaerobic effluents using hollow fibre membrane contactors, J. Membr. Sci. 502 (2016) 141–150. https://doi.org/10.1016/j.memsci.2015.12.037.
[19] M. Ayub, M.H.D. Othman, S.H.S.A. Kadir, A. Ali, I.U. Khan, M.Z.M. Yusop, T. Matsuura, A. Fauzi Ismail, M. A. Rahman, J. Jaafar, Research and Development Journey and Future Trends of Hollow Fiber Membranes for Purification Applications (1970–2020): A Bibliometric Analysis, Membranes 11 (2021) 600. https://doi.org/10.3390/membranes11080600.
[20] A. Sengupta, P.A. Peterson, B.D. Miller, J. Schneider, C.W. Fulk, Large-scale application of membrane contactors for gas transfer from or to ultrapure water, Sep. Purif. Technol. 14 (1998) 189–200. https://doi.org/10.1016/S1383-5866(98)00074-4.
[21] I. Martić, A. Maslarević, S. Mladenović, U. Lukić, S. Budimir, Water deoxygenation using hollow fiber membrane module with nitrogen as inert gas, Desalination Water Treat. (2014) 1–5. https://doi.org/10.1080/19443994.2014.888677.
[22] M. Stanojevi, B. Lazarevi, D. Radic, Review of membrane contactors designs and applications of different modules in industry, 31 (2003) 8.
[23] E. Nagy, Chapter 2 - Membrane Materials, Structures, and Modules, in: E. Nagy (Ed.), Basic Equ. Mass Transp. Membr. Layer Second Ed., Elsevier, 2019: pp. 11–19. https://doi.org/10.1016/B978-0-12-813722-2.00002-9.
[24] N. Fazil, S. Saqib, A. Mukhtar, M. Younas, M. Rezakazemi, Module Design and Membrane Materials, in: Membr. Contactor Technol., John Wiley & Sons, Ltd, 2022: pp. 99–142. https://doi.org/10.1002/9783527831036.ch4.
[25] S.D. Bazhenov, A.V. Bildyukevich, A.V. Volkov, Gas-Liquid Hollow Fiber Membrane Contactors for Different Applications, Fibers 6 (2018) 76. https://doi.org/10.3390/fib6040076.
[26] C. Kalakech, Q. Sohaib, G. Lesage, J.-P. Mericq, Progress and challenges in recovering dissolved methane from anaerobic bioreactor permeate using membrane contactors: A comprehensive review, J. Water Process Eng. 50 (2022) 103218. https://doi.org/10.1016/j.jwpe.2022.103218.
[27] X. Yang, R. Wang, A.G. Fane, C.Y. Tang, I.G. Wenten, Membrane module design and dynamic shear-induced techniques to enhance liquid separation by hollow fiber modules: a review, Desalination Water Treat. 51 (2013) 3604–3627. https://doi.org/10.1080/19443994.2012.751146.

[28] E. Centeno Mora, C.A. de L. Chernicharo, Modelling and optimization of transverse flow hollow fibre membrane contactors for the recovery of dissolved methane from anaerobic effluents, Sep. Purif. Technol. 293 (2022) 121136. https://doi.org/10.1016/j.seppur.2022.121136.
[29] K.L. Wang, E.L. Cussler, Baffled membrane modules made with hollow fiber fabric, J. Membr. Sci. 85 (1993) 265–278. https://doi.org/10.1016/0376-7388(93)85280-A.
[30] I. Song, P.S. Soulia, P.J. Novak, W.A. Arnold, N.C. Wright, Dissolved gas recovery from water using a sidestream hollow-fiber membrane module: First principles model synthesis and steady-state validation, J. Membr. Sci. 689 (2024) 122134. https://doi.org/10.1016/j.memsci.2023.122134.
[31] M. Younas, M. Rezakazemi, Introduction to Membrane Contactor Technology, in: Membr. Contactor Technol., John Wiley & Sons, Ltd, 2022: pp. 17–44. https://doi.org/10.1002/9783527831036.ch2.
[32] J.J. Cai, K. Hawboldt, M.A. Abdi, Analysis of the effect of module design on gas absorption in cross flow hollow membrane contactors via computational fluid dynamics (CFD) analysis, J. Membr. Sci. 520 (2016) 415–424. https://doi.org/10.1016/j.memsci.2016.07.054.
[33] S. Rode, P.T. Nguyen, D. Roizard, R. Bounaceur, C. Castel, E. Favre, Evaluating the intensification potential of membrane contactors for gas absorption in a chemical solvent: A generic one-dimensional methodology and its application to CO2 absorption in monoethanolamine, J. Membr. Sci. 389 (2012) 1–16. https://doi.org/10.1016/j.memsci.2011.09.042.
[34] Z.-G. Peng, S.-H. Lee, T. Zhou, J.-J. Shieh, T.-S. Chung, A study on pilot-scale degassing by polypropylene (PP) hollow fiber membrane contactors, Desalination 234 (2008) 316–322. https://doi.org/10.1016/j.desal.2007.09.100.
[35] J. Shao, H. Liu, Y. He, Boiler feed water deoxygenation using hollow fiber membrane contactor, Desalination 234 (2008) 370–377. https://doi.org/10.1016/j.desal.2007.09.106.
[36] A. Ito, K. Yamagiwa, M. Tamura, M. Furusawa, Removal of dissolved oxygen using non-porous hollow-fiber membranes, J. Membr. Sci. 145 (1998) 111–117. https://doi.org/10.1016/S0376-7388(98)00068-4.
[37] M. Uenishi, N. Fukushima, M. Mizuta, J. Kamo, T. Tsuru, Gas-permeable composite hollow-fiber membrane with a three-layered structure, J. Membr. Sci. 467 (2014) 175–187. https://doi.org/10.1016/j.memsci.2014.04.042.
[38] H.S. Lau, S.K. Lau, L.S. Soh, S.U. Hong, X.Y. Gok, S. Yi, W.F. Yong, State-of-the-Art Organic- and Inorganic-Based Hollow Fiber Membranes in Liquid and Gas Applications: Looking Back and Beyond, Membranes 12 (2022) 539. https://doi.org/10.3390/membranes12050539.
[39] H. Mahmud, A. Kumar, R.M. Narbaitz, T. Matsuura, A study of mass transfer in the membrane air-stripping process using microporous polyproplylene hollow fibers, J. Membr. Sci. 179 (2000) 29–41. https://doi.org/10.1016/S0376-7388(00)00381-1.
[40] X. Tan, S.P. Tan, W.K. Teo, K. Li, Polyvinylidene fluoride (PVDF) hollow fibre membranes for ammonia removal from water, J. Membr. Sci. 271 (2006) 59–68. https://doi.org/10.1016/j.memsci.2005.06.057.
[41] J. Cookney, E. Cartmell, B. Jefferson, E.J. McAdam, Recovery of methane from anaerobic process effluent using poly-di-methyl-siloxane membrane contactors, Water Sci. Technol. 65 (2012) 604–610. https://doi.org/10.2166/wst.2012.897.
[42] P. Bernardo, E. Drioli, G. Golemme, Membrane Gas Separation: A Review/State of the Art, Ind. Eng. Chem. Res. 48 (2009) 4638–4663. https://doi.org/10.1021/ie8019032.
[43] J. Wang, Z. Shi, Y. Zang, H. Jia, M. Teraguchi, T. Kaneko, T. Aoki, Macromolecular Design for Oxygen/Nitrogen Permselective Membranes—Top-Performing Polymers in 2020—, Polymers 13 (2021) 3012. https://doi.org/10.3390/polym13173012.
[44] X. Tan, G. Capar, K. Li, Analysis of dissolved oxygen removal in hollow fibre membrane modules: effect of water vapour, J. Membr. Sci. 251 (2005) 111–119. https://doi.org/10.1016/j.memsci.2004.11.005.
[45] M. Breniaux, L. Zeng, F. Bayrounat, R. Ghidossi, Gas transfer management by membrane contactors in an oenological context: Influence of operating parameters and membrane materials, Sep. Purif. Technol. 227 (2019) 115733. https://doi.org/10.1016/j.seppur.2019.115733.
[46] Y. Han, X. Huang, Y. Lu, D. Zhu, X. Shi, Study of intrinsic oxygen mass transfer characteristic and model on polypropylene hollow fiber membrane contactor, Int. Commun. Heat Mass Transf. 121 (2021) 105045. https://doi.org/10.1016/j.icheatmasstransfer.2020.105045.

[47] O. Kattan, K. Ebbers, A. Koolaard, H. Vos, G. Bargeman, Membrane contactors: An alternative for de-aeration of salt solutions?, Sep. Purif. Technol. 205 (2018) 231–240. https://doi.org/10.1016/j.seppur.2018.05.038.
[48] E. Centeno Mora, C. de L. Chernicharo, Use of membrane contactors for removing and recovering dissolved methane from anaerobic reactors effluents: state-of-the-art, challenges, and perspectives, Rev. Environ. Sci. Biotechnol. 19 (2020) 673–697. https://doi.org/10.1007/s11157-020-09546-w.
[49] E. Centeno Mora, C.L. Souza, T. Bressani-Ribeiro, C. a. L. Chernicharo, Dissolved methane, (2024). https://doi.org/10.2166/9781789063479_0207.
[50] P. Velasco, V. Jegatheesan, M. Othman, Recovery of Dissolved Methane From Anaerobic Membrane Bioreactor Using Degassing Membrane Contactors, Front. Environ. Sci. 6 (2018). https://www.frontiersin.org/articles/10.3389/fenvs.2018.00151 (accessed March 21, 2023).
[51] P. Velasco, V. Jegatheesan, M. Othman, Modeling of hollow fiber membrane contactors (HFMCs) for the recovery of dissolved methane from anaerobic effluents, Sep. Purif. Technol. 286 (2022) 120488. https://doi.org/10.1016/j.seppur.2022.120488.
[52] W. Rongwong, S. Wongchitphimon, K. Goh, R. Wang, T.-H. Bae, Transport properties of CO2 and CH4 in hollow fiber membrane contactor for the recovery of biogas from anaerobic membrane bioreactor effluent, J. Membr. Sci. 541 (2017) 62–72. https://doi.org/10.1016/j.memsci.2017.06.090.
[53] P. Velasco, V. Jegatheesan, M. Othman, Effect of long-term operations on the performance of hollow fiber membrane contactor (HFMC) in recovering dissolved methane from anaerobic effluent, Sci. Total Environ. 841 (2022) 156601. https://doi.org/10.1016/j.scitotenv.2022.156601.
[54] M. Henares, M. Izquierdo, J.M. Penya-Roja, V. Martínez-Soria, Comparative study of degassing membrane modules for the removal of methane from Expanded Granular Sludge Bed anaerobic reactor effluent, Sep. Purif. Technol. 170 (2016) 22–29. https://doi.org/10.1016/j.seppur.2016.06.024.
[55] M. Henares, M. Izquierdo, P. Marzal, V. Martínez-Soria, Demethanization of aqueous anaerobic effluents using a polydimethylsiloxane membrane module: Mass transfer, fouling and energy analysis, Sep. Purif. Technol. 186 (2017) 10–19. https://doi.org/10.1016/j.seppur.2017.05.035.
[56] M. Henares, P. Ferrero, P. San-Valero, V. Martínez-Soria, M. Izquierdo, Performance of a polypropylene membrane contactor for the recovery of dissolved methane from anaerobic effluents: Mass transfer evaluation, long-term operation and cleaning strategies, J. Membr. Sci. 563 (2018) 926–937. https://doi.org/10.1016/j.memsci.2018.06.045.
[57] W. Rongwong, K. Goh, G.S.M.D.P. Sethunga, T.-H. Bae, Fouling formation in membrane contactors for methane recovery from anaerobic effluents, J. Membr. Sci. 573 (2019) 534–543. https://doi.org/10.1016/j.memsci.2018.12.038.
[58] G.S.M.D.P. Sethunga, H.E. Karahan, R. Wang, T.-H. Bae, PDMS-coated porous PVDF hollow fiber membranes for efficient recovery of dissolved biomethane from anaerobic effluents, J. Membr. Sci. 584 (2019) 333–342. https://doi.org/10.1016/j.memsci.2019.05.016.
[59] G.S.M.D.P. Sethunga, J. Lee, R. Wang, T.-H. Bae, Influence of membrane characteristics and operating parameters on transport properties of dissolved methane in a hollow fiber membrane contactor for biogas recovery from anaerobic effluents, J. Membr. Sci. 589 (2019) 117263. https://doi.org/10.1016/j.memsci.2019.117263.
[60] X. Cao, H.-S. Lee, X. Feng, Extraction of dissolved methane from aqueous solutions by membranes: Modelling and parametric studies, J. Membr. Sci. 596 (2020) 117594. https://doi.org/10.1016/j.memsci.2019.117594.
[61] R. Jiménez-Robles, C. Gabaldón, V. Martínez-Soria, M. Izquierdo, Simultaneous application of vacuum and sweep gas in a polypropylene membrane contactor for the recovery of dissolved methane from water, J. Membr. Sci. 617 (2021) 118560. https://doi.org/10.1016/j.memsci.2020.118560.
[62] A. McLeod, B. Jefferson, E.J. McAdam, Toward gas-phase controlled mass transfer in micro-porous membrane contactors for recovery and concentration of dissolved methane in the gas phase, J. Membr. Sci. 510 (2016) 466–471. https://doi.org/10.1016/j.memsci.2016.03.030.
[63] F. Barati, M. Ghadiri, R. Ghasemi, H.M. Nobari, CFD Simulation and Modeling of Membrane-Assisted Separation of Organic Compounds from Wastewater, Chem. Eng. Technol. 37 (2014) 81–86. https://doi.org/10.1002/ceat.201300278.

[64] R.-S. Juang, S.-H. Lin, M.-C. Yang, Mass transfer analysis on air stripping of VOCs from water in microporous hollow fibers, J. Membr. Sci. 255 (2005) 79–87. https://doi.org/10.1016/j.memsci.2005.01.022.
[65] H. Haghshenas, M.T. Sadeghi, M. Ghadiri, Mathematical modeling of aroma compound recovery from natural sources using hollow fiber membrane contactors with small packing fraction, Chem. Eng. Process. Process Intensif. 102 (2016) 194–201. https://doi.org/10.1016/j.cep.2016.01.015.
[66] H. Mahmud, A. Kumar, R.M. Narbaitz, T. Matsuura, Mass transport in the membrane air-stripping process using microporous polypropylene hollow fibers: effect of toluene in aqueous feed, J. Membr. Sci. 209 (2002) 207–219. https://doi.org/10.1016/S0376-7388(02)00320-4.
[67] S.A. Tarafder, C. McDermott, C. Schüth, Vacuum assisted removal of volatile to semi-volatile organic contaminants from water using hollow fiber membrane contactors: I: Experimental results, J. Membr. Sci. 292 (2007) 9–16. https://doi.org/10.1016/j.memsci.2007.01.002.
[68] B. Wu, X. Tan, W.K. Teo, K. Li, Removal of Benzene/Toluene from Water by Vacuum Membrane Distillation in a PVDF Hollow Fiber Membrane Module, Sep. Sci. Technol. 40 (2005) 2679–2695. https://doi.org/10.1080/01496390500283456.

Chapter 3. Modeling Mass Transfer Efficiency in Lumen-Side HFMC for Liquid Degassing

3.1 Introduction

In HFMCs for degassing (e.g., removing O_2, or CH_4 from liquids like water), the choice between lumen-side and shell-side liquid flow is a key design consideration. While shell-side flow is the industrial standard for high-throughput applications, lumen-side excels in scenarios like low-flow or lab-scale degassing. This is based on commercial examples (e.g., 3M™ Liqui-Cel™ MM series) and modeling studies. In this design, the liquid flows through the lumen of the hollow fibers, while the gas (sweep gas or vacuum) flows around the outside (the shell side). This contrasts with the more common shell-side liquid flow, where the liquid is outside the fibers and the gas/vacuum is inside.

Commercial lumen side HFMC modules have a standard design that uses a parallel flow arrangement, with the two phases flowing in either a countercurrent or co-current direction. The best-known commercial degassing membrane product is Liqui-Cel™, produced by Celgard LLC [1]. Liqui-Cel contactors are equipped with porous Celgard X50, or X40 polypropylene membranes that are supplied in the form of fiber mats: parallel hollow fibers are connected by a polymer thread. The average external diameter of the hollow fibers is 300 μm while the average internal diameter of the fibers is 220 μm. The fiber mat has been designed to simplify the packing of membranes into commercial Liqui-Cel contactor housings. Liqui-Cel modules are divided into several product series according to their specific design and performance characteristics:

MM Series or mini modules are designed for applications that require high gas transfer and relatively low liquid flow rates. These modules are available in a range of sizes to accommodate different process requirements and flow rates.

Another successful commercial example of HFMC modules is SEPAREL [2], DIC Corporation's product line, which offers a range of commercial modules designed for various applications, with a particular focus on ink degassing. The key feature of SEPAREL modules is the hollow fiber membrane structure, which consists of a porous membrane and an outer non-porous very thin skin layer. This membrane design enables efficient gas transfer while maintaining low permeability to liquids. The non-porous skin layer is particularly useful for applications involving liquids with high surface tension, as it prevents membrane wetting. Preventing membrane wetting is crucial, as it ensures the integrity and efficiency of the membrane separation process, regardless of the liquid's permeability.

In SEPAREL's PF series internal flow design, the liquid flows through the lumen of the fiber, while the gas flows around the fibers. One of the main features of this design is its relatively simple structure, which contributes to its high durability. In addition, the PF series is versatile, suitable for a wide range of liquid types, and facilitates reverse cleaning.

Importantly both the outer and inner layers of the SEPAREL hollow fiber membranes are composed of Poly(4-methyl-1-pentene) (PMP). Technical documents indicate that the external diameter of the hollow fibers is between 180 and 240 µm with an average membrane thickness of 35 µm [2].

Building on the literature review of degassing technologies and HFMC fundamentals in Chapters 1 and 2, which highlighted issues such as scaling inefficiencies in conventional columns, as well as the need for compact, high-area designs, this chapter introduces a simple, one-dimensional mass transfer model for lumen-side liquid flow.

This model addresses several key gaps in the existing literature by directly linking mass transfer efficiency (η_{iL}) to the liquid flow rate (Q_L) across the membrane area ($A_{M,int}$), and by predicting frictional pressure drops using Hagen–Poiseuille's law for the practical sizing of commercial modules such as Liqui-Cel.

Validation against experimental data on oxygen and methane stripping provides actionable tools for industrial applications in water treatment, paving the way for the extension to shell-side configurations in Chapter 4.

This chapter is an adapted version of our published article "A simple model for sizing hollow fiber membrane contactors in degassing applications, relationship between mass transfer efficiency, liquid flow rate, membrane area and pressure drop; part I: liquid-in-lumen configuration. Separation and Purification Technology", 365, 132551. https://doi.org/10.1016/j.seppur.2025.132551 (Open access under CC BY 4.0; reproduced with permission).

3.2 Modeling of stripping operation in HFMCs

Mass transfer modelling is important, as it relates geometrical and operational parameters to stripping efficiency. Mass transfer models are thus necessary for the optimal design of HFMCs. Several studies have focused on modeling mass transfer in HFMCs [3–9]. For example, A. Ito *et al*. [10] have developed a mass transfer model for vacuum and sweep gas modes in the removal of oxygen from water using a dense silicone rubber membrane. In their work, it is the membrane that primarily controls mass transfer, illustrating the importance of knowing the membrane characteristics in the degassing process. Centeno Mora and Chernicharo [11] have proposed a two-dimensional finite element model to simulate cross-flow in HFMCs. By incorporating a detailed representation of flow dynamics and mass transfer within the HFMC, the model led to a better experimental fit than existing black-box models, which solely consider inlet and outlet concentrations.

Although a lot of modelling work has been undertaken, there is still a need for simple, comprehensive models that can be easily applied to improve the operational efficiency of HFMCs. The aim of the present work is to fill this gap by developing a simple yet accurate modelling approach for degassing in HFMCs. The assumptions made in the following and the resulting equations are mostly

based on the general consensus found in other published work [4–6] . However, particular attention is paid to estimating the composition of the gas side in vacuum stripping, which is a parameter that is frequently not considered.

Depending on the geometry of the HFMC module, the gas-liquid flow directions are either parallel or crossed. Whatever the geometry of the module, the gas and the liquid can flow either on the shell side of the module around the fibers, or on the lumen side of the hollow fibers. In what follows, only lumen-side liquid flow and parallel gas flow is considered. This limits the number of equations and makes the approach easier to explain and understand. A similar analysis is carried out within our research group to describe the situation in which the liquid flows on the shell side. The equations are similar, but not the same (See chapter 4).

3.2.1 Species transfer in a HFMC: resistances in series model

The transport of gas through a composite membrane in the form of a hollow fiber is considered. The membrane consists of a porous support and, eventually, a thin dense layer deposited on the outer fiber surface. For liquid flowing through the fiber lumen, the dense layer is in contact with the gas phase located on the shell side of the membrane contactor. The pores of the porous membrane are considered to be filled with gas. As different gases are generally involved, the transferred species is denoted by *i*. The membrane contactor and transmembrane transport are illustrated in Figure 3.1 on the example of a sweep gas mode.

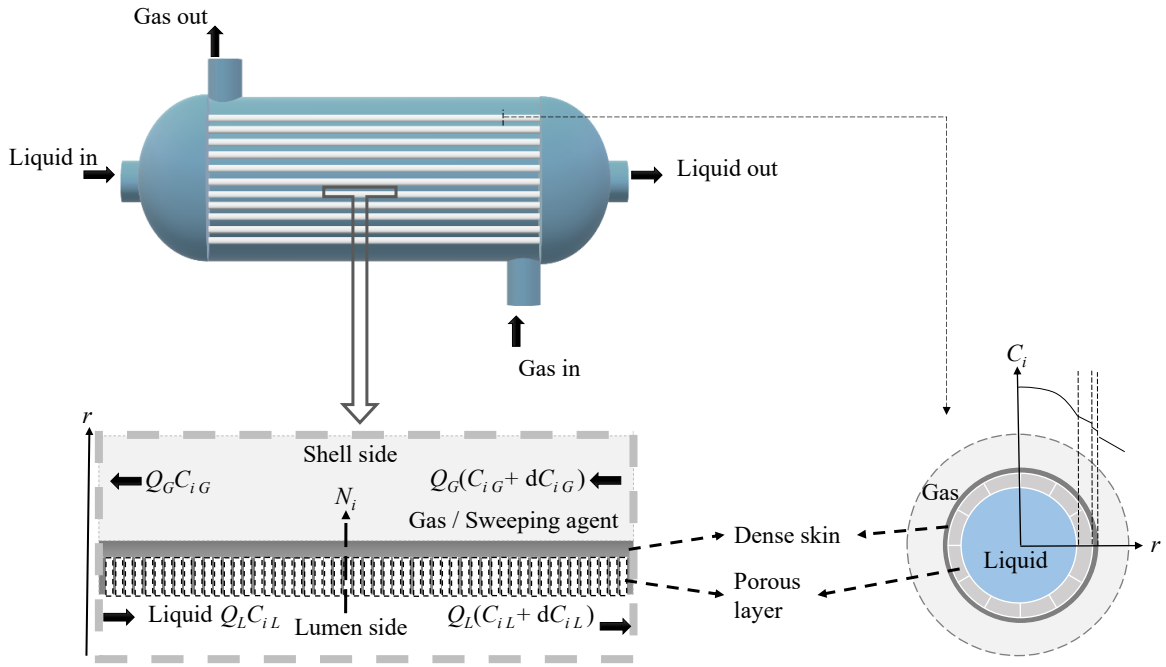

Figure 3.1 HFMC module and mass transfer gradients for liquid in lumen flow for sweep gas stripping

If considered a porous membrane with a dense outer skin, transmembrane transport can be described as a four-stage process, consisting of the diffusion of molecules across four physically separate domains. In the case of transfer from the liquid phase on the lumen side to the gas phase on the shell

side, the steps can be described as follows. First, the species diffuses from the liquid bulk to attain the membrane surface. At the inner surface of the fiber the species crosses the gas-liquid interface and enters the gas-filled membrane pores. It diffuses through the pores, then solubilizes in the outer dense skin and diffuses through it. At the interface between the dense membrane and the gas phase, the species desorbs and diffuses towards the gas bulk. Notations and expressions of characteristic lengths, mass transfer coefficients and mass transfer resistances of the four domains are shown in Table 3.1. It should be noted that, in general, the dense skin is located between the porous membrane and the liquid phase, to avoid membrane wetting. For a liquid flowing in the lumen of the fiber, the outer dense skin is of no use, as it separates two gaseous phases. It is nevertheless added in the following analysis, to present a generic approach.

Table 3.1 Characteristic diameters, mass transfer coefficient and resistances in the four domains

Domain	**Characteristic diameter**, m	**Local volumetric mass transfer coefficient**, m s^{-1}	**Mass transfer resistance**, s m^{-1}
Liquid phase	$d_{M\,int}$	$k_{i\,L}$	$R_{i\,M\,p}=\dfrac{1}{k_{i\,L}}$
Porous support	$d_{M\,lm\,p}\cong\dfrac{d_{M\,ext}-d_{M\,int}}{\ln\left(d_{M\,ext}/d_{M\,int}\right)}$	$k_{i\,M\,p}$	$R_{i\,M\,p}=\dfrac{d_{M\,int}}{d_{M\,lm\,p}}\dfrac{m_i}{k_{i\,M\,p}}$
External dense skin layer	$d_{M\,lm\,d}\cong d_{M\,ext}$	$k_{i\,M\,d}$	$R_{i\,M\,d}=\dfrac{d_{M\,int}}{d_{M\,ext}}\dfrac{m_i}{k_{i\,M\,d}}$
Gas phase	$d_{M\,ext}$	$k_{i\,G}$	$R_{i\,M\,G}=\dfrac{d_{M\,int}}{d_{M\,ext}}\dfrac{m_i}{k_{i\,G}}$

N.B. : The definitions of the symbols are given in the nomenclature

In steady-state, the material flux is the same through the different domains. An overall mass transfer coefficient can be defined and its value estimated by combining the mass flux expressions in the four domains. The expression for the molar flux of species *i*, N_i, as a function of to the liquid and gas bulk concentrations, $C_{i,L}$ and $C_{i,G}$, the overall liquid side volumetric mass transfer coefficient $K_{i\,OL}$, and the volumetric partition coefficient, m_i , is presented in Table 3.2.

The equations used to estimate the mass transfer coefficients in the four domains are presented in Table 3.2. The modelling approach is described in more detail in [12]. The starting point for estimating the fluid-membrane mass transfer coefficients is the modelling of fluid phase flow. It is done for both, the gas and the liquid phase. Under typical operating conditions in HFMCs, the flow in the fiber lumen and the flow around the fibers, are both laminar. Estimating mass transfer for liquid flowing on the shell side is a three-dimensional problem. A frequently proposed two-dimensional approximation is flow

through an annulus having the hydraulic diameter of the outer flow section [13]. The hydraulic diameter is defined as the diameter of a tube whose ratio of solid surface to flow volume is identical to that of the porous medium. It has been shown elsewhere [14] that the limiting Sherwood number of the shell-side flow can be estimated to a first approximation using the two-dimensional approach. The local and the average fluid-membrane mass transfer coefficients were estimated using a Sherwood – Graetz correlation as developed in [15]. In the following, the average mass transfer coefficient estimated over the entire length of the fiber is considered. For Graetz numbers below 30, the concentration profile is fully developed in the flow channel, and the Sherwood number reaches a limiting minimum value.

A pore diffusion model is used to estimate the mass transfer coefficient in the porous membrane, while a solution-diffusion model is used to estimate the mass transfer coefficient in the dense polymer layer. These relations represent the current state of knowledge of mass transfer in HFMCs.

Table 3.2: Local molar flux and associated transfer coefficients and resistances

Parameter	Expression
Overall species mass transfer flux with respect to the gas-liquid interface corresponding to the lumen-side membrane area	$N_i = K_{i\,OL}(C_{i\,L} - m_i C_{i\,G})$ $m_i \triangleq \frac{C_{i\,L}}{C^*_{i\,G}}$ Ratio of molar concentrations of species *i* at equilibrium N_i Molar flux of species *i*, $\mathrm{mol_i\ m_{ls}^{-2}}$ m_i Volumetric partition coefficient of species *i*, $\mathrm{m_G^3 m_L^{-3}}$ $C_{i\,L}$ Liquid bulk molar concentration of species *i*, $\mathrm{mol_i m_L^{-3}}$ $C_{i\,G}$ Gas bulk molar concentration of species *i*, $\mathrm{mol_i m_G^{-3}}$ $C^*_{i\,G}$ Gas molar concentration of species *i* in equilibrium with $C_{i\,L}$, $\mathrm{mol_i m_G^{-3}}$ $K_{i\,OL}$ Overall volumetric liquid side mass transfer coefficient of *i*, $\mathrm{m_L^3 m_{ls}^{-2} s^{-1}}$
Overall liquid side volumetric mass transfer coefficient	$\frac{1}{K_{i\,OL}} = \frac{1}{k_{i\,L}} + \frac{d_{M\,int}}{d_{M\,lm\,p}}\frac{m_i}{k_{i\,M\,p}} + \frac{d_{M\,int}}{d_{M\,ext}}\frac{m_i}{k_{i\,M\,d}} + \frac{d_{M\,int}}{d_{M\,ext}}\frac{m_i}{k_{i\,G}}$
Overall mass transfer resistance	$R_{i\,OL} = R_{i\,L} + R_{i\,M\,p} + R_{i\,M\,d} + R_{i\,G}$
Liquid and gas side average mass transfer coefficients: Sherwood - Graetz correlation	$Sh_{i\,j} = ((3.66)^3 + 4.21 Gz_{i\,j})^{1/3}$ $Sh_{i\,j} \triangleq \frac{k_{i\,j}.d_h}{D_{i\,j}}$, $j = G$ or L $\quad Gz_{i\,j} \triangleq \frac{u_j d_h^2}{D_{i\,j} Z}$ $\quad f \triangleq \frac{V_{fibers}}{V_{fb}}$

valid for confined laminar flow with uniform wall concentration [15]	Shell side: $d_h = d_{h\,ss} = d_{M\,ext}\,\frac{1-f}{f}$	Lumen-side: $d_h = d_{h\,ls} = d_{M\,int}$
	$Sh_{i\,j}$	Sherwood number for species *i* in phase *j*
	$Gz_{i\,j}$	Graetz number for species *i* in phase *j*
	Z	Total fiber length, m
	u_j	Interstitial fluid velocity, m s^{-1}
	$k_{i\,j}$	Volumetric mass transfer coefficient of species *i* in phase *j*
	$D_{i\,j}$	Diffusion coefficient of species *i* in phase *j*
	$d_{h\,ss}$	Hydraulic shell-side flow diameter, m
	$d_{h\,ls}$	Hydraulic lumen-side flow diameter, m
	f	Compacity of the fiber bundle, -
Mass transfer coefficient of porous support: pore diffusion model	$k_{i\,M\,p} = \frac{\varepsilon_M D_{i\,G}}{\tau_M \delta_{M\,p}}$	$\delta_{M\,p} \cong \frac{d_{M\,ext} - d_{M\,int}}{2}$
	$\delta_{M\,p}$	Thickness of the porous membrane, m
	ε_M	Membrane porosity, -
	τ_M	Membrane tortuosity, -
Mass transfer coefficient within the dense layer: solution-diffusion approach	$k_{i\,M\,d} = \mathcal{P}_i \frac{RT}{\delta_{M\,d}}$	
	$\delta_{M\,d}$	Thickness of the dense layer, m
	$\mathcal{P}_i$	Membrane Permeability, mol m^{-1} s^{-1} Pa^{-1}
	R	Ideal gas constant, Pa m^3 mol^{-1} K^{-1}
	T	Temperature, K

The literal expressions for the ratios of the gas side and membrane-side transfer resistances to the liquid side transfer resistance are given in Table 3.3. The value of these ratios is estimated as a function of the volumetric partition coefficient, using typical values for the other physical and geometrical parameters of the system. It can be seen that, for a volumetric partition coefficient, m_i, close to or less than unity, all the ratios are significantly less than unity, demonstrating that the entire mass transfer resistance is located in the liquid domain.

Table 3.3: Mass transfer resistance ratios in HFMCs for typical geometrical and physical parameters

Considered ratio	Expression	Typical range
Gas side over liquid side	$\frac{R_{iG}}{R_{iL}} = m_i \frac{1-f}{f} \frac{D_{iL}}{D_{iG}}$	$\frac{R_{iG}}{R_{iL}} \cong m_i \times 10^{-4}$
Porous membrane over liquid side	$\frac{R_{iMp}}{R_{iL}} \cong \frac{RMT}{2-RMT} \frac{\tau_M}{\varepsilon_M} \frac{1-f}{f} \frac{m_i Sh_{L\lim} D_{iL}}{D_{iG}}$ $RMT = \frac{2\delta_M}{d_{M\,ext}} = \frac{d_{M\,ext} - d_{M\,int}}{d_{M\,ext}}$	$\frac{R_{iMp}}{R_{iL}} \cong m_i \times 1.3 \times 10^{-3}$
Dense membrane over liquid side	$\frac{R_{iMd}}{R_{iL}} = \frac{\delta_{Md}}{d_{M\,ext}} \frac{1-f}{f} \frac{m_i Sh_{L\lim} D_{iL}}{\mathcal{P}_i RT}$	$\frac{R_{iMd}}{R_{iL}} \cong m_i \times 0.025$
Order of magnitude of the parameters	$f \cong 0.5$; $\frac{D_{iL}}{D_{iG}} \cong 10^{-4}$; $D_{iL} \cong 10^{-9}$ $m^2 s^{-1}$; $\frac{\varepsilon_M}{\tau_M} \cong 0,05$; $RMT \cong 0.3$; $Sh_{j\lim} \cong 3.66$ Under typical operating conditions, the average Sherwood number, Sh_{ij}, is less than 1.5 times the limiting value, $Sh_{j\lim}$. PMP SEPAREL membrane: dense layer thickness (estimation) $\delta_{Md} \cong 1\mu m$ $1050 < \mathcal{P}_{O_2}(PMP) < 2250$ barrer (at 25 °C) [16] ;1 barrer = 3.35 10^{-16} mol $m^{-1}s^{-1}Pa^{-1}$	

3.2.2HFMC model assumptions used for both vacuum and sweep gas stripping

The contactor model's assumptions are essentially based on the general consensus found in other published works. The model is one-dimensional. The contactor operates in steady state. The flow regime in both phases is laminar. Axial dispersion is neglected in the liquid phase, leading to the assumption of ideal plug flow. The species transferred are diluted in the liquid phase, resulting in a constant volumetric flow rate. The gas side is considered to be isobaric. Because of the low concentration of the species transferred, isothermal operation is considered. The above assumptions result in a constant volumetric gas-liquid partition coefficient for the transferred species. In addition, for the sake of simplicity, a

constant overall mass transfer coefficient is considered for each species. It is estimated by taking into account only the correlations regarding the mass transfer coefficient on the liquid side.

3.2.3 HFMC model for vacuum stripping

In vacuum stripping, there is no gas inlet. The gas flow at the outlet is due to liquid to gas transmembrane mass transfer. All dissolved gases are desorbed in order to approach equilibrium conditions. In addition, the solvent evaporates to reach its equilibrium vapor pressure. The composition of the outlet gas phase is the result of these phenomena. Due to the continuity of the pressure, the gas side composition can be considered uniform and equal to the outlet composition.

The HFMC transfer model used for vacuum stripping is detailed in Table 3.4. Given the above assumptions, a liquid side differential mass balance can be established. The mass transfer model is obtained by integrating the mass balance over the volume of the HFMC. The model relates two dimensionless numbers, a liquid-side mass transfer efficiency, $\eta_{i\,L}$, and a number of transfer units, $NTU_{i\,OL}$. It is well known and commonly applied in literature. However, the mass transfer efficiency is often taken to be equal to the species recovery rate, RR_i. This can lead to experimental results being misused. The definitions of mass transfer efficiency and recovery rate are given in Table 3.4. They are identical only when the concentration of species *i* is zero in the gas phase. This is generally not the case in vacuum stripping, as near-zero concentrations of the stripped species in the gas imply high vacuum volumetric flow rates and therefore high vacuum power.

Table 3.4: HFMC mass transfer model for vacuum stripping

Item considered	Definition or expression
Local liquid phase mass balance on species i	$Q_L \,\mathrm{d}C_{i\,L} = -K_{i\,OL}\left(C_{i\,L} - m_i C_{i\,G\,out}\right) a_{M\,int}\,\mathrm{d}V_{fb}$ $a_{M\,int} = \dfrac{4f\left(1-RMT\right)}{d_{M\,ext}}$ Q_L Liquid phase volumetric flow rate, $m^3\ s^{-1}$ $a_{M\,int}$ Specific lumen-side membrane area, $m^2\ m^{-3}{}_{fb}$ $\mathrm{d}V_{fb}$ Fiber bundle differential volume, m^3 The subscripts *in* and *out* designate concentrations at the contactor inlet and outlet. Ideal plug flow is considered for the liquid phase. Specific assumption: the composition of the gas is considered to be uniform and equal to the composition of the outlet.

Liquid side number of transfer units and total lumen-side membrane area	$NTU_{i\,OL} \triangleq \frac{K_{i\,OL} A_{M\,int}}{Q_L}$ $\qquad A_{M\,int} = a_{M\,int} V_{fb}$ $A_{M\,int}$ Total lumen-side membrane area, m^2
Liquid side mass transfer efficiency	$\eta_{iL} \triangleq \frac{\text{flux of } i \text{ transferred to the gas}}{\text{Maximum transferable flux of } i\text{, equilibrium at the outlet}}$ $\eta_{iL} = \frac{A_{M\,int} Q_L (C_{iL\,in} - C_{iL\,out})}{A_{M\,int} Q_L (C_{iL\,in} - m_i C_{iG\,out})} = \frac{C_{iL\,in} - C_{iL\,out}}{C_{iL\,in} - m_i C_{iG\,out}}$
Integration of the mass balance over the HFMC volume leading to the mass transfer model	$\ln\left(\frac{C_{i\,L\,out} - m_i C_{i\,G\,out}}{C_{i\,L\,in} - m_i C_{i\,G\,out}}\right) = -NTU_{i\,OL}$ thus $\eta_{i\,L} = 1 - \exp\left(-NTU_{i\,OL}\right)$
Ideal gas law	$C_{iG} = \frac{P_{i\,vac}}{RT}$
Recovery rate of the transferred species in the gas phase	$RR_i \triangleq \frac{\dot{V}_L\,(C_{iL\,in} - C_{iL\,out})}{\dot{V}_L\,C_{iL\,in}} = \frac{C_{iL\,in} - C_{iL\,out}}{C_{iL\,in}}$
Relation between the recovery rate and the liquid side mass transfer efficiency	$RR_i = \eta_{iL}\left(1 - \frac{P_{i\,vac}}{RT}\frac{m_i}{C_{i\,L\,in}}\right)$

The procedure for estimating the gas flow rate and composition in the vacuum stripping of multi-component mixtures is shown in Table 3.5. Overall mass balances can be established for all species transferred. The desorption flux depends on the initial gas concentration and on the mass transfer efficiency. The latter depends on the number of transfer units of the species. As the concentration of the solvent is very high, its partial pressure within the gas is taken to be its saturation vapor pressure. The total pressure on the gas side is the sum of the saturation vapor pressure of the solvent and the partial pressures of the other species transferred. The latter are estimated using the ideal gas law and the overall mass balances for the transferred species. As dissolved gases have comparable diffusion coefficients, the number of transfer units for all dissolved gases is assumed to be the same. This leads to identical mass transfer efficiencies. The resulting equation is used to estimate the product of mass transfer efficiency and the ratio between the volumetric flow rates of the liquid and the gas and finally the outlet concentrations of the transferred species. In order to estimate the composition of the gas outlet, the inlet concentrations of all the dissolved gases must be known. The vacuum pressure and therefore the outlet

gas side concentration of species *i* must be selected in order to achieve the desired recovery rate for a given mass transfer efficiency.

Table 3.5: Gas flow rate and composition in the vacuum stripping of multi-component mixtures

Item considered	Definition or expression
Mass balance for the transferred gases and resulting molar outlet gas concentration	$Q_{G\,out}C_{i\,G\,out} = Q_L\left(C_{i\,L\,in} - C_{i\,L\,out}\right) = Q_L\eta_{i\,L}\left(C_{i\,L\,in} - m_i C_{i\,G\,out}\right)$ Thus $C_{i\,G\,out} = \frac{P_{i\,vac}}{RT} = \frac{\left(Q_L / Q_{G\,out}\right)\eta_{i\,L}C_{i\,L\,in}}{1+\left(Q_L / Q_{G\,out}\right)m_i\eta_{i\,L}}$ $Q_{G\,out}$ Gas phase volumetric outlet flow rate, $m^3\ s^{-1}$
Total and partial pressures of the species in the gas outlet	$P_{vac} = P^{sat}_{solvent} + \sum_{i=1}^{N} P_{i\,vac} = P^{sat}_{solvent} + RT\frac{Q_L\eta_L}{Q_{G\,out}}\sum_{i=1}^{N}\frac{C_{i\,L\,in}}{1+m_i\frac{Q_L\eta_L}{Q_{G\,out}}}$ P_{vac} Vacuum pressure, Pa An identical mass transfer efficiency, η_L, is assumed for all the species transferred.

3.2.4HFMC models for stripping with a sweep gas or in combo mode

The operation of stripping with a sweeping gas can be modelled by considering an ideal countercurrent plug flow of the gas and liquid phases. The HFMC transfer model used for stripping with a sweep gas is detailed in Table 3.6. Given the above assumptions, differential mass balances in the liquid and gas phases can be established and combined. It should be noted that the expression for mass transfer efficiency given in Table 3.6 is different from that given in Table 3.4. This is due to different assumptions. Indeed, in the Vacuum model described in Table 3.4, the composition of the gas side is considered to be uniform and equal to that of the outlet flow, whereas it varies in the Sweep gas model described in Table 3.6, where plug flow is considered for both the gas and liquid phases. In the latter case, since an ideal counter-current plug flow is considered, the maximum transferable flow is reached when the composition of the outlet liquid flow is in equilibrium with the composition of the inlet gas flow.

The mass transfer model is obtained by integrating the mass balances over the volume of the HFMC. The model relates three dimensionless numbers, a mass transfer efficiency, $\eta_{i\,L}$, a number of transfer units, $NTU_{i\,OL}$ and a partition ratio, λ_i. The model is well known and commonly applied in literature. If the species concentration of *i* is zero in the inlet gas stream, which is generally the case, the mass transfer efficiency is equal to the recovery rate of the species. For effective striping, i.e. to achieve

high recovery rates, the partition ratio must be greater than or equal to unity. If the partition ratio is well above unity, the gas phase concentration of species *i* at the contactor outlet tends towards zero and the mass transfer model tends towards the model established for vacuum stripping under high vacuum conditions.

Table 3.6: HFMC mass transfer model for stripping with a sweep gas assuming ideal counter-current plug flow

Item considered	Definition or expression
Local liquid and gas phase mass balances on species i	$Q_L \, \mathrm{d}C_{i\,L} = -K_{i\,OL}\left(C_{i\,L} - m_i C_{i\,G}\right) a_{M\,int} \, \mathrm{d}V_{fb}$ Q_G Gas phase volumetric flow rate, $m^3\ s^{-1}$ $Q_L \, \mathrm{d}C_{i\,L} = Q_G \, \mathrm{d}C_{i\,G}$ Specific assumptions: ideal gas-liquid counter-current plug flow. The volumetric flow rate of the gas phase is considered to be constant.
Dimensionless numbers	$NTU_{i\ OL} \triangleq \frac{K_{i\ OL} A_{M\ int}}{Q_L}$ $\lambda_i \triangleq \frac{Q_G}{m_i Q_L}$ λ_i Partition ratio, -
Liquid side mass transfer efficiency	$\eta_{i\,L} = \frac{A_{M\,int} Q_L \left(C_{i\,L\,in} - C_{i\,L\,out}\right)}{A_{M\,int} Q_L \left(C_{i\,L\,in} - m_i C_{i\,G\,in}\right)} = \frac{C_{i\,L\,in} - C_{i\,L\,out}}{C_{i\,L\,in} - m_i C_{i\,G\,in}}$ As counter-current plug flow is considered, the expression of mass transfer efficiency differs from that given in Table 3.4 for the Vacuum model.
Integration of the mass balance over the HFMC volume leading to the mass transfer model	$\eta_{i\,L} = \frac{\lambda_i \left(1 - \exp\left(\frac{(\lambda_i - 1)}{\lambda_i} NTU_{i\,OL}\right)\right)}{1 - \lambda_i \exp\left(\frac{(\lambda_i - 1)}{\lambda_i} NTU_{i\,OL}\right)}$

In the combo mode, which uses a combination of sweep gas and vacuum, depending on the flow rate of the sweep gas and the amount of vacuum applied, the spatial concentration gradient in the gas phase lies somewhere between the limiting cases of uniform composition, characterizing vacuum operation, and ideal plug flow, characterizing, at least theoretically, sweep gas stripping.

As in vacuum stripping, the gas flow rate and composition at the contactor outlet can be estimated using mass balances. Related equations are given in Table 3.7. The equations are given for two cases. A model considering ideal counter-current gas-liquid plug flow referred to as the *Sweep gas model* and a model considering ideal liquid plug flow and uniform composition on the gas side, referred to as the *Vacuum model*.

Table 3.7: Gas flow rate and composition in sweep gas and combo mode stripping

Item considered		Definition or expression
Overall mass balance		Sweep gas $Q_{G\,out}C_{sw\,G\,out} = F_{sw\,G\,in} + Q_L\left(C_{sw\,L\,in} - C_{sw\,L\,out}\right)$ Stripped gases $Q_{G\,out}C_{i\,G\,out} = Q_L\left(C_{i\,L\,in} - C_{i\,L\,out}\right)$ *sw* Index indicating the sweep gas $C_{sw\,L\,in}$ Liquid inlet concentration of the sweep gas, $mol_{sw}\ m^{-3}$ $F_{sw\,G\,in}$ Molar inlet flowrate of the sweep gas, $mol_{sw}\ s^{-1}$
Sweep gas model Ideal gas-liquid counter-current plug flow	Molar concentrations	Sweep gas $C_{sw\,G\,out} = \frac{F_{sw\,G\,in}}{Q_{G\,out}} + \frac{Q_L}{Q_{G\,out}}\eta_{sw}\left(C_{sw\,L\,in} - m_{sw}\frac{P_{vac}}{RT}\right)$ Stripped gases $C_{i\,G\,out} = \frac{Q_L}{Q_{G\,out}}\eta_i\left(C_{i\,L\,in} - m_i C_{i\,G\,in}\right) = \frac{Q_L}{Q_{G\,out}}\eta_i C_{i\,L\,in}$ $C_{i\,G\,in} = 0$ for all species, except the stripping agent N.B.: The expression of the mass transfer efficiency is given in Table 3.6.
	Total and partial pressures of the species in the gas outlet	$P_{vac} = P_{solvent}^{sat} + RT\left(\frac{F_{sw\,G\,in}}{Q_{G\,out}} - \frac{Q_L}{Q_{G\,out}}\eta_L m_{sw}\frac{P_{vac}}{RT}\right)$ $+RT\frac{Q_L}{Q_{G\,out}}\eta_L\sum_{i=1}^{N}C_{i\,L\,in}$ An identical mass transfer efficiency, η_L, is assumed for all the species transferred.
Vacuum model Ideal liquid plug flow uniform gas-side composition	Molar concentrations	Sweep gas $C_{sw\,G\,out} = \frac{\frac{F_{sw\,G\,in}}{Q_{G\,out}} + \frac{Q_L}{Q_{G\,out}}\eta_{sw}C_{sw\,L\,in}}{1 + m_{sw}\frac{Q_L}{Q_{G\,out}}\eta_{sw}}$ Stripped gases $C_{i\,G\,out} = \frac{\frac{Q_L}{Q_{G\,out}}\eta_i C_{i\,L\,in}}{1 + m_i\frac{Q_L}{Q_{G\,out}}\eta_i}$ $C_{i\,G\,in} = 0$ for all species, except the stripping agent N.B.: The expression of mass transfer efficiency is given in Table 3.4.

Total and partial pressures of the species in the gas outlet	$$P_{vac} = P_{solvent}^{sat} + RT\frac{\left(F_{sw\,G\,in} / Q_{G\,out}\right) + \left(Q_L / Q_{G\,out}\right)\eta_L C_{sw\,L\,in}}{1 + \left(Q_L / Q_{G\,out}\right) m_{sw}\eta_L}$$ $$+ RT\left(Q_L / Q_{G\,out}\right)\eta_L \sum_{i=1}^{N} \frac{C_{i\,L\,in}}{1 + m_i\eta_L\left(Q_L / Q_{G\,out}\right)}$$ An identical mass transfer efficiency, η_L, is assumed for all the species transferred.

3.2.5Appropriate operating condition of HFMC stripping

By using mass transfer models, it is possible to select the number of transfer units in the operation that leads to a reasonable high mass transfer efficiency. For example, in vacuum mode, a number of transfer units of 4 leads to a mass transfer efficiency of 0.98. In sweep gas mode and for a partition ratio of 3, a number of transfer units of 4 leads to a mass transfer efficiency 0.95. A value of 4 for the number of transfer units therefore seems to correspond to an appropriate operating condition.

As shown in Table 3.8, the Graetz number at the outlet of the HFMC can be expressed as a function of the ratios between the Sherwood number and the number of transfer units. The Sherwood number is a function of the Graetz number. It is therefore possible to establish a relationship between the Graetz number and the number of transfer units. A number of transfer units of 4 leads to a Graetz number of 4 and a Sherwood number of 4. This Sherwood number is close to the minimum Sherwood number controlled by diffusion.

Knowing the Sherwood number and the number of transfer units makes it possible to estimate the appropriate ratio between the liquid flow rate and the internal membrane area. Estimated values for water deoxygenation using commercial fibers are given in Table 3.8.

Table 3.8: Appropriate operating conditions of HFMC stripping operations

Item considered	Expression
Relation between the Graetz number at the fiber outlet and NTUi OL	$$Gz_{i\,L} = \frac{4Q_L}{A_{M\,int}}\frac{d_{M\,int}}{D_{i\,L}}\frac{K_{i\,OL}}{K_{i\,OL}} = \frac{4Sh_{i\,L}}{NTU_{i\,OL}} = \frac{4\times((3.66)^3 + 4.21Gz_{i\,L})^{1/3}}{NTU_{i\,OL}}$$
Application to appropriate operating conditions	For $NTU_{i\,OL} = 4$ we obtain $Gz_{i\,L} = 4.0$ leading to $Sh_{i\,L} = 4.0$ Vacuum mode: $\eta_{i\,L} = 0.98$; Sweep gas mode with $\lambda_i = 3$: $\eta_{i\,L} = 0.95$

Resulting ratio between the liquid flow rate and the internal membrane area		$\frac{Q_L}{A_{M\,int}} = \frac{Sh_{i\,L}}{NTU_{i\,OL}} \frac{D_{i\,L}}{d_{M\,int}} \cong \frac{4.0}{4.0} \frac{2\times10^{-9}}{d_{M\,int}} = \frac{D_{i\,L}}{d_{M\,int}} \frac{\mathrm{m_L^3}}{\mathrm{s\ m_{int}^2}}$	
Application to commercial fibers and water deoxygenation at 20 °C $D_{O2\,L} = 2\times10^{-9}\,\mathrm{m^2 s^{-1}}$	SEPAREL	$d_{M\,int} = 1.4\times10^{-4}\,\mathrm{m}$	$\frac{Q_L}{A_{M\,int}} = 1.4\times10^{-5} \frac{\mathrm{m_L^3}}{\mathrm{s\ m_{int}^2}}$
	Liqui-Cel	$d_{M\,int} = 2.2\times10^{-4}\,\mathrm{m}$	$\frac{Q_L}{A_{M\,int}} = 0.91\times10^{-5} \frac{\mathrm{m_L^3}}{\mathrm{s\ m_{int}^2}}$

3.2.6 Liquid pressure drop and optimal fiber length

Liquid pressure drop is a major process parameter because it contributes to operating costs. The estimation of the liquid pressure drop using Hagen-Poiseuille's law and its expression as a function of the process parameters are shown in Table 3.9. For a given efficiency and therefore a given number of transfer units and Sherwood number, a given internal fiber diameter and a given liquid viscosity and diffusion coefficient, the pressure drop is proportional to the square of the fiber length. Thus, the length of the fibers can be adjusted to obtain the desired pressure drop. The application to commercial fibers and water deoxygenation is shown in Table 3.9. At appropriate operating conditions, i.e. $NTU_{i\,OL} = 4$, to limit the pressure drop to 0.1 bar, the length of SEPAREL fibers is 0.12 m, while that of Liqui-Cel fibers is 0.3 m.

The relationship between liquid pressure drop and fiber length for a given process performance helps to explain why it is impossible to increase the size of HFMC modules for stripping operations. HFMC modules with long fiber lengths do not perform well because, for an appropriate pressure drop, the ratio between the liquid flow rate and the internal membrane area is far too low, whereas for an appropriate ratio between the liquid flow rate and the internal membrane area, the pressure drop is far too high.

The impossibility of increasing the length of the fibers means that the only way of increasing the throughput is to increase the number of fibers. The resulting HFMC geometry, with a large number of fibers, is not easy to achieve. This is the reason for the success of cross-flow HFMCs, where the liquid flows outside the fibers in a radial direction leading to a shorter length travelled by the liquid within the HFMC and thus a smaller pressure drop.

Table 3.9: Liquid side frictional pressure drop

Item considered	Definition or expression
Hagen-Poiseuille law for the estimate of the liquid phase pressure drop	$\Delta P_{f\,L} = \frac{32\mu_L}{d_{M\,int}^2} u_L Z$ u_L Interstitial liquid velocity, m s^{-1}
Liquid phase pressure drop as a function of geometry and operating conditions	$\Delta P_{f\,L} = \frac{128\mu_L Z^2}{d_{M\,int}^3}\frac{Q_L}{A_{M\,int}} = \frac{128\mu_L Z^2}{d_{M\,int}^4}\frac{Sh_{i\,L}D_{i\,L}}{NTU_{i\,OL}}$
Application to commercial fibers and water deoxygenation at 20 °C using appropriate operating conditions	$NTU_{i\,OL} = 4$; $Sh_{i\,L} = 4.0$; $D_{i\,L} = 2\times10^{-9}\,\mathrm{m^2 s^{-1}}$; $\mu_L = 10^{-3}\,\mathrm{Pa\,s}$; $\Delta P_{f\,L} = 10^4\,\mathrm{Pa}$ SEPAREL $d_{M\,int} = 1.4\times10^{-4}\,\mathrm{m}$; $Z = 0.12\,\mathrm{m}$ Liqui-Cel $d_{M\,int} = 2.2\times10^{-4}\,\mathrm{m}$; $Z = 0.30\,\mathrm{m}$

3.3 Model validation by comparison with published data

The model predictions were compared with experimental data reported in the literature on the removal of dissolved oxygen and methane from water in commercial HFMC modules. Data provided by technology suppliers as well as scientific papers were taken into account, including vacuum and combo mode striping. The parameters that varied included contactor geometry, operating temperature, initial liquid phase composition, liquid flow rate and vacuum pressure and, in combo mode, sweep gas flow rate.

3.3.1 Geometric characteristics of the commercial HFMC modules

The geometric characteristics of the seven commercial HFMC modules considered are presented in Table 3.10. The total fiber length and gas-liquid contact length were estimated on the basis of the mechanical designs provided by the supplier. For the Liqui-Cel modules, compacity was determined on the basis of bibliographic information. This was used to estimate the number of fibers, *N*, and the lumen side membrane area, $A_{M\,int}$. The shell side membrane area of the SEPAREL modules was indicated by the supplier. The lumen side membrane area was estimated using the ratio of the external and internal fiber diameters. Internal membrane areas range from 0.158 m^2 in the Liqui-Cel MM 1x5.5 module to 20 m^2 in the SEPAREL PF-030 module. Fiber lengths range from 0.08 m in the SEPAREL PF-001D module to 0.44 m in the SEPAREL PF-030 module. As shown in Table 3.10, for the three Liqui-Cel modules and for the SEPAREL PF-0001D and PF-004D modules, the experimental pressure drops, given by the supplier, are close to those estimated using the Hagen-Poiseuille law, allowing us to

conclude that the geometry considered is consistent. For the SEPAREL PF-015PP and PF-030 modules, the pressure drop estimated by the Hagen Poiseuille equation was 2.5 times higher than that indicated by the supplier. This discrepancy could not be explained.

Table 3.10: Geometrical characteristics of the commercial HFMC modules and analysis of their pressure drop

Supplier	**Series**	$A_{M\,int}$ m^2	$d_{M\,ext}$ µm	$d_{M\,int}$ µm	Z_{tot} m	Z m	N -	f -	$Q_{L\,max}$ L min^{-1}	$\frac{\Delta P_{f\,L\,exp}}{\Delta P_{f\,L\,model}}$ -
Liqui-Cel [1]	MM 1x5.5	0.158	300	220	0.146	0,136	1679	0.33	0.7	1.04
	MM 1.7x5.5	0.564			0.144	0,134	6094	0.37	2.5	1.07
	MM 1.7x8.75	0.914			0.227	0,217	6094	0.37	3	1.06
SEPAREL [2]	PF-001D	0.333	210	140	0.09	0.08	9400	0.18	1	1.30
	PF-004D	2.667			0.2	0.19	3.20×10^4	0.16	3	1.08
	PF-015PP	10			0.44	0.41	5.60×10^4	0.19	500	0.41
	PF-030	20			0.44	0.41	1.11×10^5	0.18	1000	0.42

3.3.2 Physical systems and operating modes and ranges

The physical systems as well as the operating modes and ranges of the experiments are presented in Table 3.11. Oxygen and methane stripping are studied at 20 and 25 °C. The effluent to be stripped was pure water or an aqueous effluent from a fermenter. Vacuum and combo mode stripping experiments are analyzed.

Table 3.11: Physical systems and operating modes and ranges

Module Series	**Solute**	**Effluent**	**Initial solute concentration** mg. L^{-1}	**Stripping mode**	**Vacuum pressure** kPa	**Gas flowrate**[1] Q_G, L h^{-1}	T °C	**Ref**
MM 1x5.5 MM 1.7x5.5 MM 1.7x8.75	O_2	Water	9.1 (estimation, RR_{O_2} is given)	Vacuum	6.67	-	20	[1]
MM 1x5.5	CH_4	Water	21.65 ± 0.62	Combo	53.3; 61.3; 81.3; 91.3	0.5; 1.0; 1.5	25	[17]
PF-001D PF-004D PF-015PP PF-030	O_2	Water	8.1	Vacuum	5.3; 8.0; 13.3; 18.6; 24	-	25	[2]
1 It's assumed that these flowrates are NTP conditions (273 K, 1 bar)								

3.3.3 Physicochemical and thermodynamic data

Physio-chemical and thermodynamic data were estimated using conventional correlations. Although the oxygen diffusion coefficient in water, $D_{O_2 L}$, is an important parameter, the values reported in the literature at 20°C are scattered, with experimental values ranging from 1.76×10^{-9} m^2 s^{-1} to 2.22×10^{-9} m^2 s^{-1} and predicted values using correlations ranging from 1.97×10^{-9} m^2 s^{-1} to 2.18×10^{-9} [18]. In the following, the value of 2.00×10^{-9} m^2 s^{-1} was used at 20°C. The Stokes-Einstein equation ($D_{O_2 L} \times \mu_L / T$ = constant) was used in order to estimate the diffusion coefficient of oxygen at 25 °C. For the diffusion coefficient of methane, the value given by [17] was used.

The thermodynamic equilibrium constant for oxygen and methane were estimated using the procedure given in [19]. In vacuum operation, gas flow rate and gas phase composition were estimated using the mass balance shown in Table 3.5, whereas the mass balances shown in Table 3.7 were used in the combo mode operation.

3.3.4 Supplier data for vacuum stripping of oxygen in Liqui-Cel modules

Values of the oxygen recovery rate in three different HFMC modules with internal membrane areas ranging from 0.16 to 0.91 m^2 are given by the technology supplier [1]. The volumetric liquid flow rate varied from 0.05 to 3 L min^{-1}. The highest flow rates were applied to the modules with the largest membrane area. The experiments were carried out with air-saturated water at 20 °C. At this temperature, the volumetric partition coefficients of oxygen, m_{O_2}, is 0.0338 m^3_G m^{-3}_L while that of nitrogen, m_{N_2}, is 0.0170 m^3_G m^{-3}_L. The diffusion coefficient of oxygen in the liquid, $D_{O_2 L}$, is 2.0×10^{-9} m^2 s^{-1}. Experiments were made in vacuum mode with the vacuum set to 6.67 kPa. The partial pressures of oxygen, nitrogen and water vapor in the extracted gas phase are estimated at values of 1.41, 2.92 and 2.34 kPa respectively, using the mass balance presented in Table 3.5. The ratio of oxygen mass transfer efficiency to oxygen recovery rate was 1.076 for all experiments, meaning that the maximum achievable oxygen recovery rate was 0.93.

In Figure 3.2, the experimental values of the mass transfer efficiency of oxygen are plotted as a function of the specific liquid flow rate, i.e. the ratio between the volumetric liquid flowrate and the internal membrane area. Vacuum model predictions are plotted as a solid line. It can be seen that, when plotting efficiency as a function of specific liquid flow rate, all the measurements fall on a single line and compare very well with the Vacuum model.

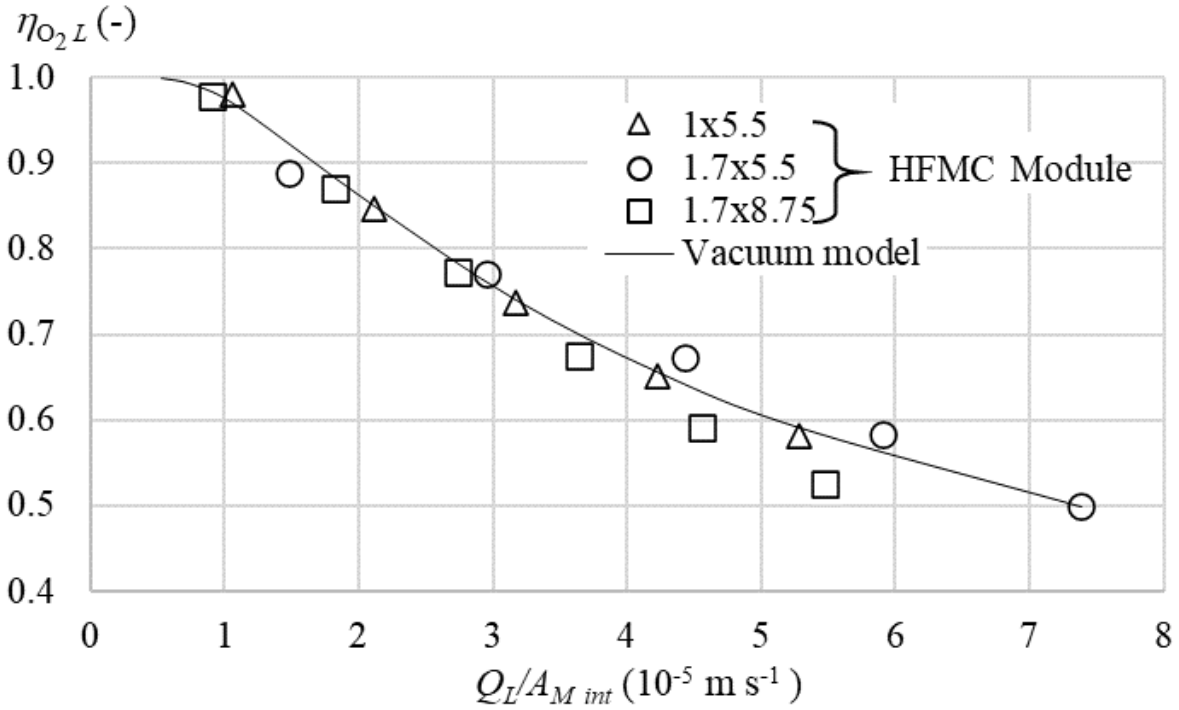

Figure 3.2: Mass transfer efficiency as a function of the specific liquid flowrate, supplier data [1] compared to vacuum model; vacuum set to 6.67 kPa; 20°C.

In Figure 3.3, the Sherwood number characterizing the mass transfer of oxygen estimated using the experimental recovery rate and the Vacuum model given in Table 3.4 is plotted as a function of the specific liquid flow rate. As shown in Table 3.8, the specific liquid flow rate is proportional to the Graetz number of the species and the ratio of the diffusion coefficient of the species to the internal fiber diameter, giving in these experiments $Gz_{O2\,L} = 4.16\times10^5\, Q_L/A_{M\ int}$. The Sherwood number estimated using the Graetz equation given in Table 3.2 is indicated in Figure 3.3 by the solid line. The Sherwood numbers estimated using the Vacuum model fall on a single line and compare well with the Graetz correlation, thus validating the modelling approach.

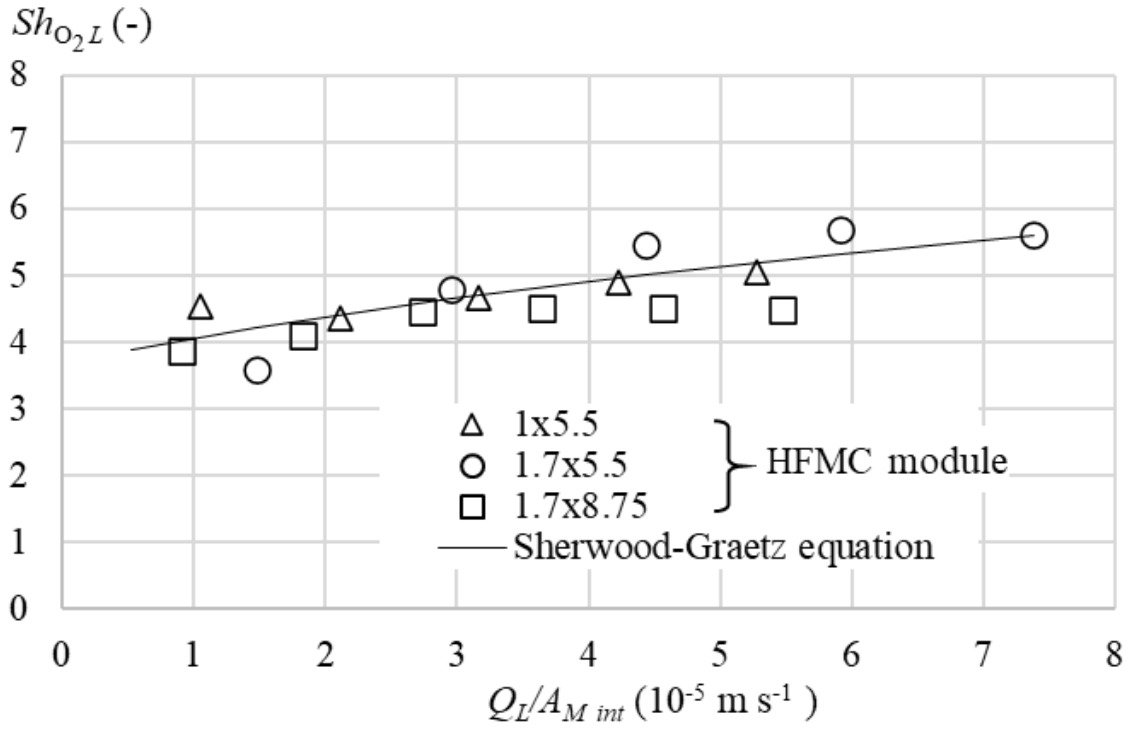

Figure 3.3: Sherwood number as a function of the specific liquid flow rate, Vacuum model using supplier data [1] ; vacuum set to 6.67 kPa; 20°C; comparison with Graetz correlation

3.3.5 Methane stripping from water in combo mode using the MM 1x5.5 Liqui-Cel module

Jiménez-Robles *et al* [17] investigated the benefits of using a combo mode, sweep gas and vacuum, to generate the driving force required to strip methane from water. The authors used the MM 1x5.5 Liqui-Cel module with the liquid flowing on the lumen side and the gas flowing in counter-current. The experiments were performed at 25 °C. The volumetric liquid flow rate varied from 0.08 to 0.47 L min^{-1}. The liquid was saturated with pure methane at atmospheric pressure. The initial mean measured concentration of dissolved methane was 21.65 mg L^{-1}, corresponding to 1.35 mol m^{-3}. The vacuum applied varied between 51.3 and 91.3 kPa. The sweep gas was nitrogen. Volumetric sweep gas flow rates of 0.5, 1 and 1.5 L h^{-1} were applied. The reference conditions for the gas flow are not given, we assumed STP, i.e. 1 bar and 0°C. At 25°C, the volumetric partition coefficients of methane, m_{CH4}, is 0.0338 m^3_G m^{-3}_L while its diffusion coefficient in the liquid, $D_{CH_4 L}$, is 1.76×10^{-9} m^2 s^{-1}. The volumetric partition coefficients of nitrogen, m_{N2}, is 0.0161 m^3_G m^{-3}_L. The equilibrium water vapor pressure is 3.17 kPa.

In Figure 3.4, the experimentally determined mole fractions of methane in the outlet gas phase are compared with the mole fractions estimated using the mass balance presented in Table 3.7 when

considering the Vacuum model. In Figure 3.4a, the initial nitrogen concentration in the liquid effluent was set to zero, whereas it was considered to be in equilibrium with atmospheric pressure in Figure 3.4b. With the assumption of no nitrogen in the liquid to be treated ($C_{sw\,L\,in}$ = 0) (Figure 3.4a) the experimentally determined mole fractions of methane are on average 13% lower than the calculated mole fractions. With the assumption of $C_{sw\,L\,in}$ at equilibrium with atmospheric pressure (Figure 3.4b), the experimentally determined mole fractions of methane are on average 2% higher than the calculated mole fractions. The actual concentration of nitrogen at the inlet is not indicated in the paper from which the measurements were taken [17]. In the following, when required, the experimentally determined mole fraction of methane in the outlet gas phase was considered. It varied from 0.09 to 0.47 and increased with the increase of the specific liquid flow rate. This is explained by the increase of the methane desorption flux.

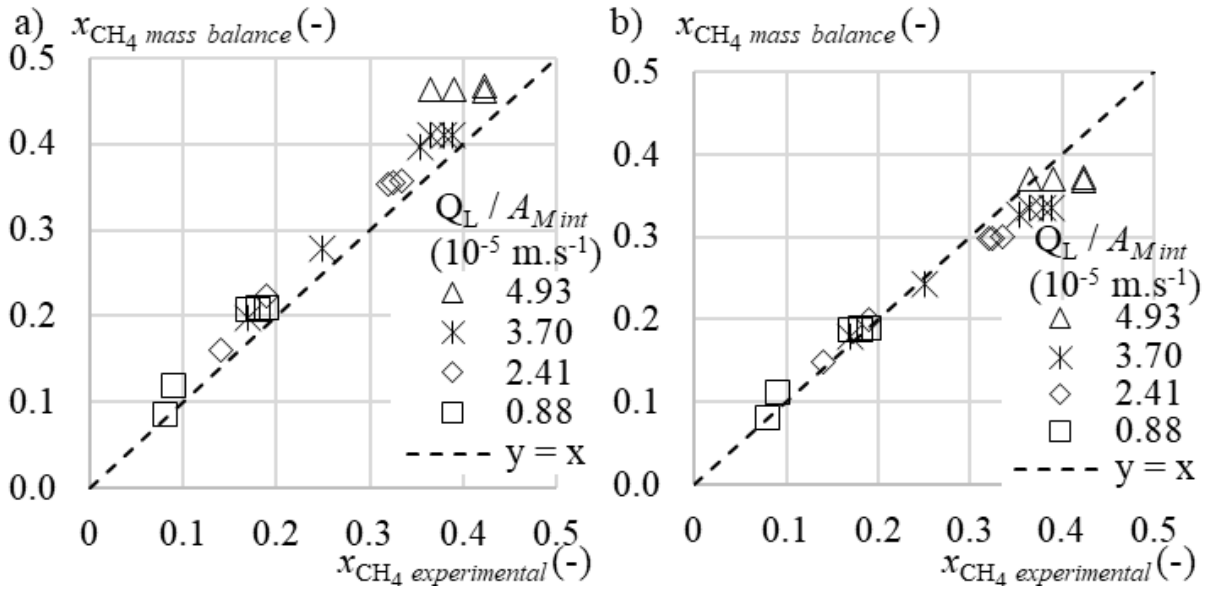

Figure 3.4: Parity plot comparing experimental and calculated mole fractions of methane in the outlet gas phase considering the Vacuum model (see Table 3.7). Measurements taken from literature [17]; vacuum levels between 51.3 and 91.3 kPa; 25 °C ; a) $C_{sw\,L\,in}$ = 0 ; b) $C_{sw\,L\,in}$ in equilibrium with P_{sw} = 1 atm.

As the measurements were made in combo mode, applying simultaneously sweep gas and vacuum, the degree of back mixing of the gas phase is difficult to estimate. Moreover, as shown in Table 3.10, the module used i.e. MM 1x5.5 Liqui-Cel is quite short, 14 cm contact length, and the gas inlet and outlet are on the side of the cartridge. So ideal plug flow is not to be expected. Despite this complex module geometry, ideal counter-current flow is considered in the Sweep gas model, neglecting back-mixing and three-dimensional distributions. In the Vacuum model, the gas phase is considered to have

a uniform composition, so that three-dimensional flow distribution and back-mixing do not influence the calculation results. Both models were applied to interpret experimental data.

The Sherwood number estimated using the Sweep gas model given in Table 3.6 is plotted in Figure 3.5 as a function of the specific liquid flow rate. The Sherwood number given by the Graetz equation given in Table 3.2 is shown by a solid line. The Sherwood numbers estimated using the Sweep gas model are significantly lower than those estimated by the Graetz equation. Probably this can be explained by the overestimation of the mean concentration gradient in the Sweep gas model which neglects back mixing.

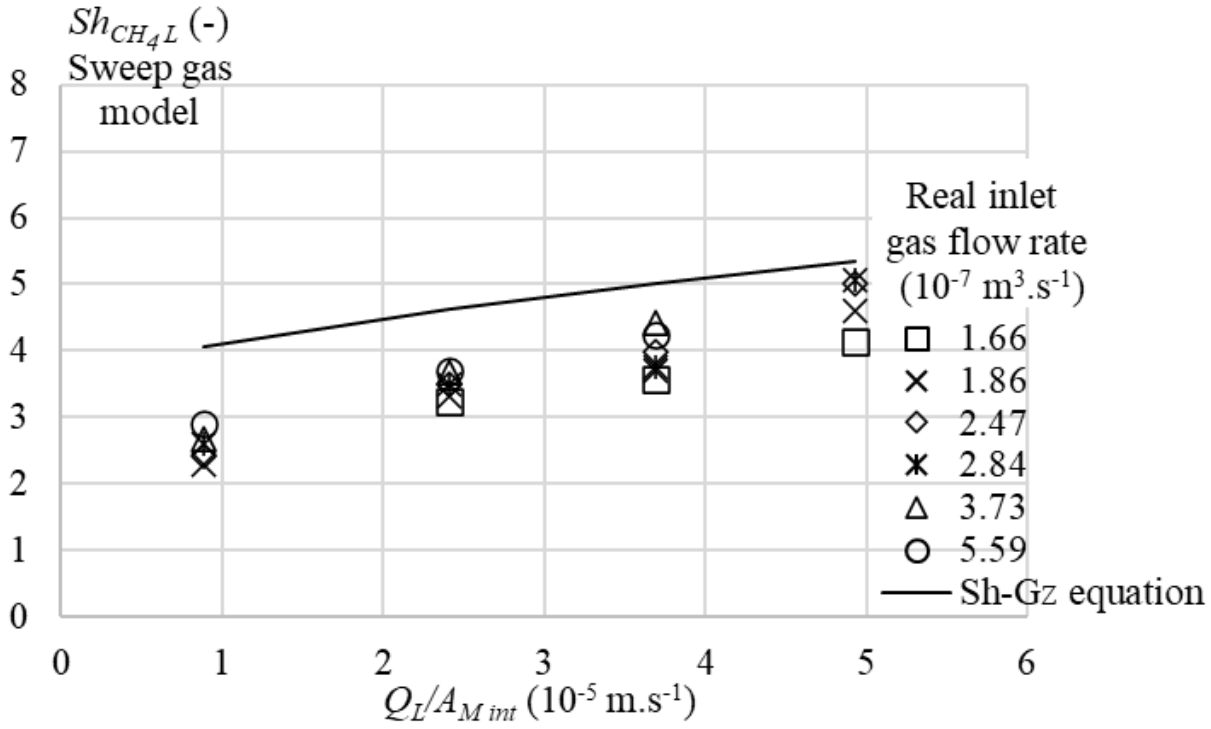

Figure 3.5: Sherwood number as a function of the specific liquid flow rate, sweep gas model using literature data [17]; vacuum levels between 51.3 and 91.3 kPa; 25 °C; comparison with Graetz correlation

The Sherwood number estimated using the Vacuum model given in Table 3.4 is plotted in Figure 3.6 as a function of the specific liquid flow rate. In the Vacuum model, mass transfer efficiencies differ from recovery rates. Depending on operating conditions, the ratio of the two parameters varied from 1.07 to 1.64. The Sherwood number given by the Graetz equation is shown in Figure 3.6 by a solid line. Even though the values are dispersed, the calculated Sherwood numbers are consistent with the Graetz equation. Only for the highest specific liquid flow rate they are significantly over the line. This might be explained by the higher outlet gas flow rates observed in these conditions, leading to a lower degree of back mixing of the gas phase.

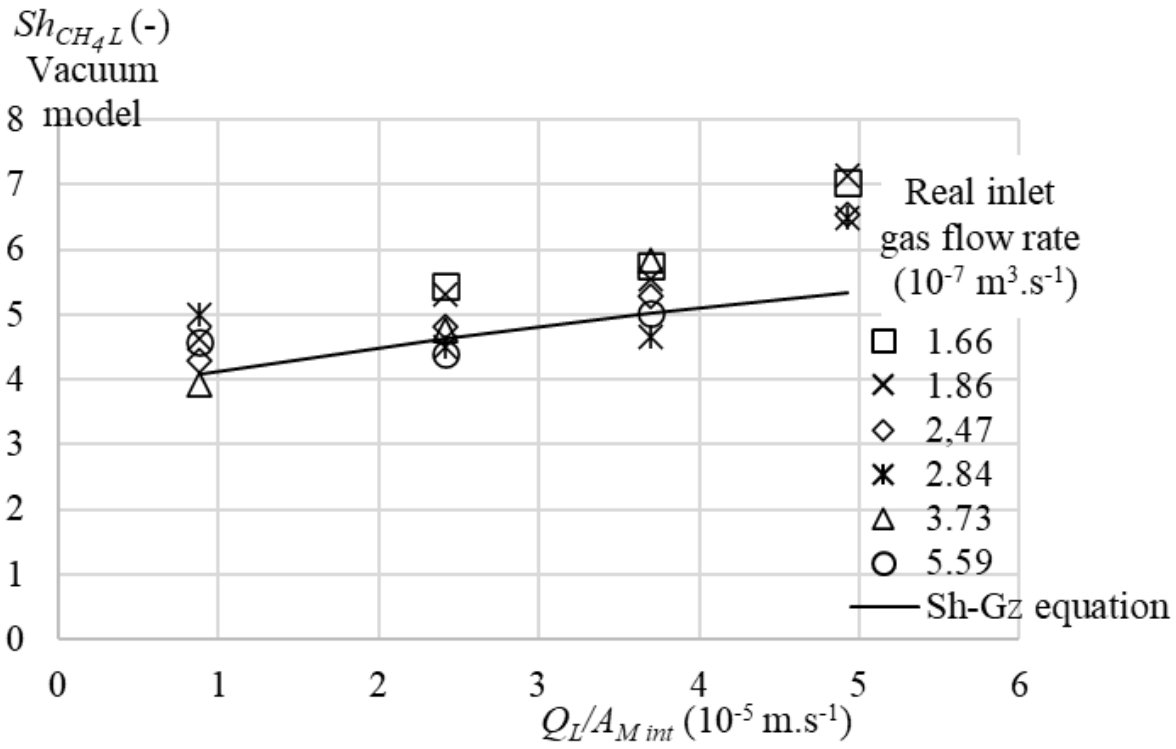

Figure 3.6: Sherwood number as a function of the specific liquid flow rate, Vacuum model using literature data [17]; vacuum levels between 51.3 and 91.3 kPa; 25 °C; comparison with Graetz correlation

3.3.6 Supplier data for vacuum stripping of oxygen in SEPAREL modules

Values of the oxygen outlet concentration in four SEPAREL HFMC modules with internal membrane areas ranging from 0.33 to 20 m^2 are given through graphs by the technology supplier [2]. Experiments were carried out with air-saturated water at 25°C in vacuum mode with vacuum pressures ranging from 5.3 kPa to 24 kPa, leading to oxygen mass transfer efficiency to oxygen recovery rate ratios of between 1.03 and 1.41.

At 25 °C, the volumetric partition coefficients of oxygen, m_{O_2}, is 0.0316 $m^3_G\ m^{-3}_L$ while that of nitrogen, m_{N_2}, is 0.0161 $m^3_G\ m^{-3}_L$. The diffusion coefficient of oxygen in the liquid, $D_{O_2\,L}$, is 2.29×10^{-9} m^2 s^{-1}. The saturation vapor pressure of water is 3.17 kPa. The volumetric liquid flow rate varied from 0.4 to 1000 L min^{-1}. The highest flow rates were applied to the modules with the largest membrane areas. Experiments in the modules with the greatest membrane area were restricted to $Q_L/A_{M\,int}$ values of less than 1.4 10^{-5} m s^{-1}, corresponding to NTU values greater than 4 and mass transfer efficiencies greater than 0.95. Under these conditions, the oxygen concentration at the outlet was close to equilibrium with the gas, resulting in low accuracy in estimating the mass transfer efficiency, $\eta_{O_2\,L}$.

The experimental value of oxygen pressure in the gas phase was estimated by assuming that the tangential value of oxygen concentration in the liquid phase, determined on the graphs given in [2] for very low $Q_L/A_{M\,int}$ values, was in equilibrium with the gas phase under vacuum. In Figure 3.7, the partial pressures obtained are compared with that estimated using the mass balance presented in Table 3.5. The agreement is good. However, the calculated pressures are slightly higher than the experimentally determined pressures. The discrepancy decreases with the increase of pressure. It may be due by the assumption of uniformity of gas composition in the model. Caution must be exercised, as the experimentally determined outlet oxygen pressure is not precise. Besides, the fact that the model's assumptions lead to a higher oxygen pressure, and therefore to less favorable transfer conditions, makes the model's estimates conservative. In the following, the oxygen pressures based on outlet concentrations were used to relate the recovery rate to the mass transfer efficiency.

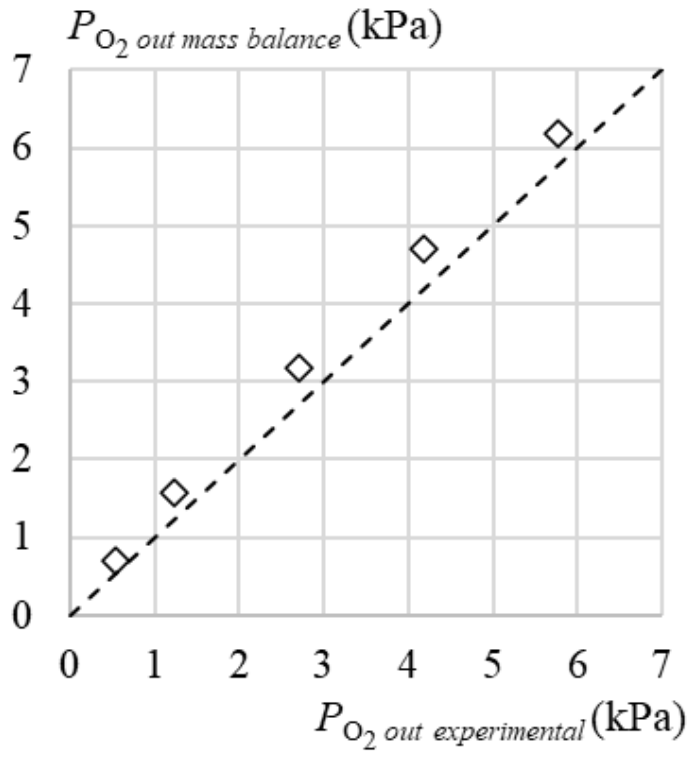

Figure 3.7: Parity plot comparing experimental oxygen outlet pressures [1] to that estimated using a mass balance; vacuum levels of 5.3, 8, 13.3, 18.6, and 24 kPa; 25°C.

In Figure 3.8, the values of the mass transfer efficiency, estimated using the experimental oxygen recovery rate and the experimental equilibrium oxygen vacuum pressure, are plotted as a function of the specific liquid flow rate, i.e. the ratio between the volumetric liquid flowrate and the internal membrane area. Vacuum model predictions are plotted as a solid line. It is interesting to note that the highest specific liquid flow rate studied in the PF-015PP and PF-030 modules was very low, at 1.39×10^{-5} m s^{-1}, leading to a mass transfer efficiency greater than 0.9. These low values are most likely due to pressure

drop constraints. As in Figure 3.3, illustrating the analysis of Liqui-Cel modules, the experimental values of the mass transfer efficiency obtained in SEPAREL modules with different membrane areas lie, at least approximately, on the same line. But the values based on experience are scattered. The dispersion of the data can be explained, at least in part, by the lack of precision when estimating the mass transfer efficiency with the data provided by the supplier's documents. Indeed, following its expression shown in Table 3.4, the estimation of the mass transfer efficiency involves the difference between the outlet concentration of the transferred species and its equilibrium concentration. The accuracy of this parameter is low when the outlet concentration is close to equilibrium. However, even for low mass transfer efficiencies, the Vacuum model seems to overestimate the values estimated using experiments.

To explain the difference between the predictions of the Vacuum model and the mass transfer efficiencies determined experimentally, a Gaussian distribution was considered for the internal fiber diameter. Indeed, a uniform distribution of fiber dimensions is assumed in the Vacuum model, but the data sheet for SEPAREL fibers indicates an external fiber diameter of between 180 and 240 µm and a membrane thickness of 35 µm. To take into account the heterogeneity of fiber diameters, a Gaussian distribution of fiber inner diameter with a mean value of 140 µm and a standard deviation of 15 µm was considered. The distribution of liquid flow was then estimated, assuming a uniform distribution of pressure drop. The resulting relationship between mass transfer efficiency and specific liquid flow is shown as a dotted line in Figure 3.8. This relationship better represents the average experimental results.

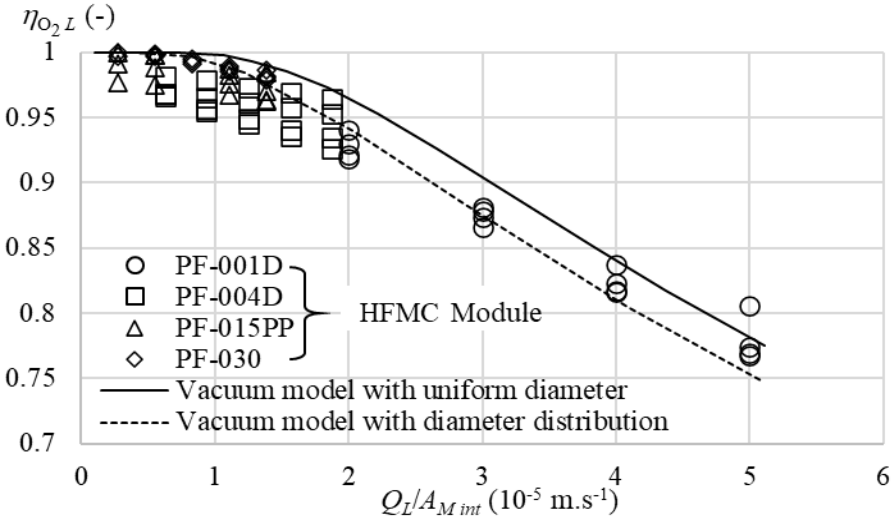

Figure 3.8 : Mass transfer efficiency as a function of the specific liquid flowrate, supplier data compared to the Vacuum model; vacuum levels of 5.3, 13.3, 18.6, and 24 kPa; 25°C; diameter distribution with a standard deviation of 15 µm.

In Figure 3.9, the Sherwood number characterizing oxygen mass transfer estimated using the experimental recovery rate and the Vacuum model given in Table 3.4 is plotted as a function of the specific liquid flow rate. In the same figure, the variation of the Sherwood number as a function of the specific liquid flow rate considering a fiber inner diameter of 140 µm or a Gaussian distribution of the fiber inner diameter with a mean value of 140 µm and a standard deviation of 15 µm are represented by a solid line and a dotted line respectively. Although the values are scattered, it can be seen that, if we consider a Gaussian distribution of fiber diameter, and for specific flow rates above 1.5×10^{-5} m s^{-1}, the Sherwood numbers calculated with the Vacuum model are close to those given by the Graetz correlation. For lower specific flow rates, the experimental values are lower than those predicted using the mass transfer correlation, but as mentioned, the precision involved in estimating the experimental Sherwood number is extremely low in this range. Interpreting the gap is therefore difficult.

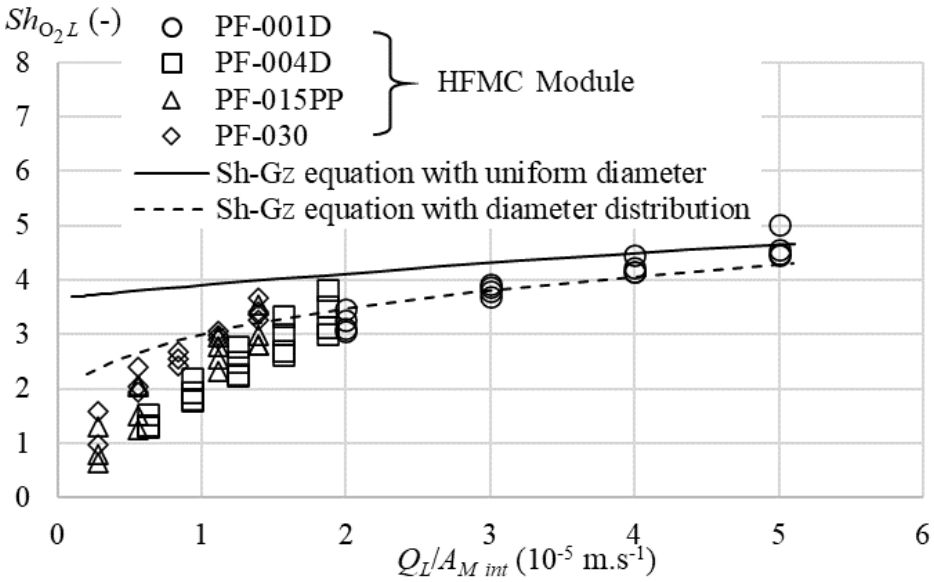

Figure 3.9: Sherwood number as a function of the specific liquid flow rate, Vacuum model using supplier data [2]; vacuum levels of 5.3, 13.3, 18.6, and 24 kPa; 25°C; comparison with Graetz correlation for a uniform diameter and a Gaussian diameter distribution

Although the experimental values are not known with great accuracy, it can be concluded that for specific flow rates higher than 1.5×10^{-5} m s^{-1} and for all applied vacuums, the Vacuum model correctly predicts the mass transfer efficiency obtained in the four SEPAREL modules if a diameter distribution is taken into account. In fact, the diameter distribution reduces the mass transfer efficiency compared with a uniform diameter, the latter leading to ideal plug flow.

3.4 Main findings and outlook

Liquid degassing in HFMC modules with lumen-side liquid flow and parallel gas flow can be described by a one-dimensional isothermal model approach. Due to the low solubility of gases, the dominant resistance to mass transfer is generally in the liquid phase. It can therefore be assumed that the overall mass transfer coefficient is equal to the liquid-side mass transfer coefficient. As the flow is always laminar, the latter can be estimated using a Sherwood-Graetz correlation.

In the contactor model, the liquid phase can be assumed to be in ideal plug flow or, if required, a lumen-side fiber diameter distribution can be applied. Depending on the mode of operation, vacuum or sweep gas stripping, the composition of the gas phase may be considered to be uniform or spatially distributed, the most favorable distribution for transfer being ideal counter-current plug flow. The actual distribution is almost certainly somewhere in between, particularly in combo mode, combining vacuum and sweep gas operation.

All contactor models lead to a relationship between mass transfer efficiency and the number of transfer units. In vacuum stripping, the mass transfer efficiency is generally not equal to the recovery rate of the target species. The relation between the two parameters is shown in Table 3.4. It involves the gas-side pressure of the target species. The latter can be estimated using a mass balance, which must include all the gases initially dissolved in the solvent, since they are stripped at the same time as the target species. The vacuum pressure must be regulated to obtain the desired recovery rate for a given mass transfer efficiency. In sweep gas operation, if assumed a counter-current plug flow for the gas phase and a sweeping gas that does not contain the target species at the inlet, the recovery rate is equal to the mass transfer efficiency. The flow rate of the sweep gas must be sufficiently high to enable the target species to be eliminated.

As shown in Table 3.8, following the definitions of the dimensionless numbers involved, it appears that the number of transfer units is proportional to the ratio between the Sherwood number and the Graetz number. Since the Sherwood number is correlated to the Graetz number, there is a relationship between the number of transfer units and the Sherwood number. Mass transfer efficiencies greater than 0.9 require a number of transfer units of about 4, which leads to fully developed concentration profiles in the fiber lumen and Sherwood and Graetz numbers of about 4. The value of the Sherwood number is close to its minimum, which indicates that the mass transfer is entirely dominated by diffusion. The Graetz number is proportional to the specific liquid flow rate, the inner fiber diameter and the inverse of the diffusion coefficient. So, for a given diffusion coefficient and fiber diameter, the Graetz number, and therefore the mass transfer efficiency, depend solely on the specific liquid flow rate.

The transfer models were validated using experimental data reported in the literature on the removal of dissolved oxygen and methane from water in commercial HFMC modules. Parameters that

varied included contactor geometry, operating temperature, initial liquid phase composition, liquid flow rate and vacuum pressure and, in combo mode, sweep gas flow rate. The influence of Gaussian diameter distribution on the mass transfer efficiency of HFMC has been demonstrated.

As the experiments aim to achieve high recovery rates and therefore high mass transfer efficiencies, the Sherwood numbers shown in Figures 3.3, 3.5, 3.6 and 3.9 are within a very narrow range. For instance, in vacuum stripping, in order to attain efficiencies comprised between 0.50 and 0.98, the NTU number must be comprised between 0.7 and 4.0, leading to Graetz numbers comprised between 21.3 and 4.0 and Sherwood numbers between 5.17 and 4.4. Experiments and theory are in good agreement.

One of the important operating costs of the degassing operation is the frictional pressure drop of the liquid phase. For a liquid flowing through the fiber lumen, it can be estimated using Hagen-Poiseuille's law. As shown in Table 3.9, for a given Sherwood and NTU numbers, the frictional pressure drop is proportional to the square of the fiber length and to the inverse of the inner fiber diameter raised to the power of four. The smaller the inner fiber diameter, the shorter the fibers must be in order to limit the frictional pressure drop. This constraint poses a serious problem for increasing the scale of the degassing operation, as it requires a large number of fibers in parallel. It explains the benefits of cross-flow design with external and radial liquid flow, as it reduces the length of the liquid path and therefore its pressure drop.

The model developed can be expressed to external liquid flow in HFMC modules designed for parallel or cross flow of the gas and liquid phases. For external liquid flow, the compacity of the fiber bundle is an important geometrical parameter, as it is related to the hydraulic flow diameter and therefore to the relation between the mass transfer coefficient and the Sherwood number. Unfortunately, the compacity is generally not known with good accuracy, which makes estimating the Sherwood number highly imprecise. More generally, a major limitation to the validation of any transfer model in HFMC degassing is related to the uncertainty that exists concerning the physico-chemical parameters of the systems, the geometric parameters characterizing the modules and, finally, the fluid distribution, which is not necessarily uniform. As the determination of transfer parameters using uncertain experimental values is somewhat hazardous, it is preferable, as proposed in this work, to use conservative predictive models based on general mass transfer correlations, without parameters regressed on the specific technology.

3.5 References

[1] 3M™ Liqui-Cel™ Membrane Contactors for Semiconductor and Microelectronics, (n.d.). https://www.3m.com/3M/en_US/liquicel-us/industries/semiconductor-and-microelectronics/ (accessed August 20, 2024).

[2] SEPAREL, DIC Corp. (n.d.). https://www.separel.com/en/products/water.html (accessed June 24, 2024).

[3] P. Velasco, V. Jegatheesan, K. Thangavadivel, M. Othman, Y. Zhang, A focused review on membrane contactors for the recovery of dissolved methane from anaerobic membrane bioreactor (AnMBR) effluents, Chemosphere 278 (2021) 130448. https://doi.org/10.1016/j.chemosphere.2021.130448.

[4] J. Cookney, A. Mcleod, V. Mathioudakis, P. Ncube, A. Soares, B. Jefferson, E.J. McAdam, Dissolved methane recovery from anaerobic effluents using hollow fibre membrane contactors, J. Membr. Sci. 502 (2016) 141–150. https://doi.org/10.1016/j.memsci.2015.12.037.

[5] I. Song, P.S. Soulia, P.J. Novak, W.A. Arnold, N.C. Wright, Dissolved gas recovery from water using a sidestream hollow-fiber membrane module: First principles model synthesis and steady-state validation, J. Membr. Sci. 689 (2024) 122134. https://doi.org/10.1016/j.memsci.2023.122134.

[6] E.L.H. Ng, K.K. Lau, W.J. Lau, F. Ahmad, Holistic review on the recent development in mathematical modelling and process simulation of hollow fiber membrane contactor for gas separation process, J. Ind. Eng. Chem. 104 (2021) 231–257. https://doi.org/10.1016/j.jiec.2021.08.028.

[7] Y. Han, X. Huang, Y. Lu, D. Zhu, X. Shi, Study of intrinsic oxygen mass transfer characteristic and model on polypropylene hollow fiber membrane contactor, Int. Commun. Heat Mass Transf. 121 (2021) 105045. https://doi.org/10.1016/j.icheatmasstransfer.2020.105045.

[8] X. Cao, H.-S. Lee, X. Feng, Extraction of dissolved methane from aqueous solutions by membranes: Modelling and parametric studies, J. Membr. Sci. 596 (2020) 117594. https://doi.org/10.1016/j.memsci.2019.117594.

[9] Z. Ren, Y. Yang, W. Zhang, J. Liu, H. Wang, Modeling study on the mass transfer of hollow fiber renewal liquid membrane: Effect of the hollow fiber module scale, J. Membr. Sci. 439 (2013) 28–35. https://doi.org/10.1016/j.memsci.2013.03.030.

[10] A. Ito, K. Yamagiwa, M. Tamura, M. Furusawa, Removal of dissolved oxygen using non-porous hollow-fiber membranes, J. Membr. Sci. 145 (1998) 111–117. https://doi.org/10.1016/S0376-7388(98)00068-4.

[11] E. Centeno Mora, C.A. de L. Chernicharo, Modelling and optimization of transverse flow hollow fibre membrane contactors for the recovery of dissolved methane from anaerobic effluents, Sep. Purif. Technol. 293 (2022) 121136. https://doi.org/10.1016/j.seppur.2022.121136.

[12] D. Albarracin-Zaidiza, B. Belaissaoui, S. Rode, Hybrid amine-based PCC processes, membrane contactors for PCC, in: Absorpt.-Based Post-Combust. Capture Carbon Dioxide, Elsevier, 2016: pp. 365–395. https://doi.org/10.1016/B978-0-08-100514-9.00015-9.

[13] M.-C. Yang, E.L. Cussler, Designing hollow-fiber contactors, AIChE J. 32 (1986) 1910–1916. https://doi.org/10.1002/aic.690321117.

[14] Evaluating the intensification potential of membrane contactors for gas absorption in a chemical solvent: A generic one-dimensional methodology and its application to CO2 absorption in monoethanolamine, J. Membr. Sci. 389 (2012) 1–16. https://doi.org/10.1016/j.memsci.2011.09.042.

[15] C. Gostoli, Recovery of Biosynthetic Products Using Membrane Contactors, in: H. Nakajima (Ed.), Mass Transf. - Adv. Asp., InTech, 2011. https://doi.org/10.5772/21345.

[16] S.M. Matson, V.P. Makrushin, I.S. Levin, N.A. Zhilyaeva, E.G. Litvinova, V.S. Khotimskiy, Structure and properties of poly(4-methyl-2-pentyne) synthesized with NbBr5 and TaBr5-based catalytic systems, Polymer 202 (2020) 122682. https://doi.org/10.1016/j.polymer.2020.122682.

[17] R. Jiménez-Robles, C. Gabaldón, V. Martínez-Soria, M. Izquierdo, Simultaneous application of vacuum and sweep gas in a polypropylene membrane contactor for the recovery of dissolved methane from water, J. Membr. Sci. 617 (2021) 118560. https://doi.org/10.1016/j.memsci.2020.118560.

[18] A.G. Novoselov, A.V. Chebotar, S.A. Sorokin, A.B. Duzhiy, I.G. Arendatelev, Oxygen diffusion in water. estimation of the coefficients of molecular diffusion, AIP Conf. Proc. 2486 (2022) 020016. https://doi.org/10.1063/5.0106867.

[19] R. Fernández-Prini, J.L. Alvarez, A.H. Harvey, Henry's Constants and Vapor–Liquid Distribution Constants for Gaseous Solutes in H2O and D2O at High Temperatures, J. Phys. Chem. Ref. Data 32 (2003) 903–916. https://doi.org/10.1063/1.1564818.

Chapter 4. Modeling Mass Transfer Efficiency in Shell-Side HFMC for Liquid Degassing

4.1 Introduction

Chapter 3 addressed lumen-side HFMC configurations modelling and the several key gaps in the existing literature by directly linking mass transfer efficiency (η_{iL}) to the liquid flow rate (Q_L) across the internal membrane area ($A_{M,int}$), and by predicting frictional pressure drops using Hagen–Poiseuille's law for the practical sizing of commercial modules such as Liqui-Cel. This chapter extends that framework to shell-side cross-flow configurations, prevalent in high-capacity commercial units like Liqui-Cel EXF and SEPAREL EF, where liquid flows transversely outside fibers.

A common HFMC degassing product line is Liqui-Cel™, manufactured by 3M [1]. Liqui-Cel™ contactors feature porous polypropylene membranes, in particular Celgard X-50 or X-40, which are supplied arranged as fiber mats. These mats consist of parallel hollow fibers that are connected by a polymer thread, with a mean external diameter of 300 μm and an internal diameter of the X-50 and X-40 fibers of respectively 220 and 200 μm. Membrane porosity is 0.4 and 0.25 respectively, and average pore size is 0.04 and 0.03 μm respectively. [2]. The fiber mat design facilitates the process of packing membranes in the contactor housings. Liqui-Cel™ modules are classified into different series, according to their geometrical characteristics.

The EXF series, or extra flow modules, are characterized by a special flow path design. A schematic view is shown in Figure 4.1. In these modules, the fiber mat is wrapped around an axial perforated tube distributing the liquid, with the fibers aligned parallel to the tube axis. This design is particularly advantageous for applications requiring high liquid flow rates. Notably, the EXF series includes a baffle, placed in the center of the liquid distribution and collection tube. The baffle divides the module into two compartments, directing the liquid towards the shell side of the fibers in the first compartment. The liquid then reaches the periphery of the fiber bundle, travels in the gap between the fiber bundle and the module wall and enters the second compartment. It then crosses again the fiber bundle and flows perpendicularly to the fibers towards the axial perforated tube, through which it exits the device. This configuration results in a liquid flow that is transverse to the lumen-side gas flow within each compartment.

Another important example of commercial HFMC modules is SEPAREL®, a product line developed by DIC Corporation. SEPAREL® modules are designed for a variety of applications, with a focus on ink degassing. They feature a unique hollow-fiber membrane structure, consisting of a porous substrate covered by a dense outer layer made from the same polymer. This design facilitates efficient gas transfer while ensuring good wetting resistance, making it highly effective for gas-liquid separation processes [3]. The SEPAREL® EF series modules, described in Figure 4.2, share a similar concept to that of Liqui-Cel™'s EXF series, with one major difference: the SEPAREL® EF series has no baffle inside the module. The membrane material is poly(4-methyl-1-pentene) (PMP), known for its excellent chemical resistance and mechanical stability. Technical specifications indicate that the hollow fibers in

these modules have external diameters ranging from 180 to 240 µm, with average external and internal diameters of 210 and 140 mm respectively, and a membrane thickness of 35 µm.

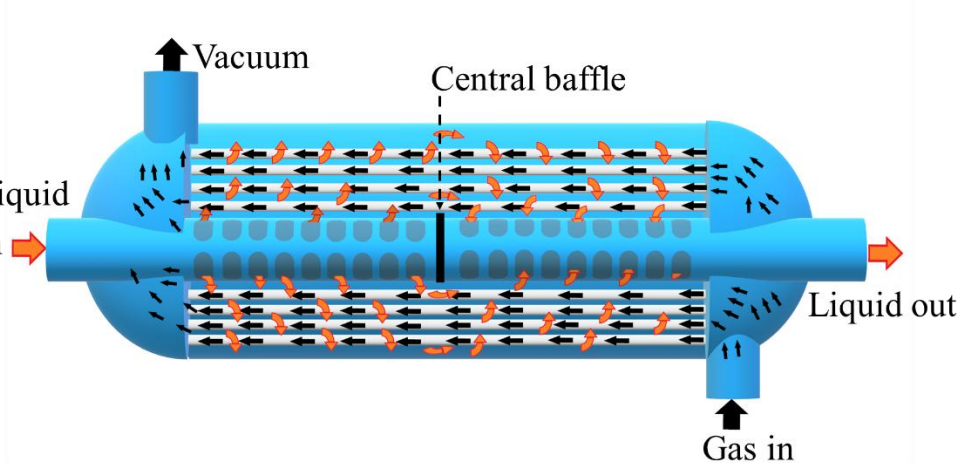

Figure 4.1: Schematic view of a Liqu-cel™ EXF module operated in combo mode

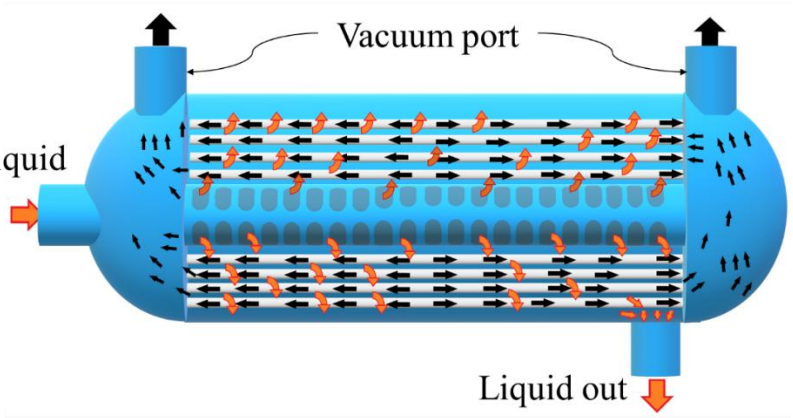

Figure 4.2: Schematic view of a SEPAREL® EF module operated in vacuum mode

In this chapter, degassing of liquids using hollow fiber membrane contactors (HFMC) operating in liquid -in-shell cross-flow is modelled. Vacuum and excess sweep gas operation modes are considered assuming ideal liquid plug flow and uniform gas composition. The model permits to relate the mass transfer efficiency to a number of transfer units. If the partial pressure of the striped species is not zero in the gas phase, the mass transfer efficiency differs from the recovery rate, the two parameters being linked by mass balances. The model allows to estimate mass transfer coefficients from recovery rate measurements. Based on these estimates, carried out for commercial HFMCs of various sizes, a new mass transfer correlation linking a Sherwood number and a cross-flow Graetz number is proposed. The system has few degrees of freedom. It's demonstrated for the first time that mass transfer efficiency can be expressed as a function of the fiber diameter, the diffusion coefficient of the stripped species, the liquid flow rate and the external membrane area. When expressed in this way, both the efficiency and the Sherwood number appear on a single curve, no matter the size of the device. HFMC sizing is thus simple. For example, vacuum stripping of oxygen in SEPAREL® EF modules can be done with an

efficiency of 0.98 for a ratio between the liquid flow rate and the external membrane area of 2.15 10^{-5} m^3_L s^{-1} $m^{-2}_{M\,ext}$. For a given efficiency, the liquid pressure drop can be controlled by adjusting the fiber bundle diameter.

This chapter is an adapted version of the manuscript under submission: Alhmiedy *et al*. (submitted 2025). A model for hollow fiber membrane contactors in degassing applications; part II: mass transfer correlation, pressure drop and sizing equations for liquid-in-shell cross-flow.

4.2 Mass transfer model of degassing in a cross-flow liquid-in-shell configuration

4.2.1 Short literature review of reactor models

The modelling of the stripping operation is aimed at relating operational and geometrical parameters to mass transfer efficiency. In this study, focus is exclusively put on cylindrical cross-flow configurations operating with liquid-in-shell flow, as this geometry and operating mode are prevalent in commercial HFMC modules. Liquid-in-lumen flow has been considered in a preceding paper [4]. The equations to be used are similar, but not identical.

Modeling degassing in HFMCs requires the knowledge of both the mass transfer area, which is proportional to the fiber volume, and the trans-membrane flux of stripped species. The latter depends on the transmembrane mass transfer coefficient and the mixing cup concentrations of the species in the liquid and gas phases. The mixing cup concentrations, the mass transfer coefficient and therefore the transmembrane flux are a priori spatially distributed over the volume of the fiber bundle. In order to estimate their spatial distribution, a hydrodynamic model of gas and liquid flow must be postulated. For each species, the total mass flow transferred from the liquid to the gas is estimated by integrating the local flux over the surface of the fibers, making it possible to estimate their recovery rate. Several approaches for modeling degassing in cylindrical cross-flow HFMC modules with liquid flow on the shell side have been published.

Simple empirical models rely on degassing experiments conducted under vacuum, sweep gas or combined mode. An isothermal system is generally considered. Ideal plug flow is assumed for the liquid phase. In vacuum degassing, the spatial distribution of the gas phase composition is assumed to be uniform. For degassing with excess sweep-gas, the concentration of the stripped species in the gas phase is set to zero. The resulting contactor model is one-dimensional and admits an analytical solution. Based on the measured recovery rate of the transferred species, an average overall mass transfer coefficient can be estimated. The average overall mass transfer coefficient is then correlated (i) to the geometry of the HFMC, i.e. fiber diameter or hydraulic diameter of the external flow, compacity of the fiber bundle (relative fiber volume) and, in some cases, length of the liquid flow path, (ii) to the physical characteristics of the system, i.e. liquid viscosity and diffusion coefficient of the stripped species, and

(iii) to the operating conditions, i.e. superficial or interstitial liquid flow velocity [5–8]. Typically, mass transfer correlations are expressed as a power law relationship between a Sherwood number, a Reynolds number and the cube root of the Schmidt number. Reynolds number power and pre-exponential factor are regressed. More than 30 correlations for the shell-side mass-transfer coefficient in cross-flow through HFMCs have been published using this methodology [7] [8].

When operating in sweep gas mode with moderate gas flow rates, corresponding to a partition ratio, λ_i, close to unity, the HFMC module exhibits two-dimensional concentration distributions in both the gas and the liquid phases, necessitating a two-dimensional reactor model for accurate description. In commercial applications, this operating condition is favorable, as it leads to low operating costs and high concentrations of the species removed in the sweep gas, which facilitates their subsequent recovery. Mora and Chernicharo [9] investigated the recovery of dissolved methane from anaerobic effluents in a Liqui-Cel™ EXF 2.5x8 module. They developed a two-dimensional finite element model to describe the recovery of dissolved methane under operating conditions leading to two-dimensional concentration distributions. As in the empirical models described above, the average overall mass transfer coefficient was fitted using experimentally obtained methane recovery rates.

4.2.2 The challenge of estimating the external mass-transfer coefficient

The main difficulty in modeling mass transfer operations within HFMCs with shell-side liquid flow lies in estimating the liquid-side mass transfer coefficient. As mentioned above, the prevalent approach in the literature consists in fitting very simple correlations between the Sherwood, the Reynolds and the Schmidt numbers to experimental data. However, this empirical methodology does not allow extrapolation to geometrical and hydrodynamic conditions beyond those investigated experimentally, thus limiting its applicability for HFMC scale-up studies.

Due to the complex geometry of the fiber bundle, the estimation of the liquid to fiber mass transfer coefficient is a three-dimensional problem requiring numerical resolution. The prevailing method for estimating the transfer coefficient through a numerical approach involves the assumption that the fibers are organized in a structured square or triangular lattice, akin to the design of shell-and tube heat exchangers. In addition to the spatial distribution of the fibers, the transfer coefficient depends on the boundary condition at the fiber surface. Two limiting boundary conditions are commonly used, uniform mass flux at the fiber surface or a uniform surface concentration. In the following, only solutions based on constant surface concentration conditions are discussed, as this boundary condition corresponds best to most of the degassing applications. Furthermore, the transfer coefficient also depends on the direction of liquid flow relative to the fibers, which can be axial, perpendicular or at an intermediate angle. It is noteworthy that given the heat/mass transfer analogy, Nusselt number data developed for flow through tube bundles can be directly adapted to estimate Sherwood numbers for analogous mass transfer

scenarios. A detailed literature review of modeling external transfer in fiber bundles is beyond the scope of the present paper. A short review is given in Cancilla *et al.* [10] and some relevant work is discussed hereunder.

4.2.3 Modelling of the external mass transfer coefficient in axial flow

A frequently proposed two-dimensional approach for estimating the mass transfer coefficient for shell-side axial flow is the equivalent annulus or Happel's free surface approximation, in which the flow takes place in a fictious annular duct bounded by a free surface, which approximates the actual polygonal area surrounding each fiber. As in the case of laminar flow in circular pipes, the mass transfer coefficient can be estimated by a relationship between the Sherwood number and the Graetz number, and, as in circular pipes, the Sherwood number tends towards a non-zero minimum asymptotic value for low Graetz numbers. The equivalent annulus model and corresponding Sherwood - Graetz correlations are described in detail by Gostoli [11]. For fiber bundle compacities lower than 0.45, the correlations give results that are comparable to those obtained through numerical simulations in regular triangular arrays. However, the authors point out that, for higher compacities, the discrepancy between this approach and numerical simulations becomes substantial.

Miyatake and Iwashita [12] numerically investigated convective heat transfer in the laminar flow regime for a fluid flowing axially between triangular square arrays of cylinders, with a uniform surface temperature boundary condition. The energy equation was solved using the finite difference method to determine the local temperature distributions, as well as local and logarithmic mean Nusselt numbers. Their results allowed deriving correlations for predicting the logarithmic mean Nusselt number as a function of the thermal Graetz number and σ, the lattice pitch (i.e. center-to-center distance between adjacent fibers) to fiber diameter ratio. In what follows, in order to limit the number of defined parameters, these equations are presented in terms of Sherwood number and material Graetz number of the liquid flow, considering that the liquid flow is external in the HFMC and applying the analogy between heat and mass transfer. Geometries, definition of the dimensionless numbers and the correlation developed by the authors for triangular arrays and compacities above 0.75 are reported in Table 4.1. The correlations established for other compacities and those established for square arrays can be found in the original paper [12].

In the region of low axial Graetz number, i.e. fully developed mass transfer region, the Sherwood number tends towards a non-zero minimum value. The variation of this minimum value is shown in Figure 4.3 as a function of compacity for triangular and square arrays. For the two geometries, the minimum Sherwood number increases with compacity. For triangular arrays it reaches a plateau value of around 10 for compacities between 0.6 and 0.8. For square arrays, the plateau value, attained for compacities above 0.3, is around 4.

The variation of the logarithmic mean Sherwood number with the axial Graetz number for triangular and square arrangements and different compacities estimated by the correlations developed in [12] is illustrated in Figure 4.4. In all cases, the Sherwood number increases with the axial Graetz number. For high compacities, the Sherwood - Graetz relation is found to be independent on the compacity.

As shown in Table 4.2, the axial Graetz number can be expressed as a function of the superficial axial liquid velocity. Moreover, it can be shown that it is proportional to the ratio between the liquid flowrate and the external membrane area.

Table 4.1: Geometries, definitions and correlations of external mass transfer in axial flow through regular arrays of cylinders [12]

Item considered	**Description or expression**
ANALYTICAL SYSTEMS	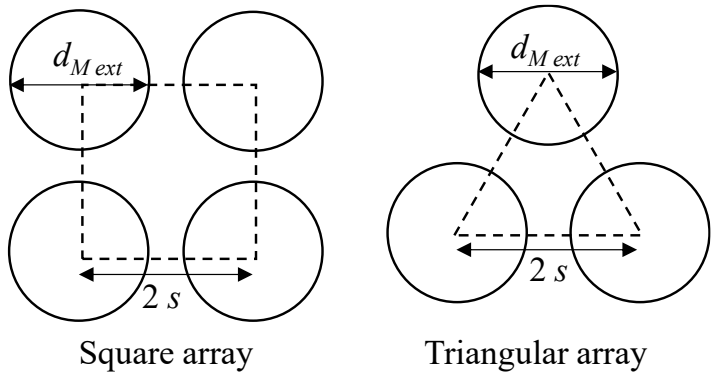
GEOMETRICAL PARAMETERS	Pitch to diameter ratio: $\sigma = \frac{2s}{d_{M\ ext}}$ Square array: $f = \frac{\pi d_{M\,ext}^2}{4\left(2s\right)^2} = \frac{\pi}{4\sigma^2}$ Triangular array: $f = \frac{\pi d_{M\,ext}^2}{8\sqrt{3}s^2} = \frac{\pi}{2\sqrt{3}\sigma^2}$ $d_{M\,ext}$ External fiber or cylinder diameter, m s Half pitch between the fibers, m σ Pitch to diameter ratio, - f Compacity of the fiber bundle, -

DIMENSIONLESS NUMBERS RELATED TO MASS TRANSFER	$Sh_{i\ L\ lm} \triangleq \frac{k_{i\ L\ lm} d_{M\ ext}}{D_{i\ L}}$ $Gz_{i\ L\ axial} \triangleq \frac{Q_{L\ per\ fiber}}{D_{i\ L} Z_{fb}}$ $Sh_{i\ L\ lm}$ Logarithmic mean Sherwood number for species *i* in the liquid, - $Gz_{i\ L\ axial}$ Graetz number for species *i* in the axial liquid flow, - $k_{i\ L\ lm}$ Logarithmic mean liquid side mass transfer coefficient of *i*, m s^{-1} $D_{i\ L}$ Diffusion coefficient of species *i* in the liquid, m^2 s^{-1} $Q_{L\ per\ fiber}$ Volumetric flow rate per fiber, m^3 s^{-1} Z_{fb} Fiber length in contact with the liquid flow, m
CORRELATION FOR A TRIANGULAR ARRAY WITH UNIFORM SURFACE CONCENTRATION	For $f > 0.75$ $\quad Sh_{i\ L\ lm} = 9.26(1 + 0.0179 Gz_{i\ L\ axial}^{1.46})^{0.25}$ $Sh_{i\ L\ lm}$ Logarithmic mean Sherwood number for species *i*, -

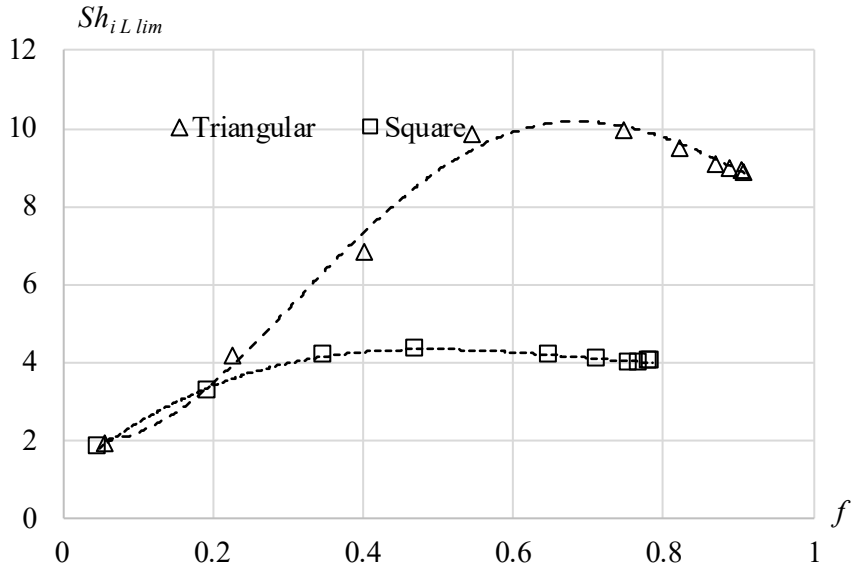

Figure 4.3 : Limiting Sherwood number for external parallel flow in regular fiber arrays as a function of array compacity [12]

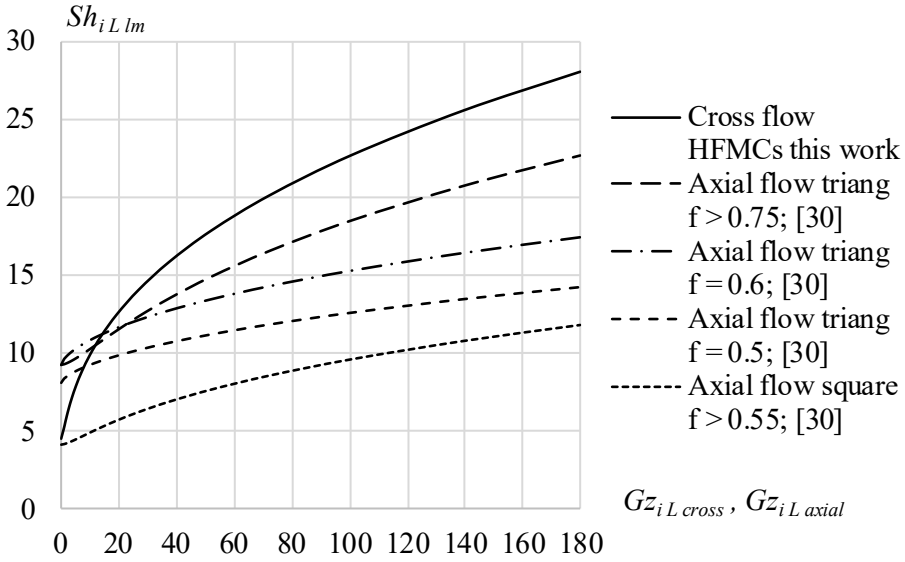

Figure 4.4: Correlation of the mean Sherwood number as a function of the Graetz number. Correlation established in this work for cross flow in commercial HFMCs and correlations of Mitayake for external axial flow in regular fiber arrays for different array geometries and compacities [12]

Table 4.2: Axial Graetz number as a function of axial liquid velocity and as a function of the ratio between liquid flow rate and external fiber area

Item considered	Expression
AXIAL GRAETZ NUMBER AS A FUNCTION OF THE SUPERFICIAL LIQUID VELOCITY AND THE LENGTH OF THE FLOW PATH	$u_{L\,axial} = \frac{Q_{L\,per\,fiber}}{\Omega_{tot\,per\,fiber}} = \frac{Q_{L\,per\,fiber}}{\Omega_{fiber}} \frac{\Omega_{fiber}}{\Omega_{tot\,per\,fiber}} = \frac{Q_{L\,per\,fiber}}{d_{M\,ext}^2} \frac{4}{\pi} f$ $Gz_{i\,L\,axial} = \frac{Q_{L\,per\,fiber}}{D_{i\,L} Z_{fb}} = \frac{u_{L\,axial} d_{M\,ext}^2}{D_{i\,L} Z_{fb}} \frac{\pi}{4f}$ $u_{L\,axial}$ Superficial axial liquid velocity, m s^{-1} Ω_{fiber} Fiber cross section, m^2 $\Omega_{tot\,per\,fiber}$ Total area perpendicular to the liquid flow direction, for a single fiber, m^2
AXIAL GRAETZ NUMBER AS A FUNCTION OF THE RATIO BETWEEN THE LIQUID FLOW RATE AND THE EXTERNAL MEMBRANE AREA	$Q_L = u_{L\,axial} \Omega_{tot}$ $A_{M\,ext} = \frac{4 V_{fb} f}{d_{M\,ext}} = \frac{4 \Omega_{tot} Z_{fb} f}{d_{M\,ext}}$ $Gz_{i\,L\,axial} = \frac{u_{L\,axial} d_{M\,ext}^2}{D_{i\,L} Z_{fb}} \frac{\pi}{4f} = \pi \frac{Q_L d_{M\,ext}}{A_{M\,ext} D_{i\,L}}$ Q_L Overall liquid flow rate, $m^3\,s^{-1}$ Ω_{tot} Total area of the fiber bundle perpendicular to the liquid flow direction, m^2 $A_{M\,ext}$ Overall external membrane area, m^2 V_{fb} Volume of the fiber bundle, m^3

Bao and Lipstock [13] investigated fully-developed mass transfer in axial flow through regular arrays as well as through randomly packed fiber bundles with a constant surface concentration boundary condition. The results obtained in regular arrays were consistent with the limiting Sherwood numbers reported by Miyatake and Iwashita [12]. In randomly packed fiber bundles, the authors showed that mass transfer rates are controlled by the lowest fiber packing regions through which most of the flow occurs (flow channeling). For this reason, the limiting Sherwood number can decrease dramatically. The authors indicate that adding structure to the bundle, for example by weaving fibers to mats, helps to increase the limiting Sherwood number.

4.2.4 Modelling of the external mass transfer coefficient in cross-flow

Few studies deal with the modelling of the external mass transfer coefficient in cross-flow through fiber bundles [10]. Cancilla *et al.* [14] performed numerical simulations for fully developed mass transfer in steady-state laminar flow through regular triangular and square arrays of cylinders. As in the paper of Bao and Lipstock [13], the authors have estimated the limiting value of the Sherwood number for fully developed concentration profiles. For all simulations, the compacity was set to 0.5. Reynolds numbers were defined with the superficial flow velocity and the hydraulic diameter of the external flow section. The compacity was set to 0.5, so that the hydraulic diameter is equal to the outer fiber diameter. Reynolds numbers ranging from 10^{-4} to 10^{2} were studied. Axial flow, cross-flow and combinations were considered.

The concentration fields in cross-flow configurations exhibit significantly greater complexity compared to those observed in axial flow. The limiting value of the Sherwood number depends on the flow angle of attack of the regular lattice and increases with the Reynolds number. For Reynolds number value between 0.05 and 50, which are typical for degassing applications, the angle-averaged limiting Sherwood numbers for cross-flow in triangular and square arrays show similar values. Its value is about 9 for a Reynolds number of 0.01 (Figure 4.8 of [14]), which is higher than for axial flow. The value of the limiting Sherwood number increases with Reynolds number, making the cross-flow configuration even more favorable. When the average flow direction is intermediate between axial and cross flow, the limiting Sherwood number settles at the higher value between the limiting Sherwood number in purely transverse flow and that in purely axial flow [14].

Based on simulations made conducted with a square array at a Reynolds number of about 3, Cancilla *et al.* [14] report that mass transfer enhancement due to entrance effects in cross-flow is predicted fairly well by the equations derived for straight channels with uniform cross section. To the best of the author's knowledge, there are no detailed numerical studies of mass transfer in cross-flow under entrance conditions, in which concentration profiles are not fully developed.

4.2.5 Estimation of the external mass transfer coefficient in cross-flow through commercial HFMCs

The mean external mass transfer coefficient for transverse flow through commercial HFMCs is expressed in this work using a new correlation, established by a best fit to experimental mass-transfer coefficients, the estimation of which is described in Section 3. The choice of the mathematical form of the mass transfer correlation is based on the paper of Cancilla *et al*. [14], where the authors have shown that the developing Sherwood number profile in the entrance zone of the fiber bundle is similar in both cross and axial flow.

The correlation reported in Table 4.3 was obtained by regressing the experimental values shown in Section 3 (Fig. 4.6, 4.7 and 4.10), using a nonlinear generalized reduced gradient method. Its mathematical form is identical to that of the correlation presented in the last line of Table 4.1, proposed by Miyatake and Iwashita [12] for external axial flow in triangular arrays with uniform surface concentration and compacities above 0.75. The exponents of the correlation established in this work, i.e. 1.46 and 0.25, are identical to those of the correlation established by Miyatake and Iwashita [12]. However, the proportionality factors, before the brackets and between the brackets, are different, i.e. 4.5 instead of 9.26 and 0.775 instead of 0.0179. Moreover, the cross-flow Graetz number used in the present correlation is defined with respect to the logarithmic mean superficial transverse liquid velocity, $u_{L\,cross\,lm}$. For the sake of simplicity, the subscript '*lm*', indicating a logarithmic mean value for the transfer coefficient and Sherwood number will be omitted hereafter. As discussed in Section 3, this correlation exhibits a good predictive capability for experimental degassing efficiencies in commercial HFMCs of various geometries and sizes.

As demonstrated in Table 4.3, the cross-flow Graetz number is proportional to the ratio of the liquid flowrate to the external membrane area. It is moreover proportional to the ratio of the arithmetic to the logarithmic mean diameter of the fiber bundle, which is typically between 1.05 and 1.08. Interestingly, when expressed as a function of volumetric flowrate and external membrane area, the definition of the cross-flow Graetz number is very close to that of the axial-flow Graetz number, shown in Table 4.2. Finally, it should be noted that the definition of the cross-flow Graetz number takes into account the eventual presence of a central baffle, which results in an increase in the surface velocity of the liquid passing through the fiber bundle.

Table 4.3: Correlation of the external mass transfer coefficient in cross-flow

Item considered	Expression
MASS TRANSFER CORRELATION ESTABLISHED IN THIS WORK FOR EXTERNAL CROSS-FLOW IN COMMERCIAL HFMCS	$Sh_{i\,L\,lm} = Sh_{i\,L} = 4.5(1+0.775Gz_{i\,L\,cross}^{1.46})^{0.25}$ $Sh_{i\,L\,lm} \triangleq \frac{k_{i\,L\,lm} d_{M\,ext}}{D_{i\,L}}$ $Gz_{i\,L\,cross} = \frac{u_{L\,cross\,lm} d_{M\,ext}^2}{D_{i\,L}} \frac{2}{\left(D_{fb\,ext} - D_{fb\,int}\right)} \frac{\pi}{4f}$ $u_{L\,cross\,lm} = \frac{Q_L}{\Omega_{tot\,lm}} = \frac{Q_L}{\pi D_{fb\,lm}} \frac{(N_b+1)}{Z_{fb}}$ $D_{fb\,lm} = \frac{D_{fb\,ext} - D_{fb\,int}}{ln\left(\frac{D_{fb\,ext}}{D_{fb\,int}}\right)}$ $u_{L\,cross\,lm}$ Logarithmic mean superficial radial liquid velocity, m s^{-1} $\Omega_{tot\,lm}$ Logarithmic mean total area perpendicular to the liquid flow direction, which is transverse to the fiber axis, m^2 $D_{fb\,ext}$ External diameter of the fiber bundle, m $D_{fb\,int}$ Internal diameter of the fiber bundle, m $D_{fb\,lm}$ Logarithmic mean diameter of the fiber bundle, m N_b Number of baffles in the HFMC, -
CROSS-FLOW GRAETZ NUMBER AS A FUNCTION OF THE RATIO BETWEEN THE LIQUID FLOWRATE AND THE EXTERNAL MEMBRANE AREA	$A_{M\,ext} = \frac{4V_{fb}f}{d_{M\,ext}} = \frac{\pi\left(D_{fb\,ext}^2 - D_{fb\,int}^2\right)}{d_{M\,ext}} Z_{fb} f$ $V_{fb} = \frac{\pi\left(D_{fb\,ext}^2 - D_{fb\,int}^2\right)}{4} Z_{fb}$ $D_{fb\,am} = \frac{\left(D_{fb\,ext} + D_{fb\,int}\right)}{2}$ $Gz_{i\,L\,cross} = \pi(N_b+1) \frac{Q_L}{A_{M\,ext}} \frac{d_{M\,ext}}{D_{i\,L}} \frac{D_{fb\,am}}{D_{fb\,lm}}$ $D_{fb\,am}$ Arithmetic mean diameter of the fiber bundle, m

4.2.6 Resistances in series model to estimate the overall mass transfer coefficient in a HFMCs

The principle of the resistances in series model for the estimate of an overall mass transfer coefficient in HFMCs in steady state operation has been described in detail in Section 2.1 of a preceding paper [4]. Gas-filled porous membranes with or without dense skin layers can be addressed. Figure 4.5 illustrates the flow directions and the concentration profiles in a Liqui-Cel™ EXF geometry operated in

combo mode. Mass diffusion occurs from the liquid phase in the shell to the gas phase in the fiber lumen. The direction of mass transfer is thus opposite to that occurring in HFMC stripping with liquid in lumen flow discussed in [4]. Notations and definitions relative to the resistance in series model are reported in Table 4.4.

Table 4.5 shows the relation between the molar flux of species i, N_i, the gas and liquid mixed cup concentrations, $C_{i,G}$ and $C_{i,L}$, the volumetric partition coefficient, m_i, and the overall liquid side mass transfer coefficient $K_{i\,OL}$. The molar flux is expressed with respect to the membrane-liquid interface, which corresponds to the external fiber area. The relationship between the partial mass transfer coefficients in the four domains and their corresponding mass transfer resistances is detailed.

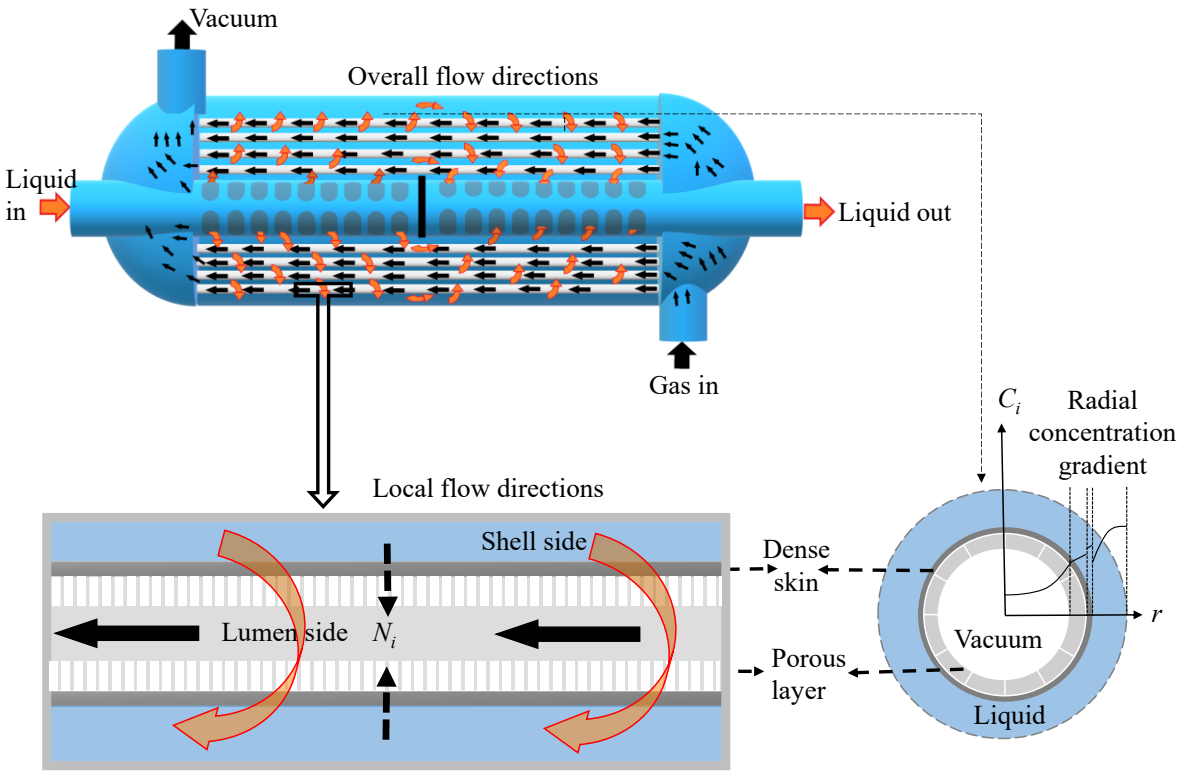

Figure 4.5: Flow directions and concentration gradients for liquid-in shell cross-flow in combo mode

Table 4.4: Notations and definitions relative to the resistance in series model

Domain	Characteristic diameter, m	Local volumetric mass transfer coefficient, m s^{-1}	Mass transfer resistance, s m^{-1}
LIQUID PHASE	$d_{M\,ext}$	$k_{i\,L}$	$R_{i\,L}=\frac{1}{k_{i\,L}}$
EXTERNAL DENSE SKIN LAYER	$d_{M\,lm\,d}\cong d_{M\,ext}$	$k_{i\,M\,d}$	$R_{i\,M\,d}=\frac{m_i}{k_{i\,M\,d}}$
POROUS SUPPORT	$d_{M\,lm\,p}\cong\frac{d_{M\,ext}-d_{M\,int}}{\ln\left(d_{M\,ext}/d_{M\,int}\right)}$	$k_{i\,M\,p}$	$R_{i\,M\,p}=\frac{d_{M\,ext}}{d_{M\,lm\,p}}\frac{m_i}{k_{i\,M\,p}}$
GAS PHASE	$d_{M\ int}$	$k_{i\,G}$	$R_{i\,G}=\frac{d_{M\,ext}}{d_{M\,int}}\frac{m_i}{k_{i\,G}}$

N.B.: The symbols are defined in the nomenclature.

Table 4.5: Overall mass transfer coefficient and additivity of the partial resistances

Item considered	Expression
OVERALL MASS FLUX OF SPECIES *i* WITH RESPECT TO THE GAS-LIQUID INTERFACE WHICH CORRESPONDS TO THE EXTERNAL, MEMBRANE AREA	$N_i=K_{i\,OL}(C_{i\,L}-m_iC_{i\,G})$ $m_i \triangleq \frac{C_{i\,L}}{C^*_{i\,G}}$ Ratio of molar equilibrium concentrations of species *i* N_i Molar flux of species *i*, with respect to the external membrane area $\mathrm{mol_i\ m_{M\,ext}^{-2}\ s^{-1}}$ m_i Volumetric partition coefficient of species *i*, $\mathrm{m_G^3 m_L^{-3}}$ $C_{i\,L}$ Liquid mixed cup molar concentration of species *i*, $\mathrm{mol_i m_L^{-3}}$ $C_{i\,G}$ Gas mixed cup molar concentration of species *i*, $\mathrm{mol_i m_G^{-3}}$ $C^*_{i\,G}$ Gas molar concentration of species *i* in equilibrium with $C_{i\,L}$, $\mathrm{mol_i m_G^{-3}}$ $K_{i\,OL}$ Overall volumetric liquid-side mass transfer coefficient of *i*, $\mathrm{m_L^3 m_{M\,ext}^{-2} s^{-1}}$
OVERALL LIQUID SIDE VOLUMETRIC MASS TRANSFER COEFFICIENT	$\frac{1}{K_{i\,OL}}=\frac{1}{k_{i\,L}}+\frac{m_i}{k_{i\,M\,d}}+\frac{d_{M\,ext}}{d_{M\,lm\,p}}\frac{m_i}{k_{i\,M\,p}}+\frac{d_{M\,ext}}{d_{M\,int}}\frac{m_i}{k_{i\,G}}$
OVERALL MASS TRANSFER RESISTANCE	$R_{i\,OL}=R_{i\,L}+R_{i\,M\,d}+R_{i\,M\,p}+R_{i\,G}$

The equations employed to estimate the mass transfer coefficients in the different domains are presented in Table 4.6. The estimation of fluid-membrane mass transfer coefficients is done through the modeling of liquid and gas flows. Laminar flow is considered in both the fiber lumen and the shell. The shell-side mass transfer coefficient is estimated by the correlations presented in Table 4.3. The lumen-side mass transfer coefficient is estimated using a Sherwood – Graetz correlation, given by Gostoli [11] and shown in Table 4.6. The estimation of the mass transfer coefficient in the porous membrane is accomplished by means of a pore diffusion model. A solution-diffusion model is employed to describe the mass transfer in the dense skin. These relations are representative of the current understanding of mass transfer in porous and dense membranes.

The expressions for the ratios of the gas and membrane transfer resistances to the liquid transfer resistance are presented in Table 4.7. The values of these ratios are determined by employing typical values for the physical and geometrical system parameters. For partition coefficients, mi, approaching or falling below unity, the resistance ratios are consistently less than one. This indicates that the majority of mass transfer resistance originates from the liquid phase.

Table 4.6: Mass transfer coefficient estimates in the different domains in HFMCs

Item considered	Expression
LIQUID-SIDE MASS TRANSFER CORRELATION FOR EXTERNAL CROSS-FLOW ESTABLISHED IN THIS WORK	$Sh_{i\,L} = 4.5(1+ 0.775Gz_{i\,L\,cross}^{1.46})^{0.25}$
GAS-SIDE MASS TRANSFER CORRELATION FOR CONFINED LAMINAR PIPE FLOW WITH UNIFORM WALL CONCENTRATION [11]	$Sh_{i\,G} = ((3.66)^3 + 4.21Gz_{i\,G})^{1/3}$ $Sh_{i\,G} \triangleq \frac{k_{i\,G} d_{M\,int}}{D_{i\,G}}$ $Gz_{i\,G} \triangleq \frac{u_G d_{M\,int}^2}{D_{i\,G} Z_{fb}}$ $Sh_{i\,G}$ Average Sherwood number for species *i* in the gas, - $Gz_{i\,G}$ Graetz number for species *i* in the gas, - $k_{i\,G}$ Volumetric gas side mass transfer coefficient of *i* , m s^{-1} $D_{i\,G}$ Diffusion coefficient of species *i* in the liquid u_G Average flow velocity of the gas through the fiber lumen, m s^{-1}
MASS TRANSFER COEFFICIENT OF POROUS SUPPORT: PORE DIFFUSION MODEL	$k_{i\,M\,p} = \frac{\varepsilon_M D_{i\,G\,pore}}{\tau_M \delta_{M\,p}}$ $D_{i\,G\,pore} = \frac{1}{1/D_{i\,G} + 1/D_{i\,G\,Knudsen}}$

	$D_{i\,G\,Knudsen} = \frac{2d_{pore}}{3}\sqrt{\frac{RT}{\pi M_{mol\,i}}}$
	$\delta_{M\,p} \cong \frac{d_{M\,ext} - d_{M\,int}}{2}$
	$\delta_{M\,p}$ Thickness of the porous membrane, m
	ε_M Membrane porosity, -
	τ_M Membrane tortuosity, -
MASS TRANSFER COEFFICIENT WITHIN THE DENSE LAYER: SOLUTION-DIFFUSION APPROACH	$k_{i\,M\,d} = \mathcal{P}_i \frac{RT}{\delta_{M\,d}}$
	$\delta_{M\,d}$ Thickness of the dense layer, m
	$\mathcal{P}_i$ Membrane Permeability, mol m^{-1} s^{-1} Pa^{-1}
	R Ideal gas constant, Pa m^3 mol^{-1} K^{-1}
	T Temperature, K

Table 4.7: Ratios of the mass transfer resistances in HFMCs for typical parameter values

Considered ratio	Expression	Typical Range
GAS SIDE OVER LIQUID SIDE	$\frac{R_{i\,G}}{R_{i\,L}} = m_i \frac{Sh_{i\,L}}{Sh_{i\,G}} \frac{D_{i\,L}}{D_{i\,G}}$	$\frac{R_{i\,G}}{R_{i\,L}} \cong m_i \times 3 \times 10^{-4}$
POROUS MEMBRANE OVER LIQUID SIDE	$\frac{R_{i\,M\,p}}{R_{i\,L}} = \frac{d_{M\,ext}}{d_{M\,p\,lm}} \frac{m_i k_{i\,L}}{k_{i\,M\,p}} \cong m_i Sh_{i\,L} \frac{RMT}{(2 - RMT)} \frac{\tau_M}{\varepsilon_M} \frac{D_{i\,L}}{D_{i\,G\,pore}}$ $RMT = \frac{2\delta_M}{d_{M\,ext}} = \frac{d_{M\,ext} - d_{M\,int}}{d_{M\,ext}}$	$\frac{R_{i\,M\,p}}{R_{i\,L}} \cong m_i \times 0.02$
DENSE SKIN OVER LIQUID SIDE	$\frac{R_{i\,M\,d}}{R_{i\,L}} = m_i \frac{k_{i\,L}}{k_{i\,M\,d}} = m_i \frac{\delta_{M\,d}}{d_{M\,ext}} \frac{Sh_{i\,L} D_{i\,L}}{\mathcal{P}_i RT}$	$\frac{R_{i\,M\,d}}{R_{i\,L}} \cong m_i \times 0.11$
TYPICAL VALUES OF THE PARAMETERS	$D_{i\,G} \cong 2 \times 10^{-5}\,m^2 s^{-1}$; $D_{i\,L} \cong 2 \times 10^{-9}\,m^2 s^{-1}$; $\tau_M \cong 2$; $Sh_{i\,L} \cong 15$; $Sh_{i\,G} \cong 5$ Liqui-Cel™ Celgard X-40 PP fibers: $d_{M\,ext}$ = 300 µm, $d_{M\,int}$ = 200 µm RMT = 0.33 ; $\varepsilon_M = 0.25$; d_{pore} = 0.03 µm $D_{i\,G\,pore} \cong 3 \times 10^{-6}\,m^2 s^{-1}$ [2] SEPAREL® PMP asymmetric fibers: $d_{M\,ext}$ = 210 µm, $d_{M\,int}$ = 140 µm, $\delta_{M\,d} \cong 1\,\mu m$ RMT = 0.33 no information about membrane porosity and pore diameter $1050 < \mathcal{P}_{O_2}(PMP) < 2250$ barrer (at 25 °C) [15], 1 barrer = 3.35 10^{-16} mol $m^{-1} s^{-1} Pa^{-1}$	

4.2.7 HFMC model for degassing in vacuum mode and in excess sweep gas mode

In the following, only operating modes and conditions leading to a one-dimensional reactor model, i.e. vacuum stripping and excess sweep gas vacuum or combo stripping are addressed. Isothermal laminar gas and liquid flow and ideal plug flow of the liquid are assumed. This assumption was confirmed (see chapter 5). Unvarying liquid volumetric flow rates and isobaric conditions on the gas side are considered. These assumptions collectively lead to constant volumetric gas-liquid partition coefficients. Furthermore, an average overall mass transfer coefficient is employed for every species, and this coefficient is estimated by considering solely the liquid side mass transfer.

In vacuum stripping, the gas flow is solely due to mass transfer of stripped gases and solvent vapor through the membrane. The outlet gas phase composition is related to these phenomena. The pressure drop in the gas phase is considered to be low, leading to uniform pressure and thus a uniform gas composition. Conversely, in excess sweep gas stripping, characterized by partition ratios far over unity, the gas phase concentration of stripped species can be neglected. In the context of high vacuum conditions, the HFMC model of vacuum stripping reduces to that of excess sweep gas, as the partial pressures of the stripped species become negligible.

The mass transfer model employed for both vacuum and excess sweep gas stripping is outlined in Table 4.8. The liquid side differential mass balance is formulated using the aforementioned assumptions. It is integrated over the contactor volume. The model establishes a relationship between two dimensionless numbers, transfer efficiency, $\eta_{i\,L}$, and number of transfer units, $NTU_{i\,OL}$. In general, The efficiency differs from the species recovery rate, RR_{iL}, the definition of which is given in Table 4.8. Efficiency and recovery rate are identical only when the species gas phase concentration is zero as it is the case in excess sweep gas stripping and in combo mode with excess sweep gas. However, this is not generally the case for vacuum stripping. Indeed, low gas phase concentrations of stripped species would necessitate high vacuum values and high volumetric gas flow rates, resulting in high vacuum power.

Table 4.8: Mass transfer model for vacuum stripping and stripping with excess sweep gas in HFMCs

Item considered	Definition or expression
LIQUID PHASE DIFFERENTIAL MASS BALANCE ON SPECIES *i*	$Q_L \, \mathrm{d}C_{i\,L} = -K_{i\,OL}\left(C_{i\,L} - m_i C_{i\,G\,out}\right) a_{M\,ext} \, \mathrm{d}V_{fb}$ $a_{M\,ext} = \dfrac{4f}{d_{M\,ext}}$ with $K_{i\,OL} = K_{i\,OL\,lm} = k_{i\,L\,lm}$ $a_{M\,ext}$ Specific shell-side membrane area, $m^2\ m^{-3}{}_{fb}$ $\mathrm{d}V_{fb}$ Fiber bundle differential volume, m^3 The subscripts *in* and *out* stand for concentrations at the contactor inlet and outlet. The liquid phase is considered to be in ideal plug flow. The composition of the gas is considered uniform and equal to the outlet composition.
LIQUID SIDE NUMBER OF TRANSFER UNITS, EXTERNAL MEMBRANE AREA	$NTU_{i\,OL} \triangleq \frac{K_{i\,OL} A_{M\,ext}}{Q_L}$ $A_{M\,ext} = a_{M\,ext} V_{fb}$
LIQUID SIDE MASS TRANSFER EFFICIENCY	$\eta_{iL} \triangleq \dfrac{\text{flux of } i \text{ transferred to the gas}}{\text{Maximum transferable flux of } i\text{, equilibrium at the outlet}}$ $\eta_{iL} = \dfrac{A_{M\,ext} Q_L \left(C_{i\,L\,in} - C_{i\,L\,out}\right)}{A_{M\,ext} Q_L \left(C_{i\,L\,in} - m_i C_{i\,G\,out}\right)} = \dfrac{C_{i\,L\,in} - C_{i\,L\,out}}{C_{i\,L\,in} - m_i C_{i\,G\,out}}$
INTEGRATION OF THE MASS BALANCE OVER THE CONTACTOR VOLUME	$\ln\left(\dfrac{C_{i\,L\,out} - m_i C_{i\,G\,out}}{C_{i\,L\,in} - m_i C_{i\,G\,out}}\right) = -NTU_{i\,OL}$ Thus $\eta_{iL} = 1 - \exp\left(-NTU_{i\,OL}\right)$
IDEAL GAS LAW	$C_{iG} = \dfrac{P_{i\,vac}}{RT}$
RECOVERY RATE OF THE TRANSFERRED SPECIES AND RELATION WITH THE MASS TRANSFER EFFICIENCY	$RR_{i\,L} \triangleq \frac{Q_L\,(C_{iL\,in} - C_{iL\,out})}{Q_L\,C_{iL\,in}} = \frac{C_{iL\,in} - C_{iL\,out}}{C_{iL\,in}}$ $RR_{i\,L} = \eta_{iL}\left(1 - \dfrac{P_{ivac}}{RT}\dfrac{m_i}{C_{i\,L\,in}}\right)$
CASE OF EXCESS SWEEP GAS STRIPPING	$P_{ivac} = 0$ leading to $\eta_{iL} = 1 - \exp\left(-NTU_{i\,OL}\right)$ with $\eta_{iL} = RR_{i\,L}$

The equations permitting to estimate the gas flow rate and composition in the vacuum stripping of multi-component mixtures is shown in Table 4.9. They are identical to those described in [4], where the interested reader might find more explanations. The selection of vacuum pressure is paramount in achieving the targeted gas-side concentration of species *i*, thereby ensuring the attainment of the desired recovery rate within the confines of the attainable thermodynamic efficiency.

Table 4.9: Gas flow rate and composition in the vacuum stripping of multi-component mixtures

Item considered	Expression
MASS BALANCE FOR THE TRANSFERRED GASES AND RESULTING MOLAR OUTLET GAS CONCENTRATION	$Q_{G\,out} C_{i\,G\,out} = Q_L \left(C_{i\,L\,in} - C_{i\,L\,out} \right) = Q_L \eta_{i\,L} \left(C_{i\,L\,in} - m_i C_{i\,G\,out} \right)$ Thus $C_{i\,G\,out} = \frac{P_{i\,vac}}{RT} = \frac{\left(Q_L / Q_{G\,out} \right) \eta_{iL} C_{iL\,in}}{1 + \left(Q_L / Q_{G\,out} \right) m_i \eta_{iL}}$ $Q_{G\,out}$ Gas phase volumetric outlet flow rate, $m^3\ s^{-1}$
TOTAL AND PARTIAL PRESSURES OF THE SPECIES IN THE GAS OUTLET	$P_{vac} = P_{solvent}^{sat} + \sum_{i=1}^{N} P_{i\,vac} = P_{solvent}^{sat} + RT \frac{Q_L \eta_L}{Q_{G\,out}} \sum_{i=1}^{N} \frac{C_{i\,L\,in}}{1 + m_i \frac{Q_L \eta_L}{Q_{G\,out}}}$ P_{vac} Vacuum pressure, Pa An identical thermodynamic efficiency, η_L, is assumed for all the species transferred.

4.2.8 Appropriate operating condition of HFMC vacuum and excess sweep gas stripping and comparison with liquid in lumen configuration

The mass transfer model permits to relate the number of transfer units to the mass transfer efficiency. For example, $NTU_{i\,OL} = 4$ leads to $\eta_{i\,L} = 0.98$. As detailed in Table 4.10, the Graetz number is related to the ratio between the Sherwood number and the number of transfer units. Since the Sherwood number itself is correlated to the Graetz number, a relation between the number of transfer units and the Graetz number can be established. For example, $NTU_{i\,OL} = 4$ leads to a Graetz number of 7.7 in the SEPAREL® EF devices and 22.3 in the Liqui-Cel™ EXF devices. The values of the resulting Sherwood numbers are 9.0 and 13.2 respectively. Knowing the values of both the number of transfer units and the Sherwood number allows for the estimation of the ratio between the volumetric liquid flow rate and the external membrane area. Values estimated for water deoxygenation using commercial fibers are presented in Table 4.10 for the two product lines of HFMC degassing devices. The external membrane area needed to deoxygenate a flow rate of 1 $m^3\ h^{-1}$ with an efficiency of 0.98, is around 12.8 m^2 for both devices.

The modelling of stripping in lumen-side liquid flow has been described in [4]. For a given fiber volume, the appropriate liquid flow rate to achieve a given mass transfer efficiency in shell side liquid cross flow configuration can be compared to that, appropriate to achieve the same efficiency in a lumen-side liquid flow configuration. The ratio of these flow rates is shown in the last line of Table 4.10. It turns out that, for the two product ranges studied, SEPAREL® EF and Liqui-Cel™ EXF, this ratio is 2.30 and 3.56 respectively. The values of the ratio are in accordance with the three-fold increase of liquid flow rate mentioned by [16] for the Liqui-Cel™ EXF 4x13 module in comparison to liquid in lumen configurations with the same fiber volume.

Table 4.10: Appropriate operating conditions of HFMC stripping operations in liquid in shell cross-flow and comparison with liquid in lumen flow

Item considered	Expression
RELATION BETWEEN THE SPECIFIC FLOW RATE, $Sh_{i\,L}$ AND $NTU_{i\,OL}$	$\frac{Sh_{i\,L}}{NTU_{i\,OL}} = \frac{Q_L}{A_{M\,ext}} \frac{d_{M\,ext}}{D_{i\,L}}$
GRAETZ NUMBER AS A FUNCTION OF $Sh_{i\,L}$ AND $NTU_{i\,OL}$	$Gz_{i\,L\,cross} = \pi(N_b + 1) \frac{Sh_{i\,L}}{NTU_{i\,OL}} \frac{D_{fb\,am}}{D_{fb\,lm}}$
RELATION BETWEEN $NTU_{i\,OL}$ AND THE GRAETZ NUMBER	$NTU_{i\,OL} = \frac{4.5\pi(N_b + 1)(1 + 0.775 Gz_{i\,L\,cross}^{1.46})^{0.25}}{Gz_{i\,L\,cross}} \frac{D_{fb\,am}}{D_{fb\,lm}}$
APPLICATION TO TYPICAL OPERATION CONDITIONS i.e. $NTU_{i\,OL} = 4$	Vacuum or excess sweep gas mode $\eta_{i\,L} = 0.98$ for $NTU_{i\,OL} = 4$ $\quad \frac{D_{fb\,am}}{D_{fb\,lm}} \cong 1.08$ SEPAREL® EF $N_b = 0$; $Gz_{i\,L\,cross} = 7.7$ leading to $Sh_{i\,L} = 9.0$ Liqui-Cel™ EXF $N_b = 1$; $Gz_{i\,L\,cross} = 22.5$ leading to $Sh_{i\,L} = 13.2$
SPECIFIC FLOW RATE IN COMMERCIAL HFMCS FOR WATER DEOXYGENATION AT 20°C $D_{O2\,L} = 2 \times 10^{-9}\ \mathrm{m^2 s^{-1}}$	SEPAREL® EF $\frac{Q_L}{A_{M\,ext}} = \frac{Sh_{i\,L}}{NTU_{i\,OL}} \frac{D_{i\,L}}{d_{M\,ext}} \cong \frac{9.0}{4.0} \frac{2 \times 10^{-9}}{2.1 \times 10^{-4}} = 2.15 \times 10^{-5}$ $\frac{m_L^3}{\mathrm{s\ m_{M\,ext}^2}}$ Liqui-Cel™ EXF $\frac{Q_L}{A_{M\,ext}} = \frac{Sh_{i\,L}}{NTU_{i\,OL}} \frac{D_{i\,L}}{d_{M\,ext}} \cong \frac{13.2}{4.0} \frac{2 \times 10^{-9}}{3 \times 10^{-4}} = 2.19 \times 10^{-5}$ $\frac{m_L^3}{\mathrm{s\ m_{M\,ext}^2}}$
RATIO OF THE LIQUID FLOW RATES FOR A GIVEN FIBER VOLUME BETWEEN LIQUID	SEPAREL® EF $\frac{Q_{L\,ss}}{Q_{L\,ls}} = \frac{A_{M\,ext}}{A_{M\,int}} \frac{(Q_{L\,ss}/A_{M\,ext})}{(Q_{L\,ls}/A_{M\,\mathrm{int}})} = \frac{2.1 \times 10^{-4}}{1.4 \times 10^{-4}} \frac{2.15 \times 10^{-5}}{1.4 \times 10^{-5}} = 2.30$ Liqui-Cel™ EXF

IN SHELL CROSS-FLOW AND LIQUID IN LUMEN FLOW [4]	$\frac{Q_{L\,ss}}{Q_{L\,ls}} = \frac{A_{M\,ext}}{A_{M\,int}} \frac{(Q_{L\,ss}/A_{M\,ext})}{(Q_{L\,ls}/A_{M\,\mathrm{int}})} = \frac{3\times10^{-4}}{2\times10^{-4}} \frac{2.19\times10^{-5}}{0.91\times10^{-5}} = 3.56$

4.2.9 Friction-induced liquid pressure drop and relation with the fiber bundle dimensions

Liquid head loss, or friction-induced liquid pressure drop, is an important parameter, as it determines the process feasibility and contributes to operating costs. The relation between liquid head losses and process parameters is outlined in Table 4.11. The differential frictional pressure drop expressed by the Ergun equation has been integrated considering flow through a symmetrical cylindrical ring. By using Ergun's equation instead of Kozeny's equation, both pressure losses due to viscosity and inertia are taken into account. For the viscous contribution, the Kozeny constant given by Happel [17] for cross flow through fiber bundles for a solid volume fraction f_{total}= 0.54 is considered, i.e. h_K = 5.5. For the inertial contribution, the Burke constant is set to the value given by Ergun, i.e. h_B = 0.29.

The solid volume fraction was estimated via shell-side residence time measurements in a Liqui-Cel™ EXF 2.5x8 module. The estimate i.e. 0.554 was close to the estimate of fiber volume fraction made on the basis of the lumen-side residence time (see chapter 5), which was 0.54. The difference between the two solid volume fractions can be explained by the way the fiber bundle is manufactured. In fact, the fibers are woven using polymer threads that form part of the porous medium. As a result, compacity, which is defined as the ratio between fiber volume and fiber bundle volume, is slightly lower than the solid volume fraction, defined as the ratio of solid volume to fiber bundle volume. The solid volume fraction due to the polymer threads is however low, about 1 %. For the pressure drop modeling, the compacity of the fiber bundle, i.e., f = 0.54, was taken into account.

Table 4.11: Liquid frictional pressure drop and optimal fiber bundle dimensions

Item considered	Expression
ERGUN EQUATION IN THE CYLINDRICAL CROSS FLOW GEOMETRY	$\Delta P_{f\,L} = \frac{2(N_b+1)^2 f}{(1-f)^3} \frac{Q_L}{d_{M\,ext}\pi Z_{fb}} \left(\frac{4h_{K\,cross} f \mu_L}{d_{M\,ext}} \ln\left(\frac{D_{fb\,ext}}{D_{fb\,int}}\right) + \frac{h_{B\,cross}(N_b+1)\rho_L Q_L}{\pi Z_{fb}} \frac{(D_{fb\,ext}-D_{fb\,int})}{D_{fb\,ext}D_{fb\,int}} \right)$ $A_{M\,ext} = \frac{4V_{fb}f}{d_{M\,ext}} = \frac{\pi\left(D_{fb\,ext}^2 - D_{fb\,int}^2\right)}{d_{M\,ext}} Z_{fb} f$

ERGUN EQUATION EXPRESSED IN DEPENDENCE ON THE SPECIFIC LIQUID FLOW RATE, i.e. $Q_L/ A_{M\,ext}$	$\Delta P_{f\,L} = \frac{16(N_b+1)^2 f^3}{(1-f)^3 d_{M\,ext}^3} \frac{Q_L}{A_{M\,ext}} \left(D_{fb\,ext} - D_{fb\,int}\right)^2$ $\times \left(h_{K\,cross}\mu_L \frac{D_{fb\,am}}{D_{fb\,lm}} + \frac{h_{B\,cross}(N_b+1)\rho_L}{2} \frac{Q_L}{A_{M\,ext}} \frac{D_{fb\,am}}{D_{fb\,hm}} \left(D_{fb\,ext} - D_{fb\,int}\right) \right)$ $D_{fb\,hm}$ Harmonic mean diameter of the fiber bundle, m
TYPICAL PARAMETERS FOR WATER DEOXYGENATION AT 20 °C IN HFMCS	$\eta_{O_2\,L} = 0.98$; $NTU_{O_2\,OL} = 4$; $D_{O_2\,L} = 2\times10^{-9}\,m^2s^{-1}$; $\mu_L = 10^{-3}$ Pa s; $f = 0.54$; $h_{K\,cross} = 5.5$ [17] ; $h_B = 0.29$; $\frac{D_{fb\,am}}{D_{fb\,lm}} \cong 1.08$; $\frac{D_{fb\,am}}{D_{fb\,hm}} \cong 1.2$; $\Delta P_{f\,L} = 10^4$ Pa
SEPAREL® EF	$d_{M\,ext} = 210$ µm; $\frac{Q_L}{A_{M\,ext}} = 2.15\times10^{-5}\ \frac{m_L^3}{s\,m_{M\,ext}^2}$; $D_{fb\,ext} - D_{fb\,int} = 0.16$ m
Liqui-Cel™ EXF	$d_{M\,ext} = 300$ µm; $\frac{Q_L}{A_{M\,ext}} = 2.19\times10^{-5}\ \frac{m_L^3}{s\,m_{M\,ext}^2}$; $D_{fb\,ext} - D_{fb\,int} = 0.13$ m
RATIO OF INERTIAL AND VISCOUS CONTRIBUTIONS TO PRESSURE DROP	$\frac{\Delta P_{f\,L\,inertial}}{\Delta P_{f\,L\,viscous}} = \frac{h_{B\,cross}(N_b+1)\rho_L}{2h_{K\,cross}\mu_L} \frac{Q_L}{A_{M\,ext}} \frac{D_{fb\,lm}}{D_{fb\,hm}} \left(D_{fb\,ext} - D_{fb\,int}\right)$

As shown in Table 4.11, for a given mass transfer efficiency and thus a given specific liquid flow rate, a given viscosity, diffusion coefficient and outer fiber diameter, the pressure drop depends on the difference between the outer and inner diameters of the fiber bundle. This difference can thus be adjusted to achieve a target pressure drop. Applying these relationships to water deoxygenation at 20°C shows that, under the appropriate operating conditions of $NTU_{O2\,OL} = 4$ and a pressure drop limit of 0.1 bar, the difference in diameters between the external and internal fiber bundles is approximately 13 cm for the Liquid-Cel™ EXF product line and 16 cm for the Separel® EF product line.

Applying these relationships to water deoxygenation at 20 °C reveals that under appropriate operating conditions, i.e. $NTU_{O_2\,OL} = 4$, to limit the pressure drop to 0.1 bar, the difference between external and internal fiber bundle diameters is about 13 cm for the Liquid-cel™ EXF and 16 cm for the SEPAREL® EF product lines. The values are similar, because on the one hand, the fibers are smaller in SEPAREL contactors, resulting in a higher linear pressure drop, but on the other hand, the central baffle

of Liquid-cel™ EXF modules forces the liquid to pass twice through the fiber bundle, which naturally increases the pressure drop.

As Table 4.11 also shows, the ratio between inertial and viscous contributions to pressure loss increases with the specific liquid flow rate and with the module's external and internal diameters. Depending on operating conditions, the inertial contribution can exceed 10% and should therefore not be neglected a priori.

4.3 Model validation through comparison with published data

Model predictions were compared to experimental data obtained using commercial HFMC modules to remove dissolved oxygen from pure or saline water, or to recover methane from anaerobic effluents. These experimental results encompass the removal of dissolved oxygen from both pure and saline water, as well as methane recovery from anaerobic effluents. They were obtained from data given by technology suppliers [18], [19], and scientific papers [16], [20], [9], considering various operational modes including vacuum, sweep gas and combo-mode stripping with excess sweep gas. The experimental data allows assessing the effects of various parameters, in particular the HFMC geometry, initial liquid phase composition, operating temperature, liquid and gas flow rates as well as vacuum pressure.

4.3.1 Geometric characteristics of the HFMC modules

Two major commercial cross-flow HFMC product lines, the Liqui-Cel™ EXF series manufactured by 3M™ and the SEPAREL® EF series manufactured by DIC Corporation were studied. Accurate geometric data, which are not reported by the manufacturers in details, are difficult to obtain and often imprecise, which is an obstacle to modeling hydrodynamics and mass transfer. In order to obtain geometric parameters as exact as possible, several sources were used and compared. In addition, residence time distribution measurements were performed.

An internal image of the fiber bundle of a Liqui-Cel™ EXF 2.5x8 module is obtained from MRI measurements. It is shown in Figure 4.6. The proton MRI experiment was performed on a 2.9 Tesla imager (RS2D, Mundolsheim, Fr) equipped with a 170 mm diameter 1H 123.8 MHz volume coil (Doty Scientific – Columbia SC USA) using a standard axial spin echo 2D sequence from the RS2D PRIM software library. The matrix size is 512x512, the image thickness 1.5 mm and the field of view 60x60 mm^2, giving a spatial resolution of 117.2µm/px^2. Before acquisition the module was filled with water by flushing it through the “gas-in” and “vacuum” connectors (see Figure 4.1) using an ISCO type pump. On the resulting image the water inside the fibers appears in white, while the fibers, air and plastic casing don’t contribute to the measured signal and thus appear in black. The image shown in Figure 4.6 confirms the internal and external bundle diameters, the number of fiber layers (i.e 39 layers), and the

total number of fibers (about 10 100 fibers). The resulting estimated compacity, i.e. 0.536, is close to that given in Table 4.12.

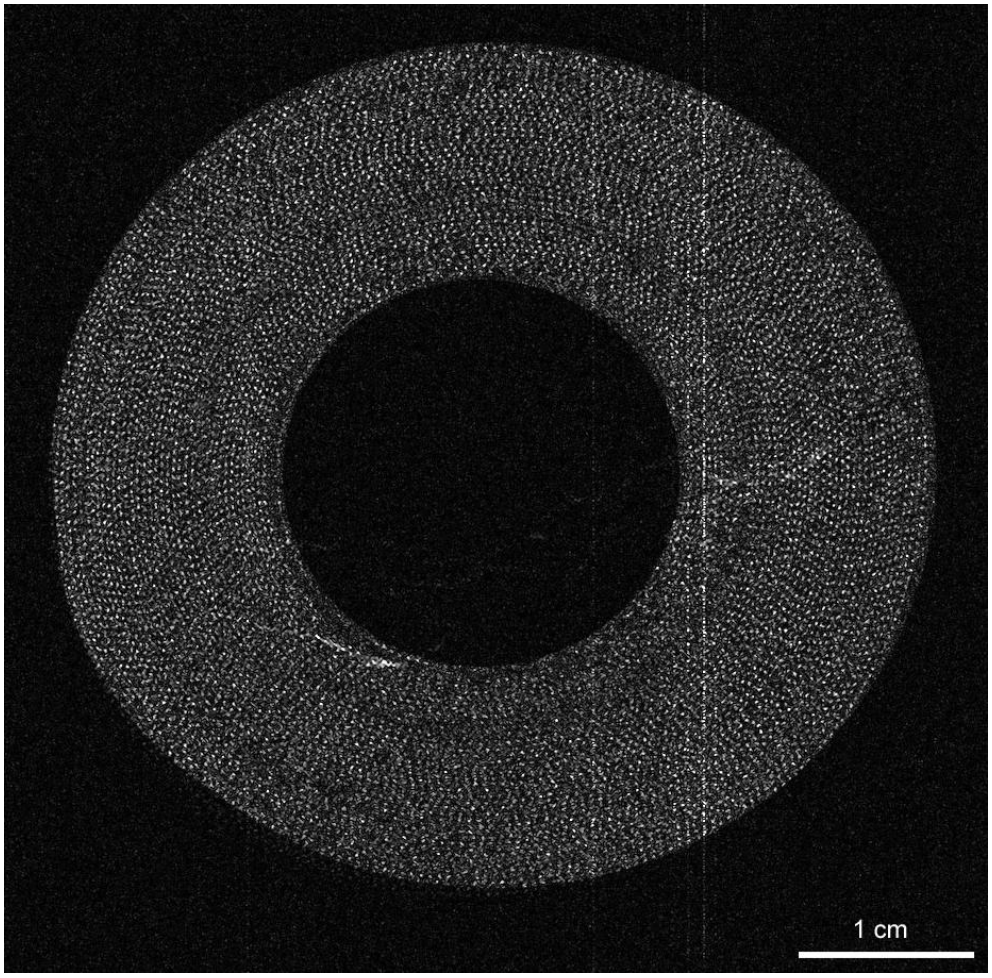

Figure 4.6: Cross-section of the fiber-bundle of a Liqui-Cel™ EXF 2.5x8 module obtained by MRI measurements.

As already mentioned, measurements of the residence time distributions of the shell-side and lumen-side flow through commercial modules were carried out. For the Liqui-Cel™ EXF 2.5x8 module equipped with Celgrad X-40 fibers with an external diameter of 300 μm and an internal diameter of 200 μm, the number of fibers calculated from the mean residence time in the fiber lumen was 10 260. The value compares well with those given by Sengupta *et al*. [16] (10 200) and by Schöner *et al*. [7] (9 950). However, as the estimated fiber length in this work is lower than that given by Sengupta *et al*. [16] (12.7 instead of 16 cm), the membrane external area is estimated to 1.22 m^2 instead of 1.5 m^2 as in [16]. The resulting estimate of compacity or fiber volume fraction is $f = 0.54$, which is higher than the value 0.45 given in [16]. This is because our estimate of the external diameter of the fiber bundle is $D_{fb\ ext} = 0.047$ m as suggested in [7] and [21] which is lower than that given in [16] (0.05 m). Owing to the geometric

similarity of the fiber bundles, the compacity of all modules was set to the value determined in the Liqui-Cel™ EXF 2.5x8 module. The external membrane area was estimated, using the volume of the fiber bundle, its compacity and the external fiber diameter.

The geometric characteristics of the Liqui-Cel™ EXF modules considered in what follows are shown in Table 4.12, as well as the method used to estimate them. External membrane areas range from 1.22 to 544 m^2 and fiber lengths range from 0.127 to 1.860 m. External fiber bundle diameters range from 0.047 to 0.356 m. The ratio between the arithmetic diameter and the mean logarithmic diameter of the fiber bundle lies within a narrow range, between 1.045 and 1.084.

Table 4.12: Geometrical characteristics of the Liqui-Cel™ EXF modules considered in the following

Liqui-Cel™ EXF serie	Z_{fb} m	$D_{fb\ ext}$ m	$D_{fb\ int}$ m	V_{fb} [1] L	$\frac{D_{fb\ am}}{D_{fb\ lm}}$ [1] -	f -	$A_{M\ ext}$ [1] m^2
2.5x8	0.127 [2]	0.047 [3]	0.022 [3]	0.169	1.045	0.54 [4]	1.22
4x13	0.243 [5]	0.085 [5]	0.032 [5]	1.18	1.078	0.54 [8]	8.51
4x28	0.621 [5]	0.088 [5]	0.032 [5]	3.28	1.084	0.54 [8]	23.6
8x20	0.420 [2]	0.200 [6]	0.076 [5]	11.3	1.077	0.54 [8]	81.3
8x40	0.930 [2]	0.200 [6]	0.076 [5]	25.0	1.077	0.54 [8]	180
8x80	1.860 [2]	0.200 [6]	0.076 [5]	50.0	1.077	0.54 [8]	360
10x28	0.621 [2,6]	0.280 [7]	0.114 [7]	31.9	1.066	0.54 [8]	230
14x28	0.621 [2,6]	0.356 [7]	0.152 [7]	50.5	1.059	0.54 [8]	363
14x40	0.930 [2]	0.356 [7]	0.152 [7]	75.6	1.059	0.54 [8]	544

1. Calculation from geometry.
2. Estimation from the supplied overall fiber bundle length, subtracting the lengths of the pottings (2×0.035 m) and that of the central baffle isolation (0.02 m).
3. Values given by Schöner *et al*. [7] and close to those given by Fougerit *et al*. [21] corroborated by MRI measurements made by the authors.
4. Estimation based on MRI measurements and corroborated by lumen side and shell side residence time distribution measurements made by the authors.
5. Values given by Sengupta *et al*. [16].
6. Estimation from the cartridge dimension and a typical external to internal diameter ratio.
7. Values given by or considered equal to those given by Kattan *et al*. [20].
8. Considering geometrical similitude between the porous media of all HFMCs.

N.B.: The first and the second number of the series are related to the module diameter and length respectively. All modules have a central baffle, thus $N_b = 1$. They are generally equipped with porous PP fibers. The nominal external fiber diameter is 300 μm. The nominal internal fiber diameter is 200 μm for the X-40 fibers and 220 μm for X-50 fibers [2].

The characteristics of the SEPAREL® EF modules investigated here are reported in Table 4.13. The external membrane area of the different modules is specified in the technical documents given by

the supplier. The size of the fiber bundles has been estimated based on the mechanical designs of the modules provided by the supplier. The inner diameter of the fiber bundle was set at the outer diameter divided by 2.5, leading to a ratio between the arithmetic diameter and the mean logarithmic diameter of the fiber bundle of 1.069. Using the estimated dimensions, the compacities of the fiber bundles is estimated to be about 0.55, close to that determined in the Liqui-Cel™ EXF 2.5x8 module.

Table 4.13: Geometrical characteristics of the SEPAREL® EF modules considered in the following

SEPAREL® EF serie	$A_{M\,ext}$ [1] m^2	Z_{fb} [2] m	$D_{fb\,ext}$ [2] m	$D_{fb\,int}$ [3] m	V_{fb} [4] L	$\frac{D_{fb\,am}}{D_{fb\,lm}}$ [4] -	f [5] -
010 A60	10	0.18	0.090	0.036	0.962	1.069	0.546
020 A20	20	0.36	0.090	0.036	1.92	1.069	0.546
040 P	40	0.36	0.125	0.050	3.71	1.069	0.566

1. Supplier data [18]
2. Estimate based on mechanical designs provided by the supplier.
3. Estimate based on external fiber bundle diameter and an external to internal fiber bundle diameter ratio of 2.5.
4. Calculation from speculative geometry.
5. Calculation from the external membrane area and the fiber bundle volume.

N.B.: The first number of the series indicates the external membrane area. No central baffle. The modules are equipped with PMP membrane which have a porous core and a dense skin layer. The nominal external and internal fiber diameters are respectively 210 and 140 μm.

4.3.2 Oxygen stripping in combo-mode with excess sweep gas in Liqui-Cel™ EXF modules

Oxygen recovery rates for water stripping at 20 °C in nine Liqui-Cel™ EXF modules are provided by the supplier in graphical form [19]. The information is not very accurate, but data covering a wide range of module sizes is available. The experiments were conducted in both vacuum mode and excess sweep gas combo mode. In addition, for four Liqui-Cel™ EXF modules, oxygen recovery rates, for water stripping at 20 °C in excess sweep gas combo mode, are reported in [16].

The physicochemical and thermodynamic data used to interpret the recovery rates taken from the literature are those reported in a previous article [4]. The estimation procedure given in [22] was applied in order to estimate the equilibrium constant for oxygen and nitrogen. At 20 °C, the volumetric partition coefficients of oxygen, m_{O2}, is 0.0338 $m^3_G\ m^{-3}_L$ whereas that of nitrogen, m_{N2}, is 0.0170 $m^3_G\ m^{-3}_L$. The oxygen liquid diffusion coefficient, $D_{O2\,L}$, is 2.0×10^{-9} m s^{-1}, the equilibrium water vapor pressure is 2.34 kPa.

In vacuum mode, the pressure was 6.67 kPa. The oxygen partial pressures estimated using the mass transfer model presented in Tables 4.8 and 4.9 is about 1.43 kPa, leading to a ratio between the efficiency and the recovery rate of 1.08. This value was used for the estimate of the mass transfer efficiency. In excess sweep gas combo mode, the vacuum side oxygen pressure was negligible, allowing the use of the mass transfer model presented in the last line of Table 4.8.

In Figure 4.7, the mass-transfer efficiency given by the technology supplier (Figure 4.7a) and the liquid Sherwood number estimates (Figure 4.7b) are plotted as a function of the ratio between the volumetric liquid flowrate and the external membrane area. The Sherwood numbers were estimated using the reactor model developed in Table 4.8 and in Table 4.9. In Figure 4.8, the data from [16] are plotted in a similar way. The considered geometries are reported in Table 4.12. In both, Figure 4.7 and Figure 4.8, mass transfer model predictions using the Sherwood - Graetz correlation developed in Table 4.3 are plotted as solid lines. In the expression of the Graetz number as a function of the specific liquid flow rate, the ratio between the arithmetic and the logarithmic mean diameter of the fiber bundles was set to 1.067, which is the mean value of the different modules.

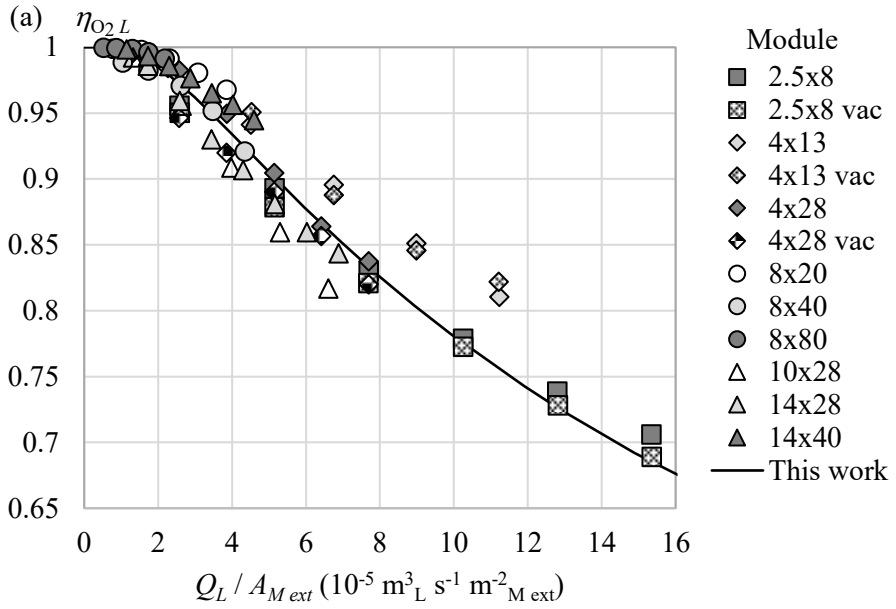

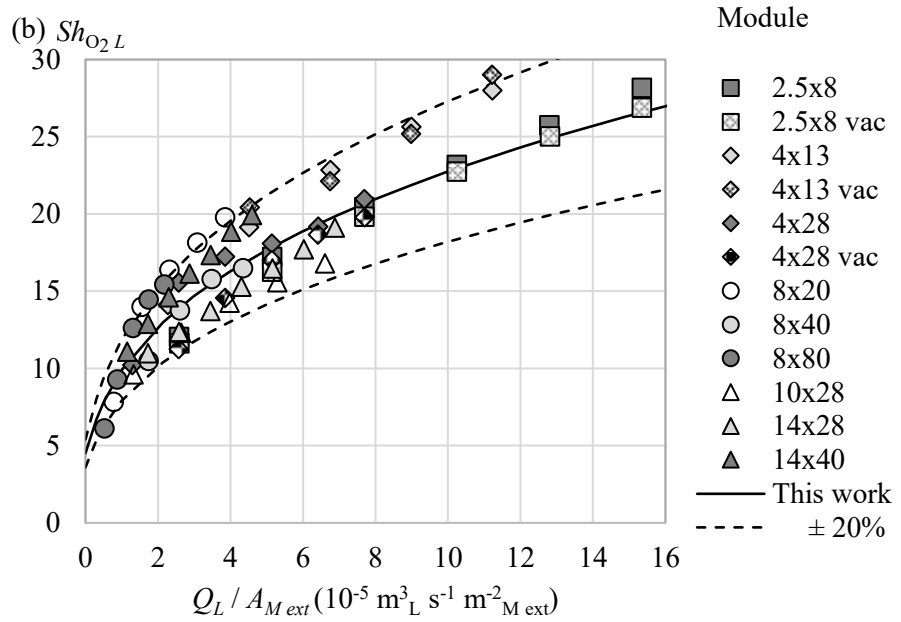

Figure 4.7: (a) Mass transfer efficiency (b) liquid Sherwood number from measurements made in Liqui-Cel™ EXF modules as a function of the specific liquid flow rate. Measurements made in vacuum mode (6.67 kPa) and excess sweep gas combo mode. Model calculations from Table 4.8 and mass transfer correlation from Table 4.3. Geometries of the modules given in Table 4.12.

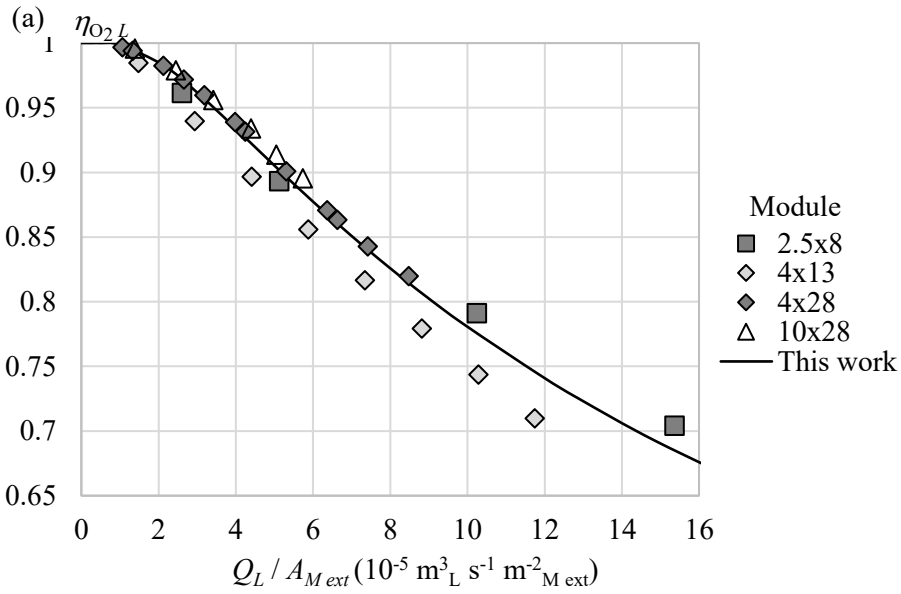

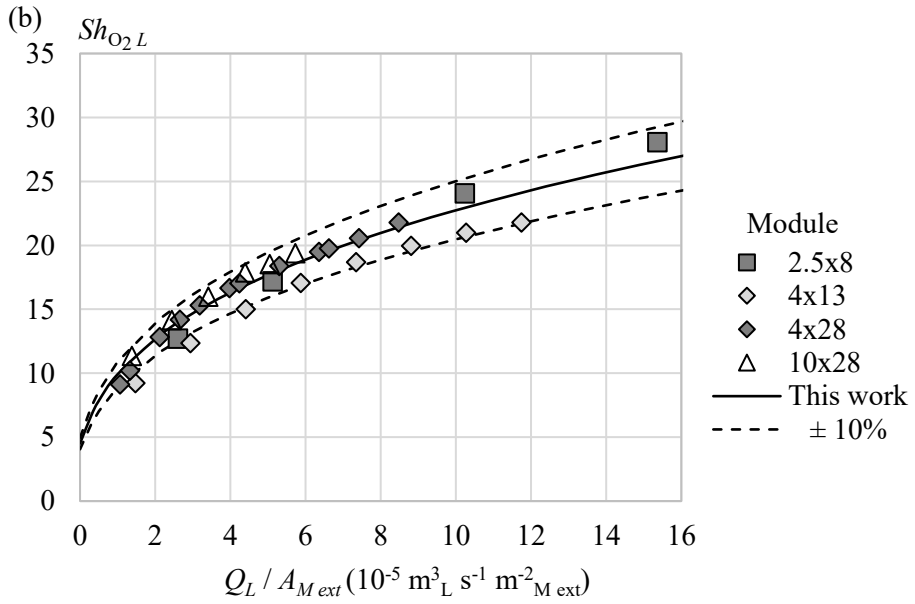

Figure 4.8: (a) Mass transfer efficiency (b) liquid Sherwood number from measurements made in Liqui-Cel™ EXF modules as function of the specific liquid flow rate, data from [16] compared to excess sweep gas model using the Sherwood - Graetz correlation. The geometries of the modules are given in Table 4.12. For the 10x28 module, the geometry given in [7] is taken into account instead of that given in [16]. Mass transfer correlation from Table 4.3.

Figure 4.7 and Figure 4.8 show that the proposed mass transfer model allows measurements performed using HFMCs of very different sizes to be represented by a single curve. Furthermore, experiments carried out in vacuum mode and in excess sweep gas combo mode led to similar mass transfer efficiencies, thus validating the mass transfer model presented in Tables 4.8 and 4.9. When comparing different modules, the data are scattered, but the geometric estimates are not precise, nor are the recovery rate values, especially those provided by the supplier, plotted in Figure 4.7. In addition, the comparison of Figures 4.7 and 4.8 shows discrepancies in the recovery rates for identical module dimensions and operating conditions, especially for the 4x13 and 10x28 modules. The reason for this difference in recovery rates could not be identified.

In Figure 4.9, the Sherwood numbers estimated from the supplier's data (Figure 4.9a) and from ref. [16] (Figure 4.9b) are plotted against the Reynolds number of the liquid cross flow. The latter is defined using the external fiber diameter and the logarithmic mean liquid velocity as given in Table 4.3, and the external fiber diameter. The resulting expression is shown in Table 4.14. Figure 4.9 reveals that the Sherwood numbers determined in modules with different fiber bundle diameters do not fall on a single curve. Indeed, for a given Reynolds number, the Sherwood number decreases with increasing liquid flow path length given by $(D_{fb\,ext} - D_{fb\,int}) / 2$. Thus, mass transfer correlations relating Sherwood number to Reynolds number established in small-diameter modules overestimate the mass transfer coefficients achievable in large-diameter modules. Once again, the comparison between Figure 4.9a and

Figure 4.9b illustrates the scatter of mass transfer data, particularly for 4x13 and 10x28 modules. However, the trend towards lower Sherwood numbers at given Reynolds numbers for larger module diameters is clear. Furthermore, given that the similarity of manufacturing the porous media for different fiber bundle diameters should lead to comparable compacities in all modules, the way in which the characteristic liquid velocity or characteristic length is defined in the Reynolds number of the cross-flow does not alter the shape of the plots and therefore cannot improve the ability of Sherwood - Reynolds correlations to incorporate scaling effects.

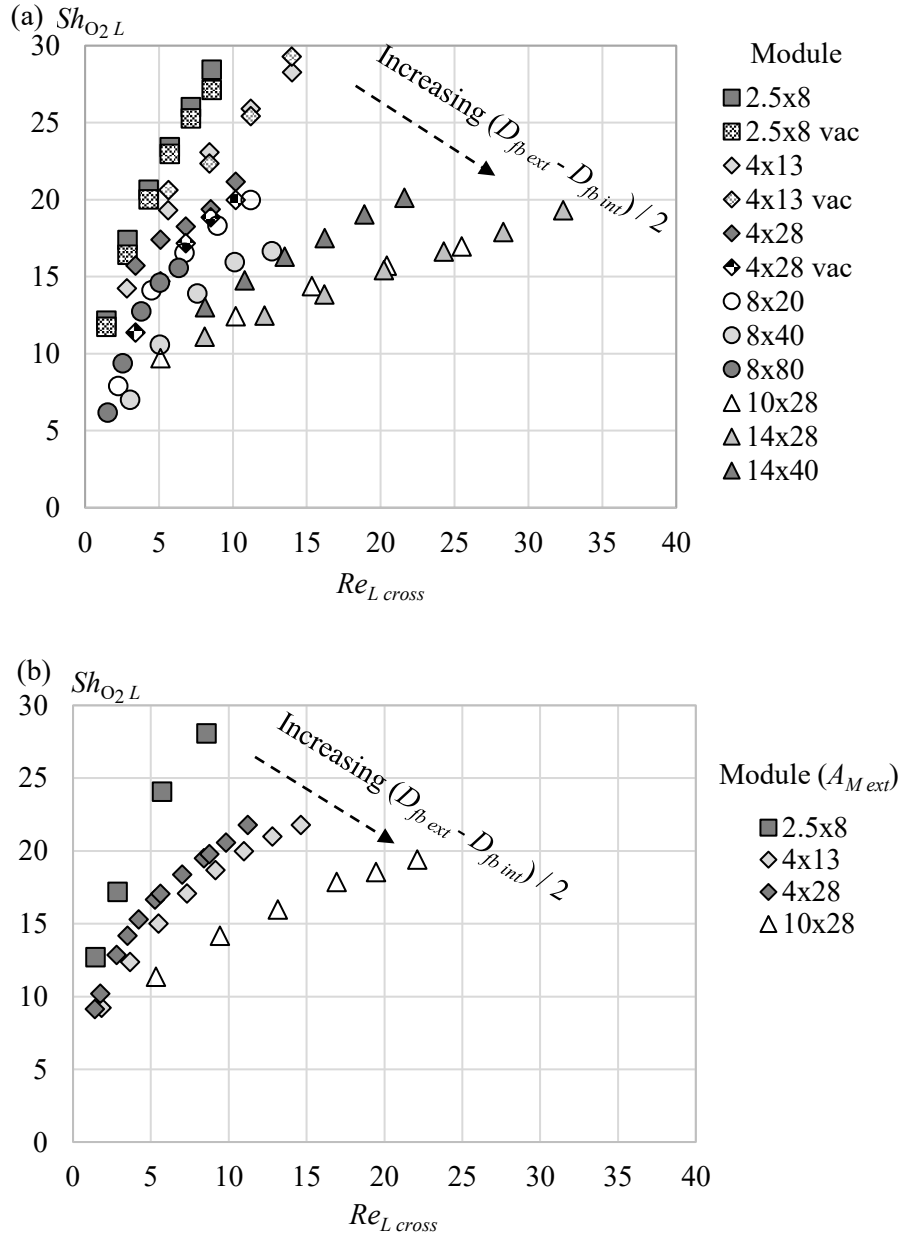

Figure 4.9: Sherwood numbers from measurements made in Liqui-Cel™ EXF modules as a function of the superficial liquid cross-flow Reynolds number (a) data from supplier [19] and (b) data from [16].

The relationship between the Graetz, Reynolds, and Schmidt numbers is reported in Table 4.14. For a given geometric device, at a fixed temperature, and with a given component to be transferred, correlating the Sherwood number to the Reynolds number is equivalent to correlating it to the Graetz number. This is why Sherwood - Reynolds correlations allow grouping measurements performed for a given system and on a given device.

Table 4.14: Relation between dimensionless numbers in mass transfer correlations

Item considered	Expression
GRAETZ NUMBER AS DEFINED IN TABLE 4.3	$Gz_{i\,L\,cross} = \frac{u_{L\,cross\,lm} d_{M\,ext}^2}{D_{i\,L}} \frac{2}{\left(D_{fb\,ext} - D_{fb\,int}\right)} \frac{\pi}{4f}$
REYNOLDS NUMBER DEFINED WITH THE MEAN SUPERFICIAL LIQUID VELOCITY AND THE EXTERNAL FIBER DIAMETER	$Re_{L\,cross} = \frac{\rho_L u_{L\,cross\,lm} d_{M\,ext}}{\mu_L}$
SCHMIDT NUMBER	$Sc_{i\,L} = \frac{\mu_L}{\rho_L D_{i\,L}}$
RELATION BETWEEN THE DIMENSIONLESS NUMBERS	$Gz_{i\,L\,cross} = Re_{L\,cross} Sc_{i\,L} \frac{d_{M\,ext}}{\left(D_{fb\,ext} - D_{fb\,int}\right)} \frac{\pi}{2f}$

4.3.3 Oxygen stripping of salt solutions in vacuum mode in a Liqui-Cel™ EXF 2.5x8 module

Kattan *et al*. [20] used a Liqui-Cel™ EXF 2.5x8 module equipped with Celgard X-40 fibers to deaerate saline solutions by vacuum stripping at a pressure of 7.0 kPa. The NaCl mass fraction of the liquid varied from 0.1 to 25% at temperatures of 20, 30 and 40°C. The oxygen solubility varied by a factor of 6.5, and the oxygen diffusion coefficient in the liquid by a factor of 2.5. The density and viscosity of the liquid and the vapour pressure of the solvent were not constant during the different experiments. As a result, not only did the Reynolds number changed in the experiments, as is often the case, but so did the Schmidt number.

The authors analysed the oxygen depletion measurements assuming zero oxygen partial pressure in the gas phase, so that the experimentally determined oxygen recovery rate was equal to the mass transfer efficiency. The mass transfer coefficients estimated in this way were correlated using a power law function between the Sherwood, the Schmidt and the Reynolds numbers. The correlation is reported in Table 4.15. The interstitial liquid velocity defined by Zheng [23] and the hydraulic diameter of the fiber bundle were used to define the Reynolds and Sherwood numbers. The best fit was obtained for a

power of 0.44 for both Reynolds and Schmidt numbers. Thus, as shown in Table 4.15, the correlation can be expressed as a power law between the Sherwood number and the Graetz number at a power of 0.44. Interestingly, this value is close to the Reynolds number power of 0.42 suggested in other investigations, where the Schmidt number was kept constant [21] [23]. The corresponding Sherwood - Reynolds correlations are parallel to the Sherwood - Graetz correlation proposed in this work, validating the value of the Graetz number exponent in the correlation presented in this paper. When relating the hydraulic diameter of the external flow to the fiber diameter, it is not clear whether to use the fiber volume fraction or the total volume fraction, including the fiber volume and the volume of the polymer yarns used for weaving. The resulting expressions for the correlation of Kattan *et al*. are presented in Table 4.15. Application of the vacuum model presented in Tables 4.8 and 4.9, along with the physico-chemical parameters reported in [20] leads to oxygen vacuum pressures ranging from 0 to 1.6 kPa and a ratio between the mass transfer efficiency and the recovery rate ranging from 1 to 1.08. The Sherwood numbers derived from the vacuum model presented in Tables 4.8 and 4.9 using the geometric parameters presented in Table 4.12 are plotted in Figure 4.10 as a function of the Graetz number. The definitions of the different numbers are given in Table 4.3. The correlation developed in this work, given in Table 4.3, and that of Kattan *et al*. shown in Table 4.15 considering the volume fraction of the fiber bundle are presented respectively by a solid and a dotted line. In addition, the Sherwood number determined in the work of Sengupta *et al*. [16] in a similar HFMC module, for oxygen stripping in pure water at 20°C is plotted by crosses. These values were already presented in Figure 4.8b.

Table 4.15: Mass transfer correlation proposed by Kattan *et al*. [20]

Expression	Correlation of Kattan *et al*. [20]
IN TERMS OF PROCESS PARAMETERS	$\frac{k_{iL} d_{M\,ext}}{D_{i\,L}} \frac{f}{(1-f)} = 0.76 \left(\frac{\rho_L}{\mu_L} d_{M\,ext} \frac{f}{(1-f)} \frac{u_{L\,cross\,lm} \ln(f)}{4\left(\sqrt{f}-1\right)} \right)^{0.44} \left(\frac{\mu_L}{\rho_L D_{i\,L}} \right)^{0.44}$ $u_{L\,cross\,lm}$ as defined in Table 4.3
IN TERMS OF SHERWOOD AND GRAETZ NUMBERS AS DEFINED IN TABLE 4.3	$Sh_{i\,L} = 0.76\, Gz_{i\,L\,cross}^{0.44} \left(\frac{\left(D_{fb\,ext} - D_{fb\,int}\right)\left(-\ln(f)\right)}{2\pi d_{M\,ext}\left(1-\sqrt{f}\right)} \right)^{0.44} \frac{(1-f)^{0.56}}{f^{0.12}}$
NUMERICAL APPLICATION	The geometric parameters of the Liqui-Cel™ EXF 2.5x8 module considered are those given in Table 4.12. The dimensionless numbers are defined in Table 4.3. $Sh_{i\,L} = 2.35\, Gz_{i\,L\,cross}^{0.44}$

As shown in Figure 4.10, for 9 of the 12 studied experimental conditions, the Sherwood numbers determined for different Graetz numbers align on the same curve, demonstrating that the Graetz number permits to correlate mass transfer measurements. However, this curve is around 30% lower than both the correlation established in the present work and the Sherwood numbers reported by Sengputa *et al* [16] in the same module, represented by crosses . The reduced mass transfer performance in the work of Kattan *et al*. could be due to membrane fouling or partial wetting of the porous fibers. Three experimental conditions show higher Sherwood numbers, which can also be observed in the original article. This could be due to the fact that these measurements were taken before fouling or wetting occurred, but this is purely speculative.

Figure 4.10 shows that the correlation established by Kattan *et al*. is almost parallel to that established in this work. It does not pass through the middle of the experimental values, due to differences of data interpretation and the geometry considered. More generally, the difference between correlations using a power-law function such as that of Kattan *et al*. and the correlation presented in Table 4.3 is that the latter tends, for low Graetz numbers, towards a minimum Sherwood number, whereas power-law functions pass through the origin. Thus, when extrapolated to low-flow conditions, power-law correlations underestimate the Sherwood number.

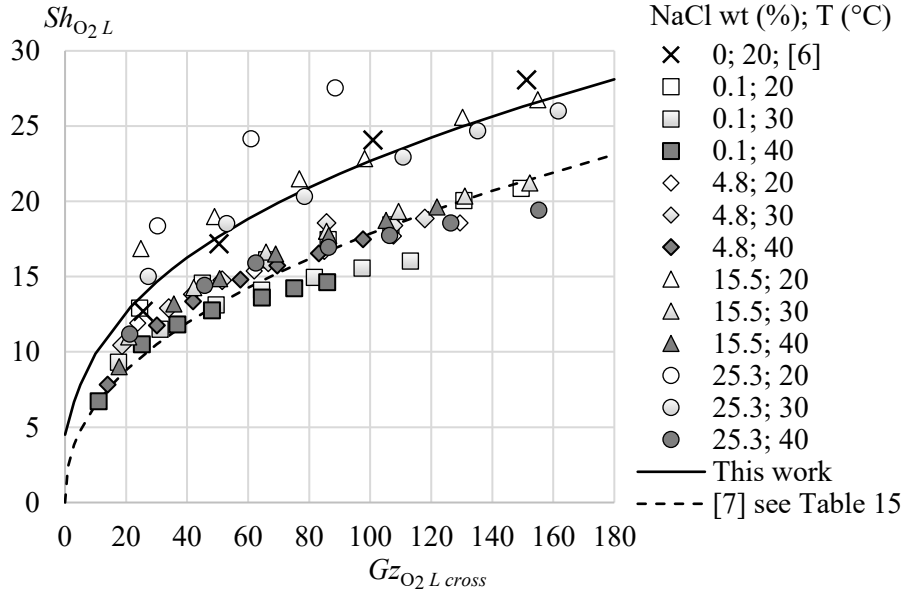

Figure 4.10: Sherwood numbers from measurement made in a Liqui-Cel™ EXF 2.5x8 module as a function of the Graetz number. Data from [20]; vacuum stripping at 7.0 kPa; physicochemical parameters given in [20], geometrical parameters given in Table 4.12. Mass transfer correlations from Table 4.3 (solid line) and Table 4.15 (dotted line).

4.3.4 Methane stripping of anaerobic effluents in sweep-gas mode in a Liqui-Cel™ EXF 2.5x8 module

Mora and de Chernicharo investigated the recovery of methane dissolved in anaerobic effluents using a Liqui-Cel™ EXF 2.5x8 module [9]. In order to reduce operating costs and facilitate methane recovery, they operated in sweep gas mode with moderate gas flow rates, corresponding to a partition ratio, λ_i, close to unity. These operating conditions lead to two-dimensional concentration distributions. The authors have developed a two-dimensional finite element model to describe the recovery of dissolved methane. The overall mean mass transfer coefficient was fitted using experimentally obtained methane recovery rates. Their work provides access to Sherwood values at low Graetz numbers, which are difficult to achieve in vacuum or excess sweep gas stripping.

Experiments were carried out at 25°C. The diffusion coefficient of methane in the liquid phase was estimated to 1.49×10^{-9} m^2 s^{-1}. The external surface area of the membrane contactor considered was 1.54 m^2. In Table 4.8 of [9], Mora and de Chernicharo reported that for a liquid flow rate of 0.3 L min^{-1}, the fitted mass transfer coefficient for methane, $K_{CH_4\,L}$, ranged between 4.3 and 3.9 10^{-5} m s^{-1}. As the mass transfer coefficient is estimated from the $NTU_{CH_4\,OL}$ value, its value depends on the estimated membrane area. If we consider an external membrane area, $A_{M\,ext}$, of 1.23 m^2, as estimated herein, the average value of the adjusted mass transfer coefficient would be 5.2 10^{-5} m s^{-1}, which leads to an average Sherwood number, $Sh_{CH_4\,L}$ of 10.4 for a specific liquid flow rate, $Q_L/A_{M\,ext}$, of 0.41×10^{-5} m s^{-1} and a Graetz number, $Gz_{CH_4\,L\,cross}$, of 5.4. The Sherwood number estimated by the correlation given in Table 4.3 is 8.0, which is quite close to the value estimated by Mora and de Chernicharo [9] (i.e. 10.4), while that estimated using the correlation of Kattan *et al*. is 4.9. Mora and Chernicharo's work thus provides experimental evidence of the performance of the correlation developed in this work for low Graetz and Reynolds numbers.

4.3.5 Vacuum stripping of oxygen in SEPAREL® EF modules

The oxygen concentrations at the outlet of three SEPAREL® EF modules for the vacuum stripping of water at 25°C, at a vacuum pressure of 2.67, 6.67 and 13.3 kPa and different liquid flow rates are provided by the technology supplier in graphical form [18]. As with the recovery rates quoted by the supplier of Liqui-Cel™ EXF modules discussed in Section 3.2, the curves do not allow measurements to be known precisely. Rough estimates of the geometric characteristics of these modules are given in Table 4.13. The external membrane areas range from 10 to 40 m^2.

The oxygen inlet concentration indicated by the supplier is 8.1 mg L^{-1}. The estimation procedure for oxygen and nitrogen is given in [22]. At 25 °C, the volumetric partition coefficient of oxygen, m_{O_2}, is 0.0316 $m^3_G\,m^{-3}_L$; that of nitrogen, m_{N_2}, is 0.0161 $m^3_G\,m^{-3}_L$. The oxygen diffusion coefficient estimated using the value given in Section 3.2 and the Stokes-Einstein equation ($D_{O2\,L} \times \mu_L / T$ = constant) is 2.29

$\times 10^{-9}$ m^2 s^{-1}. The equilibrium vapor pressure of water is 3.17 kPa. The lowest vacuum pressure applied, 2.67 kPa, is below the water saturation pressure. For these measurements, the partial oxygen gas phase pressure was set to zero. The oxygen partial pressures estimated using the mass transfer model presented in Tables 4.8 and 4.9 for vacuum pressures of 6.67 and 13.3 kPa are 1.13 and 3.17 kPa respectively. The oxygen partial pressures estimated using the experimental liquid-phase oxygen concentration at the outlet for the lowest value of $Q_L/A_{M\,ext}$ reported in the EF 40 series, assuming equilibrium with the gas phase are slightly lower, i.e. 0.86 and 2.51 kPa. These values were used for the estimate of the ratio between the mass transfer efficiency and the recovery rate, leading to ratios of 1.05 and 1.14 respectively for vacuum pressures of 6.67 and 13.3 kPa. Because the model's assumptions lead to higher equilibrium oxygen pressures than the measured values and thus less favorable transfer rates, the model's estimates are conservative.

In Figure 4.11, the mass-transfer efficiency (Figure 4.11a) and the liquid Sherwood number (Figure 4.11b) estimated using the mass transfer model are plotted over the specific liquid flow rate, $Q_L/A_{M\,ext}$. Almost all Sherwood number values estimated from the experimental data are within ± 20% of the correlation, validating both the modeling approach and the accuracy of the mass transfer correlation. However, the values are scattered, particularly for the EF 20 series, where the estimated values are higher than those predicted by correlation. This may be due to poor estimation of geometric data or experimental inaccuracy.

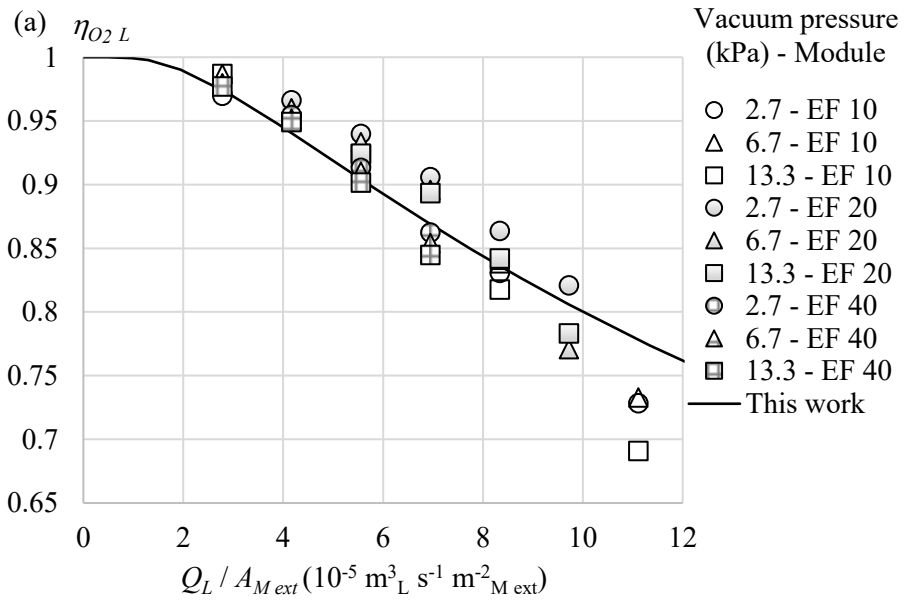

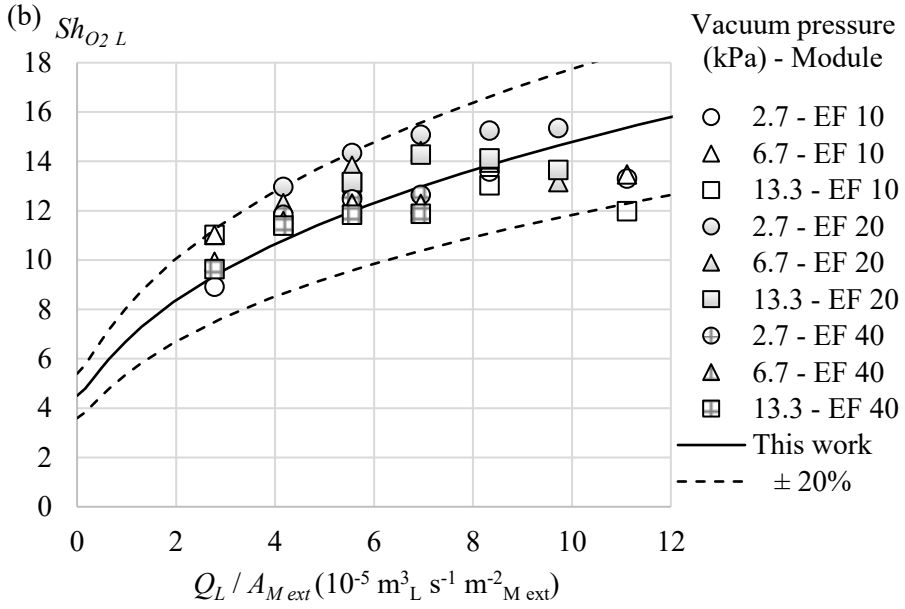

Figure 4.11: (a) Mass transfer efficiency (b) liquid Sherwood number from measurements made in SEPAREL® EF modules; supplier data [18] compared to vacuum model; vacuum set to 2.7, 6.7 and 13.3 kPa; 25°C. Geometric parameters of Table 4.13.

4.3.6 Comparison between mass transfer in Liqui-Cel™ EXF and SEPAREL® EF modules

Comparison between Figure 4.11 and Figures 4.7 and 4.8 representing Liqui-Cel™ EXF modules shows that typical specific flow rates are in the same range, i.e. between 1 and 14 10^{-5} m s^{-1}. However, for a given specific flow rate, the corresponding Graetz number, estimated using the expression given in Table 4.3, is 2.5 times smaller for experiments carried out in the SEPAREL® EF units. This is because, firstly, the outer diameter of the fibers used in SEPAREL® EF units is smaller (210 μm versus 300 μm in the Liqui-Cel™ EXF modules) secondly, the oxygen diffusion coefficient in the experiments is higher, the operating temperature being higher (25°C versus 20°C in the measurements carried out in the Liqui-cel™ EXF series) and, thirdly and most importantly, SEPAREL® EF modules have no central baffle. The lower Graetz number results in a decrease in Sherwood number of around 30% for a given specific liquid flow rate.

The fact that a single correlation is able to predict mass transfer performance in modules produced by different suppliers using fibers of different diameters is probably due to the fact that the module manufacturing procedure is comparable and, as a result, the fiber fraction and solid fraction of the resulting fiber bundles are fairly close.

4.3.7 Supplier data for liquid pressure drop in Liqui-Cel™ EXF and SEPAREL® EF modules

Although the pressure loss curves characterizing commercial HFMC modules are available in the technical literature, they reflect the pressure loss of the liquid in the module as a whole, but do not necessarily make it possible to estimate the contribution of the pressure loss of the flow through the fiber bundle. Indeed, the modules' hydraulic connection devices and fluid distribution and collection devices can add significant head losses, impossible to estimate when their geometry is unknown. Consequently, the Ergun equation presented in Table 4.11 could not be validated with published data.

4.4 Main findings

The liquid degassing process in HFMC modules with shell-side cross-flow can be modelled using an isothermal approach. As shown in Table 4.7, the predominant resistance to mass transfer is located in the liquid phase. This is due to the low solubility of gases. Consequently, it can be postulated that the overall mass transfer coefficient equals the liquid-side mass transfer coefficient. Since the liquid flow is laminar, the mass transfer coefficient can be estimated using a correlation between the Sherwood and the Graetz number. This type of correlation is commonly used in laminar pipe flow with a developing concentration profile. It was suggested in a previous paper for degassing in HFMCs with liquid circulating in the fiber lumen [4].

By analogy to parallel flow, a new expression of the Graetz number for shell-side cross-flow is presented in Table 4.3. It is proportional to the external fiber diameter, the reciprocal of the diffusion coefficient of the transferred species and the ratio of liquid flow rate to external membrane area. The resulting definition of the cross flow Graetz number is very close to that given in a previous article for the lumen-side Graetz number [4] and to that defined by Miyatake *et al*. [12]. for shell-side axial flow, presented in Table 4.2. The main difference is that it varies when a central baffle is introduced into the contactor design, as is the case with the Liqui-Cel^{TM} EXF series. To the best of our knowledge, the use of a Graetz number is suggested in this article for the first time for shell-side cross-flow through HFMC contactors. As shown in Figure 4.4, the new Sherwood - Graetz correlation derived in the present article and presented in Table 4.3 compares well with correlations based on numerical simulations for external axial flow through triangular arrays of cylinders for solid fractions above 0.75.

In order to relate the global mass transfer fluxes measured in HFMC modules to mass transfer coefficients and thus to Sherwood numbers, a contactor model needs to be established. In gas-liquid cross-flows, mass transfer models may require a two-dimensional approach and hence numerical resolution. However, the experimental data used in this work were obtained using combo stripping with excess sweep gas or vacuum stripping. The contactor model established for these operating conditions is shown in Table 4.8. It leads to an expression relating the mass transfer efficiency to the number of transfer units. The former is related to the recovery rate by an expression involving the partial pressure

of the target species in the gas phase. In the case of excess sweep gas stripping, this pressure is zero, leading to equality between mass transfer efficiency and recovery rate. In vacuum stripping, the partial pressure of the target species can be estimated using a mass balance, including all dissolved gases, since they are stripped along with the target species. The related equations are provided in Table 4.9. To achieve the desired recovery rate for a given mass transfer efficiency, the vacuum pressure must be adjusted. As in [22], recovery rate and mass transfer efficiency were considered distinctively.

The contactor model was used to estimate Sherwood numbers from experimental recovery rates given in the literature for water deoxygenation in commercial HFMCs of different sizes. As shown in Figures 4.7, 4.8 and 4.11, the correlation established in this work and reported in Table 4.3 is consistent with Sherwood number estimates. The observed dispersion can be largely attributed to the limited geometrical information available for the different modules. As shown in Figure 4.9, the correlation of Sherwood number with Reynolds number, generally suggested in the literature, allows measurements to be grouped for given radial dimensions of the fiber bundle, but fails when radial dimensions vary. In addition, conventional power-law correlations fail to predict Sherwood numbers for low specific liquid flow rates. These operating conditions are important, as they are used in sweep gas stripping with moderate gas flow rates [9].

As demonstrated for the liquid-in-lumen flow configuration discussed in [4], the liquid-in-shell cross-flow configuration has few degrees of freedom. As shown in Table 4.10, it turns out that the number of transfer units characterizing the mass transfer operation can be expressed as a function of the Graetz number alone, and therefore as a function of the specific liquid flow rate, defined with respect to the external membrane area. Since mass transfer efficiency always depends on the number of transfer units, the former depends solely on the specific liquid flow rate, regardless of the size or geometry of the fiber bundle. Remarkably, the specific liquid flow rate leading to a mass transfer efficiency of 0.98 in vacuum or excess sweep gas stripping is almost the same for the Liqui-cel™ EXF and SEPAREL® EF series, i.e. 2.1 10^{-5} and 2.2 10^{-5} m^3_L s^{-1} $m^{-2}_{M\ ext}$ respectively. This is due to the fact that the central baffle of the Liqui-cel™ EXF modules leads to higher Graetz and Sherwood numbers, compensating for the larger fiber diameter compared to the SEPAREL® EF modules. Comparison with the previous paper [4] shows that for both product ranges and for a given fiber volume, the ratio of liquid flow rates leading to the same mass transfer efficiency between shell-side cross-flow and lumen-side flow is around 3, in accordance with literature [16].

Frictional liquid pressure drop, is an important parameter, as it determines process feasibility and contributes to operating costs. For shell-side liquid flow, it can be predicted using an Ergun type equation. The Ergun equation requires information on the geometry of the porous medium. The structure of the porous medium that characterizes fiber bundles in commercial HFMC contactors is complex, as the fibers are woven with polymer yarns to form a fabric that is wrapped around a central distribution

tube. As a result, the porous medium contains both polymer fibers and polymer threads of different characteristic dimensions. However, the volume occupied by the polymer threads is small compared to that occupied by the fibers, and the relative fiber volume, *f*, can therefore be used in the expression of the liquid head loss due to its flow through the porous medium. As shown in Table 4.11, for the first time, liquid pressure drop is related to specific liquid flow rate and liquid path length.

4.5 References

[1] 3M™ Liqui-Cel™ Membrane Contactors for Semiconductor and Microelectronics, (n.d.). https://www.3m.com/3M/en_US/liquicel-us/industries/semiconductor-and-microelectronics/ (accessed August 20, 2024).

[2] Liqui-Cel Design & Operating Procedures, (n.d.). https://gmpua.com/Equipment/Deaeration/Operating%20Procedure.pdf (accessed April 22, 2025).

[3] SEPAREL, DIC Corp. (n.d.). https://www.separel.com/en/products/water.html (accessed June 24, 2024).

[4] O. Aljasem Alhmiedy, B. Belaissaoui, S. Rode, A simple model for sizing hollow fiber membrane contactors in degassing applications, relationship between mass transfer efficiency, liquid flow rate, membrane area and pressure drop; part I: liquid-in-lumen configuration, Sep. Purif. Technol. 365 (2025) 132551. https://doi.org/10.1016/j.seppur.2025.132551.

[5] C.A. Scholes, S. Shen, Mass transfer correlations for membrane gas-solvent contactors undergoing carbon dioxide desorption, Chin. J. Chem. Eng. 26 (2018) 2337–2343. https://doi.org/10.1016/j.cjche.2018.05.005.

[6] J.-M. Zheng, Z.-W. Dai, F.-S. Wong, Z.-K. Xu, Shell side mass transfer in a transverse flow hollow fiber membrane contactor, J. Membr. Sci. 261 (2005) 114–120. https://doi.org/10.1016/j.memsci.2005.02.035.

[7] P. Schöner, P. Plucinski, W. Nitsch, U. Daiminger, Mass transfer in the shell side of cross flow hollow fiber modules, Chem. Eng. Sci. 53 (1998) 2319–2326. https://doi.org/10.1016/S0009-2509(98)00097-9.

[8] S. Shen, S.E. Kentish, G.W. Stevens, Shell-Side Mass-Transfer Performance in Hollow-Fiber Membrane Contactors, Solvent Extr. Ion Exch. 28 (2010) 817–844. https://doi.org/10.1080/07366299.2010.515176.

[9] E. Centeno Mora, C.A. de L. Chernicharo, Modelling and optimization of transverse flow hollow fibre membrane contactors for the recovery of dissolved methane from anaerobic effluents, Sep. Purif. Technol. 293 (2022) 121136. https://doi.org/10.1016/j.seppur.2022.121136.

[10] N. Cancilla, M. Ciofalo, A. Cipollina, A. Tamburini, G. Micale, Straight fiber bundles with non-uniform porosity: Shell-side hydrodynamics and mass transfer in cross flow, Chem. Eng. Sci. 291 (2024) 119947. https://doi.org/10.1016/j.ces.2024.119947.

[11] C. Gostoli, Recovery of Biosynthetic Products Using Membrane Contactors, in: H. Nakajima (Ed.), Mass Transf. - Adv. Asp., InTech, 2011. https://doi.org/10.5772/21345.

[12] O. Miyatake, H. Iwashita, Laminar-flow heat transfer to a fluid flowing axially between cylinders with a uniform surface temperature, Int. J. Heat Mass Transf. 33 (1990) 417–425. https://doi.org/10.1016/0017-9310(90)90177-V.

[13] L. Bao, G.G. Lipscomb, Well-developed mass transfer in axial flows through randomly packed fiber bundles with constant wall flux, Chem. Eng. Sci. 57 (2002) 125–132. https://doi.org/10.1016/S0009-2509(01)00368-2.

[14] N. Cancilla, L. Gurreri, G. Marotta, M. Ciofalo, A. Cipollina, A. Tamburini, G. Micale, CFD prediction of shell-side flow and mass transfer in regular fiber arrays, Int. J. Heat Mass Transf. 168 (2021) 120855. https://doi.org/10.1016/j.ijheatmasstransfer.2020.120855.

[15] S.M. Matson, V.P. Makrushin, I.S. Levin, N.A. Zhilyaeva, E.G. Litvinova, V.S. Khotimskiy, Structure and properties of poly(4-methyl-2-pentyne) synthesized with NbBr5 and TaBr5-based catalytic systems, Polymer 202 (2020) 122682. https://doi.org/10.1016/j.polymer.2020.122682.

[16] A. Sengupta, P.A. Peterson, B.D. Miller, J. Schneider, C.W. Fulk, Large-scale application of membrane contactors for gas transfer from or to ultrapure water, Sep. Purif. Technol. 14 (1998) 189–200. https://doi.org/10.1016/S1383-5866(98)00074-4.

[17] J. Happel, Viscous flow relative to arrays of cylinders, AIChE J. 5 (1959) 174–177. https://doi.org/10.1002/aic.690050211.

[18] DIC Corporation, Module Specifications of SEPAREL contactors, (2024).

[19] 3M™ Liqui-Cel™ Data Sheets, (n.d.). https://www.3mnz.co.nz/3M/en_NZ/liquicel-nz/resources/data-sheets/ (accessed April 22, 2025).

[20] O. Kattan, K. Ebbers, A. Koolaard, H. Vos, G. Bargeman, Membrane contactors: An alternative for de-aeration of salt solutions?, Sep. Purif. Technol. 205 (2018) 231–240. https://doi.org/10.1016/j.seppur.2018.05.038.

[21] V. Fougerit, V. Pozzobon, D. Pareau, M.-A. Théoleyre, M. Stambouli, Gas-liquid absorption in industrial cross-flow membrane contactors: Experimental and numerical investigation of the influence of transmembrane pressure on partial wetting, Chem. Eng. Sci. 170 (2017) 561–573. https://doi.org/10.1016/j.ces.2017.03.042.

[22] R. Fernández-Prini, J.L. Alvarez, A.H. Harvey, Henry's Constants and Vapor–Liquid Distribution Constants for Gaseous Solutes in H2O and D2O at High Temperatures, J. Phys. Chem. Ref. Data 32 (2003) 903–916. https://doi.org/10.1063/1.1564818.

[23] J.-M. Zheng, Z.-W. Dai, F.-S. Wong, Z.-K. Xu, Shell side mass transfer in a transverse flow hollow fiber membrane contactor, J. Membr. Sci. 261 (2005) 114–120. https://doi.org/10.1016/j.memsci.2005.02.035.

Chapter 5. Residence time distribution Analysis in commercial HFMC

5.1 Introduction and Theoretical Background

In process engineering, real reactors often exhibit complex mixing characteristics that deviate from ideal models, necessitating tools like Residence Time Distribution (RTD) to quantify flow non-idealities and predict performance. Real reactors, whether reactive or non-reactive, contrast with ideal plug flow reactors (PFRs) or continuous stirred-tank reactors (CSTRs), where mixing is uniform or absent, respectively. RTD characterization is the first stage in optimization, design and scale up of processes in different unit operations [1].

RTD is a chemical engineering concept introduced by Danckwerts in 1953 as the probability density function of the residence time for a molecule, particle, or fluid aggregate within the system, providing a statistical measure to characterize mixing and enable the use of simple models despite the rise of computational fluid dynamics [2,3].

The RTD measurement relies on tracer experiments in open, non-reactive, incompressible systems at constant volumetric flow rate Q_L. The RTD function, denoted as $E(t)$, represents the fraction of fluid exiting the system at time t after entering at time zero. It is defined such that the integral of $E(t)$ over all time is unity:

$$\int_0^\infty E(t)dt = 1$$

Many different combinations of CSTRs and PFRs were introduced in practical modeling cases. CSTRs in a series model is one commonly used model. Large number of tanks indicates a PFR-like reactor ($n \rightarrow \infty$), and a small number leads to a CSTR-like reactor ($n = 1$) [4].

RTD experiments typically involve tracer techniques to probe the system's hydrodynamics. Common methods include [2]:

- Pulse Injection Method: A small amount of tracer (e.g., non-reactive dye like methylene blue or salt like NaCl) is injected as a Dirac delta pulse at the inlet. The effluent concentration is then monitored over time using compatible detection techniques. The RTD function $E(t)$ is directly obtained from the normalized concentration-time curve: $E(t) = \frac{C(t)}{\int_0^\infty C(t)\,dt}$

  where $C(t)$ is the outlet tracer concentration of the liquid phase at time t.

  From $E(t)$, key parameters such as the mean residence time $\tau = \int_0^\infty t * E(t)dt = \frac{V}{Q}$, and the variance $\sigma^2 = \int_0^\infty (t-\tau)E(t)\,dt$ are derived.

  The dimensionless RTD, *E(θ)*, can be expressed $E(\theta) = \tau E(t)$

  With $\int_0^\infty E(\theta)d\theta = 1$, where θ is the dimensionless time, defined by $\theta = \frac{t}{\tau}$.

Pe and *J* are fitted parameters to match the RTDs obtained using tracer experiences and analysis using the DTS pro software. They are linked to the mean residence time, τ and the variance of the RTDs through the following expressions:

$$J = \frac{\tau^2}{\sigma^2}$$

$\frac{\sigma^2}{\tau^2} = \frac{2}{Pe} - \frac{2}{Pe^2}(1 - e^{-Pe})$, where: τ : mean residence time, and σ^2 Variance of the RTD.

- Step Change Method: A continuous step input of tracer is introduced, and the effluent concentration is measured until steady state. The cumulative RTD $F(t) = \int_0^t E(t)dt$ is derived from the normalized response. This approach is useful for systems with longer residence times than the one in pulse injection method.

Detection techniques can be categorized into online and offline methods. Inline detection allows for real-time monitoring and recording directly using optical or conductive sensors, such as NIR spectroscopy or electrical conductivity measurements. It requires fast sample acquisition, signal conversion, and data storage processes. When one or more of these steps cannot be finished immediately, offline detection is selected. For instance, digital imaging analysis can hardly be inline due to the slow extraction of tracer concentration from digital photos [1].

The hollow fiber membrane contactor is a separation unit that is used in various chemical processes. The internal geometry of commercial modules is often confidential. The way in which fluid is distributed, and the contact time strongly influence performance. Therefore, understanding how fluid moves through the module is essential.

In an early experimental study on flow non-idealities in hollow fiber dialyzers, Noda *et al*. (1979) [5] investigated the impact of shell-side flow maldistribution on solute extraction performance, aiming to quantify deviations from ideal flow behavior using tracer-based RTD analysis and a simplified bypass model. Custom dialyzers were constructed with cellulosic hollow fibers (Hohlfaser D21 M; fiber OD 300 μm, ID 240 μm, length 100 cm) axially aligned in a glass shell (ID 6 mm), potted with silicone rubber to segregate flows, yielding surface areas of ~ 0.15–0.19 m^2 and void volumes of 10 – 15 mL per side; two packing densities were tested: well-packed (250 fibers, 70% efficiency) and loosely packed (200 fibers, 55% efficiency). The configuration was counter-current axial flow, vitamin B_{12} feed (~500 ppm aqueous buffer) in the lumen side, and dialysate buffer in the shell side; tracer studies used blue Dextran pulses in distilled water on the shell side at 3.52 mL/min (~25°C). Well-packed units exhibited near-ideal fractional extraction $E \approx \theta/(1+\theta)$ (deviation <5% for dialysis coefficient $\theta = hS/Q$, where h is overall permeability, S is surface area, and Q is flow rate; θ range 0.1–10), while loosely packed ones showed 20–40% lower E due to channeling, confirmed by RTD metrics: mean residence time $\tau \approx$ 3.25 min and variance $\sigma^2 \approx$ 31% versus $\tau \approx$3.18 min and $\sigma^2 \approx$ 15 % for well-packed, indicating early

breakthrough and long tails in exit age distribution functions. A two-parameter bypass model (mean bypass fraction $\beta \approx 0.8$, maldistributed segment fraction B ≈0.75) correlated non-ideal data effectively. It linked maldistribution to fiber clustering and emphasized packing efficiency as a key design factor for minimizing axial dispersion in low-Reynolds-number laminar flows. However, the study was limited to lab-scale devices with primarily axial shell-side flow, without significant transverse (radial or cross-flow) components common in commercial designs.

In a theoretical investigation of shell-side hydrodynamics in HFM devices, Lemanski and Lipscomb (1995) [6] analyzed the influence of RTD on mass-transfer performance, aiming to quantify its effect on solute removal efficiency while assuming constant lumen-side concentration and membrane dominant resistance to simplify boundary layer and flow orientation complexities. The HFM geometry was based on an axisymmetric Althin hemodialyzer bundle with parallel-aligned fibers along the axial direction, featuring a fiber bundle radius R, length L, and annular clearance AC [5]= 0.0714 between the bundle and outer shell; large annular regions near shell inlet/outlet ensured uniform fluid distribution. The flow configuration involved shell-side entry perpendicular to the fibers transitioning to axial parallel flow, modeled as low Reynolds number ($Re < 1$) Darcian flow through an anisotropic porous medium with axial permeability K_{zz} and radial K_{rr} (e.g., for triangular packing at porosity $\varepsilon = 0.6$, $K_{zz} = 7.2 \times 10^{-10}\ r^2$, $K_{rr} = 17 \times 10^{-10}\ r^2$, where r is fiber radius); dilute solute removal occurred from the shell-side fluid, with lumen-side concentration fixed at zero. Operating conditions emphasized high Péclet numbers ($Pe > 100$) to neglect diffusion and Taylor dispersion, parameterized by module geometry number [$MG = (K_{rr}/K_{zz})^{1/2}$ (L/R)] and mass-transfer number [$MT = k.a.\tau$] (where k is intrinsic mass-transfer coefficient, a is specific surface area, τ is space time).

In an experimental and modelling study on non-ideal shell-side hydrodynamics in hollow fiber modules (HFMs), Wang *et al*. (2003) [7] quantified the impact of random fiber packing on flow maldistribution and mass transfer efficiency using RTD measurements and a Voronoi tessellation-based random distribution model incorporating a normal probability density function $f(\phi) = \frac{1}{\sigma\sqrt{2\pi}} \exp\left(-\frac{(\phi-\mu)^2}{2\sigma^2}\right)$ (where ϕ is the fiber-associated cross-sectional area, μ is the mean value of the normal probability density function, and σ quantifies packing irregularity), aiming to relate irregularity to non-ideal flow and overall extraction performance in counter-current membrane extraction. Three polypropylene HFMs were tested with varying packing densities $\phi = 0.4 – 0.6$ (corresponding to 200–400 fibers, effective length $L = 15$ cm, outer diameter OD = 300 μm), potted at ends to segregate flows, yielding shell void fractions $\varepsilon = 1 - \phi$ and total areas ~ 0.03 – 0.05 m^2; the configuration was counter-

[5] The annular clearance refers to the radial distance between the fiber bundle and the outer shell of the hollow-fiber module.

current with parallel axial fiber alignment, organic extractant (30% TBP in kerosene) flowing through the shell side and aqueous phenol feed (~1000 mg/L) through the lumen side, with RTD tracer studies (NaCl pulses) on the shell at volumetric flow rates Q = 5 – 20 mL/min (~25°C, Re < 50). Results revealed that higher σ (irregularity) broadened RTD curves (e.g., variance σ^2 > 0.5 at ϕ = 0.4), inducing channeling and reducing overall mass transfer coefficient K_{ow} (based on aqueous phase) by 30–50% compared to ideal plug flow predictions across distribution coefficients[6] m =1 – 10, with non-ideal shell flow also diminishing lumen-side coefficients by up to 20% due to uneven solute loading; the model correlated experimental K_{ow} within ±15%, emphasizing random packing's role in axial dispersion though limited to low-Re laminar extraction without transverse enhancements.

In an experimental and modeling study on scale effects in hollow fiber renewal liquid membrane systems for copper extraction, Ren *et al*. (2013) [8] investigated the influence of module geometry on shell-side non-ideal flow and overall mass transfer performance. They aimed to characterize flow maldistribution via residence time distribution (RTD) curves and Peclet number $Pe = ud_e/D$ (where u is superficial velocity, d_e equivalent diameter, and D axial dispersion coefficient) while proposing a correlation linking Pe to the overall mass transfer coefficient K_{ov} . Five polypropylene HFMs were tested with identical packing density $\phi \approx 0.3$ and effective fiber length L = 30 cm but varying inner shell diameters d_i = 0.8 – 2.5 cm (L/d_i = 37.5 - 12, fiber counts ~ 95 - 1000, surface areas 0.04 – 0.42 m^2); the configuration was counter-current with parallel axial flow, aqueous $CuSO_4$ feed (initial copper concentration 60 mg/L at pH 2.6) in the lumen side, H_2SO_4 stripper and renewing organic liquid membrane (LIX984N in kerosene) co-flowing in the shell side; operating conditions included ambient temperature (~25°C), low-Reynolds-number laminar flows (Re < 50, volumetric rates 10–200 mL/min), and single-pass, recycling, or cascade modes with RTD tracer (KCl) pulses on the shell side. Results showed Pe increasing with L/d_i to a maximum at L/d_i = 20 before declining due to enhanced channelling in larger modules. The K_{ov} is directly proportional to Pe across single-pass, recycling, and cascade modes (e.g., $K_{ov} \propto Pe^{0.5}$ in the proposed correlation). The developed mathematical model (incorporating axial dispersion and resistance-in-series) matches experimental extraction efficiencies within ±10%, emphasizing module aspect ratio's (L/d_i) role in mitigating shell-side bypassing, though the study is limited to lab-scale devices due to the simplified geometry.

Zhang *et al*. (2014) [9] investigated flow non-idealities in HFMCs for CO_2 absorption. The research aimed to quantify the relationship between shell-side RTD and mass transfer performance using a multi-continuous stirred tank reactor (CSTRs) model, and to evaluate vibration as a process

[6] The distribution coefficients is the equilibrium partition coefficient m = C_o^* / C_w for the solute (phenol) between organic (TBP/kerosene) and aqueous phases.

intensification technique. The bench-scale cylindrical module used polypropylene hollow fibers (inner diameter: 0.4 mm, outer diameter: 0.6 mm, length: 0.3 m) potted at both ends. The total membrane area ranged from ~ 0.008 to 0.08 m^2, with shell void fractions of 0.64 - 0.96, depending on the packing density. A regular axial fiber alignment was used to minimize flow maldistribution. The flow configuration was counter-current, with pure CO_2 gas flowing through the fiber lumens and deionized water as the absorbent liquid on the shell side. The system incorporated transverse vibration (0–20 Hz) in axial or radial directions. Shell-side RTD was characterized via pulse injections of a potassium chloride tracer at liquid velocities of 0.01– 0.1 m/s and ~25°C. Operating under laminar flow conditions (Re < 100), the dimensionless variance $\sigma_\theta^2 = \sigma^2/\tau^2$(where σ^2 is variance and τ is mean residence time) derived from RTD curves to estimate CSTRs cells $N = 1/\sigma_\theta^2$ (e.g., N ≈ 5–20); results showed enhanced flow uniformity and mass transfer coefficients k_L (up to 2.5 fold increase via penetration theory, $k_{L,i} = \sqrt{D_L/(\pi\, t_N)}$, where $t_N = \tau/N$ is cell residence time) at low velocities or high packing, with greater intensification when liquid flowed shell-side or vibration was vertical to flow, as the RTD-CSTRs model ($Q_{RTD} = \sum_{i=1}^{N} A_{m,i}\, k_{L,i} \Delta C_{L,i}$, where $A_{m,i}$ is cell area and $\Delta C_{L,i}$ is local driving force) matched experimental k_L values within ±10%, highlighting vibration's efficacy for manipulating channeling though limited to small-scale, aqueous systems without scale-up validation.

Kavousi *et al*. (2016) [10] examined the hydrodynamics and oxygen transfer efficiency of confined hollow fiber bundles using combined tracer-response experiments and CFD modelling. Dense PDMS fibers (ID 300 µm, OD 500 µm, length 42 cm) were arranged in bundles of 4 – 37 fibers within a vertical glass column (ID 25 mm, length 800 mm). Fibre spacing varied between 2, 4 and 6 mm to study the effect of packing density. Water was circulated upward on the shell side at velocities of 2.7, 4.8 and 6.9 cm/s, while pure oxygen was supplied inside the fibres at 50 –100 mbarg. Tracer studies, using pulse injections of HCl detected by a conductivity probe, provided residence time distribution (RTD) curves for model validation. Results showed that mean residence time decreased with increasing velocity but exhibited no consistent trend with fiber number or spacing. Larger bundles and smaller spacing produced broader RTD curves with longer tails, indicating dead zones and deviations from plug flow. Variance and skewness of RTD functions decreased at higher velocities, reflecting improved mixing. CFD predictions were in good agreement with experiments and enabled the derivation of a correlation for Sherwood number based on local velocity fields. Oxygen transfer rate decreased with increasing fiber number and was most sensitive to inter-fiber spacing. The study highlighted that flow maldistribution is controlled by the interaction of bundle size, spacing, and shell-to-bundle diameter ratio, and cannot be predicted from inlet velocity alone.

Breniaux *et al*. (2019) [11] investigated gas transfer in hollow fibre membrane contactors for wine applications, comparing a commercial polypropylene (PP) module , MinimoduleTM from 3M® Liqui-Cel® (Celgard, Charlotte, NC), with a prototype, made by LGC (Laboratoire de Génie Chimique,

Toulouse), polypropylene contactor coated with a dense Teflon layer (PPT). The PP module contained 2300 fibres (ID 110 µm, OD 150 µm, length 0.115 m, area 0.18 m²), while the PPT module contained 1210 fibres (ID 140 µm, OD 191 µm, length 0.192 m, area 0.20 m²). Gas (CO_2 or O_2) was introduced on the lumen side, and water, or red wine was circulated through the shell side in a closed-loop system at 21 °C, with optimized liquid flow rate of 300 mL.min^{-1} with conductivity detection at the outlet, and gas flow rate of 120 mL.min^{-1}. RTD was characterized by pulse injection of NaCl, revealing longer residence times in the prototype due to larger dead volume, though values remained below 60 s. Gas transfer capacity was evaluated through the volumetric mass transfer coefficient ($K_L.a$), which reached ~2×10^{-4} s^{-1} in both modules.

Houlker *et al*. (2021) [12] conducted a study to reconcile mass transfer discrepancies between parallel and transverse flow HFMCs by explicitly accounting for shell-side hydrodynamics using RTD analysis. The study compared a 0.5 m^2 parallel flow module (7 400 fibers) with a 1.2 m^2 transverse (baffled) flow module (10 200 fibers). The two modules comprised of the same polypropylene microporous hollow-fibers (G542 and EXF-2.5x8 respectively; 3M, Wuppertal, Germany). The operational setup involved counter-current flow, with deionized water as the liquid absorbent and pure CO_2 as the gas phase. A key finding was that while lumen-side mass transfer for both configurations was well-predicted by the Lévêque solution for laminar flow, shell-side performance diverged significantly. The parallel flow module suffered from severe shell-side maldistribution, leading to a lower CO_2 capture ratio compared to its lumen side. In contrast, the transverse flow module exhibited superior shell-side performance due to its central baffle, which promoted better fluid distribution. RTD analysis quantitatively confirmed these flow patterns, revealing a significantly reduced mean residence time (τ) and a high dispersion number indicative of strong bypass and channeling. Critically, the authors demonstrated that using the experimentally determined τ instead of the theoretical residence time allowed for the reconciliation of shell-side mass transfer data from both geometries. This led to the development of a generalized dimensionless correlation for the shell-side Sherwood number ($Sh = k_l \cdot d_h/D_m$, where k_l is the liquid phase mass transfer coefficient, d_h is the hydraulic diameter, and D_m is the molecular diffusivity): $Sh = 1.27 \cdot Re^{0.793} \cdot Sc^{0.33} \cdot (d_h/L)$.

In this chapter, the hydrodynamic behavior of the commercial hollow fiber membrane contactor (Liqui-Cel 2.5x8) is characterized using RTD analysis. This characterization is essential for understanding the flow patterns within the module, which directly influence the efficiency of mass transfer processes, as discussed in previous chapters. The Liqui-Cel 2.5x8 module, manufactured by 3M, is a widely used Extra-Flow design featuring microporous polypropylene hollow fibers arranged in a shell-and-tube configuration with a central baffle to promote transverse flow and minimize channeling on the shell side. The primary objectives are:

- To evaluate the RTD for two flow configurations: liquid flowing on the shell side and on the lumen side.
- To identify non-ideal flow behaviors, such as dispersion and dead zones, which can affect the efficiency of mass transfer processes.
- Estimate the actual volume occupied by the liquid in each configuration, thereby enabling the effective geometry of the commercial module under study to be deduced.

RTD analysis was conducted using a tracer injection technique, followed by signal acquisition at the HFMC inlet and outlet using calibrated conductivity sensors. The acquired signals were then pretreated in order to retrieve the baseline and deconvoluted in order to estimate the temporal variation of the normalized salt concentration. The resulting curves were analyzed using DTS Pro software (version 4.21). Different reactors models were used to describe the experimental curves measured in both, shell-side and lumen-side liquid flow experiments. The models were selected based on their ability to represent the complexities of the real flow behavior in membrane modules.

5.2 Experimental Design and System Characterization

The experimental setup, illustrated in Figure 5.1 was assembled to investigate RTD in the commercial HFMC module Liqui-Cel EXF 2.5x8 provided by 3M company. The module has a cylindrical design with an external outer diameter of 2.5 inches (6.35 cm) and a total length of 10.9 inches (27.7 cm) and contains a bundle of microporous polypropylene hollow fibers. These fibers have an outer diameter of 300 µm and provide a total effective membrane area of 1.27 m^2. The module is designed for shell side liquid flow rates of up to 700 L/h. Tap water was introduced into the module through a mass flow controller (M55-RGD-22-0-S, Bronkhorst). All experiments were conducted at ambient temperature. The hydrodynamic characterization was performed using a tracer technique. A sodium chloride (NaCl) solution was selected as the tracer due to its high solubility, non-reactivity with the polypropylene membrane material, and easily detectable conductivity signal. Conductivity and temperature were continuously monitored using an in-line conductivity meter (Jumo 20/00437646) equipped with a temperature transmitter. A volume comprised between 0.25 and 1 mL of a concentrated NaCl tracer was introduced as a pulse input at the module inlet via a manual syringe injection. The setup was connected to a computer for real-time data acquisition and storage, allowing monitoring of tracer injection. Different flow rates were investigated to elucidate their influence on flow patterns. Experiments were conducted from 80 to 235 L/h for the shell-side liquid flow configuration and 80 to 200 L/h for the lumen-side liquid flow. Following each tracer experiment, the system was flushed rigorously with tap water to return to the baseline of the conductivity sensors and avoid interference from residual tracer.

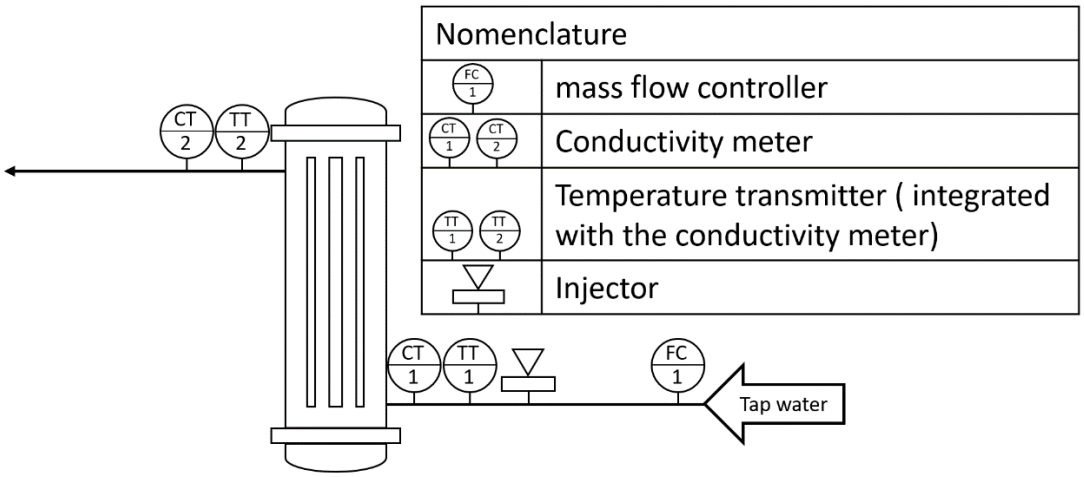

Figure 5.1 Schematic of experimental set up used for determining RTD in Liqui-cel EXF 2.5x8

5.3 Conductivity Sensor Calibration and Response Time Characterization

5.3.1 Conductivity Sensor Calibration

The conductivity probe was calibrated using three standard solutions (84, 147, and 1413 µS/cm at 25°C) provided by (VWR® Chemicals, Ireland). These standards were chosen to cover a wide range of conductivity values, ensuring the probe's accuracy across low, mid, and high conductivity ranges, which is essential for its intended applications. At the measurement temperature of 21°C, the corresponding conductivity values of the standards were adjusted to 77.44, 135.6, and 1304 µS/cm, respectively. The probe was immersed in each standard solution, and the measured values were recorded as 74.4, 141.2, and 1340 µS/cm. The calibration process involved rinsing the probe with deionized water between measurements. The percentage errors for the low, mid, and high conductivity standards were calculated as 3.93%, 4.13%, and 2.76%, respectively, indicating acceptable accuracy for all used standards. The results are summarized in Table 5.1.

The relationship between sodium chloride (NaCl) concentration in an aqueous solution and its electrical conductivity is also investigated. Four NaCl solutions were prepared at concentrations of 5 g/L, 2.5 g/L, 1 g/L, and 0.5 g/L, each dissolved in distilled water to ensure complete ionization. The conductivity of each solution was measured using our calibrated conductivity meter, with the temperature maintained at 21.7°C to control for temperature-dependent conductivity variations.

In accordance with Kohlrausch's law for strong electrolytes, the results demonstrated a proportional increase in conductivity with increasing NaCl concentrations. The conductivity-to-concentration ratio demonstrated relative stability across the solutions, with minor deviations

attributable to experimental variability or measurement precision. These findings are presented in Figure 5.2.

Table 5.1. Calibration of conductivity sensors with standards solutions at 21°C

Standard conductivity at 25°C (µS/cm)	Reference	Lot No.	expected conductivity at 21°C (µS/cm)	Measured conductivity at 21°C (µS/cm)	Percentage Error (%)
84	84131.260	230321	77.44	74.4	3.93
147	84132.260	230278	135.6	141.2	4.13
1413	84135.260	240246	1304	1340	2.76

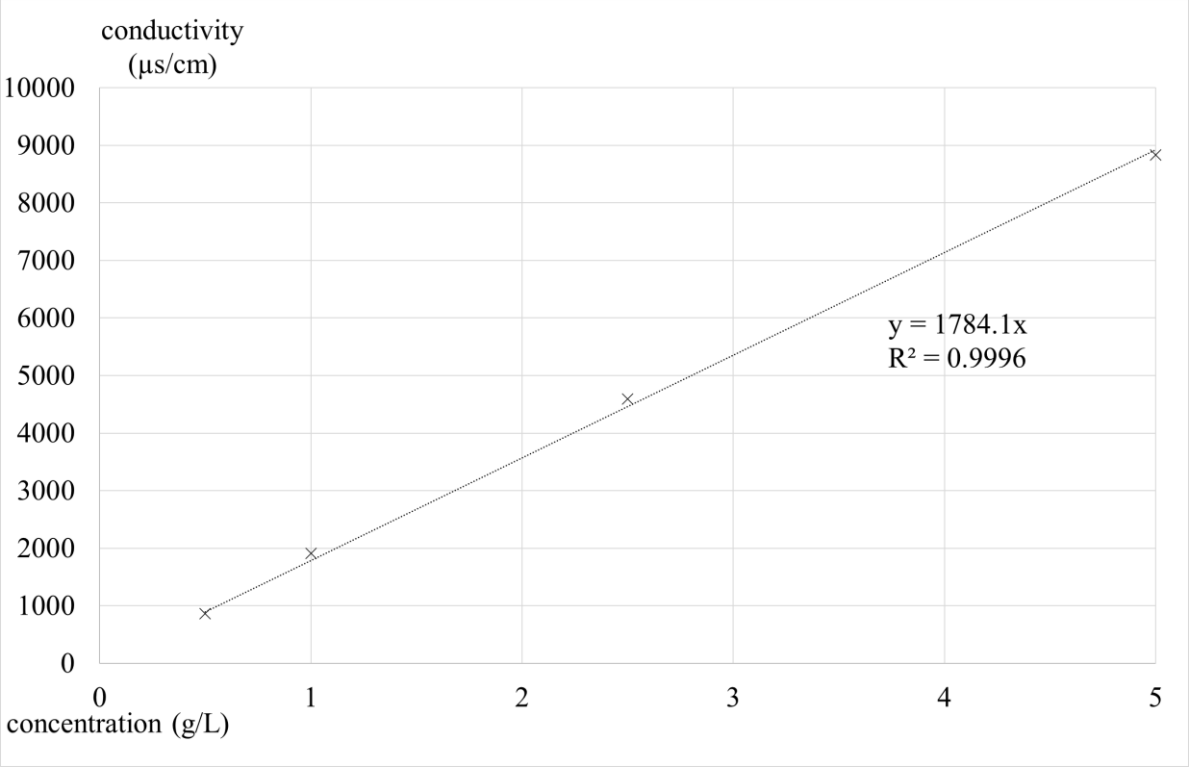

Figure 5.2 Electrical conductivity as a function of NaCl concentration in aqueous solution

5.3.2 Characterization of Sensor Dynamic Response

The dynamic response of the conductivity sensor was determined to characterize the relation between the measured conductivity signals and the instantaneous salt concentrations of the liquid flowing through the conductivity sensor. A step-response test was performed by rapidly transferring the sensor from deionized water (baseline) to a standard solution with a known conductivity of 1480 µS/cm.

The resulting change in conductivity was recorded at a sampling interval of 0.5 s (dt = 0.5 s) until a stable plateau was reached. The procedure was repeated three times for reproducibility. The response data was subsequently fitted to both first order and critically damped second-order dynamic models as illustrated in Figure 5.3.

The first-order model, described by $S(t) = E_0\, K\, (1 - e^{\frac{dt}{t_{RT}}})$ where;

E_0 : is the amplitude of the step (final plateau value), t_{RT}: sensor response time, K : is the system gain which quantifies the relationship between the input signal (the true conductivity) and the steady-state output signal (e.g., the probe's measured conductivity).

The critically damped second-order model, described by $s(t) = E_0\, K\, [1 - (1 + \omega_0 t)e^{-\omega_0 t}]$ whereas; ω_0: represents the undamped natural frequency. (See appendix 5-A)

Based on three replicate measurements, the first-order model yielded a time constant t_{RT} of 4.2 ± 0.15 seconds (mean ± standard deviation σ), while the second-order model provided an angular frequency ω_0 of 2.19 ± 0.08 rad/s.

The corresponding residuals of the model fits are presented in Figure 5.4. The impulse response functions derived from these characterized models were subsequently used to evaluate and correct for the distortion of the RTD signal introduced by the sensor dynamics. The deconvolution methodology is presented in Section 5.4 (Data Processing).

First-order correction assumes a simpler exponential, whereas second-order (critically damped) better accounts for the experimental sensor's dynamics, suggesting that the sensor response is reasonably approximated by a second order model.

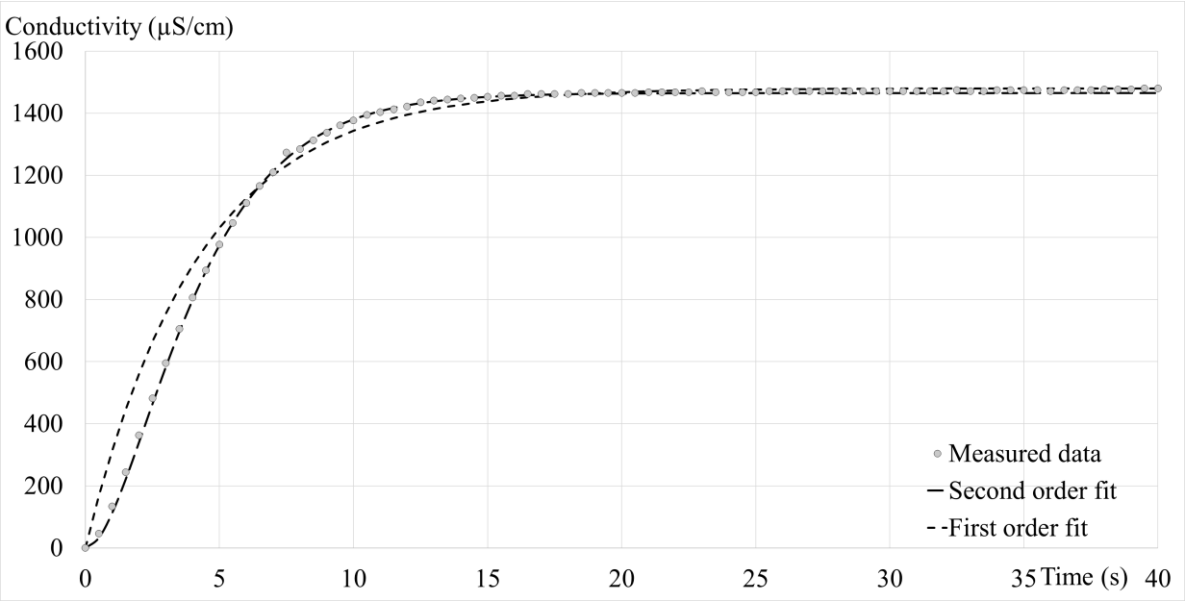

Figure 5.3 Step response of conductivity sensor.

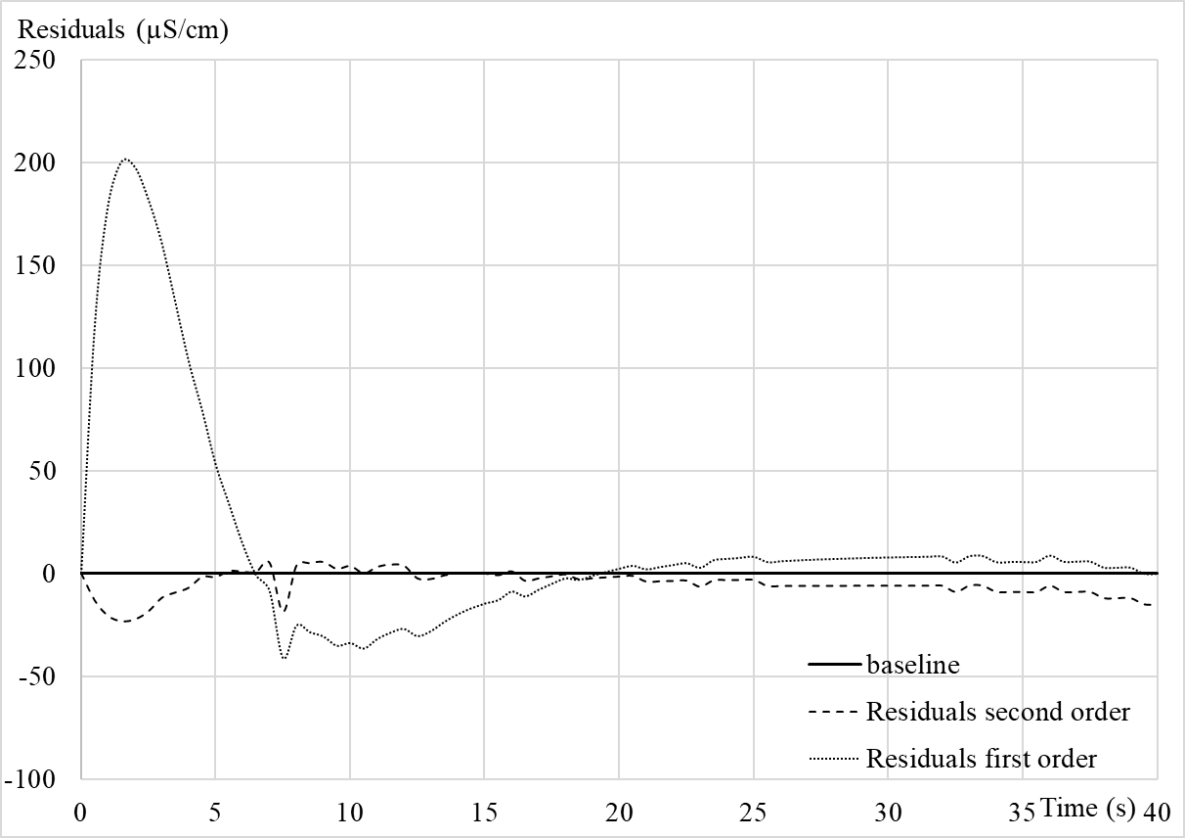

Figure 5.4 Residuals of model fits.

5.4Data Processing

The data processing pipeline, detailed in Figure 5.5 transforms the raw measured signal through signal conditioning, deconvolution via the critically damped second-order model, and normalization to yield the dimensionless concentration profile *C*(t)*, enabling quantitative comparison with applied reactor models. The consequence of data processing is demonstrated in Figures 5.6.

Appendix 5-B shows comparative visualizations of the treated conductivity signals, displaying the uncorrected signal, the first-order correction and the second-order deconvolution.

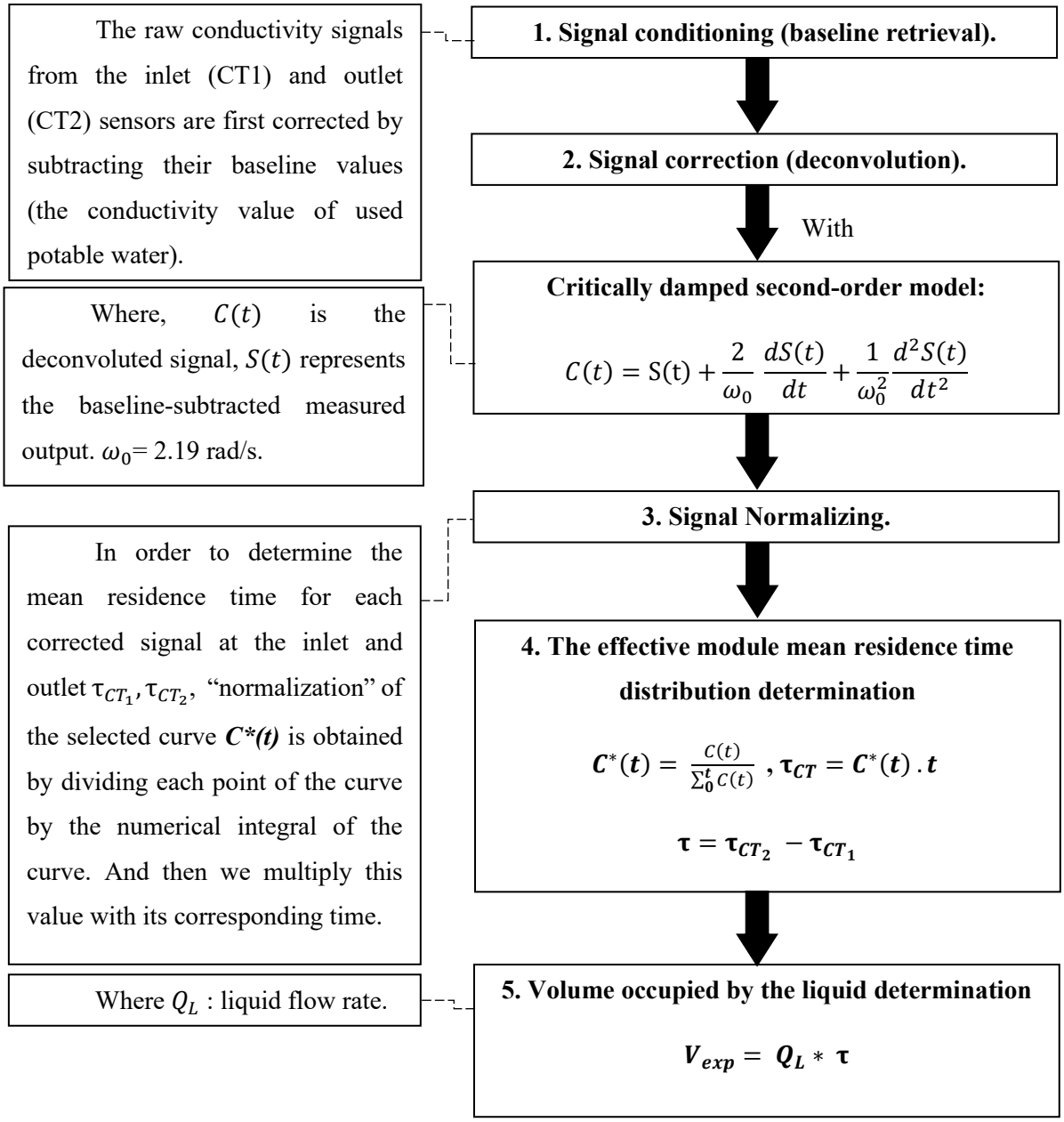

Figure 5.5 Schematic of data processing steps to achieve the dimensionless concentration profile.

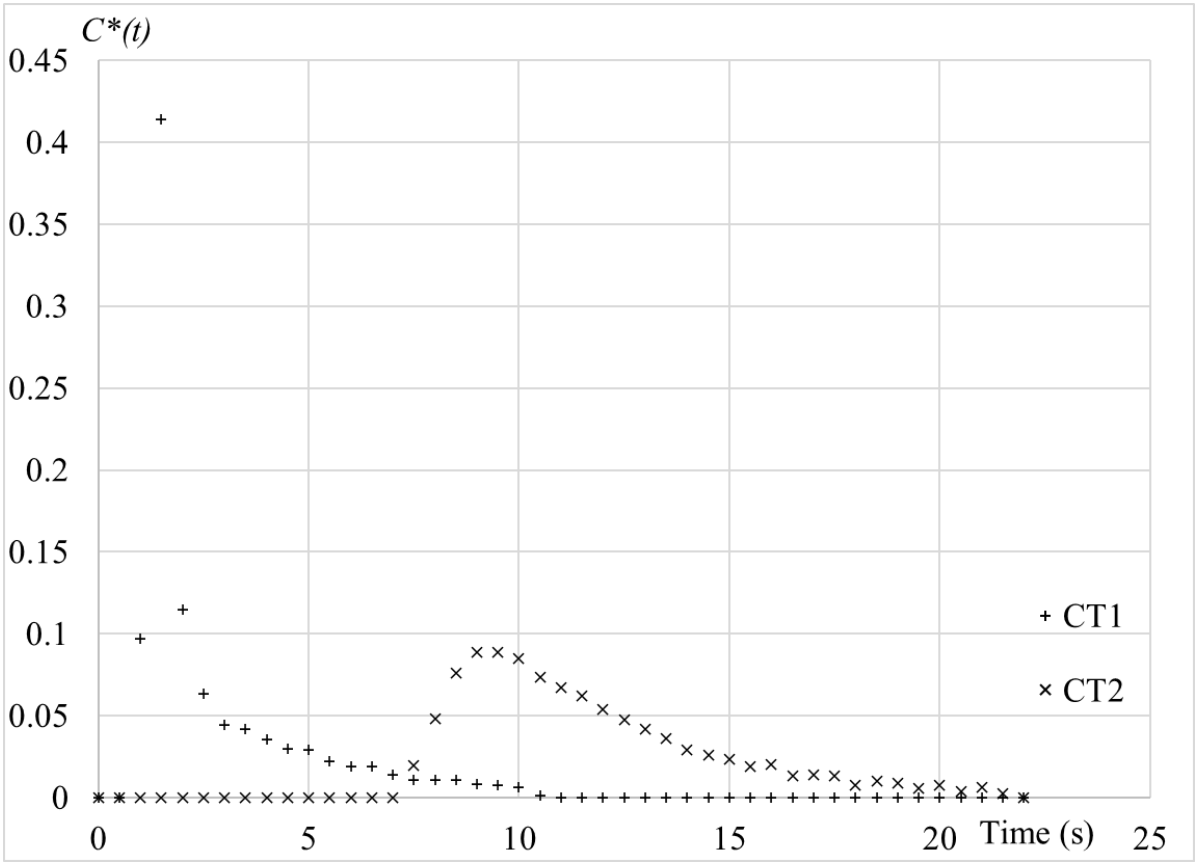

Figure 5.6. Treated conductivity signals (with second order deconvolution correction) at Q_L = 100 L/h showing mean residence time τ = 8.89 s.

5.5 Modeling Approach (Application of DTS Pro Software)

DTS Pro is an advanced computational software developed by UL PROPULS[7] for simulating fluid flow dynamics using RTD models. This tool is particularly valuable for interpreting tracer experiment data in reactor systems, offering applications across both industrial and laboratory-scale processes. The software is based on a modular network structure, where individual components are interconnected to form a directed flow path with a single input and output. Nodes within the network serve as junctions, enabling the integration of multiple branches and facilitating complex system representations [13].

The primary objective of using DTS Pro is to identify the suitable reactor model behavior that closely fits the experimentally obtained dimensionless concentration distribution at the reactor outlet,

[7] UL PROPULS is a French technology transfer company affiliated with the University of Lorraine that bridges research labs and industry by commercializing innovative tools for process engineering and scientific event organization.

for a given inlet signal. The parameters of the defined reactor model are regressed in order to fit to the measured output signal, knowing the measured input signal which, in general, is not a perfect Dirac function. The methodology of estimating the outlet signal involves the convolution of the input signal with the system's impulse response. The parameters of the reactor model are regressed to minimize the difference between the computed response and the experimentally measured output signal from the system.

The Sum of Squared Errors (SSE) analysis was performed to assess the fit of each reactor model to the experimental data. SSE represents the standard deviation of the residuals (the sum of the squared errors) and is calculated using the equation $SSE = \sum(y_p - y_o)^2$. Lower SSE values indicate a better fit.

To assess the reproducibility of the RTD measurements and fitted model parameters across multiple experimental and simulation replicates, the coefficient of variation (*CV*) was calculated for key parameters such as Peclet number and number of tanks (*J*). The *CV*, expressed as a percentage, quantifies the relative variability within the dataset and is defined as:

$CV = \frac{\sigma}{\mu} \times 100$, where σ is the standard deviation and μ is the mean of the parameter values obtained from the replicates.

This metric was computed directly in the data analysis spreadsheet using built-in statistical functions, with the mean and standard deviation derived from the processed conductivity signals and DTS Pro model fits.

5.5.1 Shell side configuration

In the shell-side configuration, the DTS Pro enables RTD simulation through the use of reactor models that closely match the provided dimensionless concentration curve. Four models are evaluated: continuous stirred-tank reactors in series (CSTRs), the plug flow reactor with boundary limits (closed to the diffusion) (PFR-D), CSTRs exchanging with a dead zone, and two CSTRs in parallel. These models were chosen based on their ability to mimic the behavior of the actual system. The parameters fitted in the different models are reported in Table 5.2. The four reactor models are presented in the following.

A. Continuous stirred-tank reactors in series (CSTRs)

This model assumes that the real reactor can be approximated as a series of *J* equally sized, ideal CSTRs, where each CSTR contributes to the overall residence time distribution (RTD). The perfect mixing cells in series with two parameters (see Table 5.2) permits progressive passing from the perfect mixing-cell (*J*=1) to the plug flow reactor (*J* infinite). The conceptual layout is shown in Figure 5.7.

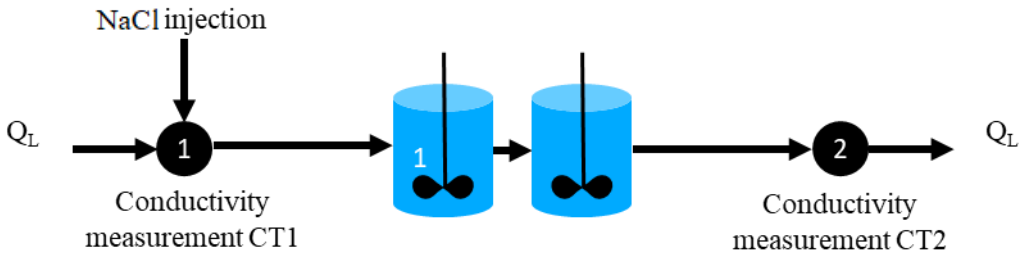

Figure 5.7 Illustrated CSTR in series model (CSTRs)

B. Plug flow reactor with boundary limits (closed to the diffusion) (PFR-D)

This scenario represents a PFR with closed-closed boundary conditions, meaning the flow is purely convective at the inlet and outlet, preventing axial dispersion across the system boundaries. In contrast, an ideal PFR has no axial mixing anywhere within the reactor. Relevant parameters and a schematic of the flow pattern are provided in Table 5.2 and Figure 5.8, respectively.

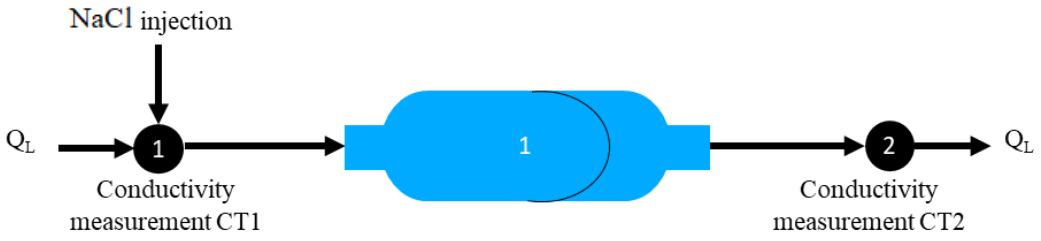

Figure 5.8 Schematic of plug flow reactor closed to the diffusion (PFR-D)

C. CSTRs exchanging with a dead volume

In this scenario, the main fluid flow passes through a series of perfectly mixed cells (ideal CSTRs in series). However, a fraction of the fluid exchanges with a stagnant (dead) zone, as illustrated in Figure 5.9, leading to delayed mixing and a tailing effect in the RTD curve. The principal parameters are indicated in Table 5.2.

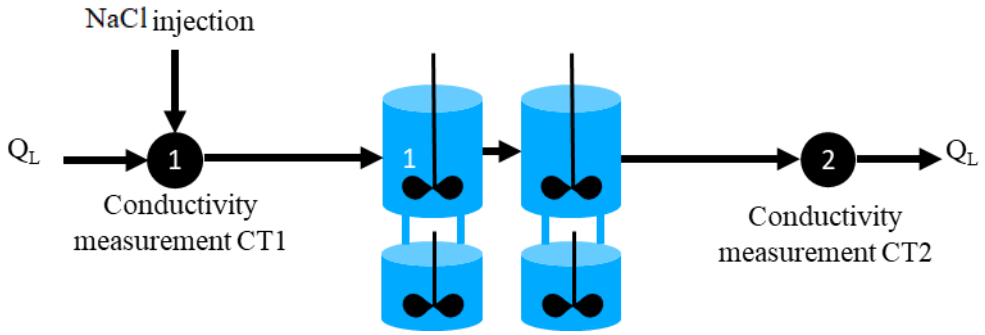

Figure 5.9 . Perfect mixing cells in series exchanging with a dead volume

D. Two CSTRs in parallel

This configuration comprises two individual CSTRs branches operating in parallel, each with its own RTD parameters (see Table 5.2). This configuration is applied to capture tailing of RTD curves. Figure 5.10 presents the dual-pathway design.

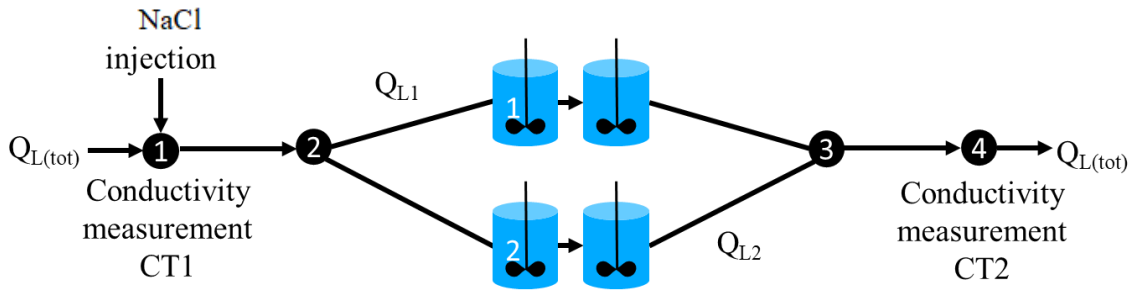

Figure 5.10. Two CSTRs in parallel configuration

5.5.2Lumen side configuration

The lumen-side configuration demonstrates lower complexity compared to the shell-side one. Structurally, the lumen comprises two functional compartments: a distribution chamber for introducing feed liquid into the fibers and a collection chamber for the outlet stream, together housing the fiber bundle. This physical arrangement lends itself to mathematical representation, where each compartment is modeled as a continuously stirred tank reactor (CSTR), while the fiber bundle is characterized as plug flow reactor with axial dispersion (PFR with diffusion), as shown in Figure 5.11. The key parameters are provided in Table 5.2.

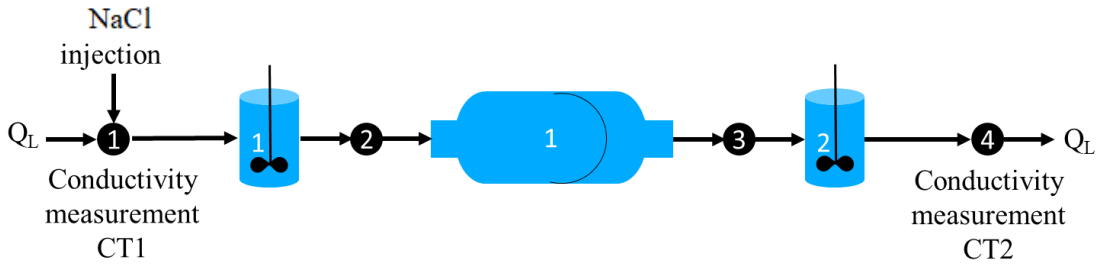

Figure 5.11 Lumen side configuration with the distribution chambers modelled as two continuously stirred tank reactors (CSTRs) and the fiber bundle as plug flow reactor

Table 5.2. Parameters are required for each reactor model.

Reactor model	**Parameters**	**Degrees of Freedom**	**Independent parameters**
Plug flow reactor with axial dispersion with boundary limits closed to the diffusion	- Mean residence time: τ Or Volume: V - Peclet number: Pe - Water flow rate Q_L	2	Pe and V
Perfect mixing cells in series (CSTRs)	- Mean residence time: τ or Volume: V - Number of mixing-cell: J - Water flow rate Q_L	2	J and V
Perfect mixing cells in series (CSTRs) exchanging with a dead zone	- Mean residence time (in the principal outflow): τ_{act} - Volume of the principal outflow (total active volume): $V_{act} = J^* V_1$, where V_1 volume of one of the mixing cells in series and V_2 the volume of the associated dead zone. - Number of mixing-cell: J - Exchange time constant $t_m = \frac{V_2}{\beta Q}$, where β is the proportion of flow rate exchanging with the dead volume	4	V_{act}, J, K, and β

	- Volume ratio : $K = \frac{V_2}{V_1}$ - Water flow rate Q_L		
Two CSTRs in parallel	- Mean residence time: τ Or Volume: V (for each CSTRs, V_1, V_2) - Number of mixing-cell: J (for each CSTRs) - $\frac{Q_2}{Q_1} = 0.3$ - Water flow rate Q_L	5	V_1 , V_2 , J_1, J_2, $\frac{Q_2}{Q_1}$
Lumen side configuration	- For each chamber: mean residence time: τ or Volume: V (it's supposed that they have the same volume) - For the fiber bundle: mean residence time: τ , and Peclet number: *Pe* - V for each distribution chamber is fixed by geometric analysis - Water flow rate Q_L	2	*V* of plug flow reactor, and *Pe*

5.6 Results and discussion

5.6.1 Shell side configuration

The RTD experiments were conducted at a liquid flow rate of 75 to 235 L/h on the shell side of the module, using NaCl tracer injections. These flow rates fall within the module's operational range (up to 700 L/h). The raw conductivity signals were processed as described in Section 5.4, including baseline subtraction, correction of the dynamic response of the conductivity probes, and normalization. The mean residence times (τ) calculated from the corrected signals decrease with increasing flow rate, as expected ($\tau \propto 1/Q_L$), while the effective volumes (V) remain relatively consistent around 0.23–0.24 L across all conducted experiments.

To quantify the observed non-idealities, the experimental inlet and outlet dimensionless concentration curves were fitted, using DTS Pro software, to four selected models: axial dispersion plug flow, CSTRs (perfect mixing cells in series), CSTRs exchanging with a dead volume, and two CSTRs in parallel. The fitting results and interpretations are discussed in the following subsections.

A. Continuous stirred-tank reactors in series (CSTRs)

The RTD experiments were conducted at flow rates (Q_L) of 79, 100, 150, 193, 200 and 235 L/h on the shell side, yielding the parameters summarized in Table 5.3. Figure 5.12 shows the comparison between the dimensionless concentration curve and the CSTRs model prediction at 100 L/h.

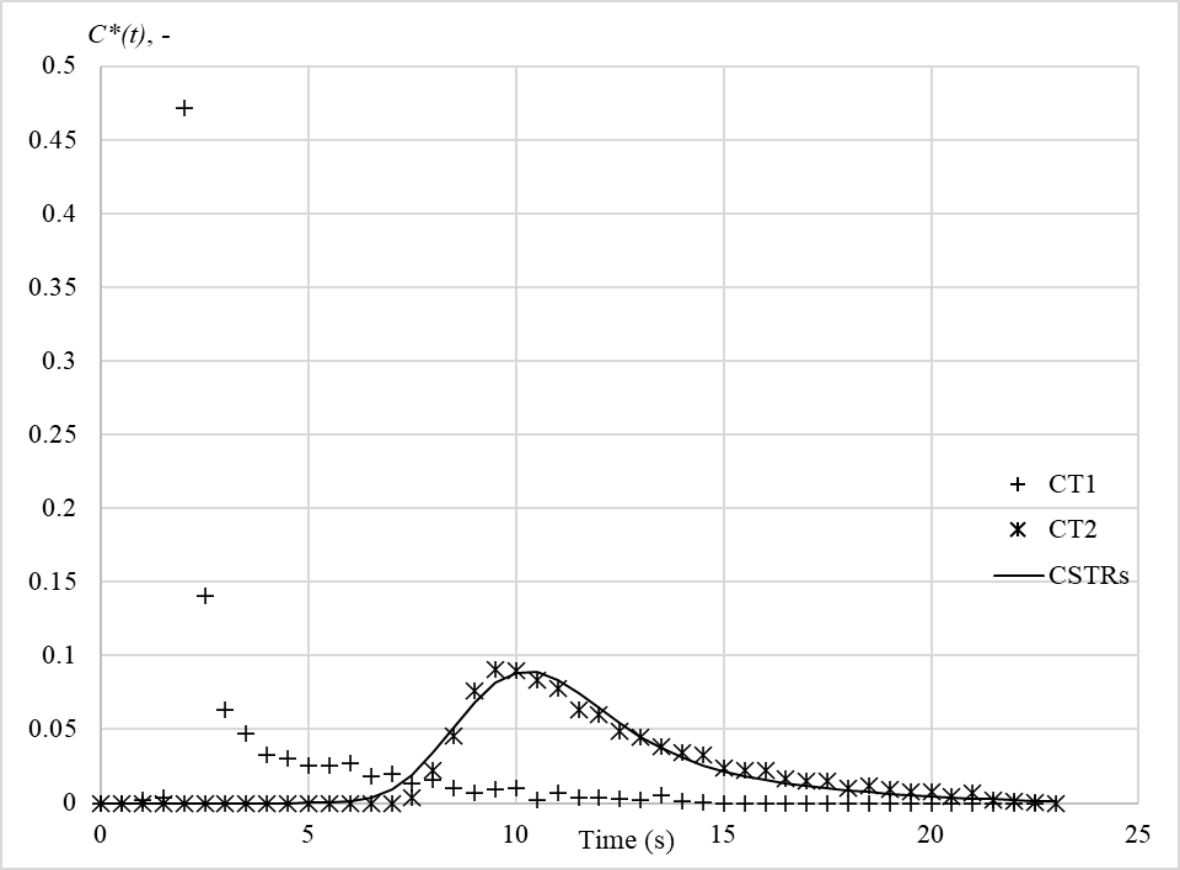

Figure 5.12 Comparison of Experimental Dimensionless Concentration Curve and CSTRs Model Prediction at 100 L/h (Shell-Side).

Table 5.3 Derived parameters for CSTRs reactor model

Q_L (L/h)	J (-)	V model, L	V exp, L	SSE, -
79	17.78	0.226	0.234	0.0044
100	17.45	0.226	0.233	0.0011
150	16.71	0.217	0.237	0.0062
193	17.58	0.227	0.245	0.0048
200	15.51	0.222	0.236	0.0057
235	16.47	0.226	0.240	0.0080
Average	16.91	0.224	0.238	0.0050
CV (%)	5	1.6	2	-

The regressed volumes (V model) show excellent agreement with experimental values (V exp), with an average difference of ~ 5.7% (0.224 L vs. 0.238 L) and tight variability (CV < 2%). The optimized number of CSTRs (J) ranged from 15.51 to 17.78, averaging 16.91 with a coefficient of variation (CV) of 5 % corresponding to Peclet numbers of 33.8 (Pe ≈ 2J). This level of dispersion suggests that the shell-side flow is far from fully mixed (Pe → 0), aligning with the Extra-Flow design's intent to minimize bypassing through the central baffle. The model provides an initial fit, but the SSE values are relatively high (e.g., Average = 0.005). More importantly, the model is not able to represent the relative stiff initial increase of the concentration profiles at the contactor outlet. This mismatch indicates that the CSTRs model cannot fully capture the real flow behavior. A more complex reactor model is needed to represent the extended tailing while achieving a lower SSE.

B. Plug flow reactor with boundary limits (closed to the diffusion) (PFR-D)

The plug flow model provides also a baseline representation of the shell-side hydrodynamics, assuming a uniform velocity profile with axial mixing. The RTD experiments were conducted at flow rates (Q_L) of 79, 100, 150, 193, 200 and 235 L/h on the shell side, yielding the parameters summarized in Table 5.4.

Figure 5.13 plots the fitted Peclet numbers (Pe) against flow rate (Q_L), while Figure 5.14 shows the comparison between the dimensionless concentration curve and the PFR-D model prediction at 100 L/h.

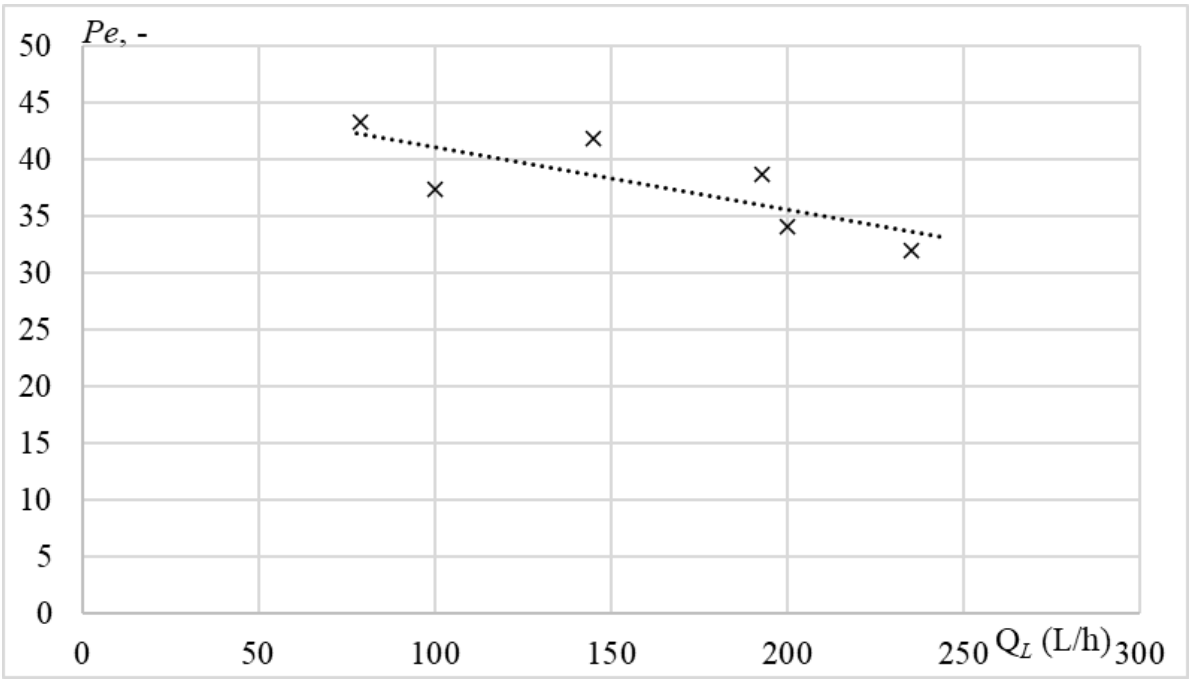

Figure 5.13 Fitted Péclet Number (Pe) as a Function of Shell-Side Flow Rate (Q_L) for the PFR-D Model

The Peclet numbers decrease with increasing Q_L, from 43 at 79 L/h to 32 at 235 L/h, averaging 37.9 with a coefficient of variation (CV) of 11.5 %. This trend reflects increased dispersion at high flow rates, yet a high Pe value confirms plug-like behavior, which is in line with the intended design of the module's geometry.

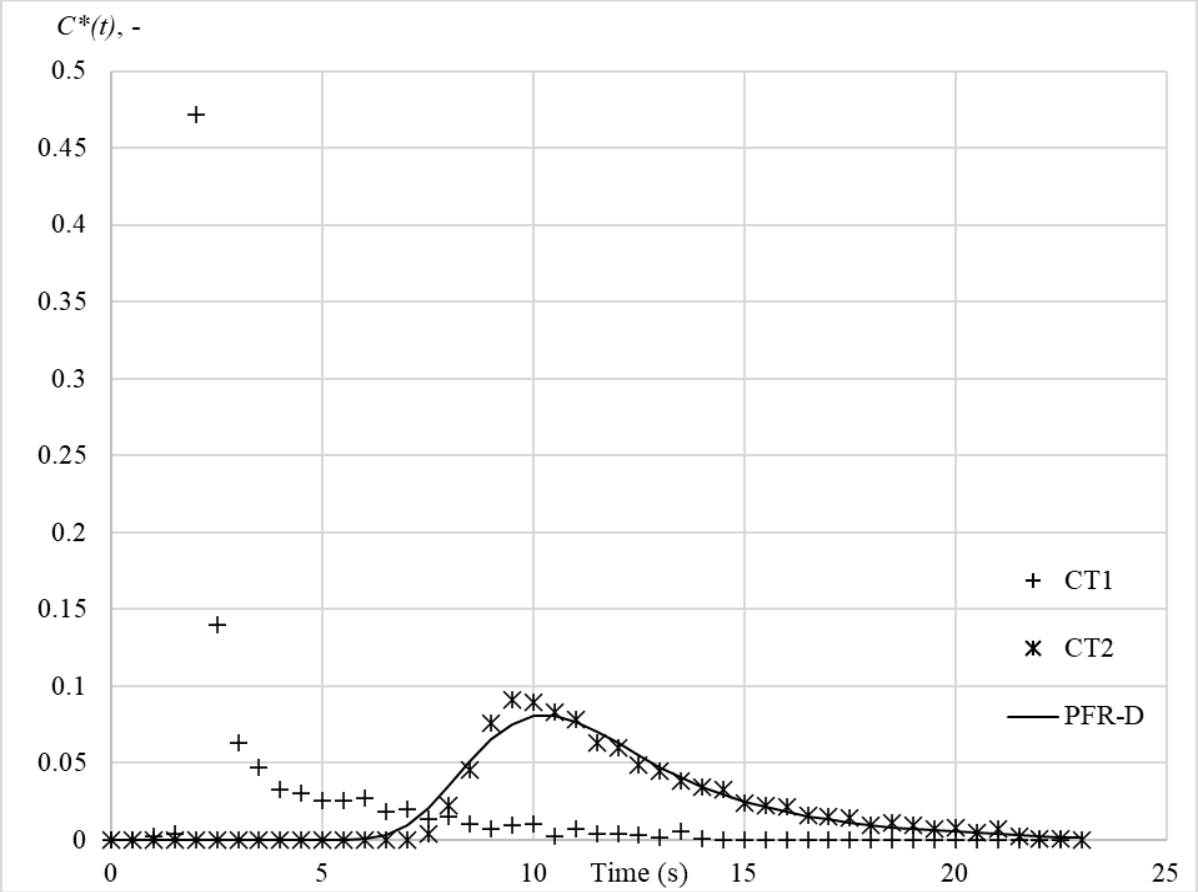

Figure 5.14 Comparison of experimental dimensionless concentration curve and PFR-D model prediction at 100 L/h (shell-side).

The regressed volumes (V model) average 0.217 L with a CV of 3.4 %, underestimating experimental values (V exp) by ~ 8.9% on average (0.217 L vs. 0.238 L) and showing moderate variability (CV = 1.8% for V exp). The average SSE of 0.0019 outperforms the CSTRs model's 0.005, indicating superior overall curve matching. However, like the CSTRs approach, the PFR-D fails to capture the pronounced long tailing in the dimensionless concentration profiles, underestimating late-time tracer retention and suggesting unmodeled dead zones or bypass flow. A more advanced model incorporating exchange dynamics is warranted for precise tail representation and lower residuals.

Table 5.4 Derived parameters for PFR-D reactor model

Q_L (L/h)	Pe (-)	V_{exp}, L	V_{model}, L	SSE, -
79	43.3	0.234	0.226	0.0014
100	37.4	0.233	0.213	0.0013
150	41.9	0.237	0.214	0.0017
193	38.7	0.245	0.207	0.0019
200	34.1	0.236	0.213	0.0018
235	32	0.240	0.225	0.0030
Average	37.9	0.238	0.217	0.0019
CV (%)	11	1.8	3.4	-

C. CSTRs exchanging with a dead volume

The axial dispersion (PFR-D) and basic CSTRs models reproduced the main RTD peak, but both failed to capture the overall shape of the experimentally determined outlet curves. To address this, the CSTRs with dead volume model was employed. In this framework, the shell-side hydrodynamics are represented as a series of J perfectly mixed cells V_1 (the active flow path), each exchanging mass with an associated stagnant volume V_2. This exchange mechanism enables the model to reproduce both the main RTD peak and the long trailing region.

The analysis covered 19 experiments conducted at shell-side flow rates (Q_L) between 80 and 235 L/h. The total liquid holdup including dead zones is expressed as: $V_{Model} = J(V_1 + V_2)$ .The fitted parameters across all replicates are summarized in Table 5.5. Figure 5.15 shows the comparison between the dimensionless concentration profile and the CSTRs exchanging with dead zone model prediction at 145 L/h.

Table 5.5 Derived Parameters for the CSTRs exchanging with dead volume model.

Parameter	Average value (CV%)
V_{exp} (L)	0.240 (2.4 %)
V_{act} (L)	0.192 (1.8%)
V_{Model} (L)	0.230 (1.9 %)
$J\ (-)$	71.49 (1.5 %)
$K\ (-)$	0.199 (3.3 %)
$\beta\ (-)$	0.014 (13 %)
SSE	5.39 E-04

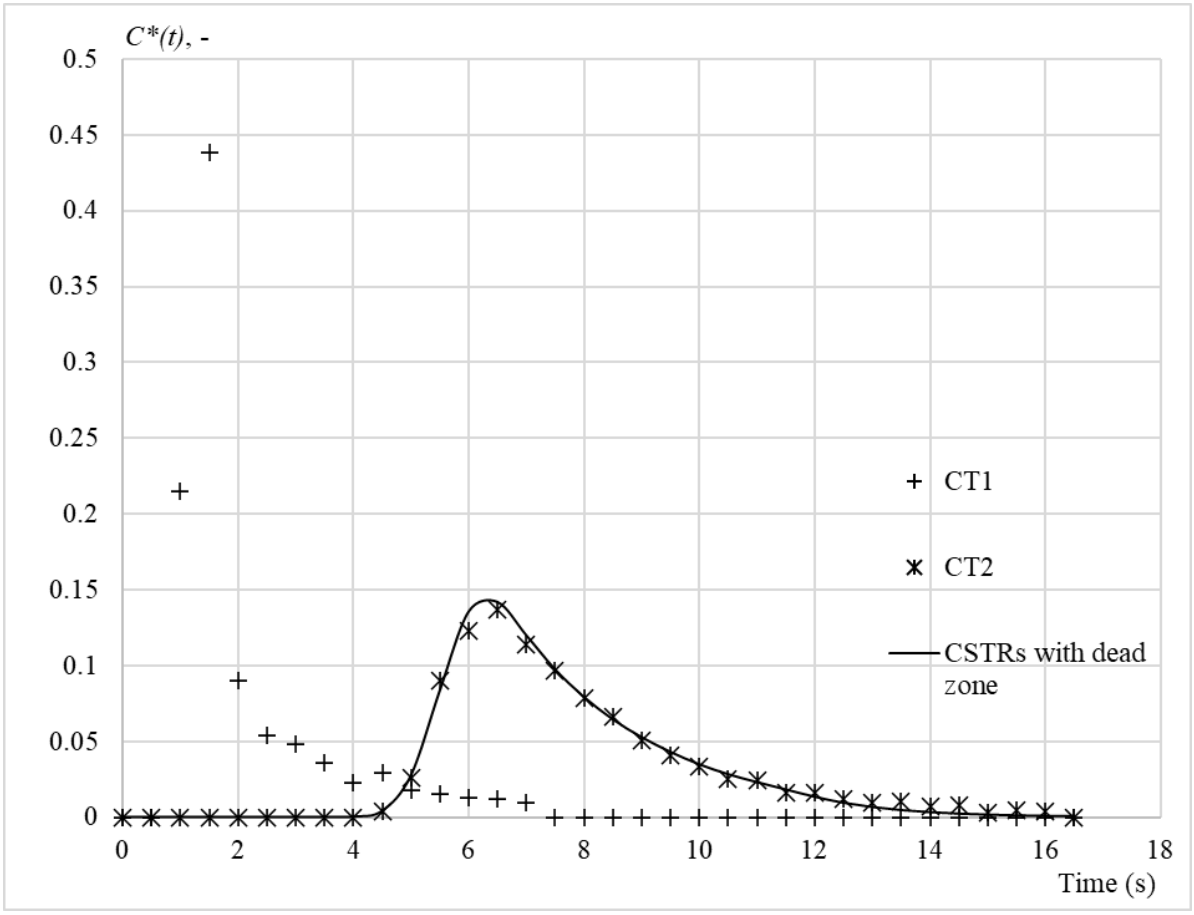

Figure 5.15 Comparison of experimental dimensionless concentration curve and CSTRs exchanging with dead zone model prediction at 145 L/h (shell-side).

The regressed volumes (V model) closely match experimental derived values (V exp), differing by ~ 4% on average (0.230 L vs. 0.240 L) with low variability (CV < 3%). The optimized number of CSTRs (J) averaged 71.5 with a low CV of 1.5%, confirms plug flow behavior. The dead zone volume ratio ($K = V_2/V_1$) averaged 0.199 (CV = 3.3%), suggesting stagnant regions comprise about 17% of the active volume per cell, while the exchange flow proportion (β) averaged 0.014 (CV = 13%), reflecting limited but persistent interaction with dead zones. SSE averaged 5.39×10^{-4}, substantially lower than the CSTRs model (0.005) and PFR-D (0.00185), confirming superior fit, particularly in capturing tailing via exchange dynamics. Figure 5.16 plots the regressed parameters K, β, and J versus flow rate Q_L, revealing that their values remain almost unchanged (as mentioned in Table 5.5) over the Q_L range.

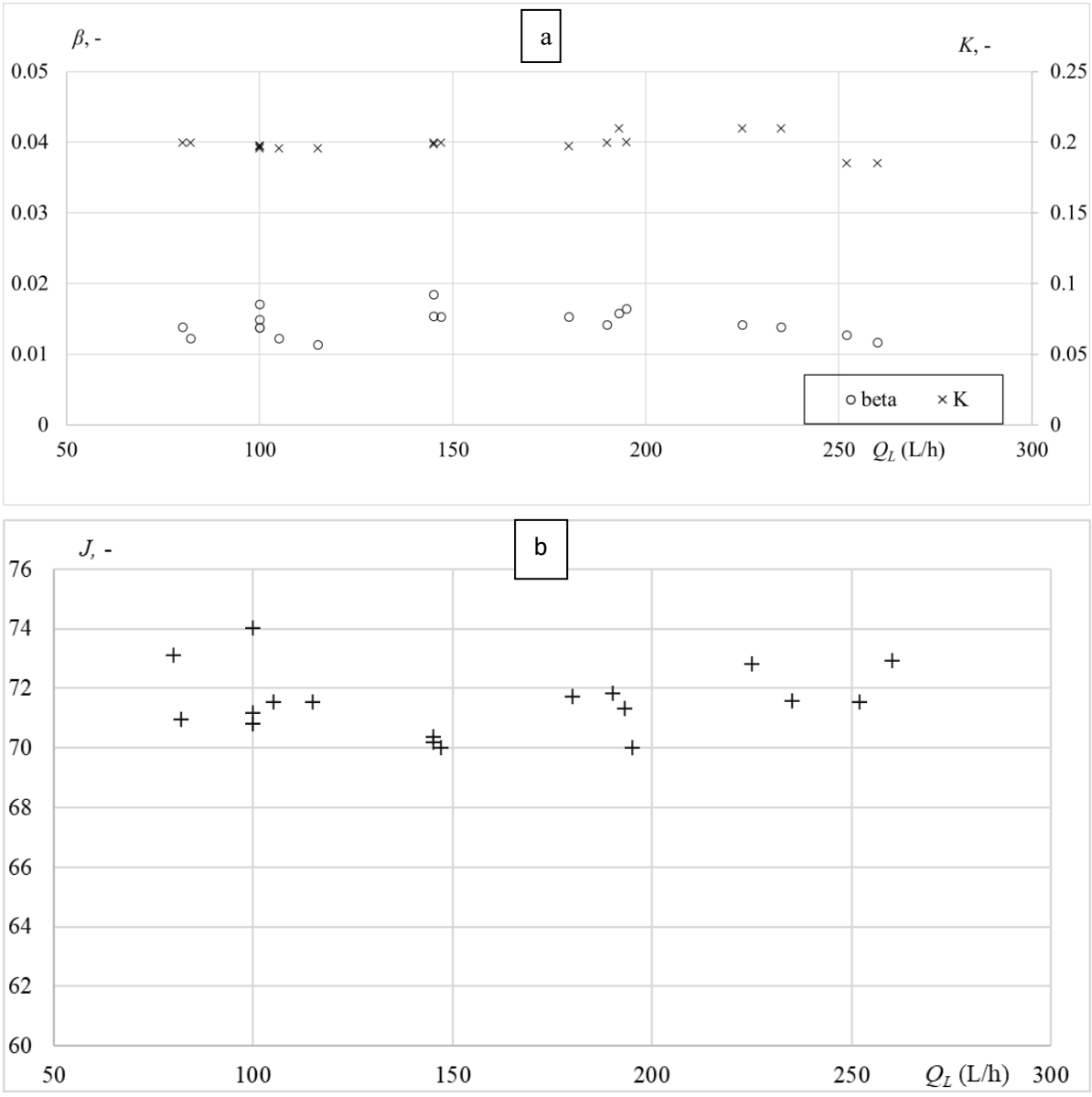

Figure 5.16 regressed parameters for the CSTRs with dead zone model as a function of shell-side flow rate (Q_L): a) dead zone ratio K and exchange proportion β. b) number of CSTRs J

The cumulative exchange proportion $J^*\beta$ quantifies the total fraction of the flow rate that interacts with dead zones across all (J) perfectly mixed cells in the CSTRs exchanging with a dead zone model for the shell-side flow. Analysis of the simulation data revealed an average value of $J^*\beta$ of approximately ≈ 1. From the definition of the active volume, $J = \frac{\tau_{act}*Q}{V_1}$ can be determined, and the exchange time constant leads to $\beta = \frac{V_2}{t_m Q}$, and thus to the relation $\frac{\tau_{act}}{t_m} = \frac{V_1}{V_2}$ indicating that the time spent in the principal flow region (τ_{act}) versus the exchange time (t_m) with the stagnant zones, scales with their respective volumes. This inspired the exploration of a two CSTRs in parallel model to further investigate potential parallel flow paths with distinct mixing characteristic that could better represent the complex shell-side hydrodynamics and channelling effects in the HFMC.

D. Two CSTRs in parallel

The observed scaling relationship in the CSTRs exchanging with a dead zone model, where $\frac{\tau_{act}}{t_m} = \frac{V_1}{V_2}$, underscores the proportional influence of active and stagnant volumes on residence times, prompting further exploration of alternative configurations to better delineate the shell-side flow complexities in the Liqui-Cel 2.5x8 HFMC. Motivated by this insight and the potential for simplified mass transfer correlations, the two CSTRs in parallel model was employed. This approach conceptualizes the shell-side hydrodynamics as two flow branches, each comprising a series of perfectly mixed cells with independent parameters (V, and J per branch), allowing for distinct fast and slow paths that may arise from channelling or non-uniform flow distribution. The model conducted at flow rates (Q_L) of 79, 100, 150, 193, 200 and 235 L/h on the shell side using DTS Pro software, with the assumption that $\frac{Q_2}{Q_1} = 0.3$, yielding the parameters summarized in Figure 5.18. This initial value has been adjusted to better fit the experimental data. The applied model effectively captured the dimensionless concentration profile (see Figure 5.17). Average Fitted parameters across replicates are summarized in Table 5.6

Table 5.6 Average fitted parameters for the two CSTRs in parallel model

Parameter	Average value (CV%)
V_1 (L)	0.158 (1.7 %)
V_2 (L)	0.07 (0.3 %)
$J_1\ (-)$	37.4 (5.8 %)
$J_2\ (-)$	30.3 (2.9 %)
SSE	5.45E-04

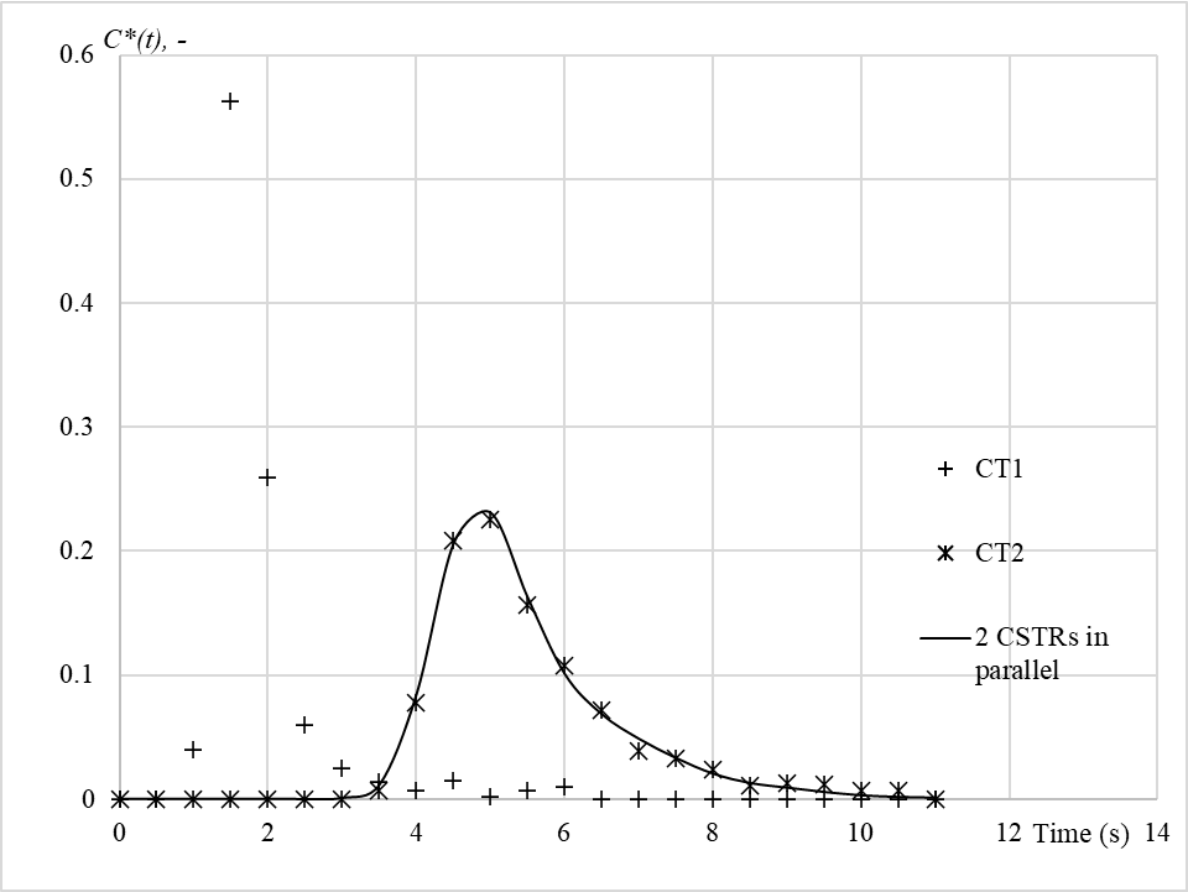

Figure 5.17 Comparison of experimental dimensionless concentration profile and two CSTRs in parallel model prediction at Q_L = 235 L/h

The regressed volumes for the fast path (V_1) averaged 0.158 L with a low CV of 1.7%, and representing ~69.5% of total hold-up, while the slow path volumes (V_2) remained stable at 0.069 L (CV = 0.3%), comprising ~30.5% of the total hold-up, yielding a consistent V_2/V_1 ratio of ~0.44 (CV = 1.6%) that aligns with the fixed Q_2/Q_1 split of 0.3, indicative of a dominant fast channel with minor bypassing. The number of CSTRs in the fast path (J_1) ranged from 35 to 40, averaging 37.4 with a CV of 5.8%, suggesting moderately dispersive mixing in the primary flow, whereas J_2 stabilized around 30 (CV = 2.9%), reflecting a more uniform slow path possibly along fiber peripheries. Total modelled volumes ($V_1 + V_2$) averaged 0.227 L, closely matching Vexp of 0.238 L (a difference of~4.6%). SSE averaged 5.45×10^{-4} comparable to the CSTRs exchanging with dead zones model (5.39×10^{-4}) and markedly lower than CSTRs (0.005) and PFR-D (0.00185), confirming robust capture of dual-path dynamics and tailing without overcomplication.

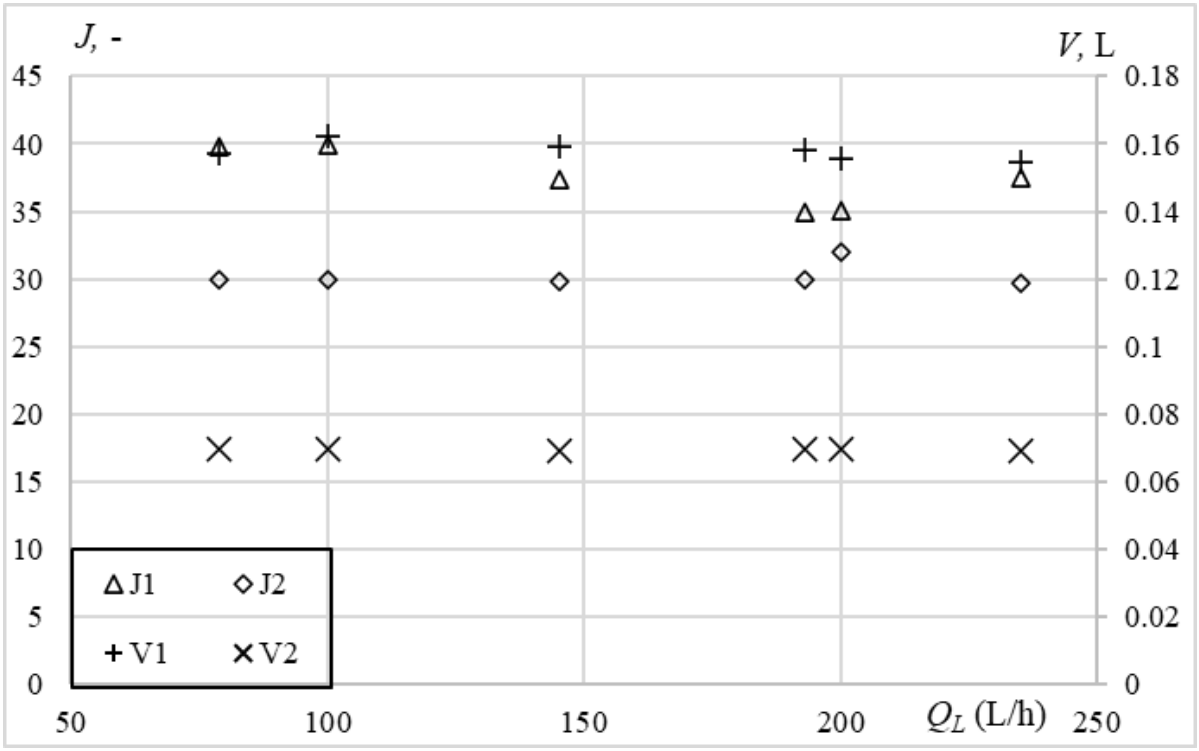

Figure 5.18 Fitted Parameters (Volumes V1 and V2, Number of CSTRs J1 and J2) for the Two CSTRs in Parallel Model Across Shell-Side Flow Rates.

5.6.2 Lumen side configuration

The RTD model for the lumen side comprises two continuously stirred tank reactors (CSTRs), with one representing the distribution chamber and the other representing the collection chamber. These are connected in series with a plug flow reactor (PFR) with boundary limits (closed to the diffusion), in order to simulate the flow within the fibres. This configuration was implemented in DTS Pro software to fit experimental RTD data obtained from tracer injection experiments conducted at flow rates of 70, 83, 155, 195 and 250 L/h on the lumen side. The volume of each distribution/collection chamber, determined by geometric analysis and fixed at 0.0312 L, providing a baseline for the total hold-up volume (0.0624 L for both chambers combined). The key fitted parameters from the model were the effective liquid volume occupied within the fibers (V) and the Peclet number (Pe) for the PFR, which quantifies the ratio of advective to dispersive transport. Figure 5.19 shows the comparison between the dimensionless concentration curve and the proposed model at flowrate 70 L/h.

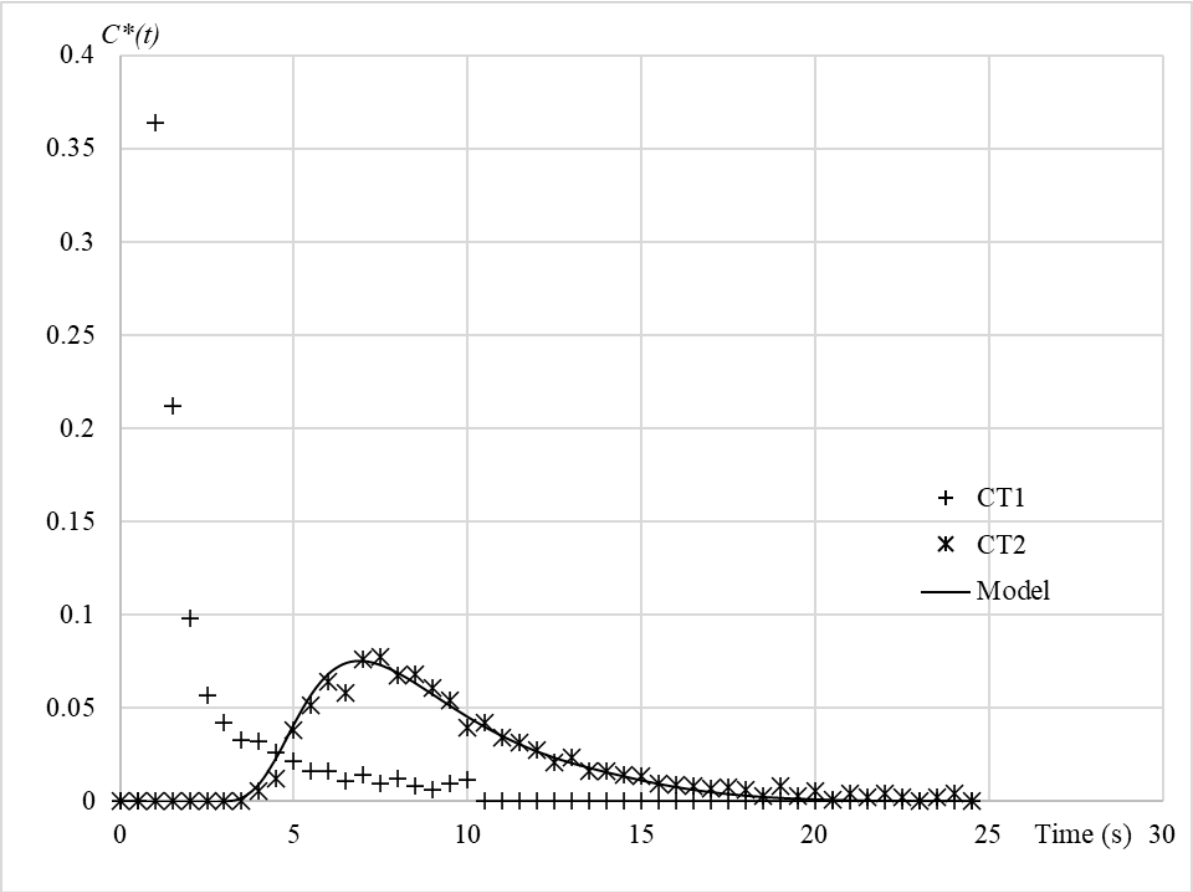

Figure 5.19 Comparison between the dimensionless concentration curve and the proposed model at flowrate 70 L/h (lumen side).

The fitted fiber volumes (V) exhibit strong consistency across the tested flow rates, with an average value of 0.0683 L . The coefficient of variation (CV) is of 7.1% indicating that the model reliably captures the real reactor behavior within the fibers, independent of flow rate changing. When combined with the fixed chamber volumes (total 0.0624 L), the overall system hold-up is approximately 0.1307 L. For reference, the fiber module supplier reported an overall lumen-side volume of 0.15 L; however, the measurement methodology was not specified. In hollow fiber membrane systems, such volumes are commonly determined via gravimetric methods or direct filling techniques (e.g., displacing air or measuring liquid uptake under controlled pressure to quantify accessible lumen hold-up). The approximately 13% discrepancy between the modeled hold-up (0.1307 L) and supplier value (0.15 L) [14] may arise from inclusion of additional interstitial spaces or manufacturing tolerances in fiber packing density. The Peclet number (Pe) from the model fits is plotted against lumen-side flow rate (Q_L) in Figure 5.20, illustrating the trend of decreasing Pe with increasing Q_L.

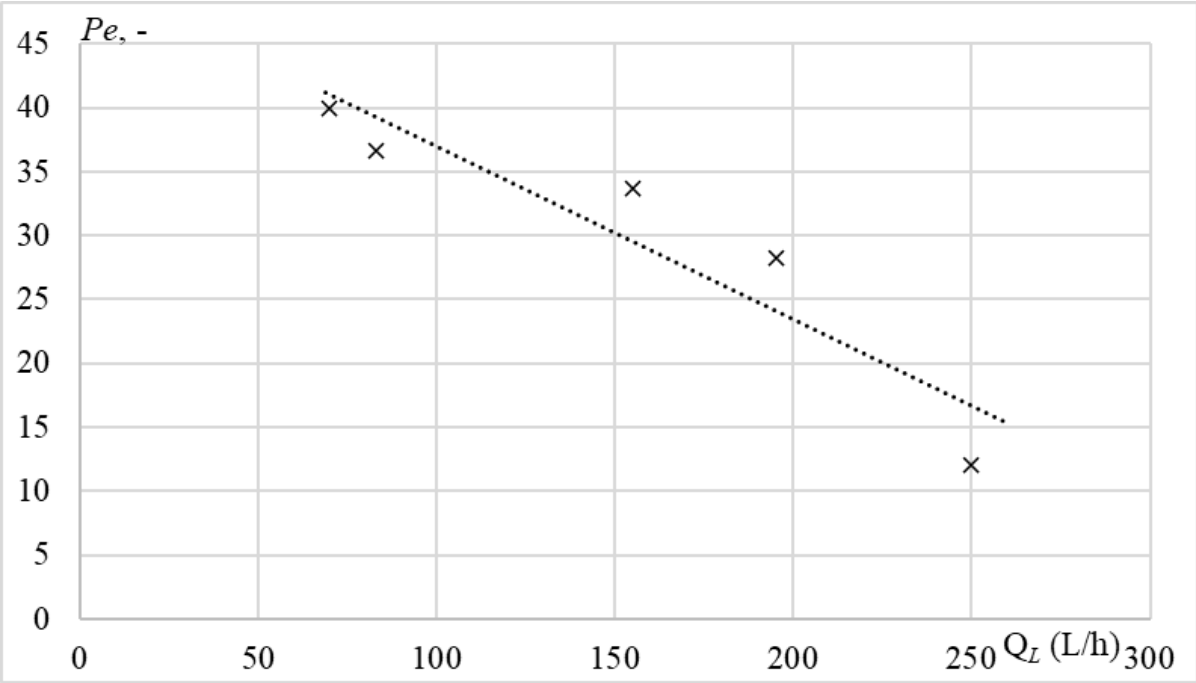

Figure 5.20 fitted Péclet number as a function of lumen-side flow rate (Q_L)

The Peclet number exhibits an inverse relationship with flow rate, indicating enhanced axial dispersion at higher flowrates. Despite this, the fact that Pe remains greater than 10 across all tested conditions confirms that advection dominates, thereby validating the plug flow reactor (PFR) assumption.

5.6.3 Residence time distribution analysis in the shell side

To illustrate the residence time distribution (RTD) characteristics captured by the selected models, the dimensionless RTD E(θ) and RTD E(t) curves were simulated for pulse tracer inputs using the average fitted parameters from the DTS Pro optimizations. These curves represent the probability density of fluid elements residing in the shell side for a given time, highlighting mixing, dispersion, and tailing behaviors. Simulations were performed at a representative flow rate of 145 L/h, yielding mean residence times of approximately 5.67 s for both models: two CSTRs in parallel and CSTRs with dead zones (see figure 5.21 and 5.22 for corresponding *E(t)* and *E(θ)* respectively). The two CSTRs in parallel model emphasizes dual-path hydrodynamics with a pronounced early peak from the fast channel and minor tailing from the slow path. In contrast, the CSTRs exchanging with dead zone model exhibits a sharp initial peak from axial advection followed by an extended tail due to gradual release from stagnant regions, aligning with observed experimental tailing.

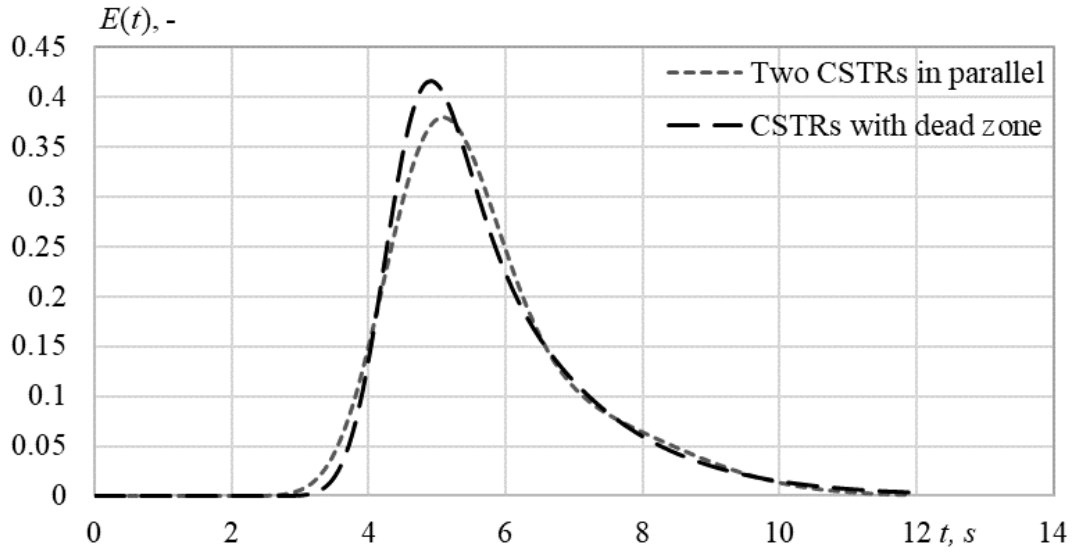

Figure 5.21 simulated RTD *E(t)* curves for shell-side at 145 L/h using average fitted parameters.

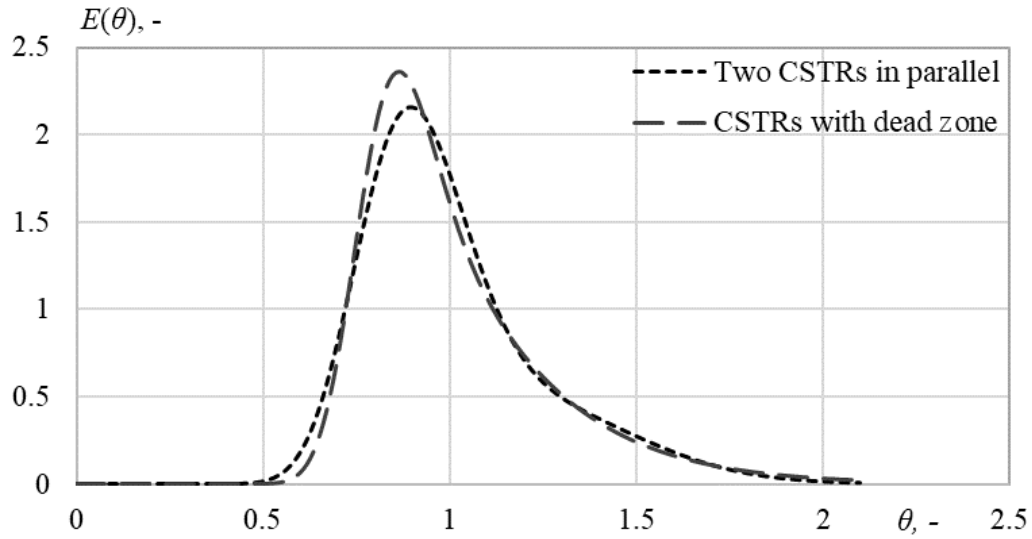

Figure 5.22 simulated dimensionless RTD *E(θ)* curves for shell-side at 145 L/h using average fitted parameters.

5.7Conclusions and Perspectives

The The RTD analysis conducted on the Liqui-Cel 2.5 × 8 hollow fiber membrane contactor provides a comprehensive characterization of its hydrodynamic behavior under both shell-side and lumen-side flow configurations, revealing insights critical for optimizing mass transfer processes in gas-liquid contactor applications. On the shell side, tracer experiments across flow rates of 80–235 L/h demonstrated consistent effective hold-up volumes (~0.24 L) and mean residence times scaling

inversely with flow rate. The results confirmed purely plug-flow characteristics with high Pe ~38 and J ~17, in simpler reactor models (PFR-D and CSTRs approaches), escalating to J ~71 in advanced ones (CSTRs with dead zones and two CSTRs in parallel). Despite evident non-idealities such as tailing indicative of channelling and stagnant zones (~17% dead volume fraction), the flow behavior is clearly plug flow dominated, aligning with the Extra-Flow design's central baffle for enhanced transverse mixing and minimal bypassing. The lumen-side configuration further reinforced this, yielding stable fiber hold-up (~0.068 L) and overall system volumes (~0.131 L) with Pe > 10 across 70–250 L/h, validating the CSTR-PFR-CSTR hybrid as a reliable representation of near-ideal plug flow within fibers, though ~13% below supplier estimates (0.15 L) due to inclusion of additional interstitial spaces or manufacturing tolerances in fiber packing density.

Although models such as CSTRs with dead zones and two CSTRs in parallel effectively fitted the experimental RTD curves (SSE ~5×10^{-4}) outperforming simpler PFR-D and CSTRs approaches, their interpretive power is constrained by the inherent complexity of the module's internal geometry, which cannot be fully captured by these idealized reactor analogies. These models provide valuable approximations for non-ideal flow but cannot unequivocally reflect the true fluid behavior, as they rely on lumped parameters that may oversimplify heterogeneous phenomena like baffle-induced recirculation. A more realistic approach could involve computational fluid dynamics (CFD) simulations, which would enable detailed resolution of velocity fields, turbulence, and multiphase interactions within the actual geometry, potentially validating or refining the RTD-derived insights.

Future work could extend this study through CFD validation to bridge empirical models with physical realism, explore higher flow rates or alternative tracers for enhanced precision, and integrate RTD insights into overall process intensification.

5.8 References

[1] Y. Gao, F.J. Muzzio, M.G. Ierapetritou, A review of the Residence Time Distribution (RTD) applications in solid unit operations, Powder Technol. 228 (2012) 416–423. https://doi.org/10.1016/j.powtec.2012.05.060.
[2] A.E. Rodrigues, Residence time distribution (RTD) revisited, Chem. Eng. Sci. 230 (2021) 116188. https://doi.org/10.1016/j.ces.2020.116188.
[3] S. Rode, Opérations polyphasiques en génie des procédés: hydrodynamique, transferts, réactions, séparations mécaniques, Ellipses, Paris, 2019.
[4] P. Markström, N. Berguerand, A. Lyngfelt, The application of a multistage-bed model for residence-time analysis in chemical-looping combustion of solid fuel, Chem. Eng. Sci. 65 (2010) 5055–5066. https://doi.org/10.1016/j.ces.2010.06.029.
[5] I. Noda, D.G. Brown-West, C.C. Gryte, Effect of flow maldistribution on hollow fiber dialysis — experimental studies, J. Membr. Sci. 5 (1979) 209–225. https://doi.org/10.1016/S0376-7388(00)80449-4.
[6] J. Lemanski, G.G. Lipscomb, Effect of shell-side flows on hollow-fiber membrane device performance, AIChE J. 41 (1995) 2322–2326. https://doi.org/10.1002/aic.690411017.
[7] Y. Wang, F. Chen, Y. Wang, G. Luo, Y. Dai, Effect of random packing on shell-side flow and mass transfer in hollow fiber module described by normal distribution function, J. Membr. Sci. 216 (2003) 81–93. https://doi.org/10.1016/S0376-7388(03)00048-6.

[8] Z. Ren, Y. Yang, W. Zhang, J. Liu, H. Wang, Modeling study on the mass transfer of hollow fiber renewal liquid membrane: Effect of the hollow fiber module scale, J. Membr. Sci. 439 (2013) 28–35. https://doi.org/10.1016/j.memsci.2013.03.030.
[9] W. Zhang, Z. Hao, J. Li, J. Liu, Z. Wang, Z. Ren, Residence Time Distribution Analysis of a Hollow-Fiber Contactor for Membrane Gas Absorption and Vibration-Induced Mass Transfer Intensification, (2014). https://doi.org/10.1021/ie500583v.
[10] F. Kavousi, E. Syron, M. Semmens, E. Casey, Hydrodynamics and gas transfer performance of confined hollow fibre membrane modules with the aid of computational fluid dynamics, J. Membr. Sci. 513 (2016) 117–128. https://doi.org/10.1016/j.memsci.2016.04.038.
[11] M. Breniaux, L. Zeng, F. Bayrounat, R. Ghidossi, Gas transfer management by membrane contactors in an oenological context: Influence of operating parameters and membrane materials, Sep. Purif. Technol. 227 (2019) 115733. https://doi.org/10.1016/j.seppur.2019.115733.
[12] S. Houlker, C.J. Davey, A. Allemand, A. Brookes, A. Moore, P. Vale, M. Pidou, E.J. McAdam, Reconciliation of gas to liquid mass transfer in parallel and transverse flow (cross-flow) hollow fiber membrane contactors (HFMC) for CO2 absorption, Sep. Sci. Technol. 56 (2021) 129–140. https://doi.org/10.1080/01496395.2019.1708934.
[13] DTS Pro 4.2 - Détermination de la distribution des Temps de Séjour, Progepi (n.d.). https://www.progepi.fr/processlab/logiciels/dts-pro/ (accessed August 13, 2025).
[14] 3M™ Liqui-Cel™ Membrane Contactors for Semiconductor and Microelectronics, (n.d.). https://www.3m.com/3M/en_US/liquicel-us/industries/semiconductor-and-microelectronics/ (accessed August 20, 2024).

General Conclusions and Perspectives

This thesis examines the potential of hollow fiber membrane contactors (HFMCs) for the intensification of stripping operations, with particular emphasis on liquid degassing of aqueous effluents in industrial water treatment. Through an integrated approach encompassing theoretical foundations, process modelling, hydrodynamic characterization, and experimental validation, the work establishes HFMCs as a viable alternative to conventional gas-liquid contactors, mitigating longstanding challenges in efficiency, compactness, and scalability while aligning with process intensification principles.

The investigation begins by delineating the critical role of stripping in contaminant removal where dissolved gases such as O_2, CH_4, and VOCs, identified as pervasive threats to industrial processes in sectors including pharmaceuticals, food production, and chemicals. Conventional technologies like packed columns, tray columns, and bubble columns exhibit inherent drawbacks, including phase interdependence that induces foaming, entrainment, and pronounced axial dispersions, yielding low specific interfacial areas (<500 m^2/m^3) and suboptimal mass transfer coefficients. These limitations render them inefficient for low gas-to-liquid ratios characteristic of stripping, necessitating large volumes and elevated energy inputs.

HFMCs presented as a superior alternative to traditional gas-liquid contactors for stripping operations, thanks to their exceptionally high surface-area-to-volume ratio (up to 25,000 m^2/m^3), compact modular design, and adaptability across flow conditions, avoiding issues like flooding and unloading. Widely applicable in water deoxygenation, methane recovery from anaerobic effluents, and VOC removal from contaminated water, HFMCs utilize diverse materials like polypropylene (PP), polyvinylidene fluoride (PVDF), and polydimethylsiloxane (PDMS), which offer varying degrees of hydrophobicity, chemical stability, fouling resistance, and durability, achieving up to 99% removal efficiencies for oxygen and methane while enabling high VOC recovery and energy-efficient processes, such as net gains of 0.05–0.17 kWh/m^3 in methane extraction that also curbs greenhouse gas emissions. Despite these strengths, challenges including membrane wetting, fouling in high-total suspended solid effluents, and scalability persist, prompting innovations like omniphobic membranes, transverse-flow module geometries, air backwashing for cleaning, and hybrid driving forces (e.g., vacuum or sweep gas) to enhance versatility.

Central to this work is the development of a generic modelling framework for mass transfer efficiency. For lumen-side configurations, which suited to low-flow regimes as in Liqui-Cel™ MM and SEPAREL® PF series, one-dimensional isothermal model is presented. This model is correlated explicitly mass transfer efficiency with the ratio between the liquid flow rate and the internal membrane area, with pressure drops predicted via Hagen-Poiseuille's law. This facilitates accurate sizing for

laboratory-scale degassing. The framework extends to shell-side cross-flow, prevalent in high-capacity modules like Liqui-Cel™ EXF and SEPAREL® EF, employing a new Sherwood-Graetz correlation. This correlation effectively predicts mass transfer coefficients and shows strong agreement with experimental data from commercial modules of varying sizes. In this flow configuration, the mass transfer efficiency for a given process depends solely on the specific liquid flow rate, independent of the module's size or geometry. This is because the Number of Transfer Units (NTU) is a function of the Graetz number alone. And also, the conventional Reynolds-based correlations are less effective, especially at low flow rates. Moreover, the frictional liquid pressure drop can be estimated successfully by using an Ergun type equation.

Lastly, hydrodynamic characterization of a commercial HFMC was performed through Residence Time Distribution (RTD) analysis, employing pulse tracer techniques (e.g., NaCl). The RTD analysis confirms that the hollow fiber membrane contactor exhibits strong, dominant plug-flow behavior on both the shell and lumen sides. Although advanced models fit the data well, they are simplified approximations and cannot fully capture the module's internal complexity, such as channeling or localized stagnant zones.

Future work could extend this study by integrating a residence time distribution (RTD) model into mass transfer efficiency predictions. This would yield a more robust predictive framework that accounts for flow maldistribution in shell-side cross-flow, enabling real-time adjustments in commercial modules such as SEPAREL® EF to minimize deviations from ideal plug flow and enhance stripping recovery rates in non-ideal geometries. Future investigations could also incorporate wetting dynamics and multi-component simulations.

Résumé en Français

Dans de nombreux procédés industriels, les flux liquides contiennent des gaz dissous à faibles concentrations. Ces gaz doivent être éliminés pour assurer la qualité du produit, l'efficacité du procédé et pour minimiser les coûts d'exploitation. Pour y parvenir, le flux liquide est mis en contact étroit avec un agent de balayage et un gradient de concentration est créé entre les deux phases. L'agent de stripping peut être un vide, un gaz de balayage ou une combinaison des deux. Il dilue le soluté dans la phase gazeuse, créant une force motrice pour le transfert de matière du liquide vers le gaz. Le gaz de balayage est généralement un gaz inerte, tel que l'azote ou l'air, qui ne réagit pas avec le soluté et n'introduit pas de contaminants supplémentaires dans le système.

Le stripping est très important dans la purification des flux liquides dans divers secteurs tels que le traitement de l'eau, les industries pharmaceutiques, alimentaire et des boissons, et la fabrication chimique. Il élimine les contaminants volatils, y compris l'oxygène (O_2), le méthane (CH_4) et les composés organiques volatils (COV). Ces impuretés dégradent la qualité du produit, déclenchent la corrosion et augmentent les risques opérationnels. Par exemple, l'oxygène dissous dans l'eau accélère la corrosion dans les chaudières et les pipelines. Les COV contribuent à la pollution de l'air et peuvent violer les réglementations environnementales. Un dégazage efficace peut améliorer la fiabilité du procédé, prolonger la durée de vie des équipements et maintenir la conformité aux normes de sécurité et environnementales.

Une large gamme de techniques a été développée pour éliminer efficacement ces gaz dissous, en particulier de l'eau, en employant divers mécanismes basés sur des procédés de séparation chimique, physique et biologique. Le choix d'une approche particulière dépend de plusieurs facteurs, y compris l'application spécifique, la concentration de gaz dissous dans l'eau et le niveau de retrait désiré. Les méthodes physiques jouent un rôle significatif dans l'élimination des gaz et incluent les colonnes garnies, les colonnes à bulles, l'aération par pulvérisation, les aérateurs à plateaux et l'aération diffusée. Ces technologies facilitent le contact direct entre le flux liquide et le flux gazeux, permettant un transfert de gaz efficace. Les technologies de contact direct, y compris les colonnes garnies à contre-courant à alimentation gravitaire, les colonnes à bulles et les colonnes à plateaux, dominent l'industrie chimique. Cependant, ces systèmes souffrent de limitations inhérentes : à faibles vitesses de gaz relatives au débit liquide, ils subissent des engorgements et des entrainements ce qui conduit à des inefficacités opérationnelles, des coûts d'entretien accrus et des problèmes de mise à l’échelle. Les colonnes à bulles, adaptées aux faibles débits de gaz, présentent des dispersions axiales significatives dans les deux phases, réduisant sévèrement les performances. Globalement, ces contacteurs fournissent des aires interfaciales spécifiques inférieures à 500 m^2/m^3 et de faibles coefficients de transfert de masse du côté liquide,

résultant en des flux de matière modestes par unité de volume et nécessitant de grands volumes d'équipements.

L'intensification des procédés, un changement de paradigme originaire des années 1970, vise à révolutionner l'ingénierie chimique en réduisant la taille des usines, la consommation d'énergie et les coûts tout en préservant la productivité. Des innovations telles que les mélangeurs statiques et les contacteurs à membranes exemplifient cette approche, permettant des processus compacts et efficaces. Les contacteurs à membranes à fibres creuses (HFMC) émergent comme une technologie alternative prometteuse, opérant en mode non-dispersif pour éliminer les risques d'inondation et d'emportement. En exploitant des diamètres de fibres submillimétriques, les HFMC atteignent des aires interfaciales spécifiques élevées jusqu'à 25 000 m^2/m^3 et des coefficients de transfert de masse du côté liquide élevés, potentiellement entraînant des réductions volumétriques substantielles par rapport aux systèmes conventionnels. De plus, ils supportent une opération à contre-courant avec une dispersion axiale minimale, accommodant des ratios gaz-liquide faibles inadaptés aux colonnes garnies ou à plateaux.

L'un des principaux avantages des HFMC est leur conception compacte, qui permet une installation économisant l'espace et une intégration dans les systèmes existants. Cette compacité les rend un choix optimal pour la modernisation ou la mise à niveau des infrastructures existantes sans nécessiter de modifications significatives. Leur compatibilité avec diverses conditions de procédé et leur adaptabilité à différents scénarios les rendent polyvalents et pratiques pour une large gamme d'applications.

Les défis clés incluent la minimisation de la résistance transmembranaire, obtenue via des membranes poreuses ou des peaux denses perméables minces pour prévenir le mouillage, tout en assurant la compatibilité des matériaux et en optimisant les configurations géométriques comme les dimensions des fibres et du module pour limiter les pertes de charge et les maldistributions. Des exemples commerciaux, tels que Liqui-Cel™ de 3M et SEPAREL® de DIC Corporation, démontrent la viabilité dans des applications comme le dégazage d'encres et la capture de CO_2 post-combustion, avec des tests pilotes enregistrant des milliers d'heures opérationnelles.

Cette thèse vise à combler ces lacunes en développant une approche générique pour la conception optimale des contacteurs à membranes à fibres creuses dans les opérations de stripping. En effet, chaque opération de stripping est caractérisée par des propriétés physico-chimiques et thermodynamiques spécifiques des phases gazeuse et liquide. Cela conduit à des caractéristiques optimales d'exploitation distinctives, qui, à leur tour, déterminent le choix du matériau et de la structure de la membrane ainsi que la géométrie optimale du contacteur. Un examen approfondi du stripping dans le traitement de l'eau met en lumière l'élimination des gaz dissous et des composés organiques volatils (COV) de l'eau afin d'assurer la qualité et la sécurité requises. Il délimite les avantages et les inconvénients des contacteurs gaz-liquide conventionnels, tels que les colonnes garnies, les colonnes à plateaux et les colonnes à bulles,

qui luttent contre le moussage, l'entrainement, l'engorgement et les dispersions axiales, des problèmes accentués à faibles ratios gaz-liquide typiques du dégazage. Ces limitations résultent en de faibles aires spécifiques et coefficients de transfert de matière, augmentant les volumes d'équipements. En contraste, les technologies de membrane à contact indirect sont introduites comme alternatives, offrant des aires interfaciales et coefficients plus élevés tout en atténuant l'interdépendance des phases. Cela s'aligne avec les principes d'intensification des procédés, soulignant le rôle des HFMC dans la résolution des lacunes conventionnelles, en proposant une solution novatrice pour le stripping.

Les fondamentaux de la conception et de l'exploitation des HFMC sont explorés, détaillant les principes fondamentaux régissant leur fonctionnalité. Les avantages de l'utilisation des HFMC par rapport aux technologies de contact gaz-liquide conventionnelles ont été mis en évidence, en particulier leur capacité à opérer efficacement sous des conditions d'écoulement variables. Les éléments clés de conception, y compris les matériaux membranaires et les géométries de module, sont examinés pour démontrer comment ils contribuent à un transfert de matière amélioré et à une efficacité opérationnelle.

Le dégazage de liquide dans les HFMC avec écoulement liquide du côté lumen et écoulement gazeux parallèle est modélisé par une approche unidimensionnelle. En raison de la faible solubilité des gaz, la résistance dominante au transfert de matière est située dans la phase liquide, permettant d'équivaloir le coefficient global de transfert de matière au coefficient du côté liquide. Étant donné le régime d'écoulement laminaire, ce coefficient est estimé en utilisant une corrélation Sherwood-Graetz. Le modèle de contacteur offre une flexibilité dans ses hypothèses : L'écoulement de la phase liquide peut être considéré comme un écoulement piston idéal ou comporter une déviation de celui-ci, liée à une distribution gaussienne des diamètres de fibres pour refléter la variabilité lors de leur fabrication. De même, en fonction du mode opérationnel, stripping sous vide ou avec gaz de balayage, la composition de la phase gazeuse est traitée comme uniforme ou spatialement distribuée, avec un écoulement idéal à contre-courant représentant le scénario le plus favorable pour le transfert de matière. Toutes les configurations de modèle établissent une relation fondamentale entre l'efficacité du transfert de matière, qui estime l'approche à l'équilibre à la sortie liquide, et le nombre d'unités de transfert (NTU).. L'analyse des nombres sans dimension révèle que le NTU est proportionnel au ratio du nombre de Sherwood sur le nombre de Graetz. Par exemple, pour atteindre une efficacité élevée de 0,98 pour le stripping sous vide d'oxygène dans des fibres de 140 µm de diamètre, le débit liquide spécifique requis est de $1.4\ 10^{-5}$ $m^3_L\ s^{-1}\ m^2_{Mint}$. Des efficacités élevées au-dessus de 0,9 nécessitent des NTU autour de 4, menant à des profils de concentration pleinement développés et des nombres de Sherwood proches de leur minimum asymptotique, indiquant que le transfert de matière est entièrement dominé par la diffusion. Le modèle a été rigoureusement validé contre des données expérimentales de la littérature sur le stripping d'oxygène et de méthane dans des modules commerciaux, considérant des variations en géométrie, température, composition et conditions opérationnelles. Les résultats montrent un bon accord entre théorie et expérience, et l'influence d'une distribution de diamètre de fibre sur l'efficacité a été démontrée avec

succès. Une considération pratique importante est la perte de charge frictionnelle côté liquide, un contributeur majeur aux coûts d'exploitation, qui est prédite en utilisant la loi de Hagen-Poiseuille. Cette relation montre que la perte de charge est proportionnelle au carré de la longueur de la fibre et à la puissance inverse quatrième du diamètre interne. Cela pose un défi significatif d'échelle, car l'utilisation de diamètres plus petits pour améliorer le transfert de matière nécessite des fibres plus courtes pour limiter la perte de charge, nécessitant ainsi un très grand nombre de fibres parallèles. L'étude reconnaît les limitations dans la validation des modèles HFMC, principalement dues à des incertitudes dans les paramètres physico-chimiques, la géométrie du module (telle que la compacité du faisceau de fibres pour les modèles du côté calandre) et une distribution potentiellement non uniforme des fluides. Comme la détermination des paramètres de transfert en utilisant des valeurs expérimentales incertaines est quelque peu hasardeuse, il est préférable, comme proposé dans ce travail, d'utiliser des modèles prédictifs conservateurs basés sur des corrélations générales de transfert de matière sans paramètres régressés sur la technologie spécifique.

Ce travail étend un cadre de modélisation pour englober les configurations d'écoulement transversal du côté calandre dans les contacteurs à membranes à fibres creuses (HFMC) pour le dégazage liquide, démontrant que le procédé peut être efficacement modélisé en utilisant une approche isotherme. Le modèle considère les modes d'opération sous vide et avec excès de gaz de balayage, supposant un écoulement piston idéal du liquide et une composition gazeuse uniforme. Puisque l'écoulement liquide est laminaire, le coefficient de transfert de matière peut être estimé en utilisant une corrélation entre les nombres de Sherwood et de Graetz. Par analogie à l'écoulement parallèle, il a été suggéré pour la première fois l'utilisation d'un nombre de Graetz pour l'écoulement transversal du côté liquide, qui est proportionnel au diamètre externe de la fibre, au réciproque du coefficient de diffusion et au ratio du débit liquide sur l'aire de membrane externe. Une nouvelle corrélation de transfert de matière liant le nombre de Sherwood à ce nombre de Graetz en écoulement transversal est proposée et se compare bien avec les corrélations issues de simulations numériques. Ce modèle de contacteur a été utilisé pour estimer les coefficients de transfert de matière à partir de mesures expérimentales de taux de récupération pour la désoxygénation de l'eau dans des HFMC commerciaux de diverses tailles. Les estimations résultantes du nombre de Sherwood sont cohérentes avec la nouvelle corrélation. L'étude démontre que le système a peu de degrés de liberté, et pour la première fois, il est montré que l'efficacité du transfert de matière peut être exprimée comme une fonction du débit liquide spécifique (débit liquide par aire de membrane externe) seule, indépendamment de la taille ou de la géométrie de l'appareil. Par conséquent, à la fois l'efficacité et le nombre de Sherwood tombent sur une courbe unique, simplifiant significativement le dimensionnement des HFMC. Par exemple, pour atteindre une efficacité de 0,98 dans le stripping sous vide d'oxygène, le débit liquide spécifique requis est approximativement de 2.15 10^{-5} m^3_L s^{-1} m^{-2}_{Mext} pour les modules SEPAREL® EF, une valeur remarquablement cohérente à travers différentes séries commerciales en raison de facteurs géométriques compensatoires. La perte de charge

frictionnelle côté liquide, un paramètre critique pour la faisabilité du procédé et les coûts d'exploitation, est abordée. Il est montré que pour l'écoulement liquide du côté calandre, la perte de charge peut être prédite en utilisant une équation de type Ergun et est liée pour la première fois au débit liquide spécifique et à la longueur du chemin liquide, fournissant un kit d'outils complet pour la conception et l'optimisation des systèmes HFMC en écoulement transversal du côté calandre.

Pour valider le comportement d'écoulement piston que nous avons supposé dans notre modèle, une caractérisation hydrodynamique d'un HFMC commercial (Liqui-Cel 2.5x8) a été réalisée des deux côtés calandre et lumen via une analyse expérimentale de la Distribution de Temps de Séjour (DTS), employant des techniques de traçage par impulsion (par ex., NaCl). Les expériences emploient des capteurs de conductivité pour un monitoring en temps réel des écoulements liquides du côté calandre et lumen. La simulation utilise le logiciel DTS Pro pour ajuster les courbes expérimentales à des analogies de réacteurs comme des CSTRs (Continuous stirred-tank reactors) en série, écoulement piston avec conditions aux limites, CSTR avec zones mortes et CSTRs en parallèles, régressant des paramètres tels que les nombres de Péclet, le nombre de cellules agités et les volumes. Les résultats de l'analyse DTS confirment que le contacteur à membranes à fibres creuses exhibe un comportement d'écoulement piston dominant et fort des deux côtés calandre et lumen.

Cette approche intégrée de modélisation et expérimentale établit un cadre prédictif et versatile pour optimiser les performances des HFMC à travers des échelles et configurations diverses. Globalement, cette thèse fournit des directives de conception pratiques pour les contacteurs à membranes à fibres creuses commerciaux (HFMC), permettant des conditions opérationnelles et des performances de module optimales. Des travaux futurs pourraient étendre ces modèles pour incorporer les dynamiques de mouillage et des simulations multi-composants.

Appendix 2-A (Dissolved Oxygen Permeability)

Appendix 2-A (Dissolved Oxygen Permeability)

Selecting an appropriate material for fabricating dense membrane is crucial for achieving optimal performance. Oxygen permeability through a polymer membrane is influenced by factors such as chemical composition, molecular weight, and crystallinity, which collectively determine the ease with which oxygen molecules traverse the membrane. In the tables below you find oxygen permeability values through different types of polymer membranes.

Table A2-1. Dissolved Oxygen Permeability in Polyacetylenes (PA)s [R-(C=C)$_n$-R']

No.	Sub. Group	Sub. Sub Group	R	R'	Monomer	permeability (barrer)	T (°C)	Ref.	Remarks
1	Poly (Diphenylacetylene)s	palymitoylated indan	phenyl	1,1,3,3-tetramethylindan-5-yl	-	14 400	25	[1]	*Acetylenic monomers containing indan and other groups (1a–m) were polymerized with TaCl5-n-Bu4Sn catalyst to give high molecular weight polymers *Indane is an ortho-fused bicyclic hydrocarbon consisting of a benzene ring fused to a cyclopentane ring *Gas permeability coefficients of polymer membranes were measured with a Rikaseiki K-315-N gas permeability apparatus equipped with a MKS Baratron detector at 25 °C. The
2			p-F	1,1,3,3-tetramethylindan-5-yl	-	17 900	25		
3			m-F	1,1,3,3-tetramethylindan-5-yl	-	14 300	25		
4			p,*m*-F2	1,1,3,3-tetramethylindan-5-yl	-	18 700	25		
5			m,*m*-F2	1,1,3,3-tetramethylindan-5-yl	-	15 200	25		
6			p-Cl	1,1,3,3-tetramethylindan-5-yl	-	11 700	25		
7			p-Br	1,1,3,3-tetramethylindan-5-yl	-	11 400	25		
8			p-Me	1,1,3,3-tetramethylindan-5-yl	-	5700	25		
9			phenyl	1,1,2,2,3,3-hexamethylindan-5-yl	-	12 900	25		
10			phenyl	Indan-5-yl	-	450	25		

11			p-SiMe3	Indan-5-yl	-	86	25		downstream side of the membrane was evacuated to 0.3 Pa.
12		-	phenyl	1,1,4,4-tetramethyl-1,2,3,4-tetrahydronaphthalen-6-yl	-	3900	25	[2]	-
13		poly(diarylacetylene)s having fluorenyl groups	Phenyl	9,9-dimethylfluoren-2-yl	-	4800	25	[3]	*Gas permeability coefficients of polymer membranes were measured with a Rikaseiki K-315-N gas permeability apparatus equipped with an MKS Baratron detector at 25 °C. The downstream side of the membrane was evacuated at 0.3 Pa, while the upstream side was filled with a gas at about 1 atm (105 Pa),
14			4-Fluorophenyl	9,9-dimethylfluoren-2-yl	-	6200	25		
15			3-Fluorophenyl	9,9-dimethylfluoren-2-yl	-	5900	25		
16			3,4-Difluorophenyl	9,9-dimethylfluoren-2-yl	-	6600	25		
17			3,5-Difluorophenyl	9,9-dimethylfluoren-2-yl	-	2700	25		
18			4-Bromophenyl	9,9-dimethylfluoren-2-yl	-	5000	25		
19			4-Tert-butylphenyl	9,9-dimethylfluoren-2-yl	-	3500	25		
20			4-Trimethylsilylphenyl	9,9-dimethylfluoren-2-yl	-	470	25		

21			Phenyl	9,9-dimethyl-7-bromofluoren-2-yl	-	2000	25		
22			Phenyl	9,9-dimethyl-7-trimethylsilylfluoren-2-yl	-	5400	25		
23			Phenyl	spiro[cyclopropane-1,9′-fluoren]-2′-yl	-	660	25		
24			4-Trimethylsilylphenyl	spiro[cyclopropane-1,9′-fluoren]-2′-yl	-	1000	25		
25		Poly (diphenylacetylenes) Having Aliphatic para-Substituents	-	-	Poly(p-t-BUDPA)	1100	25	[4]	1- (p-t-Butylphenyl) -2-phenylacetylene and 1- (p-n-butylphenyl) -2-phenylacetylene were polymerized in catalytic systems based on TaC15 to give new polymers in high yields. These monomers were more reactive than diphenylacetylene (DPA) in copolymerization
26			-	-	Poly (p-n-BuDPA)	100	25		
27			-	-	Poly(p-Me,SiDPA)	1100	25		
28			-	-	$(SiMe_2O)_n$	670	25		
29		poly(diphenylacetylene)s with two or	-	-	$(TMS)_3Si_2$ DP	1300	25	[5]	-

30			-	-	m,p-$(TMS)_2DP$	1100	25		
31			-	-	p-TMSDP	1100	25		
32			-	-	TMSP	6100	25		
33		-	-	-	1-phenyl-2-p-(trimethylsilyl)phenylacetylene	1550	25	[6]	-
34	PTMSP	-	-	-	-	14 800	25	[1]	*Gas permeability coefficients of polymer membranes were measured with a Rikaseiki K-315-N gas permeability apparatus equipped with a MKS Baratron detector at 25 °C. The downstream side of the membrane was evacuated to 0.3 Pa. *Polymerized with TaCl5-n-Bu4Sn catalyst to give high molecular weight polymers
35		-	-	-	-	4500	25	[4]	-

36		-	-	-	-	6100	25	[5]	-
37		-	-	-	-	11600	25	[7]	permeability measured in the dry state (i.e., both sides of the membrane were in the gas phase) P_G
38		-	-	-	-	10800	30		
39		-	-	-	-	10100	35		
40		-	-	-	-	9330	40		
41		-	-	-	-	1110	25	[8]	* Films synthesized with TaCl5 and prepared by casting from a toluene solution of the polymer
42		-	-	-	-	3000	25	[9]	*Prepared from 2 % toluene solution. *Synthesized with TaCl5
43		-	-	-	-	4000	25	[10]	*This synthesis was carried out under dry nitrogen. Hexane solution of butyllithium (1.6M, 700 mL) was concentrated by evaporation of hexane (450 mL), and then diluted by addition of ether (600 mL). Propyne (1.0 mol, 40 g) was bubbled into this solution cooled at -30°C. * Synthesized with TaCl5

44		-	-	-	-	4500	25	[11]	synthesized with TaCl5
45		-	-	-	-	8170	25	[12]	Poly (TMSP) can be obtained by metathesis polymerization of 1-(trimethylsilyl)-1-propyne by TaCl5 and NbCl5.
46		-	-	-	-	8800	25	[13]	The membranes used in this study were synthesized in-house polymerized using TaCls as catalyst. Discs of PTMSP (9 cm in diameter and 50 to 115 p in thickness) were cast from 1.75 wt.% solutions in toluene. For sorption measurements, the discs were cut into smaller pieces.
47		-	-	-	-	13200	25	[14]	In this work, it's found that the rate of permeability loss for samples stored in vacuum is much faster than for samples exposed continuously to an organic vapor
48	poly(4-methyl-2-	-	-	-	PMP 1	2100	25	[15]	synthesized with NbBr5 and TaBr5-based catalytic systems
49		-	-	-	PMP 2	2250	25		

50		-	-	-	PMP 6	1600	25		
51		-	-	-	PMP 8	1400	25		
52		-	-	-	PMP 10	1700	25		
53		-	-	-	PMP 22	1050	25		
54		-	-	-	PMP 24	1100	25		

Table A2-2 .Oxygen permeability in other different membrane polymers.

No.	Group	Sub. Group	Polymer	Permeability (barrer)	T (°C)	Ref.	Remarks
1	Polyimides	6FDA-durene polyimide	-	134.8	35	[16]	feed pressure 2.0 atm
2			-	132.5			feed pressure 3.5 atm
3			-	132.1			feed pressure 5.0 atm
4			-	127.9			feed pressure 7.0 atm
5			-	125.1			feed pressure 10.0 atm
6		Spirobifluorene- and Dibromospirobifluorene-Based Polyimides	6FDA–SBF	35.1	35	[17]	synthesized from 9,9′-spirobifluorene-2,2′-diamine (SBF) and its bromine-substituted analogue 3,3′-dibromo-9,9′-spirobifluorene-2,2′-diamine (BSBF) with three different dianhydrides (6FDA, PMDA, and SPDA).
7			PMDA–SBF	35.5			
8			SPDA–SBF	111			
9			6FDA–BSBF	107			
10			PMDA–BSBF	116			
11			SPDA–BSBF	243			
12			PIM–PI-3b	85			
13		-	PIM-PI-1	150	30	[18]	synthesized from 9,9′-spirobifluorene-2,2′-diamine (SBF) and its bromine-substituted analogue 3,3′-dibromo-9,9′-spirobifluorene-2,2′-diamine (BSBF) with three different dianhydrides (6FDA, PMDA, and SPDA).
14			PIM-PI-3	85			
15			PIM-PI-8	545			
16		-	PI-PIM	1354.5	-	[19]	membrane thickness 45-60 (μm)
17		-	PI-PIM	1071	-		membrane thickness 80-100 (μm)
18	Fluoropolymers	PTFE	-	97.2	23	[20]	Commercial membrane.
19		PFA	-	0	23		
20		FEP	-	187.92	23		
21		ETFE	-	22.68	23		
22		CTFE	-	3.888	23		
23		ECTFE	-	6.48	23		
24		PVDF	-	1.296	23		
25		PVF	-	0.7776	23		

References

[1] Y. Hu, M. Shiotsuki, F. Sanda, B.D. Freeman, T. Masuda, Synthesis and Properties of Indan-Based Polyacetylenes That Feature the Highest Gas Permeability among All the Existing Polymers, Macromolecules 41 (2008) 8525–8532. https://doi.org/10.1021/ma801845g.

[2] Y. Hu, M. Shiotsuki, F. Sanda, T. Masuda, Synthesis and extremely high gas permeability of polyacetylenes containing polymethylated indan/tetrahydronaphthalene moieties, Chem. Commun. (2007) 4269. https://doi.org/10.1039/b712327b.

[3] A. Fukui, K. Hattori, Y. Hu, M. Shiotsuki, F. Sanda, T. Masuda, Synthesis, characterization, and high gas permeability of poly(diarylacetylene)s having fluorenyl groups, Polymer 50 (2009) 4159–4165. https://doi.org/10.1016/j.polymer.2009.06.064.

[4] H. Kouzai, T. Masuda, T. Higashimura, Synthesis and properties of poly (diphenylacetylenes) having aliphatic para-substituents, J. Polym. Sci. Part Polym. Chem. 32 (1994) 2523–2530. https://doi.org/10.1002/pola.1994.080321315.

[5] G. Kwak, T. Aoki, T. Kaneko, Synthesis and stable high oxygen permeability of poly(diphenylacetylene)s with two or three trimethylsilyl groups, Polymer 43 (2002) 1705–1709. https://doi.org/10.1016/S0032-3861(01)00739-X.

[6] M.T. and, T. Masuda*, Poly(diphenylacetylene) Membranes with High Gas Permeability and Remarkable Chiral Memory, ACS Publ. (2002). https://doi.org/10.1021/ma011537f.

[7] K. Nakamura, T. Kitagawa, S. Nara, T. Wakamatsu, Y. Ishiba, S. Kanehashi, S. Sato, K. Nagai, Permeability of Dry Gases and Those Dissolved in Water through Hydrophobic High Free-Volume Silicon- or Fluorine-Containing Nonporous Glassy Polymer Membranes, Ind. Eng. Chem. Res. 52 (2013) 1133–1140. https://doi.org/10.1021/ie300793t.

[8] T. Aoki, K. Shinohara, T. Kaneko, E. Oikawa, Enantioselective Permeation of Various Racemates through an Optically Active Poly{1-[dimethyl(10-pinanyl)silyl]-1-propyne} Membrane, Macromolecules 29 (1996) 4192–4198. https://doi.org/10.1021/ma9517254.

[9] T. Masuda, Y. Iguchi, B.-Z. Tang, T. Higashimura, Diffusion and solution of gases in substituted polyacetylene membranes, Polymer 29 (1988) 2041–2049. https://doi.org/10.1016/0032-3861(88)90178-4.

[10] K. Takada, H. Matsuya, T. Masuda, T. Higashimura, Gas permeability of polyacetylenes carrying substituents, J. Appl. Polym. Sci. 30 (1985) 1605–1616. https://doi.org/10.1002/app.1985.070300426.

[11] K. Tsuchihara, T. Masuda, T. Higashimura, Tractable silicon-containing poly(diphenylacetylenes): their synthesis and high gas permeability, J. Am. Chem. Soc. 113 (1991) 8548–8549. https://doi.org/10.1021/ja00022a066.

[12] T. Masuda, E. Isobe, T. Higashimura, K. Takada, Poly[1-(trimethylsilyl)-1-propyne]: a new high polymer synthesized with transition-metal catalysts and characterized by extremely high gas permeability, J. Am. Chem. Soc. 105 (1983) 7473–7474. https://doi.org/10.1021/ja00363a061.

[13] R. Srinivasan, S.R. Auvil, P.M. Burban, Elucidating the mechanism(s) of gas transport in poly[1-(trimethylsilyl)-1-propyne] (PTMSP) membranes, J. Membr. Sci. 86 (1994) 67–86. https://doi.org/10.1016/0376-7388(93)E0128-7.

[14] I. Pinnau, C.G. Casillas, A. Morisato, B.D. Freeman, Long-term permeation properties of poly(1-trimethylsilyl-1-propyne) membranes in hydrocarbon—Vapor environment, J. Polym. Sci. Part B Polym. Phys. 35 (1997) 1483–1490. https://doi.org/10.1002/(SICI)1099-0488(19970730)35:10%253C1483::AID-POLB2%253E3.0.CO;2-T.

[15] S.M. Matson, V.P. Makrushin, I.S. Levin, N.A. Zhilyaeva, E.G. Litvinova, V.S. Khotimskiy, Structure and properties of poly(4-methyl-2-pentyne) synthesized with NbBr5 and TaBr5-based catalytic systems, Polymer 202 (2020) 122682. https://doi.org/10.1016/j.polymer.2020.122682.

[16] W.-H. Lin, T.-S. Chung, Gas permeability, diffusivity, solubility, and aging characteristics of 6FDA-durene polyimide membranes, J. Membr. Sci. 186 (2001) 183–193. https://doi.org/10.1016/S0376-7388(01)00333-7.

[17] X. Ma, O. Salinas, E. Litwiller, I. Pinnau, Novel Spirobifluorene- and Dibromospirobifluorene-Based Polyimides of Intrinsic Microporosity for Gas Separation Applications, Macromolecules 46 (2013) 9618–9624. https://doi.org/10.1021/ma402033z.

[18] B.S. Ghanem, N.B. McKeown, P.M. Budd, J.D. Selbie, D. Fritsch, High-Performance Membranes from Polyimides with Intrinsic Microporosity, Adv. Mater. 20 (2008) 2766–2771. https://doi.org/10.1002/adma.200702400.

[19] J. Wang, Z. Shi, Y. Zang, H. Jia, M. Teraguchi, T. Kaneko, T. Aoki, Macromolecular Design for Oxygen/Nitrogen Permselective Membranes—Top-Performing Polymers in 2020—, Polymers 13 (2021) 3012. https://doi.org/10.3390/polym13173012.

[20] Fluoroplastic solutions for your applications - Adtech, Adtech Polym. Eng. (2019). https://adtech.co.uk/ (accessed June 27, 2023).

Appendix 5-A Deconvolution with Critically Damped Second-Order Model

5.9Differential Equation

The differential equation for the second-order system is:

$$s(t) + \frac{2\xi}{\omega_0} \cdot \frac{ds(t)}{dt} + \frac{1}{\omega_0^2} \cdot \frac{d^2 s(t)}{dt^2} = Ke(t)$$

5.10Transfer Function

The transfer function in the Laplace domain (using p as the Laplace variable) is:

$$H\,(p) = \frac{K\,\omega_0^2}{p^2 + 2\xi\omega_0 p + \omega_0^2}$$

5.11Step Input Response

Consider a step input $\mathrm{e(t)} = \mathrm{E_0 u(t)}$, where $\mathrm{u(t)}$ is the unit step function.

The Laplace transform is $\mathrm{E(p)} = \frac{\mathrm{E_0}}{p}$

The output in the Laplace domain is:

$$S(p) = H(p)\,E(p) = \frac{\mathrm{E_0}\,K\,\boldsymbol{\omega}_0^2}{p(p^2 + 2\xi\omega_0 p + \boldsymbol{\omega}_0^2)}$$

5.12Critical Damping Case (ξ=1)

For critical damping (ξ=1), the discriminant Δ=0, and the quadratic has a double root at

$$p = -\omega_0$$

The transfer function simplifies to:

$$H(p) = \frac{K\,\boldsymbol{\omega}_0^2}{(p + \omega_0)^2}$$

The output becomes:

$$S(p) = \frac{\mathrm{E_0}\,K\,\boldsymbol{\omega}_0^2}{p\,(p + \omega_0)^2}$$

5.13Partial Fraction Decomposition

$$S(p) = K\,\mathrm{E_0}\left[\frac{1}{p} - \frac{1}{p+\omega_0} - \frac{\omega_0}{(p+\omega_0)^2}\right]$$

5.14Inverse Laplace Transform

The time-domain output is:

$$s(t) = \mathrm{E}_0 K\ [1 - e^{-\omega_0 t} - \omega_0 t\, e^{-\omega_0 t}] = \mathrm{E}_0 K\ [1 - (1 + \omega_0 t)e^{-\omega_0 t}]$$

The system is stable since the pole is at $p = -\omega_0 < 0$.

5.15Inverse Problem: Finding Input from Output (Using a Linear Sensor)

Assuming the sensor transfer function is $H(p)$, the input in the Laplace domain is:

$$E(p) = \frac{S(p)}{H(p)} = S(p) * \frac{(p+\omega_0)^2}{K\,\boldsymbol{\omega}_0^2}$$

In the time domain:

$$e(t) = \frac{1}{K\boldsymbol{\omega}_0^2}\left(\frac{d^2 s(t)}{dt^2} + 2\omega_0 \frac{ds(t)}{dt} + \omega_0^2\, s(t)\right)$$

5.16For Critical Damping Response

$$s(t) = \mathrm{E}_0 K\ [1 - (1 + \omega_0 t)e^{-\omega_0 t}]$$

$$\frac{ds(t)}{dt} = \mathrm{E}_0 K\omega_0^2 t e^{-\omega_0 t}$$

$$\frac{d^2 s(t)}{dt^2} = \mathrm{E}_0 K\omega_0^2 e^{-\omega_0 t}\ (1 - \omega_0 t)$$

Plugging into the expression for e(t) :

$$e(t) = \frac{1}{K\omega_0^2}\ [\mathrm{E}_0 K\omega_0^2 e^{-\omega_0 t}\ (1 - \omega_0 t) + 2\,\omega_0\ \mathrm{E}_0 K\omega_0^2 t e^{-\omega_0 t} + \omega_0^2 \mathrm{E}_0 K\ (1 - (1 + \omega_0 t)e^{-\omega_0 t})$$

Simplifying and Combining:

$$e(t) = \mathrm{E}_0\, e^{-\omega_0 t}\ (1 - \omega_0 t) + 2\mathrm{E}_0\omega_0^2 t e^{-\omega_0 t} + \mathrm{E}_0\ [(1 - (1 + \omega_0 t)e^{-\omega_0 t}]$$

Appendix 5-B Comparison of Raw and Processed Conductivity Signals at the Inlet and the Outlet Transmitters

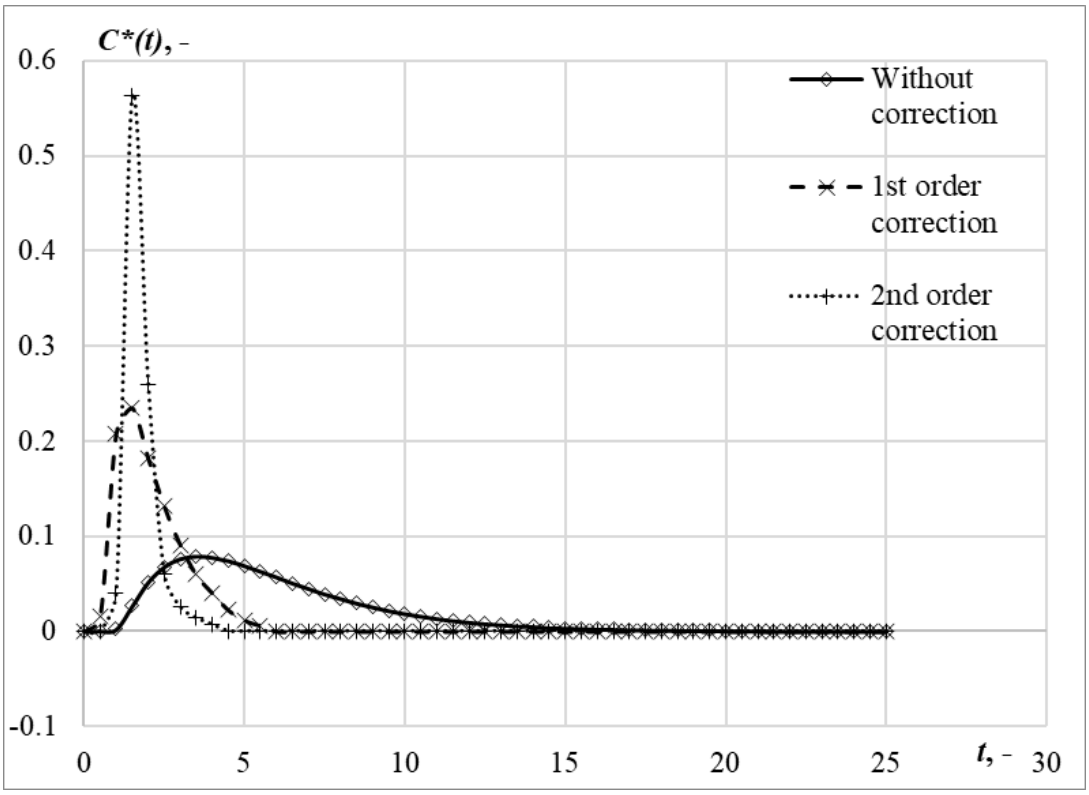

Figure B5-1. Comparison of Raw and Processed Conductivity Signals at the Inlet Transmitter

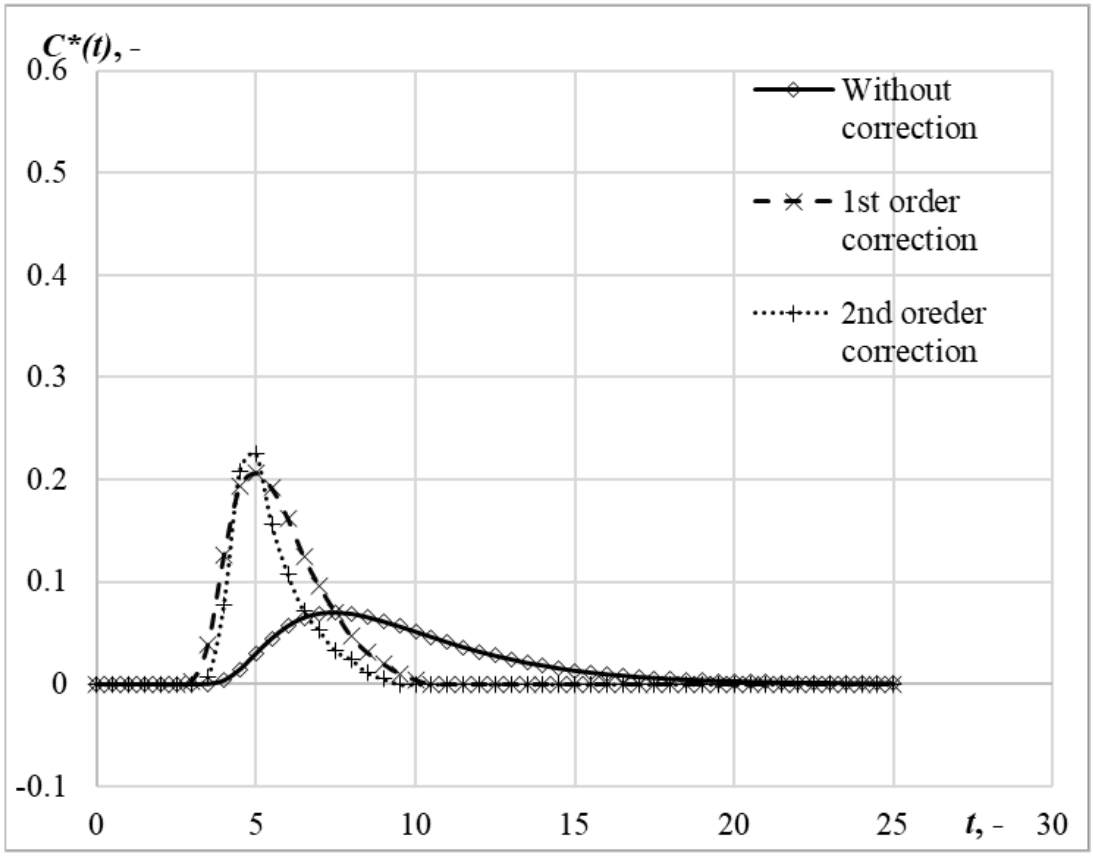

Figure B5-2 Comparison of Raw and Processed Conductivity Signals at the Outlet Transmitter